

Heteroatom Doped Porous Carbon Structures as Electrocatalysts for Fuel Cells

By

Shijina K

10CC18A39014

A thesis submitted to the
Academy of Scientific & Innovative Research
for the award of the degree of
DOCTOR OF PHILOSOPHY
in
SCIENCE

Under the supervision of
Dr. U. S. Hareesh



CSIR-NATIONAL INSTITUTE FOR INTERDISCIPLINARY
SCIENCE AND TECHNOLOGY (CSIR-NIIST)
THIRUVANANTHAPURAM-695019, KERALA, INDIA



Academy of Scientific and Innovative Research
AcSIR Headquarters, CSIR-HRDC campus
Sector 19, Kamla Nehru Nagar,
Ghaziabad, U.P. - 201 002, India

April 2022

Dedicated to My Beloved Parents

**CSIR-NATIONAL INSTITUTE FOR INTERDISCIPLINARY
SCIENCE AND TECHNOLOGY (CSIR-NIIST)**

Council of Scientific and Industrial Research (CSIR)

GOVERNMENT OF INDIA

Thiruvananthapuram-6595019, India



Dr. U. S. Hareesh
Senior Principal Scientist

Functional Materials Section
Materials Science and Technology Division

CERTIFICATE

This is to certify that the work incorporated in this Ph.D. thesis entitled "*Heteroatom Doped Porous Carbon Structures as Electrocatalysts for Fuel Cells*" submitted by *Ms. Shijina K*, to the *Academy of Scientific and Innovative Research (AcSIR)*, in partial fulfilment of the requirements for the award of the *Degree of Doctor of Philosophy* in *Science* embodies original research work carried out by the student. We further certify that this work has not been submitted to any other University or Institution in part or full for the award of any degree or diploma. Research materials obtained from other sources and used in this research work have been duly acknowledged in the thesis. Images, illustrations, figures, tables etc., used in the thesis from other sources have also been duly cited and acknowledged.

Shijina K
13.04.2022


Shijina K
(Student)

U. S. Hareesh
13.04.2022

Dr. U. S. Hareesh
(Thesis Supervisor)

STATEMENTS OF ACADEMIC INTEGRITY

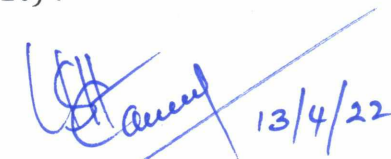
I Shijina K, a Ph.D. student of the Academy of Scientific and Innovative Research (AcSIR) with Registration No. 10CC18A39014 hereby undertake that, the thesis entitled "**Heteroatom Doped Porous Carbon Structures as Electrocatalysts for Fuel Cells**" has been prepared by me and that the document reports original work carried out by me and is free of any plagiarism in compliance with the UGC Regulations on "Promotion of Academic Integrity and Prevention of Plagiarism in Higher Educational Institutions (2018)" and the CSIR Guidelines for "Ethics in Research and in Governance (2020)".


13/4/22
Shijina K

13.04.2022

Thiruvananthapuram

It is hereby certified that the work done by the student, under my supervision, is plagiarism-free in accordance with the UGC Regulations on "Promotion of Academic Integrity and Prevention of Plagiarism in Higher Educational Institutions (2018)" and the CSIR Guidelines for "Ethics in Research and in Governance (2020)".


13/4/22
Dr. U. S. Hareesh

13.04.2022

Thiruvananthapuram

DECLARATION

I, Shijina K, bearing AcSIR Registration No. 10CC18A39014 declare that my thesis entitled, "**Heteroatom Doped Porous Carbon Structures as Electrocatalysts for Fuel Cells**" is plagiarism free in accordance with the UGC Regulations on "Promotion of Academic Integrity and Prevention of Plagiarism in Higher Educational Institutions (2018)" and the CSIR Guidelines for "Ethics in Research and in Governance (2020)". I would be solely held responsible if any plagiarised content in my thesis is detected, which is violative of the UGC regulations 2018.

Shijina K
13/4/22

Shijina K

13.04.2022

Thiruvananthapuram

ACKNOWLEDGEMENTS

The most awaited time is reached; I am going to have the prestigious doctoral degree in my life. During this amazing journey, I must thank one and all who supported and motivated me; without any of them, this thesis would not have been possible. I take this opportunity to acknowledge them and extend my sincere gratitude for helping me and making this PhD thesis a possibility.

My first and foremost gratitude to Dr. U. S. Hareesh, my supervisor for his continuous encouragement, guidance and solid support that immensely helped me professionally and personally throughout these years to accomplish my research goals. I thank him for introducing me to the world of material science and for giving enough freedom in our lab and induced free-thinking capability to design a work.

I heartily express my deep sense of gratitude to the valuable guidance and suggestions given by Dr. G. S. Sailaja, Professor, Cochin University of Science and Technology. Her inspiring guidance, encouragement and support has helped me a lot in refining my ideas throughout this journey.

I am equally indebted to Dr. Balagopal N. Nair, General Manager Noritake Co. Ltd., Japan, for facilitating this collaborative research. His patient guidance and constructive suggestions helped me a lot to overcome the initial difficulties of the research. I thank him also for his well-timed instructions in the preparation of manuscripts.

I wish to express my sincere thanks to Dr. G. M. Anilkumar, Deputy General Manager, Noritake Co. Ltd., Japan, for the technical discussions and suggestions. His continuous support, enthusiasm, motivation and vast knowledge helped me a lot during my research days.

I wish to express my sincere gratitude to Dr. Sreekumar Kurungot (Principal Scientist, CSIR-National Chemical laboratory, Pune) for extending the facilities for electrocatalytic measurements and also for his technical guidance.

I am very much thankful to Prof. Takeo Yamaguchi, Tokyo Institute of Technology, Japan, for giving me an opportunity to do a part of my research work and providing me invaluable guidance throughout my research during my stay in Japan.

I am extremely thankful to Dr. K. G. K. Warriar, former Head, MSTD, for the inspirational presence and scientific advises.

I extend my gratitude towards Dr. A. Ajayaghosh, present Director and Dr. Suresh Das, former Director of CSIR-NIIST, Trivandrum, for providing me the necessary facilities and infrastructure of the institute for carrying out this work.

I express my sincere thanks to Dr. S. Savithri, Head, MSTD, Dr. Harikrishna Bhatt, Dr. P. Prabhakar Rao and Dr. M. L. P Reddy, former Heads, MSTD for their support and extension of facilities.

I extend my sincere thanks to Dr. Karunakaran, Dr. C. H. Suresh and Dr. Luxmi Varma, present and former AcSIR program co-ordinators at CSIR-NIIST, for their timely help and advice for the academic procedures of AcSIR.

Dr. T. P. D. Rajan, Dr. Biswapriya Deb and Dr. Suraj Soman (DAC members) are gratefully acknowledged for their constant support and suggestions throughout the research period.

I am immensely thankful to Mr. A. Peer Mohamed for the technical as well as mental support during my research tenure at NIIST.

I am also thankful to Mr. Kiran Mohan for TEM analysis, Mrs. Soumya Valsalam and Mr. Harish Raj V for SEM observations. Mr. Prithviraj, Mrs. Ajuthara (XRD analysis), Dr. K.K. Maiti (Raman analysis) and Dr. Rajith I. V., (Electrochemical measurements) are greatly acknowledged for extending the respective analytical facilities.

Mrs. Manjusha, Ms. Sumitha N. S., Ms. Gayathri Dilip, Ms. Vinitha V. and Mr. Titto Sunil John are acknowledged for their assistance in my experiments and studies during their stay at NIIST.

I would like to thank my former colleagues Dr. Smitha V. S., Dr. Manjumol, Dr. Asha Krishnan, Dr. Sreeremya, Dr. Arun, Dr. Akhil K., Dr. Sankar Sasidharan, Dr. Harsha N, Dr. Manu Jose, Dr. Swetha S., Dr. Subha P. V., Dr. Mega Joy, Dr. Minju Thomas, Mr. Firozkhan, Dr. Sundar R, Dr. Narasimman R., Dr. Vidya Kattoor, Dr. Midhun Mohan, Dr. Jintu Francis, Mrs. Sreeja Chandran, Mr. Sriram, Ms. Jinu Joji, Mr. Unnikrishnan R. and Dr. Seethalekshmi Sunil for their immense support.

My special appreciation goes to my lab mates Dr. Suyana P., Mr. Visakh Vijayan, Mrs. Nimisha G., Mrs. Surya Kuttan, Ms. Vaishna Priya, Mr. Achu, Ms. Devika, Mr. Sidharth and Ms. Suja for their friendship and encouragement for making my lab hours very special, comfortable and memorable.

Dr. Gayathri Prabhu, Ms. Ramya R., Dr. Sajitha Surendran, Mrs. Neethu Mukundan, Mrs. Lakshmi, Ms. Anasooya, Dr. Jean Maria, Dr. Saranya Dr. Soumya, and Dr. Aswathi are sincerely thanked for their memorable companionship during my stay at Thiruvananthapuram.

I acknowledge Council of Scientific & Industrial Research (CSIR), New Delhi, India for providing research funding and facilities for the completion of this work.

I am deeply indebted to my parents Mr. Purushothaman and Mrs. Pushpavally, for their unconditional care and love that gave wings to my dreams. My loving siblings Shinju and Anu are always a source of strength, support and affection.

Words can't express my gratitude to my best friend and love of my life Mr. Vivek, for his care, love and support during the last stages of my thesis writing.

I thank the almighty for the blessings conferred upon me.

Shijina K

CONTENTS

Certificate	i
Statement of Academic Integrity	ii
Declaration	iii
Acknowledgements	iv
Contents	vii
List of Figures	xi
List of Tables	xx
List of Abbreviations	xxii
Preface	xxiv
Chapter 1 Introduction to Electrocatalysis in Fuel Cell	1-56
1.1 Introduction	2
1.2 Fuel Cells	4
1.2.1 Alkaline Fuel Cell	6
1.3 Oxygen reduction reaction (ORR)	7
1.3.1 ORR mechanism	8
1.4 Techniques for ORR Measurements	9
1.4.1 Cyclic Voltammetry (CV)	9
1.4.2 Rotating Disk Electrode (RDE)	11
1.4.3 Rotating Ring Disk Electrode (RRDE)	13
1.4.4 Calibration of the Reference Electrode	15
1.5 Metal Organic Framework	16
1.6 Zeolitic Imidazolate Framework	18
1.6.1 Zeolitic Imidazolate Framework-8 & 67 (ZIF-8 and ZIF-67)	21
1.7 Metal Organic Gel	22
1.8 Electrocatalyst for ORR	24
1.8.1 Pt Alloys	24
1.8.2 Metal-Free Catalysts	25
1.8.2.1 Different Types of Doped Nitrogen	25
1.8.3 Non-precious Metal Catalysts (NPMCs)	29
1.8.3.1 Metal Organic Framework Derived Carbon	30

1.8.3.2	Metal Organic Gel Derived Caron	32
1.9	Direct Borohydride Fuel Cells	33
1.9.1	Electrocatalysts for BOR	36
1.9.1.1	Noble Metal Based Catalyst	36
1.9.1.2	Non-noble Metal Based Catalyst	37
1.10	Definition of the Present Problem	38
	References	39
Chapter 2	Melamine Formaldehyde- Metal Organic Gel Interpenetrating Polymer Network Derived Fe-N-doped Porous Carbon Electrocatalysts for Oxygen Reduction Reaction	57-87
2.1	Introduction	58
2.2	Experimental	60
2.2.1	Materials	60
2.2.2	Synthesis of Fe-MOG, Fe-MOG-MF and Fe-MOG-MFN IPNs	61
2.2.3	Synthesis of Fe-N Doped Porous Carbon	61
2.2.4	Structural Characterization	61
2.2.5	Electrochemical Characterization	62
2.3	Results and Discussion	63
2.3.1	Rheological Studies	64
2.3.2	Morphology and Microstructure Analysis	64
2.3.3	Surface Area Analysis	67
2.3.4	Phase Analysis	68
2.3.5	Chemical Composition Analysis	69
2.3.6	Electrochemical Analysis	74
2.4	Conclusions	81
	References	81
Chapter 3	Chitosan Intercalated Metal Organic Gel as a Green Precursor of Fe, N co-doped Mesoporous Graphitic Carbon for Oxygen Reduction Reaction	88-116
3.1	Introduction	89
3.2	Experimental	92

3.2.1	Materials	92
3.2.2	Synthesis of Chitosan-Fe Complex Mediated MOG (Fe-MCS)	93
3.2.3	Synthesis of Chitosan Intercalated Fe-MOG (Fe-MCS-M)	93
3.2.4	Synthesis of Porous Carbon	93
3.2.5	Structural Characterization	93
3.2.6	Electrochemical Characterization	94
3.3	Results and Discussion	95
3.3.1	Thermogravimetric Analysis	96
3.3.2	Morphology and Microstructure Analysis	96
3.3.3	Surface Area Analysis	99
3.3.4	Phase Analysis	101
3.3.5	Chemical Composition Analysis	101
3.3.6	Electrochemical Analysis	105
3.4	Conclusions	112
	References	112
Chapter 4	Fe₃C Encapsulated Pod like Carbon Structures for Efficient Oxygen Reduction Reaction	117-144
4.1	Introduction	118
4.2	Experimental	119
4.2.1	Materials	119
4.2.2	Synthesis of Fe-G-MF IPN	119
4.2.3	Synthesis of Fe, N Doped Porous Carbon	120
4.2.4	Structural Characterization	120
4.2.5	Electrochemical Characterization	120
4.3	Results and Discussion	121
4.3.1	Phase Analysis	122
4.3.2	Morphology and Microstructure Analysis	124
4.3.3	Surface Area Analysis	128
4.3.4	Chemical Composition Analysis	129
4.3.5	Electrochemical Analysis	133
4.4	Conclusions	141

References	141	
Chapter 5	Zeolitic Imidazole Framework Derived Bimetallic Carbon Alloy Catalyst for the Electrocatalytic Borohydride Oxidation Reaction	145-179
5.1	Introduction	146
5.2	Experimental	149
5.2.1	Materials	149
5.2.2	Synthesis of Trimetallic ZIF	150
5.2.3	Synthesis of Carbon Alloy Catalyst	150
5.2.4	Structural Characterization	150
5.2.5	Electrochemical Characterization	151
5.3	Results and Discussion	152
5.3.1	Phase Analysis	152
5.3.2	Morphology and Microstructure Analysis	154
5.3.3	Surface Area Analysis	161
5.3.4	Chemical Composition Analysis	162
5.3.5	Electrochemical Analysis	167
5.4	Conclusions	174
	References	175
Chapter 6	Summary and scope of future work	180-183
	Abstract of the Thesis	184
	List of publication	185
	Papers presented at conferences	185
	Copy of SCI publication emanating from the thesis	187

LIST OF FIGURES

Chapter 1

1	Figure 1.1	The global energy consumption, measured in terawatt-hours (TWh) per year. (Courtesy: Vaclav Smil (2017). Energy Transitions: Global and National Perspectives. & BP Statistical Review of World Energy)	2
2	Figure 1.2	Ragone plot for energy storage devices	4
3	Figure 1.3	Fuel cell operation diagram	5
4	Figure 1.4	Schematic representation of alkaline fuel cell	7
5	Figure 1.5	Schematic showing the mechanism of (a) four-electron and (b) two-electron reduction of oxygen	9
6	Figure 1.6	Schematic showing the typical setup of cyclic voltammetry	10
7	Figure 1.7	Cyclic voltammetry wave form	10
8	Figure 1.8	Typical cyclic voltammogram of Pt/C in N ₂ and O ₂ saturated 0. M KOH solution	11
9	Figure 1.9	The scheme for the setup of rotating disc electrode	11
10	Figure 1.10	The different oxygen reduction regions in a typical RDE LSV curve at various working electrode rotation rates	13
11	Figure 1.11	(a) Top view and (b) schematic of the catalytic reaction occurring during ORR in alkaline medium at the rotating ring disk electrode	14
12	Figure 1.12	Calibration curve of the Hg/HgO reference electrode in H ₂ saturated 0.1 M KOH solution	15
13	Figure 1.13	A general scheme of a three-dimensional metal-organic framework construction	16
14	Figure 1.14	Various MOFs with surface area and the time of evolution	17
15	Figure 1.15	The bridging angles in (a) ZIF and (b) Zeolite	19

16	Figure 1.16	The structure of ZIF-8 and ZIF-67	22
17	Figure 1.17	Metal organic gel structures	23
18	Figure 1.18	Volcano plot showing oxygen reduction activity of different metals as a function of oxygen binding energy (adapted from reference)	24
19	Figure 1.19	The nitrogen configurations observed on N-doped carbon catalysts	26
20	Figure 1.20	Raman spectrum of N-doped carbon	27
21	Figure 1.21	Typical N1s spectra of N-doped carbon	27
22	Figure 1.22	Illustration of the host-guest chemistry strategy to fabricate MOF-derived Fe-N/C catalysts (adapted from reference)	32
23	Figure 1.23	Schematic of a direct borohydride fuel cell	34
24	Figure 1.24	Schematic representation of (a) H ₂ /O ₂ fuel cell fed by H ₂ generated by hydrolysis of NaBH ₄ (IBFC) and (b) direct borohydride fuel cell	35
25	Figure 1.25	Schematic of the competition between the direct borohydride electrooxidation and the hydrolysis	36

Chapter 2

26	Figure 2.1	Schematic illustration of the formation of IPN	60
27	Figure 2.2	Schematic illustration for the formation of Fe-MN-NC	63
28	Figure 2.3	Amplitude sweep measurement of Fe-MOG. Solid and open symbol represent the storage and loss modulus respectively	64
29	Figure 2.4	SEM images of (a, b) Fe-MOG, (c, d) Fe-M-NC and (e, f) Fe-MN-NC	65
30	Figure 2.5	Elemental mapping of (a) Fe-M-NC and (b) Fe-MN-NC	65
31	Figure 2.6	TEM images of Fe-M-C	66
32	Figure 2.7	TEM images of (a, b, c) Fe-M-NC and (d, e, f) Fe-MN-NC	67

33	Figure 2.8	(a) N ₂ adsorption-desorption isotherms of Fe-M-C, Fe-M-NC and Fe-MN-NC, (b) BJH cumulative pore volume and (c) pore size distribution of Fe-M-NC and Fe-MN-NC (d) NLDFT pore size distribution of Fe-M-NC and Fe-MN-NC	68
34	Figure 2.9	Powder X-ray diffraction patterns of Fe-M-NC and Fe-MN-NC	69
35	Figure 2.10	Raman spectra of (a) Fe-M-NC & Fe-MN-NC and (b) Fe-MN-NC-800 & Fe-MN-NC-1000	70
36	Figure 2.11	XPS survey scan spectrum of Fe-M-NC and Fe-MN-NC	70
37	Figure 2.12	High resolution N 1s XPS spectra of (a) Fe-M-NC and (b) Fe-MN-NC	71
38	Figure 2.13	Concentration of various types of nitrogen (in atomic percentage) present in the Fe- doped carbon catalyst samples	72
39	Figure 2.14	High resolution Fe 2p XPS spectra of (a) Fe-M-NC and (b) Fe-MN-NC	72
40	Figure 2.15	XPS survey scan spectrum of Fe-MN-NC-800 and Fe-MN-NC-1000	73
41	Figure 2.16	High resolution N 1s XPS spectra of (a) Fe-MN-NC-800 and (b) Fe-MN-NC-1000	73
42	Figure 2.17	Cyclic voltammograms of (a) Fe-MN-NC and (b) Pt/C in 0.1 M KOH solution measured at a scan rate of 50 mV sec ⁻¹ at 900 rpm	74
43	Figure 2.18	(a) Linear Sweep voltammogram (LSV) comparison of (a) Fe-M-C, Fe-M-NC, Fe-MN-NC & Pt/C and (b) Fe-MN-NC pyrolyzed at temperatures 800, 900 & 1000 °C in O ₂ saturated 0.1 M KOH solution measured at a scan rate of 5 mV sec ⁻¹ at 1600 rpm	75
44	Figure 2.19	LSVs of (a) Fe-M-C, (b) Fe-M-NC, (c) Fe-MN-NC-800, (d) Fe-MN-NC (e) Fe-MN-NC-1000 and (f) Pt/C in O ₂	76

		saturated 0.1 M KOH solution measured at different rotation rates at a scan rate of 5 mV sec ⁻¹	
45	Figure 2.20	Comparison of the Koutecky-Levich (K-L) plots of Fe-M-C, Fe-M-NC, Fe-MN-NC and Pt/C	77
46	Figure 2.21	Comparison of (a) number of electron transfer and (b) hydrogen peroxide yield at different potentials obtained from the RRDE experiment	78
47	Figure 2.22	Tafel slope comparison of Fe-M-NC and Fe-MN-NC with Pt/C	79
48	Figure 2.23	(a) LSV recorded before and after 5000 cycles ADT analysis for (a) Fe-MN-NC and (b) Pt/C in O ₂ saturated 0.1 M KOH solution with electrode rotation of 1600 rpm	80

Chapter 3

49	Figure 3.1	The conversion of chitin to chitosan by deacetylation	91
50	Figure 3.2	Schematic illustration of the formation of Fe, N co-doped carbon	95
51	Figure 3.3	TGA patterns of Fe-MCS and Fe-MCS-M in nitrogen atmosphere	96
52	Figure 3.4	SEM images of (a, b) Fe-MCS-NC and (c, d) Fe-MCS-NCM	97
53	Figure 3.5	TEM images of (a-c) Fe-MCS-NC, (d-f) Fe-MCS-NCM	98
54	Figure 3.6	(a) C-K α , N-K α , O-K α , Fe-K α map of Fe-MCS-NC, (b) Fe-MCS-NCM	98
55	Figure 3.7	Nitrogen adsorption-desorption isotherms of (a) Fe-MCS-NC _{unwashed} & Fe-MCS-NCM _{unwashed} and (b) Fe-MCS-NC & Fe-MCS-NCM	100
56	Figure 3.8	BJH pore volume and pore size distribution of (a) Fe-MCS-NC and (b) Fe-MCS-NCM	100
57	Figure 3.9	XRD patterns of Fe-MCS-NC and Fe-MCS-NCM	101
58	Figure 3.10	Raman spectra of Fe-MCS-NC and Fe-MCS-NCM	102

59	Figure 3.11	XPS survey spectra of Fe-MCS-NC and Fe-MCS-NCM	102
60	Figure 3.12	High-resolution N 1s XPS spectra of (a) Fe-MCS-NC and (b) Fe-MCS-NCM	103
61	Figure 3.13	High-resolution Fe 2p XPS spectra of (a) Fe-MCS-NC and (b) Fe-MCS-NCM	104
62	Figure 3.14	Deconvoluted C 1s spectra of (a) Fe-MCS-NC and (b) Fe-MCS-NCM	104
63	Figure 3.15	Percentage of different nitrogen species present in Fe-MCS-NC and Fe-MCS-NCM	105
64	Figure 3.16	Cyclic voltammograms of (a) Fe-MCS-NC and (b) Fe-MCS-NCM 0.1 M KOH solution measured at a scan rate of 50 mV sec ⁻¹ at 900 rpm	106
65	Figure 3.17	(a) Linear Sweep voltammogram (LSV) comparison of Fe-MCS-NC, Fe-MCS-NCM & Pt/C in O ₂ saturated 0.1 M KOH solution measured at a scan rate of 5 mV sec ⁻¹ at 1600 rpm	106
66	Figure 3.18	LSVs of (a) Fe-MCS-NC and (b) Fe-MCS-NCM in O ₂ saturated 0.1 M KOH solution measured at different rotation rates at a scan rate of 5 mV sec ⁻¹	107
67	Figure 3.19	Comparison of the Koutecky-Levich (K-L) plots of Fe-MCS-NC, Fe-MCS-NCM and Pt/C	107
68	Figure 3.20	Comparison of (a) hydrogen peroxide yield and (b) number of electron transfer at different potentials obtained from the RRDE experiment	108
69	Figure 3.21	Tafel slope comparison of Fe-MCS-NC and Fe-MCS-NCM with Pt/C	109
70	Figure 3.22	(a) LSV recorded before and after 5000 cycles ADT analysis for (a) Fe-MCS-NC and (b) Pt/C in O ₂ saturated 0.1 M KOH solution with electrode rotation of 1600 rpm	110

Chapter 4

71	Figure 4.1	Schematic illustration of the formation of Fe-G-NC	122
----	-------------------	--	-----

72	Figure 4.2	Powder X-ray diffraction patterns of Fe-G1-NC, Fe-G2-NC and Fe-G3-NC	123
73	Figure 4.3	Raman spectra of Fe-G1-NC, Fe-G2-NC and Fe-G3-NC	124
74	Figure 4.4	SEM images of (a, b) Fe-G1-NC (c, d) Fe-G2-NC and (e, f) Fe-G3-NC	125
75	Figure 4.5	AFM images of Fe-G2-NC	125
76	Figure 4.6	EDAX spectra of (a) Fe-G1-NC, (b) Fe-G2-NC and (c) Fe-G3-NC	126
77	Figure 4.7	Elemental mapping of (a) Fe-G1-NC, (b) Fe-G2-NC and (c) Fe-G3-NC	126
78	Figure 4.8	TEM images of (a, b) Fe-G1-NC (c, d, e, f, g, h) Fe-G2-NC and (i, j) Fe-G3-NC	128
79	Figure 4.9	(a) N ₂ adsorption-desorption isotherms and (b) NLDFT pore size distribution curves and (c) BJH cumulative pore volume of Fe-G1-NC, Fe-G2-NC and Fe-G3-NC	129
80	Figure 4.10	XPS survey spectrum of Fe-G1-NC, Fe-G2-NC and Fe-G3-NC	130
81	Figure 4.11	Deconvoluted N 1s spectra of Fe-G1-NC, Fe-G2-NC and Fe-G3-NC	131
82	Figure 4.12	Atomic percentage of different types of N species present in Fe-G1-NC, Fe-G2-NC and Fe-G3-NC	132
83	Figure 4.13	High resolution Fe 2p XPS spectra of Fe-G1-NC, Fe-G2-NC and Fe-G3-NC	132
84	Figure 4.14	Deconvoluted C 1s spectra of (a) Fe-G1-NC, (b) Fe-G2-NC and (c) Fe-G3-NC	133
85	Figure 4.15	Cyclic voltammograms of (a) Fe-G1-NC, (b) Fe-G2-NC, (c) Fe-G3-NC and (d) Pt/C in N ₂ and O ₂ saturated 0.1 M KOH solution measured at a scan rate of 50 mV s ⁻¹ at 900 rpm	134
86	Figure 4.16	Linear sweep voltammogram comparison of Fe-G1-NC, Fe-G2-NC, Fe-G3-NC and Pt/C in O ₂ saturated 0.1	135

		M KOH solution measured at a scan rate of 10 mV s ⁻¹ at 1600 rpm	
87	Figure 4.17	LSVs of (a) Fe-G1-NC (b) Fe-G2-NC (c) Fe-G3-NC and (d) Pt/C in O ₂ saturated 0.1 M KOH solution measured at different rotation speeds at a scan rate of 10 mV s ⁻¹ at 1600 rpm	136
88	Figure 4.18	Comparison of the Koutecky-Levich (K-L) plots of Fe-G1-NC, Fe-G2-NC, Fe-G3-NC and Pt/C	137
89	Figure 4.19	Comparison of (a) number of electrons transferred and (b) hydrogen peroxide yield at different potentials obtained from the RRDE experiment	138
90	Figure 4.20	Comparison of Tafel slopes of Fe-G1-NC, Fe-G2-NC, Fe-G3-NC and Pt/C	138
91	Figure 4.21	Methanol tolerance study of Fe-Gly-2 MF-C in comparison with Pt/C	139
92	Figure 4.22	LSVs recorded before and after the 5000 cycle ADT analysis of (a) Fe-G2-NC and (b) Pt/C in O ₂ saturated 0.1 M KOH solution with a working electrode rotation of 1600 rpm	140

Chapter 5

93	Figure 5.1	Schematic illustration of the formation of FeCoZ-NC	152
94	Figure 5.2	X-ray diffraction patterns of (a) precursor ZIFs (b) derived carbons.	153
95	Figure 5.3	Raman spectra of Z-NC, Co-NC, CoZ-NC, FeZ-NC and FeCoZ-NC	154
96	Figure 5.4	SEM image of FeCoZn-ZIF	154
97	Figure 5.5	SEM images of (a) Z-NC, (b) CoZ-NC, (c) FeZ-NC and (d) FeCoZ-NC	155
98	Figure 5.6	TEM images of Z-NC at different magnifications (a) 100 kX, (b) 300 kX, and (c) 1 mX. HR-TEM image is shown in the inset of (c)	155
99	Figure 5.7	Elemental mapping of Z-NC	156

100	Figure 5.8	TEM images of Co-NC at different magnifications (a) 120 kX, (b) 300 kX, and (c) 1 mX. HR-TEM and FFT are shown in the inset of (c)	156
101	Figure 5.9	Elemental mapping of Co-NC	157
102	Figure 5.10	TEM images of CoZ-NC at different magnifications (a) 100 kX, (b) 300 kX, and (c) 1 mX. FFT is shown in the inset of (c)	157
103	Figure 5.11	Elemental mapping of CoZ-NC	158
104	Figure 5.12	TEM images of FeZ-NC at different magnifications (a) 100 kX, (b) 300 kX, and (c) 1 mX. HR-TEM image and FFT are shown in the inset of (c)	158
105	Figure 5.13	Elemental mapping of FeZ-NC	159
106	Figure 5.14	TEM images of FeCoZ-NC at different magnifications (a) 100 kX, (b) 300 kX, and (c and d) 1 mX. HR-TEM image and FFT are shown in the inset of (c & d)	160
107	Figure 5.15	Elemental mapping of FeCoZ-NC	160
108	Figure 5.16	(a) N ₂ adsorption-desorption isotherms and (b) NLDFT pore size distribution of Z-NC, Co-NC, CoZ-NC, FeZ-NC, and FeCoZ-NC	162
109	Figure 5.17	XPS survey spectrum of Z-NC, Co-NC, CoZ-NC, FeZ-NC, and FeCoZ-NC	163
110	Figure 5.18	Deconvoluted Zn 2p XPS spectrum Z-NC, CoZ-NC, and FeCoZ-NC	163
111	Figure 5.19	Deconvoluted Co2p spectrum of (a) Co-NC, (b) CoZ-NC and (b) FeCoZ-NC.	164
112	Figure 5.20	Deconvoluted Fe2p spectrum of (a) FeZ-NC and (b) FeCoZ-NC	165
113	Figure 5.21	Deconvoluted N 1s XPS spectrum of (a) Z-NC, (b) Co-NC, (c) CoZ-NC, and (d) FeZ-NC	166
114	Figure 5.22	Deconvoluted C 1s XPS spectrum of (a) Z-NC, (b) Co-NC, (c) CoZ-NC, and (d) FeZ-NC	167
115	Figure 5.23	Deconvoluted (a) N 1s and (b) C 1s XPS spectrum of FeCoZ-NC	167

116	Figure 5.24	Comparison of CVs of FeCoZ-NC in the absence and presence of NaBH ₄ and with no electrode rotation	168
117	Figure 5.25	Comparison of CVs of Z-NC, Co-NC, CoZ-NC, FeZ-NC, and FeCoZ-NC in 1 M KOH+0.05 M NaBH ₄ with no electrode rotation	169
118	Figure 5.26	(a) CVs of FeCoZ-NC sample at different concentrations of NaBH ₄ in 1 M KOH and (b) corresponding j_p vs C_{NaBH_4} plot and, (c) $\ln j_p$ vs $\ln C_{\text{NaBH}_4}$ plot	170
119	Figure 5.27	(a) LSVs of FeCoZ-NC recorded at different scan rates in 1 M KOH+0.05 M NaBH ₄ and, (b) dependence of j_p on $v^{1/2}$	171
120	Figure 5.28	LSVs of (a) Co-NC, (b) CoZ-NC, (c) FeCoZ-NC recorded at different electrode rotation in 1 M KOH+0.05 M NaBH ₄ at a scan rate of 10 mV s ⁻¹	171
121	Figure 5.29	K-L plots comparison of Co-NC, CoZ-NC and FeCoZ-NC at 1.0 V	172
122	Figure 5.30	Number of electron transfers obtained at a disc potential of 1.0 V during RRDE measurement and (b) CA curves of FeCoZ-NC in 1 M KOH+0.05 M NaBH ₄ tested at different fixed potentials	174

LIST OF TABLES

Chapter 1

1	Table 1.1	Different types of fuel cells	6
2	Table 1.2	List of some MOFs and its applications	18
3	Table 1.3	List of some ZIFs and its applications	20
4	Table 1.4	List of some MOGs and its applications	23
5	Table 1.5	Summary of various metal free electrocatalysts for ORR	29
6	Table 1.6	Summary of various non-precious metal electrocatalysts for ORR	33
7	Table 1.7	Electron transfer number comparison of reported BOR catalysts	37

Chapter 2

8	Table 2.1	Variation of concentration of different nitrogen species with pyrolysis temperature	74
9	Table 2.2	Comparison of electrocatalytic performance of the samples	79

Chapter 3

10	Table 3.1	Comparison of the ORR performance of chitosan derived catalysts	92
11	Table 3.2	Atomic % values of C, N, and Fe of Fe-MCS-NC and Fe-MCS-NCM measured from XPS analysis	104
12	Table 3.3	Comparison of electrocatalytic performance of the samples	109
13	Table 3.4	Comparison of ORR activity of Fe-MCS-NCM catalyst with reported non precious metal catalysts in alkaline medium	111

Chapter 4

14	Table 4.1	Atomic percentages of C, O, N and Fe of various samples obtained from XPS	131
15	Table 4.2	Comparison of electrocatalytic performance of the samples	139

Chapter 5

16	Table 5.1	Details of various ZIF samples with different metal percentages	150
17	Table 5.2	Weight percentage of metals obtained from EDS	161

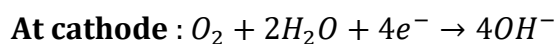
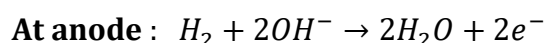
LIST OF ABBREVIATIONS

ADT	Accelerated Durability Test
AFC	Alkaline Fuel Cell
BET	Brunauer-Emmett-Teller
BJH	Barrett-Joyner-Halenda
BOR	Borohydride Oxidation Reaction
CA	Chronoamperometry
CV	Cyclic Voltammetry
DBFC	Direct Borohydride Fuel Cell
DFT	Density Functional Theory
DMFC	Direct Methanol Fuel Cell
EDAX	Energy Dispersive X-ray Analysis
eV	Electron Volts
HER	Hydrogen Evolution Reaction
HOR	Hydrogen Oxidation Reaction
HRTEM	High Resolution Transmission Electron Microscope
IBFC	Indirect Borohydride Fuel Cell
IPN	Interpenetrating Polymer Network
JCPDS	Joint Committee on Powder Diffraction Standards
K-L	Koutecky-Levich
LSV	Linear Sweep Voltammetry
MF	Melamine Formaldehyde
MOG	Metal Organic Gel
MOF	Metal Organic Framework
N	Nitrogen
NP	Nano Particle
OER	Oxygen Evolution Reaction
ORR	Oxygen Reduction Reaction
PEMFC	Proton Exchange Membrane Fuel Cell
PGM	Platinum Group Metal
RDE	Rotating Disc Electrode

RHE	Reversible Hydrogen electrode
rpm	Revolutions per Minutes
RRDE	Rotating Ring Disc Electrode
SAED	Selected Area Electron Diffraction
SAFC	Solid Alkaline Fuel Cell
SCE	Saturated Calomel Electrode
SEM	Scanning Electron Microscope
TEM	Transmission Electron Microscope
TGA	Thermogravimetric Analysis
XPS	X-ray Photoelectron Spectroscopy
XRD	X-ray Diffraction
ZIF	Zeolitic Imidazolate Framework

PREFACE

Fuel cells (FCs) are well accepted as a green energy source because of its high efficiency, and sustainability. Among the various configurations possible, alkaline fuel cells are gaining popularity by virtue of its high efficiency, lower operating temperature (< 100 °C) and the use of liquid fuels such as methanol, ethanol, formate, borohydride etc. instead of pure hydrogen. The basic chemical changes occurring in an alkaline fuel cell can be attributed to the reactions of oxygen reduction (ORR) at the cathode and hydrogen oxidation reaction (HOR) at the anode as indicated below.



The sluggish kinetics of oxygen reduction reactions (ORR) and the extensive use of expensive platinum (Pt)-based catalyst are major barriers for the commercialization of fuel cells. The search for efficient, cost-effective catalyst systems that can replace Pt- is primarily focused on heteroatom doped porous carbon structures. Co-doping of iron and nitrogen (Fe, N) is widely pursued, as Fe, N coordination on carbon implicitly induce enhanced electrocatalytic properties due to increased positive charge densities on neighboring carbon atoms. Fe/N/C catalysts with good stability are generally synthesized by high temperature treatment of a variety of precursors. Diverse methods, such as pyrolysis, chemical vapor deposition, and template methods are employed for the synthesis of porous carbons. Among these, pyrolysis of carbon precursors such as metal organic framework (MOF), zeolitic imidazolate framework (ZIF) and metal organic gel (MOG) has gained significant interest specifically due to the flexibility in design, improved morphology control and appreciable surface area with desired textural features. The thesis primarily aims at developing Fe-N doped porous carbon materials, from MOG/ZIF precursors, and evaluating its use as electrode materials for fuel cells.

The thesis comprises of six chapters. Chapter 1 gives an introduction to fuel cells, oxygen reduction reaction and a review of literature regarding the development of hetero atom doped porous carbon electrocatalyst.

Chapter 2 focuses on the synthesis, characterization and electrochemical studies of Fe, N-doped porous graphitic carbon electrocatalyst (Fe-M-NC), obtained by the pyrolysis of an interpenetrating polymer network (IPN) comprised of melamine formaldehyde (MF as hard segment) and metal organic gel (MOG as soft segment). The catalyst thus developed exhibited significant oxygen reduction reaction (ORR) activity in alkaline medium. BET surface area analysis of Fe-M-NC showed high surface area ($821 \text{ m}^2 \text{ g}^{-1}$), while TEM, Raman and XPS results confirmed Fe and N co-doping. Furthermore, a modulated porous morphology with a higher degree of surface area ($950 \text{ m}^2 \text{ g}^{-1}$) has been accomplished for the system (Fe-MN-NC) when aided by a sublimable porogen, such as naphthalene. XPS results further demonstrated that these systems exhibited a better degree of distribution of graphitic N. An onset potential value of 0.91 V vs. RHE in 0.1 M KOH solution, following an efficient four-electron ORR pathway, was obtained. The electrocatalytic activity of Fe-MN-NC is superior to that of Fe-M-NC by virtue of its higher graphitic N content and surface area.

Metal-organic gel intercalated with chitosan, a “green” precursor for the synthesis of intrinsic N-doped Fe distributed mesoporous graphitic carbon structures is described in chapter 3. Modulation of the synthetic protocol as a function of reaction kinetics and gelation time improves the microstructure, surface area and Fe distribution of the graphitic structures (Fe-MCS-NCM). A high specific surface area value of $565 \text{ m}^2 \text{ g}^{-1}$ and a higher percentage of graphitic N, apparent from the XPS data, validated that the modified synthetic method favors creation of more graphitic N sites contributing for better catalytic performance. Fe-MCS-NCM catalyst exhibited comparable electrocatalytic activity with that of the commercially available Pt/C via an efficient four-electron-dominant ORR pathway with a positive onset potential value of 0.925 V vs RHE. Good durability of >5000 cycles further confirmed the prospects of MOG-chitosan to be used as a potential catalyst for ORR.

Chapter 4 focuses the electrocatalytic ORR activity of iron carbide (Fe_3C) encapsulated hierarchical pod-like porous graphitic carbon catalyst. The catalyst was prepared by a simple pyrolysis of Fe-glycine complex integrated melamine formaldehyde resin precursor. The unique structure and stronger network of the resulting thermosetting resin facilitated the formation of porous carbon nanosheets

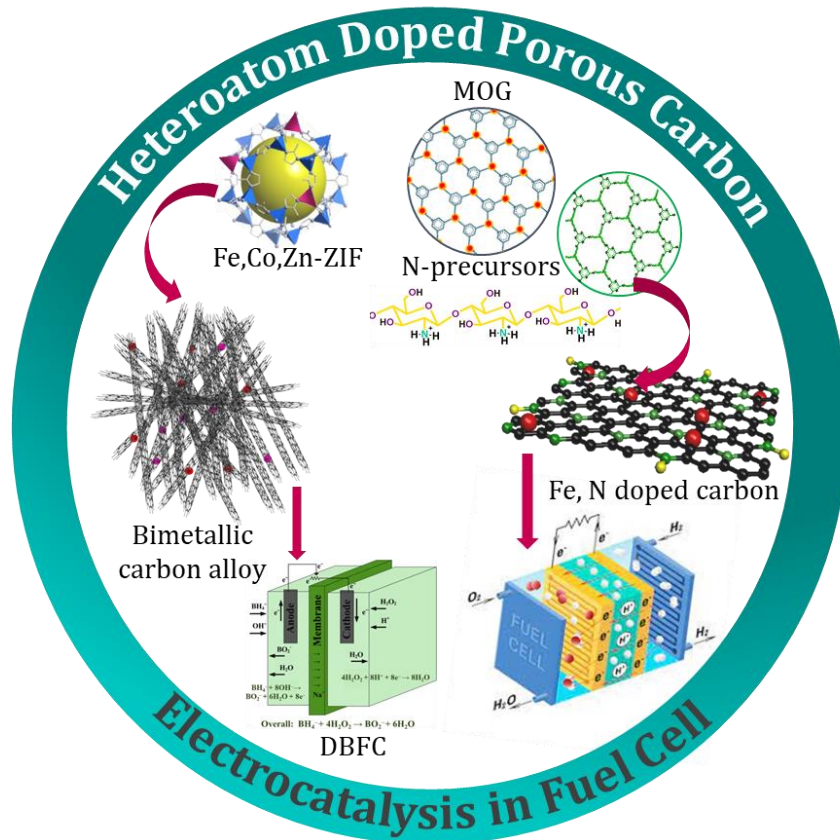
while Fe catalyzed the formation of carbon nanotubes. The best catalyst among the ones studied, Fe-G2-NC, possessed high degree of graphitization with a surface area of $205 \text{ m}^2 \text{ g}^{-1}$ and porosity of $0.54 \text{ cm}^3 \text{ g}^{-1}$. The XPS results confirmed the presence of high degree of graphitic N. The catalyst with optimized Fe content (Fe-G2-NC) exhibited high ORR activity with an onset potential of 0.95 V and a half-wave potential ($E_{1/2}$) of 0.80 V vs RHE in alkaline media through the four-electron reduction pathway. Moreover, the catalyst exhibited excellent long-term durability with good methanol tolerance.

Chapter 5 details the development of an anode catalyst for direct borohydride fuel cell. It is derived from trimetallic zeolitic imidazolate framework (ZIF) with M-N_x active centers. The catalyst exhibited enhanced porosity owing to Zn evaporation during pyrolysis. XPS studies revealed the presence of pyridinic N, graphitic N and Co-N_x active centers on the catalyst surface. The nanotubular structure of the formed carbon assists faster electron transport and the oxidation current density reached 56.5 mA cm^{-2} at 0.61 V in 0.05 M NaBH_4 +1 M KOH. The enhanced electrocatalytic performance induced by the morphological and textural features of the porous carbon catalysts enabled NaBH_4 electrooxidation via an eight-electron transfer indicating its potential as a promising catalyst for BOR.

The important findings of the Ph.D. work are summarized in the concluding Chapter 6 of the thesis.

Chapter 1

Introduction to Electrocatalysis in Fuel Cell



1.1 Introduction

Energy is one of the important issues of the 21st century. The energy demand of the world is increasing exponentially with the rise in population, whereas, our energy production is insufficient to match with the current demand. Thus, the present energy situation relying heavily on non-renewable fossil resource is unsustainable and needs to be changed. Fossil fuels such as gasoline and coal have been widely used as energy source for several hundred years due to their earth abundance and lower price compared to other fuels. However, the combustion of these fossil fuels badly pollutes the environment owing to the release of carbon dioxide, carbon monoxide, nitrogen oxides, etc., which are harmful to our health.¹ **Figure 1.1** illustrates the current status of global energy production in terms of quantity and source. From the graph, it is clear that, oil and coal continue to hold the largest share towards the global energy consumption. Even though there is a gradual increase in the consumption of fossil fuels from 1800 to 2019, there is only a little growth in the use of renewable energy resources. In this context, much attention has to be paid towards the development and utilization of sustainable and green energy technologies.

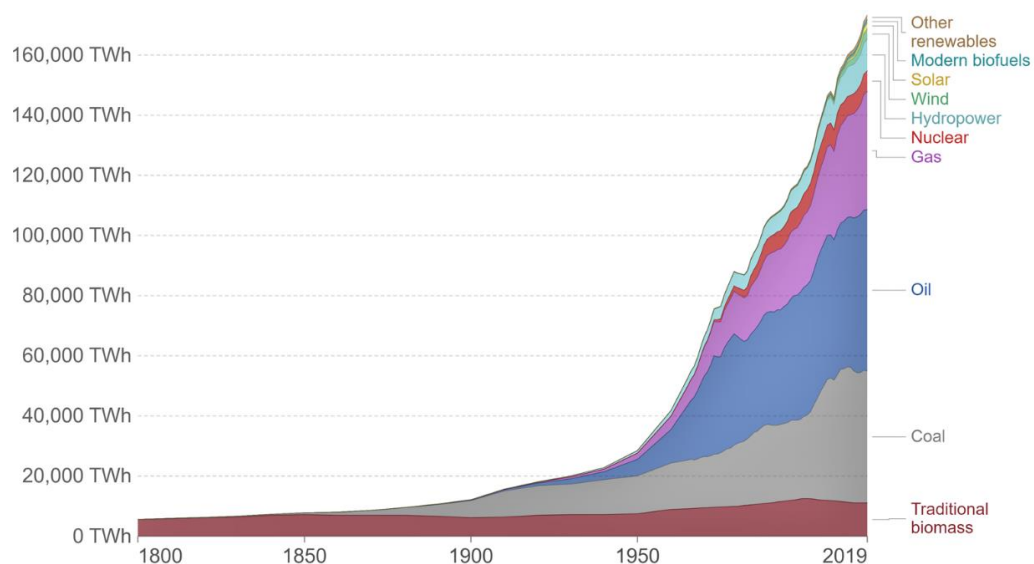


Figure 1.1 The global energy consumption, measured in terawatt-hours (TWh) per year. (Courtesy: Vaclav Smil (2017). *Energy Transitions: Global and National Perspectives*. & BP Statistical Review of World Energy).

The conversion of chemical energy into electrical energy is getting utmost importance these days owing to the significance of the development of sustainable renewable energy systems. Therefore, the use of electrochemical energy devices such as batteries, supercapacitors, and fuel cells have the potential to substitute traditional energy systems. A battery is a device that transforms chemical energy into electric energy. All batteries have three basic components - an anode, a cathode, and an electrolyte - which determine their properties and performance. Supercapacitors (SCs) are energy storage devices that bridge the gap between batteries and conventional capacitors. They can store more energy than capacitors and supply it at higher power outputs than batteries. Supercapacitors use a molecule-thin layer of electrolyte, rather than a dielectric, to separate the charge and resembles a regular capacitor except that it offers very high capacitance in a small package. Energy storage is by means of static charge rather than the electrochemical process inherent to a battery. Supercapacitors rely on the separation of charge at an electrified interface that is measured in fractions of a nanometer. A fuel cell uses stored chemical energy to generate power. It produces electricity from fuel on the anode side and an oxidant on the cathode side, which react in the presence of an electrolyte. Contrary to a battery or a supercapacitor, a fuel cell is never discharged, but operate continuously as long as the necessary flows of reactants and reaction products are maintained.²⁻⁴

The Ragone plot shown in **Figure 1.2** gives the difference between the power and energy densities for different energy supply systems.⁵ The internal combustion engine (ICE) remains the most desirable choice since it is having high specific power and specific energy. The supercapacitors are having high power density enabling them to supply a very high power in a short period usually milliseconds. Lithium-based batteries provide almost comparable energy density and power density. Fuel cells possess high energy density.

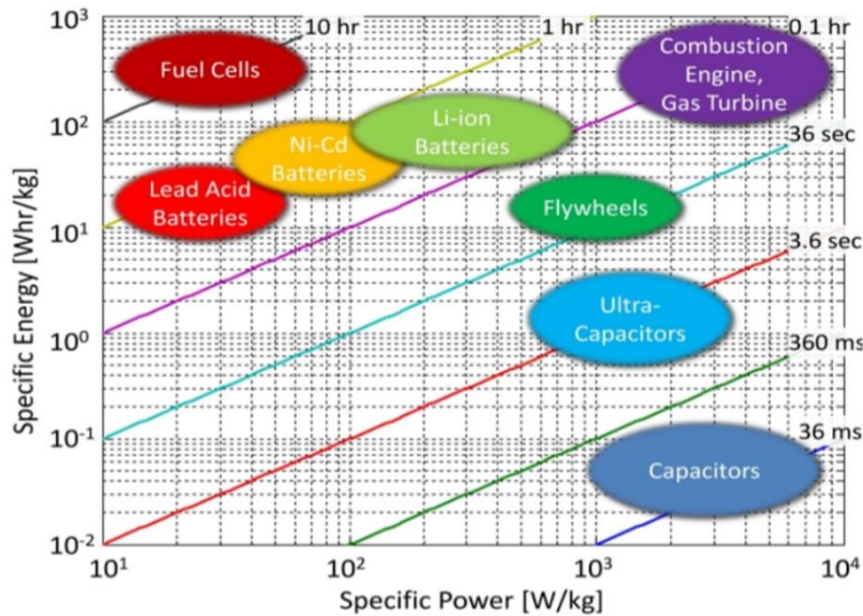


Figure 1.2 Ragone plot for energy storage devices.⁵

Of the various technology routes being studied to combat the energy crisis, fuel cells have the potential to play a significant role in any renewable energy cycle design. Fuel cells can be refuelled like a combustion engine and can directly convert chemical energy to electrical energy like a battery. Fuel cells, were originally developed to replace combustion engines and combustion power sources by virtue of the possible higher energy conversion efficiencies and lower environmental impacts. However, these are now under development for replacing batteries to power cellular telephones and notebook computers and for stationary energy storage.

1.2 Fuel Cells

The Fuel Cell concept was first demonstrated by William Robert Grove in the year 1839 and the term 'fuel cell' was coined by Ludwig Mond and Charles Langer.⁶ Soon after the first fuel cell was conceived, it was recognized as an environmental friendly energy device that relies on an electro chemical reaction. It directly converts chemical energy into electrical energy by using hydrogen and oxygen as fuels and generates water as the only by product. Moreover, fuel cells are advantageous as an alternative energy system since they are highly efficient (65 %) with no harmful emissions.⁷⁻⁸ As long as the fuel and oxidant are supplied, it continues to produce energy and hence could be employed for wider applications in automobile industry, space shuttles,⁹

communication devices,¹⁰ vehicles¹¹ and also in residential and commercial buildings.¹²⁻¹³ Fuel cell powered cars, buses and motor cycles are developed in several countries including Japan and USA. There is significant funding for research contracts on this technology.¹⁴

The structure of a simplified fuel cell is shown in **Figure 1.3**. A positive electrode (anode), a negative electrode (cathode), and an electrolyte are essential for the reaction to take place. The following equations represent the reactions occurring in a fuel cell.

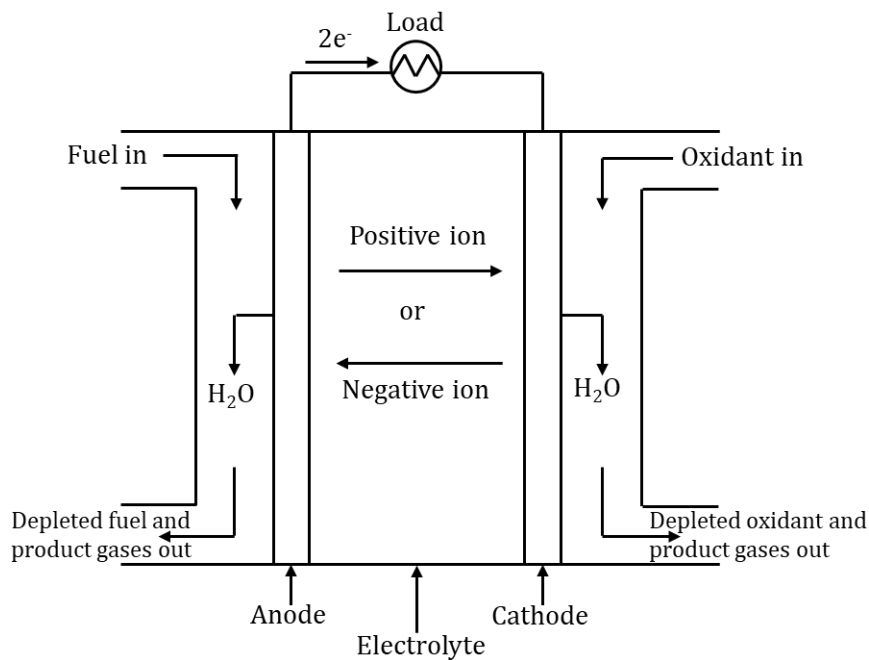
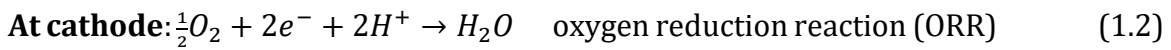
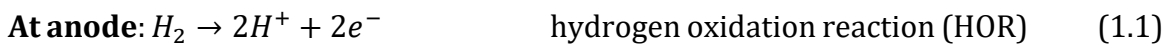


Figure 1.3 Fuel cell operation diagram.

Fuel cells are classified into different types based on the type of electrolytes used, but the basic operation is the same for all of them. Among different types of fuel cells, alkaline fuel cells (AFCs) gain much attention due to several advantages such as high efficiency, lower operating temperature (< 100 °C), minimal corrosion, relative ease of operation and the use of liquid fuels such as methanol, ethanol, formate, borohydride etc. instead of pure hydrogen. Alkaline technology is the longest

established technology for both space and submarine applications over other available cell.¹⁵ **Table 1.1** details the different types of fuel cells.¹⁶⁻¹⁸

Table 1.1 Different types of fuel cells.

	Alkaline Fuel Cell (AFC)	Polymer Electrolyte Membrane Fuel Cell	Direct Methanol Fuel Cell	Phosphoric Acid Fuel Cell	Molten Carbon Fuel Cell	Solid Oxide Fuel Cell
Electrolyte	Caustic Potash Solution	Proton/hydroxyl ion - Conducting Membrane	Proton Conducting Membrane	Concentrated Phosphoric Acid	Molten Carbonate	Ceramic
Operating temperature (°C)	<100	60-120	60-120	160-220	600-800	800-1000
Fuel	Hydrogen	Hydrogen	Methanol	Hydrogen	Natural gas, Coal	Natural gas, Coal
Charge carrier	OH ⁻	H ⁺	H ⁺	H ⁺	CO ₃ ²⁻	O ²⁻
Applications	Outer space	Vehicles, domestic supply, power stations	Vehicles, small appliances	Block type heat, power stations	Power plants, combined heat and power	Power plants, combined heat and power

1.2.1 Alkaline Fuel Cell

The main components of an alkaline fuel cell (AFC) are an anode and a cathode separated by an electrolyte and connected through an external circuit. The fuels hydrogen or oxygen is flown to the electrode. Electrodes are kept porous for the permeation of gases while the electrolyte is with minimum gas permeation. In a typical hydrogen/oxygen fuel cell, hydrogen oxidation occurs at the anode and oxygen

reduction occurs at the cathode. Schematic representation of an alkaline hydrogen/oxygen fuel cell is shown in **Figure 1.4**.

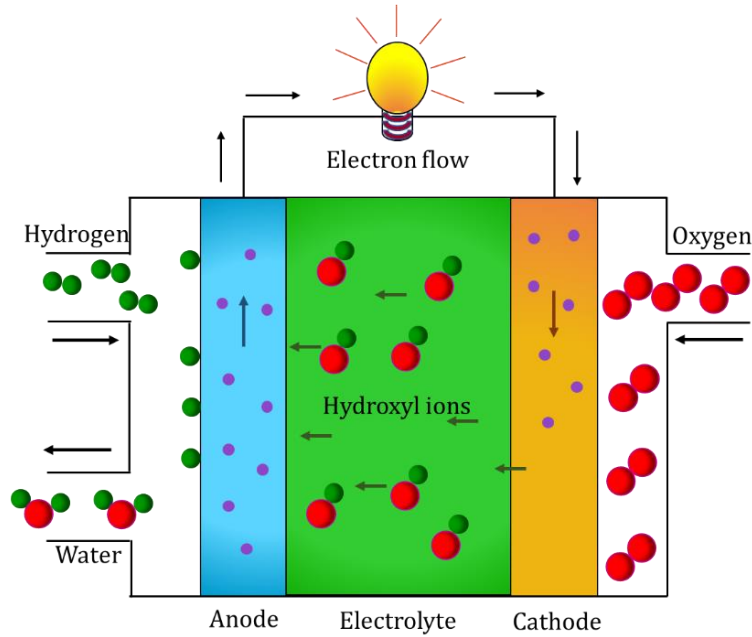
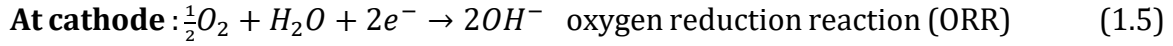
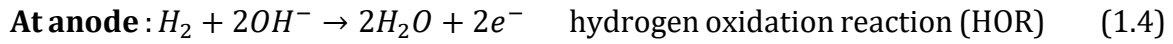


Figure 1.4 Schematic representation of alkaline fuel cell.

1.3 Oxygen Reduction Reaction (ORR)

Fuel cells offer much higher energy density and energy efficiency compared to conventional energy systems. However, their practical applications are greatly restricted due to the sluggish oxygen reduction reaction (ORR) kinetics occurring at the cathode.¹⁹⁻²⁰ Since ORR is much lower than the anodic oxidation reaction i.e., hydrogen oxidation reaction (HOR), it is imperative to use electrocatalysts at the cathode to reduce the activation energy barrier. Platinum (Pt) based electrocatalysts are widely employed due to their exceptional catalytic performance with high exchange current density and low over potential.²¹ Pt oxidize hydrogen to H^+ ions at the anode and the over potential for this half reaction is typically 50 mV.²² On the other hand, the ORR occurring at the cathode has a higher over potential of 500-600 mV with platinum-based catalyst.²³ This large over potential at the cathode decreases

the efficiency. The double bond in molecular oxygen is very strong and is difficult to be broken. The reduction process of oxygen to water (4 electron reduction) is therefore kinetically very slow. Nevertheless, the high cost and scarcity impeded the extensive use of Pt-based electrocatalysts for fuel cell applications. Moreover, Pt suffers from low selectivity, poor stability and agglomeration effects under the operation conditions.²⁴ Thus, it is very crucial to develop ORR catalysts which can overcome the demerits associated with the use of Pt-based catalysts.

1.3.1 ORR Mechanism

The ORR occurring at the cathode involves complicated electron transfers and proceed via the two possible mechanisms of four-electron and two-electron reduction pathways as shown in **Figure 1.5**. Four-electron reduction is preferred when it comes to fuel cells and metal-air batteries because only water is produced during this reaction. The two-electron reduction results in hydrogen peroxide production which accelerates degradation of fuel cell materials. In the four-electron reduction process, initially, O₂ molecule gets adsorbed on the catalyst surface followed by the cleavage of O-O bond to form O* intermediates. The reduction of O* occurs further resulting in the formation of OH*. In the subsequent step, an electron transfer in the form of hydrogen addition occurs at each OH* group resulting in the formation of two water molecules.¹⁵



In the two-electron pathway, after the adsorption of oxygen on to the catalyst surface, two proton addition takes place resulting in the formation of an adsorbed H₂O₂ molecule (H₂O₂*) which is then desorbed to form H₂O₂.



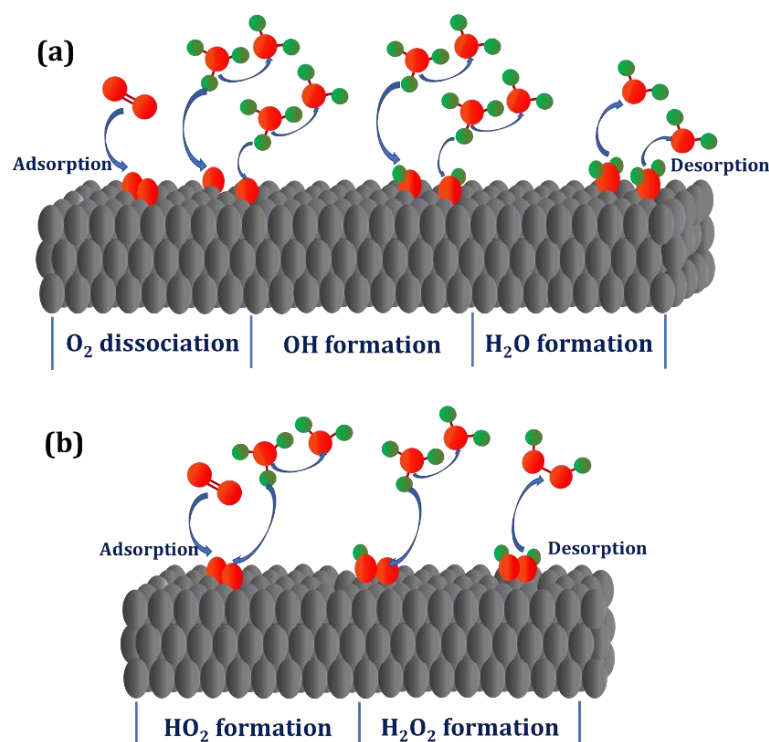


Figure 1.5 Schematic showing the mechanism of (a) four-electron and (b) two-electron reduction of oxygen.

1.4 Techniques for ORR Measurements

1.4.1 Cyclic Voltammetry (CV)

Cyclic voltammetry is often the first experiment performed in an electrochemical study of a compound or an electrode surface. The CV set up consists of three electrodes viz, working electrode, reference electrode and counter electrode dipped in an electrolyte. The potential of this working electrode is controlled with respect to a reference electrode such as a saturated calomel electrode (SCE) or a silver/silver chloride electrode (Ag/AgCl).²⁵ A schematic representation of set up for CV is given in **Figure 1.6**.

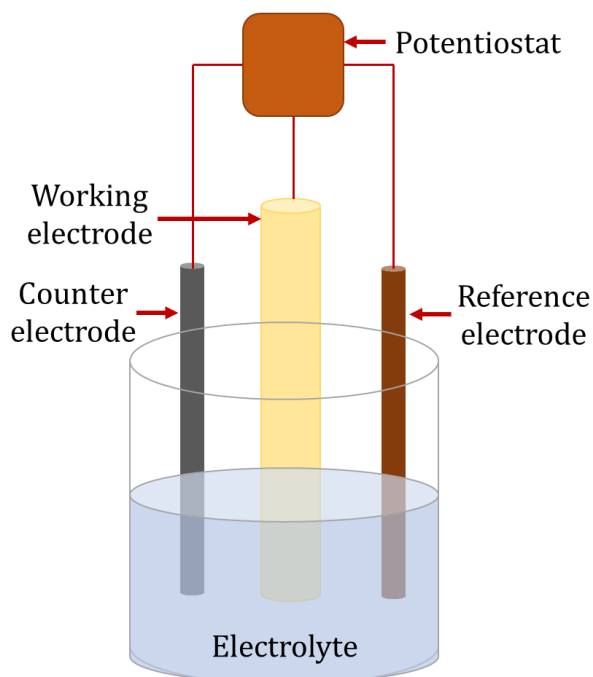


Figure 1.6 Schematic showing the typical setup of cyclic voltammetry.

In CV, the potential of the working electrode sweeps at a specific sweep rate and the resulting current vs time curve is studied (**Figure 1.7**). Usually, the sweep is reversed at a specific switching potential, and hence named as cyclic voltammetry. In a CV experiment, after the set potential is reached, the working electrode's potential is ramped in the opposite direction to return to the initial potential. These cycles of ramps in potential may be repeated as many times as needed. The current at the working electrode is plotted versus the applied voltage to get the cyclic voltammogram.²⁶⁻²⁷ A typical CV of Pt/C is shown in **Figure 1.8**.

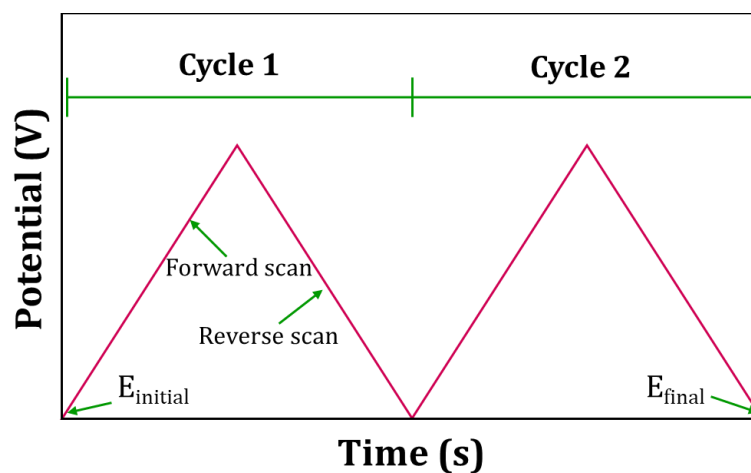


Figure 1.7 Cyclic voltammetry wave form.

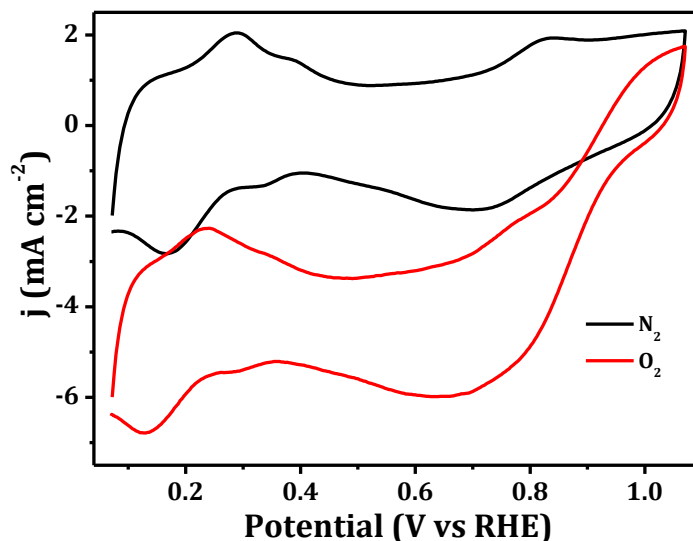


Figure 1.8 Typical cyclic voltammogram of Pt/C in N₂ and O₂ saturated 0.1 M KOH solution.

1.4.2 Rotating Disk Electrode (RDE)

The rotating disk electrode (RDE) method is one of the most widely used methods for studying kinetics and mechanism of electrochemical reactions. The rotation of electrode during the electrochemical reaction enhances the mass transfer. A schematic of the RDE setup is shown in **Figure 1.9**.

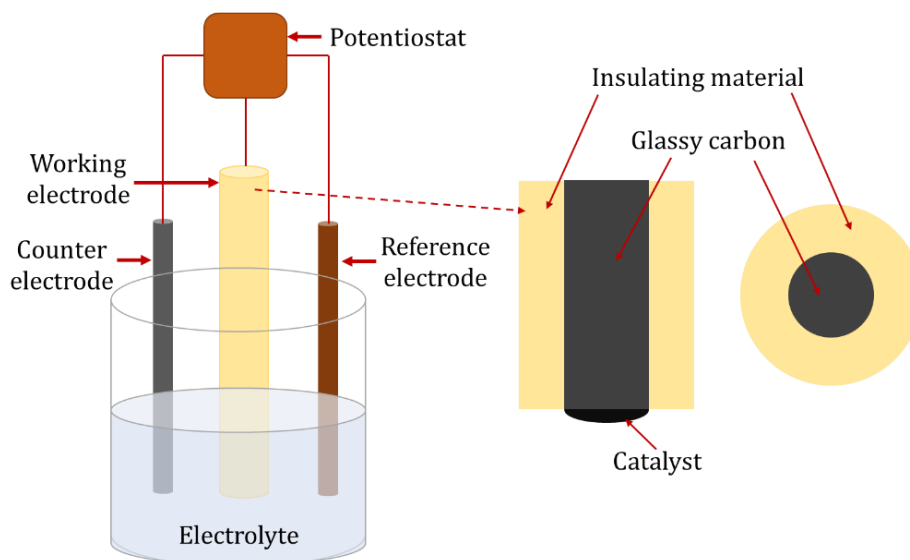


Figure 1.9 The scheme for the setup of rotating disc electrode.

It consists of a three electrode set-up, with a reference electrode, counter electrode and a glassy carbon disc as working electrode which is connected to a shaft that rotate

s at a particular angular velocity ω (s^{-1}). The catalyst ink is coated on the glassy carbon disc electrode to study its electrocatalytic activity.²⁸⁻²⁹

The electrocatalytic measurements are done by sweeping the potential from a starting value to a final value at a constant scan rate and rotation speed. This technique is called linear sweep voltammetry (LSV). LSV measurements are carried out at different working electrode rotation speeds starting from 400 to 2500 revolutions per minute. The sweep may be done in a narrower potential window with slower sweep rate usually less than 10 mV s^{-1} . For the case of O_2 reduction, the potential is slowly swept in the negative direction which results in an increase in the cathodic current reaching a maximum value called the limiting current. At this high negative potential all the oxidized entities formed at the surface of the electrode is immediately converted to their respective reduced forms. Thus, the observed current is due to the electron flow from the electrode to solution.

A typical ORR polarization curve is generally divided into three regions (**Figure 1.10**). Region I represent the kinetic region where, the rate of O_2 reduction is slow indicating a small increase in the current density with decreasing potential. This potential at which the reaction product (O_2) produced is known as the onset potential (E_{onset}). It is the bench mark of the catalyst and solely depend on the catalyst properties. A considerable rise in the current density is observed in the mixed region because of both kinetic and diffusion factors. The half wave potential ($E_{1/2}$) lies in this region and it signifies both kinetics and mass transport characteristics of the catalyst. The half-wave potential ($E_{1/2}$) is the potential at which polarographic wave current is equal to one half of the diffusion limiting current density (maximum current density, J_L). The more positive is the potential value (E_{onset} or $E_{1/2}$), the more active is the catalyst. The third region represents the diffusion limited region, where the current density increases to a maximum with increase in rotation speed of the working electrode, indicative of the diffusion of reactants that are contributing to this region.

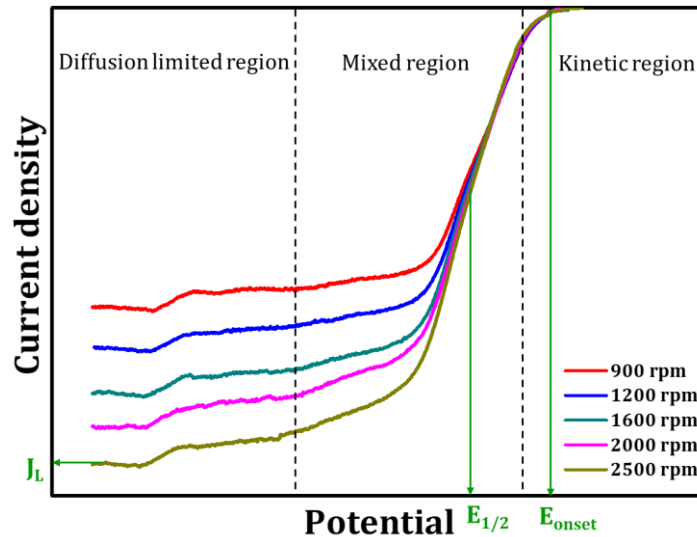


Figure 1.10 The different oxygen reduction regions in a typical RDE LSV curve at various working electrode rotation rates.

The kinetic parameters of the ORR can be analyzed on the basis of the Koutecky–Levich (K-L) equation. and the K-L equation can be represented as,

$$\frac{1}{j} = \frac{1}{j_d} + \frac{1}{j_k} \quad (1.14)$$

$$\frac{1}{j} = \frac{1}{0.62nFAC_0^*D_0^{2/3}\nu^{-1/6}\omega^{1/2}} + \frac{1}{nFAkC_0^*} \quad (1.15)$$

where, j is the measured current density, j_d is the diffusion-limiting current density, j_k is the kinetic current density, ω is the angular rotation ($\omega=2\pi f/60$, f is the rotation speed), n is the number of transferred electrons during ORR, F is the Faraday's constant (96480 C), C_0^* is the bulk concentration of O_2 ($1.22 \times 10^{-6} \text{ mol cm}^{-3}$), D_0 is the diffusion coefficient of O_2 ($1.9 \times 10^{-5} \text{ cm}^2 \text{ s}^{-1}$), ν is the kinematic viscosity of the electrolyte ($0.01 \text{ cm}^2 \text{ s}^{-1}$) and k is the electron transfer rate constant. K-L slopes obtained by plotting inverse of current density ($1/j$) against inverse of square root of angular density ($1/\omega^{1/2}$).³⁰

1.4.3 Rotating Ring Disk Electrode (RRDE)

When the ORR is occurring at the electrode, a by-product, or intermediate such as peroxide may be produced. The quantification of these intermediates could be done using RRDE collection experiment. For the evaluation of the ORR activity of the electrocatalysts, glassy carbon is normally used as the disc electrode substrate on

which the catalyst is coated. This is due to its poor ORR catalytic activity and also, they have reasonable affinity to the catalyst layer. Pt is commonly used as the ring material for detecting the ORR intermediates. Both the disc and ring are at different potential ED and ER respectively. Initially O_2 molecules move to the disc electrode where it gets reduced via 2 or 4 electron reduction pathways. The 2-electrons reduction intermediate HO_2^- was transported to the ring electrode by rotation and was detected at the ring electrode by oxidation. From the ring current, the quantity of peroxide can be detected.³¹⁻³² **Figure 1.11a & b** represents the top view of the RRDE electrode and the schematic of the catalytic reaction occurring during ORR in alkaline medium at the rotating ring disc electrode respectively.

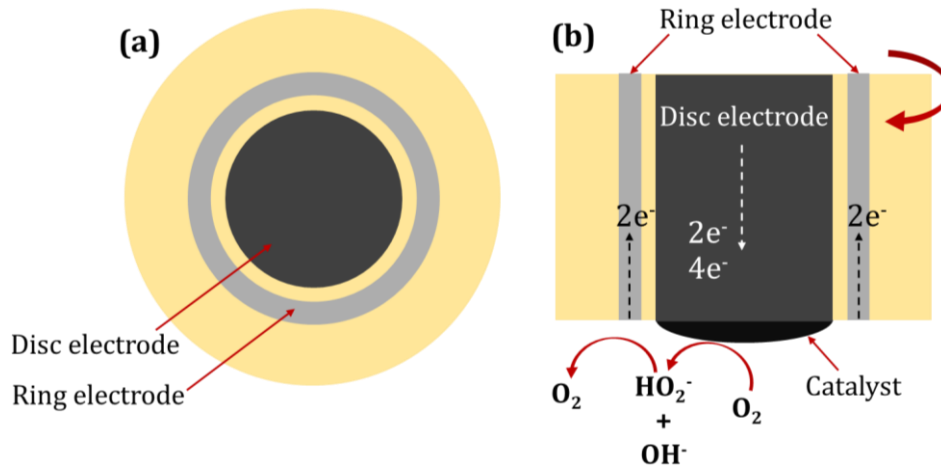
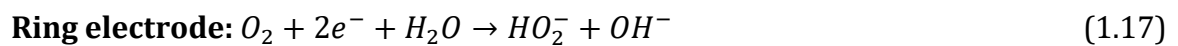
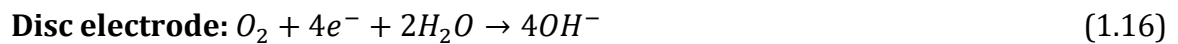


Figure 1.11 (a) Top view and (b) schematic of the catalytic reaction occurring during ORR in alkaline medium at the rotating ring disc electrode.

The different electrochemical reactions occurring at the disc and ring electrode is given by the following equations.



The yield of peroxide (H_2O_2) and number of electron transfer during the ORR process are calculated using the following equations.

$$H_2O_2\% = \left[\frac{2I_r}{I_d + I_r} \right] * 100 \quad (1.19)$$

$$n = \frac{4I_d}{I_d + \frac{I_r}{N}} \quad (1.20)$$

where 'I_r' and 'I_d' are the Faradaic ring and disc current, respectively. 'N' is the collection efficiency of the ring electrode (0.37) and the 'n' is the number of the transferred electron.

1.4.4 Calibration of the Reference Electrode

Hg/HgO electrode calibration was carried out using a three-electrode system with Pt wires as working and counter electrode and Hg/HgO as reference electrode. Prior to the measurements, the electrolyte solution (0.1 M KOH) was constantly purged with H₂ gas for at least 45 min and thereafter a constant flow was maintained during the measurements. LSV was taken at a scan rate of 1 mV/s and the potential at which current crosses zero was taken as thermodynamic potential (vs Hg/HgO) for the hydrogen electrode.

From the plot of current Vs potential, the potential at which current crosses zero is -0.870 V vs Hg/HgO (**Figure 1.12**).

Therefore,

$$E_{RHE} = E_{Hg/HgO} + 0.870 \quad (1.21)$$

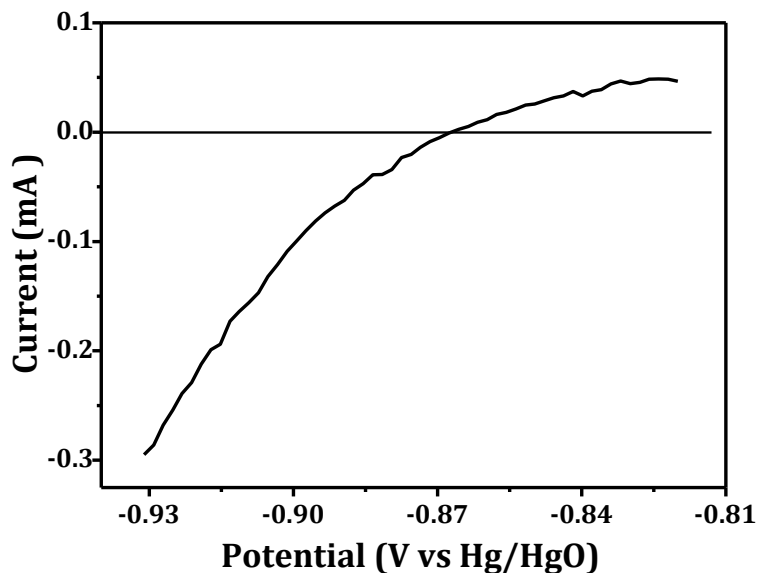


Figure 1.12 Calibration curve of the Hg/HgO reference electrode in H₂ saturated 0.1 M KOH solution.

1.5 Metal Organic Framework

Metal organic frameworks (MOFs) are a class of porous materials consisting of frameworks made by metal containing units connected by organic linkers through coordination bonds. The organic ligands or linkers are groups that donate multiple lone pairs of electrons to the metal ions, whereas the metal ions are having vacant orbital shells that can accept these lone pairs of electrons to form a MOF material.

Figure 1.13 shows a general scheme of formation of three-dimensional MOF.³³

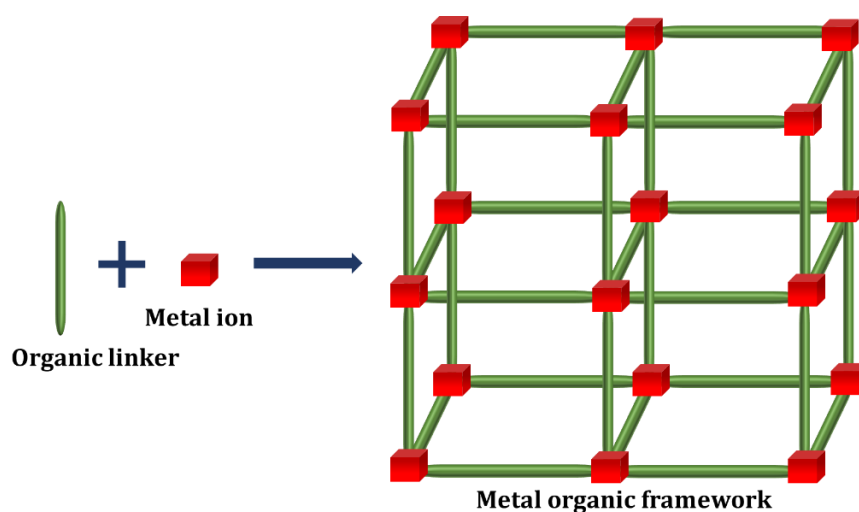


Figure 1.13 A general scheme of a three-dimensional metal-organic framework construction.

The metals have high coordination number and distinct geometries that result in variable pore sizes, densities, etc. Cu, Zn, Fe, Cr, Mg, Co, Mn, and Al etc. are typical MOF forming metals. The ligands donate electrons to metals forming the framework type structure. The final symmetry of the synthesized MOF is defined by the mode of combination of metal and ligand components. The term topology is used to describe the symmetry of MOF.³⁴ MOFs are characterized by well-defined, adjustable and highly unique porous structures with spatial confinement and are often crystalline.³⁵ A large number of MOFs with varying pore sizes are synthesized by varying the metal and organic linker or functional groups. Pioneered in the late 1990s by Prof. Omar Yaghi, MOFs have become a rapidly growing research field. The breakthrough research occurred after the development of MOF-5 $[(Zn_4O(CO_2))_6]$ octahedral linked by 1,4-benzenedicarboxylate (BDC^{2-}) with a specific surface area of $2320 \text{ m}^2 \text{ g}^{-1}$ and 61 % porosity.³⁶ The isoreticular series of MOF-5 contain 17 MOFs (from IRMOF-1 to

IRMOF-16) with the basic topology of primitive cubic net.³⁷⁻³⁸ Another MOF of interest is known as HKUST-1 ($\text{Cu}_3(\text{BTC})_2$; BTC^{3-} = benzene-1,3,5-tricarboxylate) composed of Cu paddlewheel [$\text{Cu}_2(\text{CO}_2)_4$] SBUs and a tritopic organic linker, BTC^{3-} .³⁹ **Figure 1.14** represents some of the MOFs with high surface area.⁴⁰

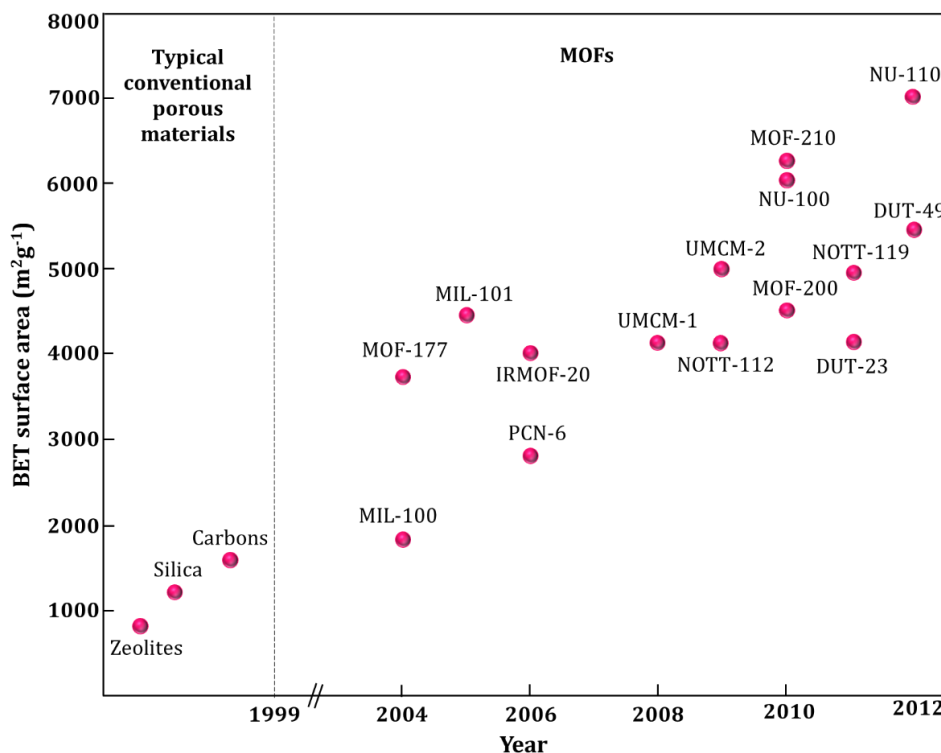


Figure 1.14 Various MOFs with surface area and the time of evolution.

These outstanding features along with relatively high chemical and thermal stability make these frameworks suitable for a wide variety of applications such as gas storage, separation, sensing, proton conduction and drug delivery.⁴¹ The pore opening of the MOFs is ~ 2 nm allowing external molecules to enter into the frameworks. The pore sizes can be tuned via network design. As the framework structure contains strong bonds such as M-O, C-C, C-H, MOFs are thermally stable (250-500 °C) compared to polymers and other organic compounds.⁴²⁻⁴³ Nevertheless, the high inherent porosity of MOFs may also induce framework collapse which limit their practical applications. Incorporating inert functional groups in the MOF framework can avoid this instability. Some MOFs and their applications are listed in **Table 1.2**.

Table 1.2 List of some MOFs and its applications

MOF	Metal centre	Organic linker	Applications
MOF-5	Zn	Terephthalate	Hydrogenation ⁴⁴
MIL-101 (Fe)	Fe	Benzenedicarboxylate	Drug delivery, allylic oxidation of alkenes ⁴⁵
IRMOF-8	Zn	2,6-Naphthalenedicarboxylate	Catalysis: Friedel-Crafts acetylation, Gas adsorption ⁴⁶
MIL-53 (Cr)	Cr	Benzenedicarboxylate	Removal of dibenzothiophene from model oil ⁴⁷
IRMOF-3	Zn	2-amino-1,4-benzenedicarboxylate	Knoevenagel reaction ⁴⁸
MOF-199	Cu	1,3,5-Benzenetricarboxylate	Catalysis, Separation of gases and sensing applications, CO ₂ adsorption ⁴⁹
MOF-177	Zn	Benzenetribenzoate	Gas adsorption ⁵⁰
IRMOF-74	Mg	2,5-Dihydroxybenzene-1,4-dicarboxylate	Light harvesting applications ⁵¹

In the search for chemically and thermally stable MOFs, another class of framework compounds was discovered in 2002 using imidazole as ligands. These are termed as zeolitic imidazolate frameworks (ZIFs) due to their topological similarity with traditional zeolites.⁵²⁻⁵³

1.6 Zeolitic Imidazolate Framework

Zeolitic imidazolate frameworks are a sub-class of MOFs consisting of metal-imidazole-metal linkage formed by self assembly approach. The metals present in ZIFs are usually Zn or Co. The structure of ZIF is similar to that of conventional zeolites where Zn²⁺ ions play the role of silicon and the bridging imidazolate anions mimic

oxygen in zeolites. A bond angle of 145° of bridged M-Im-M bonds in ZIF is equivalent to that of Si-O-Si bond in zeolites as shown in **Figure 1.15**.⁵⁴⁻⁵⁵

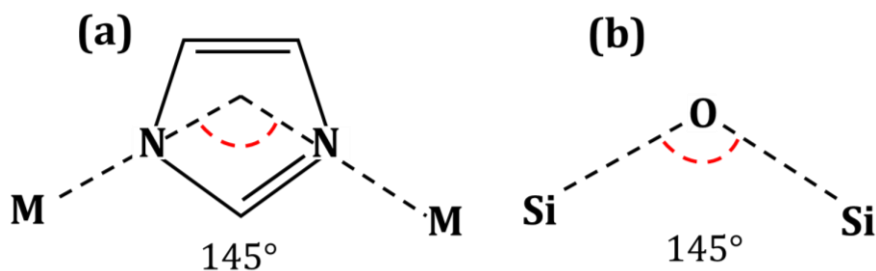


Figure 1.15 The bridging angles in (a) ZIF and (b) Zeolite.

The framework structure can be tuned by varying the functional group of the imidazole ring due to which there are more than hundred ZIFs known. ZIFs possess characteristics of both MOFs and zeolites, such as ultrahigh surface area, unimodal micropores, high crystallinity, abundant functionalities and exceptional thermal and chemical stability.⁵⁶⁻⁵⁸ These properties enable them to be a potential material in the field of catalysis, sensing, gas adsorption and separation applications.⁵⁹⁻⁶¹ The main synthetic protocol involves the mixing up of a hydrated metal salt with imidazole ligands in presence of an amide solvent at the temperature range of 85 to 150 °C. ZIF frameworks formed by the deprotonation of the imidazole ligand followed by coordination with metal ions. The imidazole moieties play a dual role in providing the critical bond angle and as topology outliner through interlink interactions. The topology can be tuned by changing the functionalities in the imidazole ring. For example, the 2-methylimidazole ligand with Zn metal gave SOD topology; on the other hand, the imidazole resulted in CAG topology. In addition to this, the use of mixed linkers results in ZIFs with different topology. Eg. ZIF-68 (Metal-Zn, Linker- 2-nitroimidazole, benzimidazole), ZIF-70 (2-nitroimidazole, imidazole) with GME topology. **Table 1.3** lists some important ZIFs and their applications.

Table 1.3 List of some ZIFs and its applications

ZIF	Metal centre	Organic linker	Topology	Applications
ZIF-7	Zn	Benzimidazole	SOD	CO ₂ adsorption and storage, biosensors, H ₂ separation ⁶²
ZIF-8	Zn	2-methylimidazole	SOD	Photocatalytic degradation, gas adsorption, Friedel-craft acylation, transesterification, biosensors, drug delivery ⁶³
ZIF-9	Co	Benzimidazole	SOD	CO ₂ adsorption and storage, NaBH ₄ hydrolysis, Knoevenagel reaction ⁶²
ZIF-65	Zn	2-nitroimidazole	SOD	N ₂ sorption, CO ₂ capture ⁶²
ZIF-67	Co	2-methylimidazole	SOD	Synthesis of quinazolines, gas adsorption, molecular separation, biosensors ⁶⁴
ZIF-90	Zn	Imidazolate-2-carboxyaldehyde	SOD	CO ₂ capture, gas sorption, sensing, olefin/paraffin separation ⁶²
ZIF-95	Zn	Chlorobenzimidazole	POZ	Gas separation, olefin/paraffin separation ⁵⁷
ZIF-20	Zn	Purine	LTA	Gas separation, CO ₂ capture ⁵⁷
ZIF-21	Co	Purine	LTA	NH ₃ sorption ⁵⁷
ZIF-68	Zn	2-nitroimidazole, benzimidazole	GME	Biosensor, CO ₂ capture ⁵⁷
ZIF-69	Zn	2-nitroimidazole, 5-chlorobenzimidazole	GME	Gas separation, CO ₂ adsorption, olefin/paraffin separation ⁶⁵

ZIF-70	Zn	2-nitroimidazole, imidazole	GME	CO ₂ capture ⁶⁵
ZIF-78		2-nitroimidazole, 6- nitrobenzimidazole	GME	CO ₂ capture ⁶⁵
ZIF-4	Zn	Imidazole	CAG	CO ₂ adsorption ⁶⁵
ZIF-14	Zn	2-ethylimidazole	ANA	CO ₂ capture ⁶²

1.6.1 Zeolitic Imidazolate Framework-8 & 67 (ZIF-8 and ZIF-67)

Zeolitic imidazolate framework-8 (ZIF-8) is a microporous material and it is one of the simplest members among the ZIF family with a network formula of Zn(2-methylimidazole)₂, briefly written as Zn(mlm)₂ where Zn ions are tetrahedrally coordinated to 2-methylimidazole (HmIm). The topology of ZIF-8 corresponds to the zeolite sodalite (SOD), and can be described as a space-filling packing of truncated octahedrons.⁶⁶ ZIF-8 has extremely high thermal, chemical, and mechanical stability. It has an excellent molecular adsorption behavior of gases like CO₂, N₂, and, CH₄.⁶³

ZIF-67 is another member (Co(Hmim)₂) isostructural to ZIF-8, and is formed by bridging 2-methylimidazolate anions and cobalt cations resulting in a sodalite (SOD) topology with a pore size of about 0.34 nm.⁶⁷ The abundant coordinated unsaturated metal sites in the ZIF-67 framework enable its use for sorption of many guest molecules, for example ammonia borane.⁶⁸ The framework structure of ZIF-8 and ZIF-67 are as shown in **Figure 1.16**. ZIFs are the most studied candidate for the development of Pt-free ORR catalysts since it can act as the carbon and nitrogen source for the electrocatalyst preparation.⁶⁹⁻⁷⁰

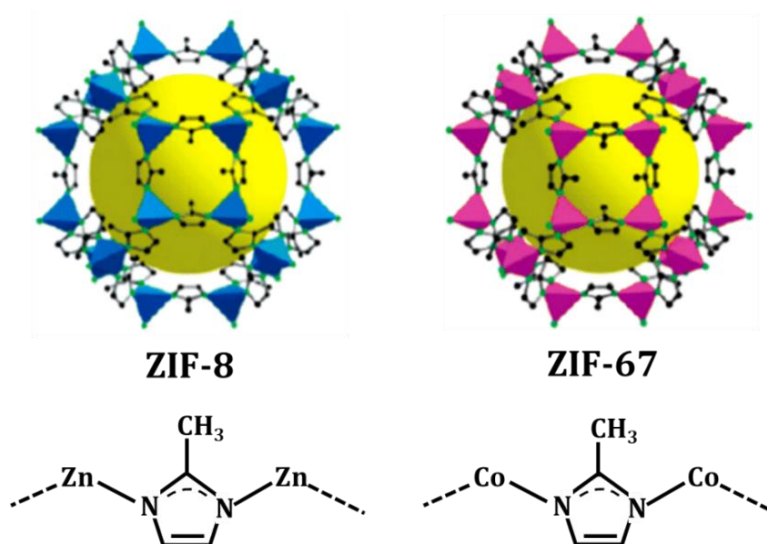


Figure 1.16 The structure of ZIF-8 and ZIF-67.

1.7 Metal Organic Gel

Metal-organic gels (MOGs) are a class of coordination polymers, formed by metal-ligand coordination extending into 3D structures.⁷¹⁻⁷² Their high surface area and porous gel structure enables rapid mass transfer and permeability.⁷³⁻⁷⁵ The moiety of the aromatic organic ligands in the framework provides π - π interaction with the guest molecules. The open metals in the coordination polymer are Lewis acid sites, and can interact with the electron-rich analytes.⁷⁶ MOGs behave like viscoelastic solids and hence are used for applications in catalysis,⁷⁷ adsorption,⁷⁸⁻⁷⁹ separation⁸⁰⁻⁸¹ and controlled release. MOGs usually contain organic solvents with sponge-like gel matrices. Like MOF, MOGs also act as template for porous carbon which inherits its structural features. The MOG templated porous carbon synthesis is of considerable importance due to relatively cheap, clean and easy synthesis procedure and tunability of structure.⁸² Typical examples of MOGs include Fe-BTC and Al-BDC gels, where BTC = 1,3,5-benzenetricarboxylate, and BDC = 1,4-benzenedicarboxylate. The MOG formation occurs in three stages where, polymerization of precursors (coordination of organic ligands with metal ions) takes place in the first stage forming nanoparticles followed by the growth/aggregation of nanoparticles in the next stage and cross-linking of particle species into networks in the final stage.⁸³ **Figure 1.17** shows the schematic of MOGs. Some of the reported MOGs and their applications are listed in **Table 1.4**.

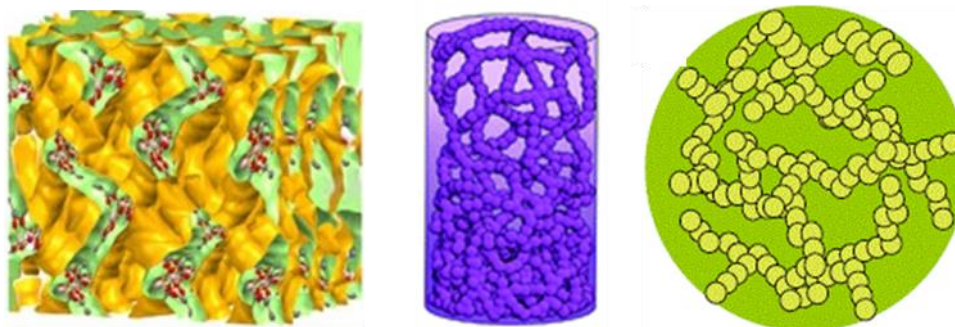


Figure 1.17 Metal organic gel structures.¹⁷²⁻¹⁷³

Table 1.4 List of some MOGs and its applications

MOG	Metal	Ligand	Applications
Fe-BTC	Fe	1,3,5-benzenetricarboxylic acid	CO ₂ capture ⁷⁹
Cr-BPDA	Cr	2,2'-bipyridine-4,4'-dicarboxylic acid	Self-healing ⁸⁴
Cr-sBDC	Cr	2-sulfoterephthalic acid	Proton conductor ⁸⁵
Al-BDC	Al	Terephthalic acid	Dye adsorption ⁸⁶
Al-BTC	Al	1,3,5-benzenetricarboxylic acid	H ₂ and CO ₂ sorption ⁸⁶
Tb-BTC	Tb	1,3,5-benzenetricarboxylic acid	Detection of antibiotics and explosives ⁸⁷
Fe-Py-OH	Fe	3-hydroxypyridine	Selective ethylene dimerization ⁸⁸
Zr-BDC-NH ₂	Zr	2-Aminoterephthalic acid	CO ₂ sorption ⁸⁹
Ca-5TIA	Ca	5-(1,2,4-triazoleyl)isophthalic acid	CO ₂ uptake ⁹⁰
Cu-BTB	Cu	1,3,5-tris(4,-carboxyphenyl)benzene	Dye adsorption ⁹¹

1.8 Electrocatalyst for ORR

There have been many efforts to increase the activity of electrocatalysts for the oxygen reduction reaction, nevertheless platinum remains the most commonly used catalyst. A typical way to compare the ability of different catalysts towards electrochemical oxygen reduction reaction is from the volcano plot as shown in **Figure 1.18**. Here, the activity is plotted against the binding energies for different metals with a single oxygen atom. Platinum sits at the top of the volcano plot while precious metals like Ir, Ru, Pd, etc. are lying near to Pt in the volcano plot.

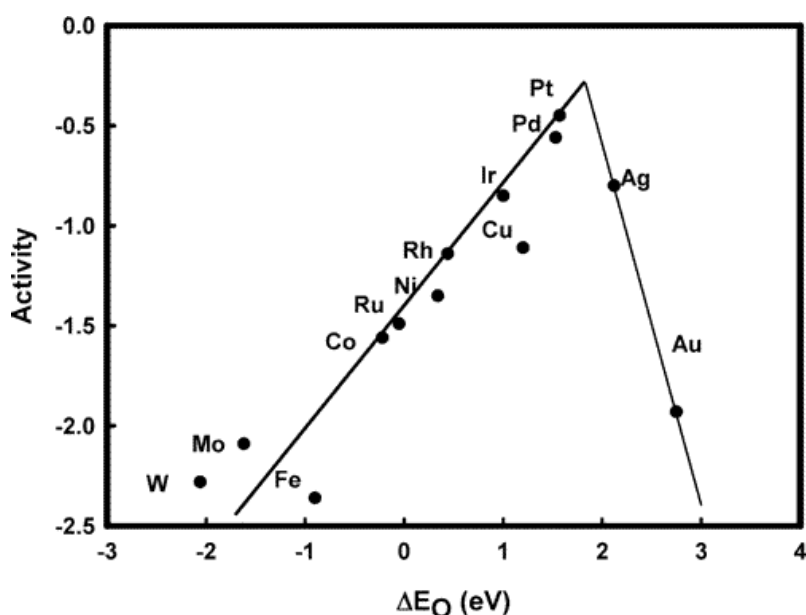


Figure 1.18 Volcano plot showing oxygen reduction activity of different metals as a function of oxygen binding energy (adapted from reference).¹⁴

The development of Pt free, inexpensive ORR electrocatalysts for the fuel cell application has been at the forefront of electro-catalyst research for some time and have thus far realized the following.

1.8.1 Pt Alloys

Alloying Pt with transition metals has been considered as a strategy for the creation of second-generation catalysts at reduced costs and improved specific activity.⁹² The improved ORR activity is based on the modification of the electronic structure of Pt, which affects the adsorption strength of oxygen-containing species on active sites. However, these alloys also suffer from leaching or dissolution, leading to

deterioration in the stability.⁹³⁻⁹⁴ Developing core-shell structure of Pt alloy catalyst where Pt shells can protect transition metal cores reduces the dissolution of core material.⁹⁵ Also, the electronic structure of the Pt surface is modified by the underlying alloy, resulting in improved ORR activity. The activities of Pt-alloy based nanoparticles (NPs) depend on both the composition and structure. Alloying Pt with transition metals like Ni, Fe, Co, Cu etc. have been realised through carefully designed solution-based synthesis leading to the formation of uniformly shaped nanoparticles.⁹⁶⁻⁹⁸ Another approach is the use of more stable carbon supports such as carbon nanotubes or graphene to reduce carbon corrosion and subsequently avoid detachment/agglomeration of the Pt catalyst.⁹⁹⁻¹⁰⁰

1.8.2 Metal-Free Catalysts

Carbon based catalysts, mainly carbon black, graphene, carbon nanotube (CNT) etc., were widely applied for electrocatalytic applications due to their electrical conductivity and surface area. However, deficiency of active sites for O₂ adsorption due to the electroneutrality hindered their broader application and thus needs modifications to its surface charge distributions to improve the localized interaction between carbon and adsorbed species. Introducing defects in the structure by doping suitable non-metallic heteroatoms like N, B, P, S etc., have been proven as a strategy to create large number of active sites owing to the difference in electronegativity. Out of these, most of the studies are focused on N-doped carbon for electrocatalytic applications.¹⁰¹⁻¹⁰³ N has similarity in size and high electronegativity compared to carbon (N-3.04 and C-2.55). The electroneutrality of carbon framework is altered by the N-doping, generating positive charge densities on the carbon adjacent to N. Such a structure is reportedly favorable for the adsorption of oxygen resulting in improved ORR activity.¹⁰⁴

1.8.2.1 Different Types of Doped Nitrogen

The electrocatalytic performance of the N-doped carbon is greatly dependent on the type of nitrogen species present in the carbon framework. There are generally three types of species; pyridinic N, pyrrolic N and graphitic N.¹⁰⁵⁻¹⁰⁶ (**Figure 1.19**). Pyridinic nitrogen is the one which occupy edges or defects of the graphene by bonding with two carbon atoms and contributes the p electron to the π electron system. The

pyrrolic nitrogen exists as N-H on a five membered ring without any free electron to contribute. Unlike pyridinic and pyrrolic, graphitic N (quaternary N) doping occurs by replacing one carbon atom of the hexagonal ring and by bonding with four other carbon atoms. It can introduce an extra electron in the delocalized π -system. Pyridinic and graphitic N is sp^2 hybridized and the hybridization of pyrrolic N is sp^3 . Oxidized N is another configuration present in N-doped graphene. Graphitic N is found as the active site for ORR according to density functional theory (DFT) calculations due to the presence of an unpaired electron in N.¹⁰⁷⁻¹⁰⁸ Pyridinic N, with a lone pair of electrons, also has the capability to weaken the O-O bond thereby enhancing the ORR activity.¹⁰⁹⁻¹¹⁰

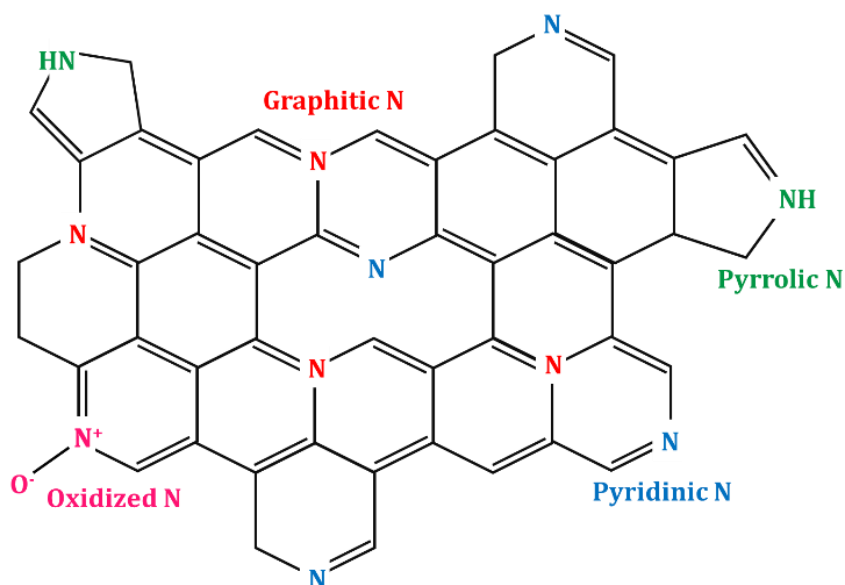


Figure 1.19 The nitrogen configurations observed on N-doped carbon catalysts.

Raman spectroscopy is a well accepted technique used to evaluate the N-doping in carbon. The N-doped carbon contains mainly three peaks in the Raman spectrum corresponding to D, G and 2D bands at wavelengths of around 1300, 1600, 2600 cm^{-1} respectively.¹¹¹ The G band signifies the vibrational mode (E_{2g}) of the sp^2 hybridized hexagonally bonded graphitic carbon while the D band results from the structurally disordered carbon atoms. 2D band is a second order band due to the disordered structure. The nitrogen doping causes the formation of defects into the carbon matrix. The intensity ratio of the D and G bands (I_D/I_G) imparts insights on the degree of distortion of the carbon structure, as the distortion increases with increasing I_D/I_G ratio.¹¹² Typical Raman spectrum for N-doped carbon is shown in **Figure 1.20**.

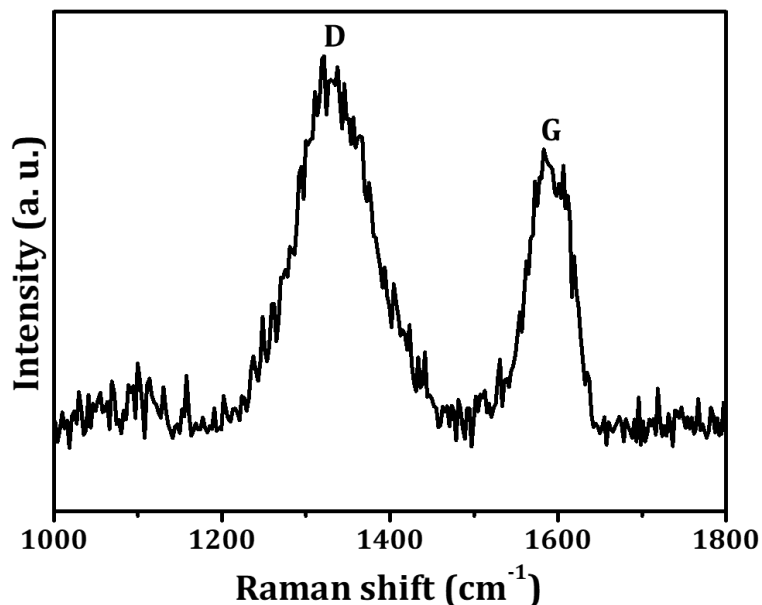


Figure 1.20 Raman spectrum of N-doped carbon.

The extent of N-doping can be measured using X-ray Photoelectron Spectroscopy (XPS). The peak corresponding to the binding energies of N1s and C1s will appear at ~ 400 eV and ~ 284 eV respectively and the ratio of N1s and C1s will provide the extent of nitrogen doping. The deconvoluted N1s spectra shown in **Figure 1.21** indicates the bonding configurations of the N in which each nitrogen will have a shift in the binding energy values. The pyridinic N appeared in the range of 398.1-399.3 eV.¹¹³ From 399.8-401.2 eV, pyrrolic N exist and quaternary N have peak in the range of 401.1-402.7 eV.¹¹⁴

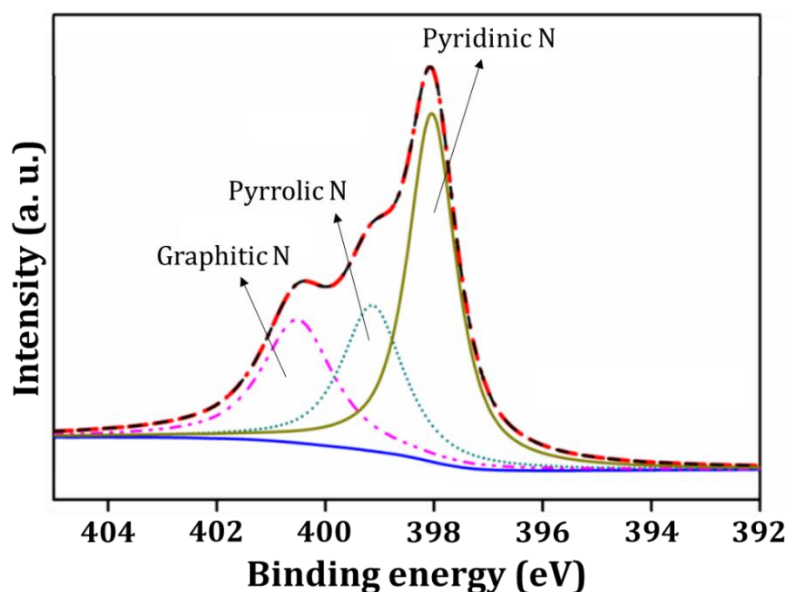


Figure 1.21 Typical N1s spectra of N-doped carbon.

Dai *et al.* in 2009 reported highly efficient N-doped carbon nanotube ORR catalyst to replace Pt. The enhanced ORR activity was due to their large surface area, good conductivity and tunable morphology. Following this pioneering work, various heteroatom-doped carbon materials were investigated. Antonietti *et al.* developed mesoporous N-doped carbon materials by carbonization of nucleobases dissolved in an all-organic ionic liquid. The catalyst exhibited only 25 mV higher overpotential than the commercial Pt catalyst.¹¹⁵ Metal free active carbon nanostructures obtained by the conversion of biomass has become an attractive approach to develop electrocatalysts from more economical, abundant, and renewable resources. Various types of biomasses such as chitin, chitosan, sucrose, cellulose derivatives, lignin etc. have been used for the synthesis of ORR electrocatalysts. Chitin is the second most abundant biopolymer in the biosphere and the most abundant natural nitrogen-containing compound.¹¹⁶ Since it is rich in N content, it directly transforms to an N-doped carbon material, without the need of additional N-dopant precursors. Li *et al.* prepared N-doped carbon fiber aerogel using prawn shells as the raw material. The prepared carbon-fiber aerogel exhibited an onset-potential of 54 mV more positive than that of Pt/C catalyst, better stability, and resistance to methanol crossover.¹¹⁷ N-doped activated carbon sheets (ACS) prepared by hydrothermal followed by pyrolysis of chitin, and activation using ZnCl₂ exhibited much higher catalytic activity toward both the ORR and the OER.¹¹⁸ Cellulose and its derivatives have been extensively used as the precursors for the production of ORR electrocatalysts. Due to the lack of heteroatoms, it is required to dope heteroatoms such as N, B, P etc. in order to boost the electrocatalytic activity. The nanocrystals of cellulose together with urea were used to produce carbon aerogels via lyophilization and carbonization. High surface area N-doped carbon nanosheets were successfully synthesized through this method without involving any catalysts or post-treatment. The catalyst exhibited 20 mV more positive halfwave potential than the commercial Pt/C catalyst.¹¹⁹ **Table 1.5** summarises the ORR performance of various metal free electrocatalysts.

Table 1.5 Summary of various metal free electrocatalysts for ORR.

Catalyst	E_{onset} (V vs RHE)	E_{1/2} (V vs RHE)	Tafel slope (mV dec⁻¹)	n
CCa	0.9	0.75	-	3.6 ¹⁰¹
NMCF	-	0.80	-	3.9 ¹⁰⁴
NCN-1000-5	0.95	0.82	86	3.92 ¹⁰⁶
N-G-1000	0.981	0.862	72	3.92 ¹⁰⁸
N-HsGDY-900	1.02	0.85	64.4	3.95 ¹¹²
meso-EmU	0.035 V vs AgCl	-	-	4.1 ¹¹⁵
Chitin-900	0.054 V vs AgCl	-	-	3.90 ¹¹⁷
ACS	-0.15 V vs. SCE	-	90	3.93 ¹¹⁸
GZ80C	0.88	0.75	81.7	3.2 ¹²⁰

1.8.3 Non-precious Metal Catalysts (NPMCs)

The development of earth-abundant NPMCs have been intensively investigated due to the possibility of eliminating the usage of Pt or other precious metals. The unique structure of NPMCs can provide vast possibilities for tuning the activity, selectivity, and durability of the catalyst.¹²¹ The non-precious metal catalysts such as metal oxides, nitrides, chalcogenides, carbide, etc. are reported so far for fuel cell applications. However, the low electrical conductivity and the non-availability of adsorption sites for oxygen species on the surfaces resulted in the lowering of ORR activity.¹²²⁻¹²³ Carbon-supported transition metal/nitrogen (MN_x/C, M = Co, Fe, Ni, etc.) compounds are found to be active and durable catalyst towards ORR. The interactions between the transition metal doped nitrogen, and the carbon support play a vital role in facilitating the ORR activity.

In 1964, Jasinski *et al.* first reported the possibility of using metal/nitrogen macrocyclic compounds as ORR catalysts in alkaline electrolyte.¹²⁴ Based on this study, variety of electrocatalysts have emerged with carbon as the support material. Yeager *et al.*, developed platinum free electrocatalyst by the simple high temperature annealing of a mixture of poly acrylonitrile (PAN), metal (Fe or Co) salt and high surface area carbon. The pyridyl nitrogen derived from the nitrile nitrogen of PAN during the high temperature annealing provides the binding site for the metal centre. The active reaction centre in such electrocatalysts is the pyridyl nitrogen coordinated metal for the ORR which resemble the coordination of metal-ligand complex.¹²⁵ Following the publication of Yeager *et al.*, many reports have been published on electrocatalysts prepared by the pyrolysis of different heteroatom containing polymer/monomers with iron salt and high surface area carbon for improved ORR. Among different polymers with heteroatom, polyaniline (PANI), polypyrrole (PPy) and polyethylenedioxythiophene (PEDOT) are used extensively for the preparation of Fe doped alloy carbon materials for ORR. During high temperature annealing, heteroatoms from these conducting polymers facilitate more uniform distribution of heteroatoms in the carbon matrix, which assist the coordination of metal centres and form carbon-alloy nanostructures.¹²⁶⁻¹²⁷ The following section discusses the non precious metal doped carbon catalysts derived by the pyrolysis of MOF and MOG precursors.

1.8.3.1 Metal Organic Framework Derived Carbon

Metal organic framework, mainly zeolitic imidazolate framework (ZIF) which contain metal as well as carbon source is most widely used for developing electrocatalyst by simple pyrolysis. Compared to traditional nanoporous carbon materials, MOFs have many unique advantages such as its simple preparation methods, ordered and controllable porous structures, high specific surface area, and the ease of doping highly dispersed heteroatoms.¹²⁸ Most of the commonly used MOF precursors are zeolitic imidazolate framework materials, mainly ZIF-8 and ZIF-67, in which ZIF-8 pyrolysis products are N-doped nanoporous carbon, and ZIF-67 can obtain N-doped carbon nanotubes and other structures during pyrolysis. The ZIF-8-derived porous carbon has a large specific surface area ($1000-2000 \text{ m}^2 \text{ g}^{-1}$) whereas the ZIF-67-derived porous carbon has an active Co-N site. Xia *et al.*, and Meng *et al.* used ZIF-67

as the precursor for the synthesis of Co-N doped hollow carbon nanotubes. The catalyst showed excellent activity towards both the ORR and the OER electrocatalysis. The increased crystallinity and in situ formed metallic Co nanoparticles contributed towards the electrocatalytic activity in addition to N-doping.¹²⁹⁻¹³⁰ A large number of studies have shown that the Fe-containing catalyst sometimes exhibits higher electrocatalytic activity compared to Co-containing catalyst. Thus, pyrolysis of Fe-doped ZIF materials are also more likely to exhibit good ORR activity. Simple pyrolysis of iron salt impregnated ZIF (mainly ZIF-8) produced Fe-N_x doped carbon. Single pyrolysis has several advantages. The proper coordination of metal and nitrogen species in the ZIF-8 can improve the Fe-N_x type reaction centres for oxygen reduction reaction.¹³¹ Recently, Deng *et al.* used a gaseous doping approach for synthesizing iron doped carbon from ZIF-8. In this method, the iron precursor ferrocene was first vaporized and trapped inside the ZIF-8. The ZIF-8 derived carbon has high density of iron single atom dopants. Moreover, the ZIF-8 morphology is well preserved with high porosity. The half-wave potential of the electrocatalyst reached 0.864 V which is 20 mV higher than Pt/C in alkaline condition.¹³² Zhang *et al.*, used chemical doping approach of Fe in to the ZIF-8 precursor. Simple thermal annealing produced single iron atom doped carbon. More interestingly, the particle size of Fe-doped-ZIF can be tuned during its synthesis where in the active reaction centers can be created in the electrocatalyst. The best ORR activity was achieved for 50 nm sized ZIF. The half-wave potential of the prepared Fe-N_x doped carbon was 0.85 V which is 30 mV lower to Pt/C in 0.5 M H₂SO₄.¹³³ Similar to Zhang's work, a host-guest strategy was adopted by Lai *et al.* to prepare Fe-N_x doped carbon from ZIF-8. They chemically produced a Fe-mlm nanocluster (guest) inside the ZIF-8 (host). The annealing of such ZIF-8 led to Fe-N_x doped porous carbon (**Figure 1.22**). This host-guest approach produced two different type coordination of iron ie. two and five coordinated configurations. The five coordinated configuration shows excellent ORR in acidic condition. DFT study shows that such five-coordinated configuration lower the energy barrier for ORR and low adsorption of -OH species at the reaction centre.¹³⁴

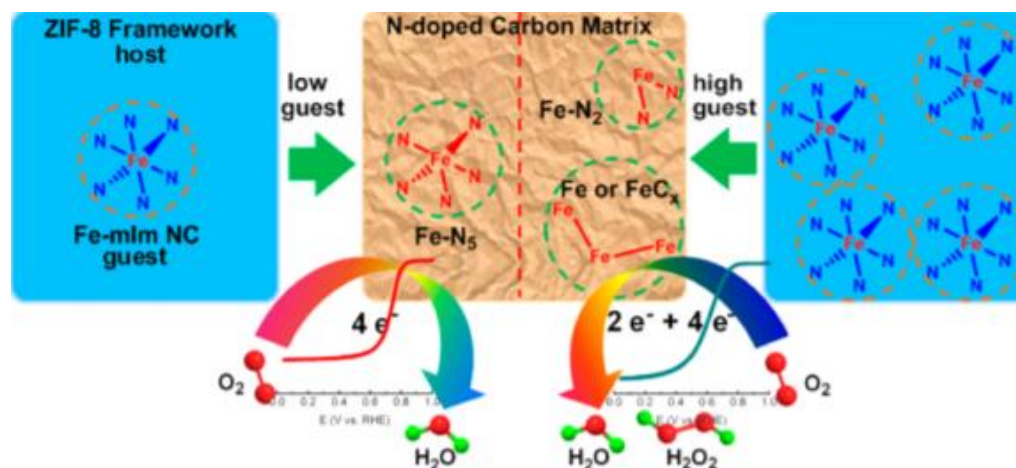


Figure 1.22 Illustration of the host-guest chemistry strategy to fabricate MOF-derived Fe-N/C catalysts (adapted from reference).¹³⁴

The nitrogen content in the ZIF derived carbon can be improved by adding graphene sheets during the synthesis process.¹²⁰ The Zn/Fe ion dispersed in graphene sheets on reaction with 2-methyl imidazole produced ZIF on the graphene sheets. Annealing this precursor yield Fe-N_x doped porous carbon showing excellent ORR activity in alkaline condition. The graphene sheets assist to accommodate more nitrogen atoms in the doped porous carbon. The peculiar morphology, high nitrogen content and Fe-N_x coordination assist for the improved ORR.¹⁰³ There are reports on the different precious metal atom incorporation in the ZIF-8 to develop excellent electrocatalyst for ORR. Pt, Pd, Rh, Au, Ru etc incorporated in to ZIF-8 followed by annealing produced metal alloyed Zn nanoparticles embedded in the carbon matrix.¹³⁵

1.8.3.2 Metal Organic Gel Derived Caron

MOGs act as rich pool, in which materials can be immobilized and dispersed throughout the whole gel matrices and therefore be used as precursors to produce highly dispersed and nano-sized ORR electrocatalysts. Wang *et al.* synthesized a urea/CNTs-decorated MOG(Fe) and used it as precursors for the first time to synthesize an effective ORR catalyst through pyrolysis. They have obtained particles with average size of 10 nm having core@shell structures with Fe-Fe₂O₃ cores and NC shells. By virtue of the unique structure, the material exhibited a superior oxygen reduction with an onset potential of 0.92 V, and half-wave potential of 0.72V.¹³⁶ A self-templated carbonization strategy was presented by Zhang *et al.* for a general synthesis of heterostructures of transition metal phosphide @nitrogen /phosphorus

dual-doped carbon quasiaerogels using a metallogel containing bimetallic clusters (BMOG) as the precursor. Owing to the 3D inter-connected and highly conductive quasiaerogel framework of heteroatom-doped carbon and large number of electrochemically active sites, the material worked as an ORR/HER bifunctional electrocatalyst. The catalyst exhibited excellent electrochemical performance towards the ORR with a half-wave potential of 0.85 V versus RHE, high crossover tolerance to methanol and excellent long-term durability.¹³⁷ Zhang *et al.* used a bimetallic zinc/cobalt organic gel (Zn/Co-MOG) as the precursor for the synthesis of cobalt/nitrogen dual-doped porous carbon nanosheet composites (Co/N@PCS). Due to hierarchical porous structure and fast ion/electron transport, the Co/N@PCS exhibited an excellent ORR electrocatalytic activity. The half-wave potential of the Co/N@PCS was 0.87 V vs. RHE with long-term cycling stability and excellent methanol tolerance.¹³⁸ Summary of the ORR performances of various non-precious metal electrocatalysts are listed in **Table 1.6**.

Table 1.6 Summary of various non-precious metal electrocatalysts for ORR.

Catalyst	E_{onset} (V vs RHE)	$E_{1/2}$ (V vs RHE)	Tafel slope (mV dec ⁻¹)	N
FeGZ-10C	0.95	0.82	87.6	3.8 ¹⁰³
NCNTF	0.97	0.87	64	3.97 ¹²⁹
N-CNT	0.87	0.85	-	3.93 ¹³⁰
Fe-N/C	0.97	0.75	63	3.97 ¹³¹
C-FeZIF	0.94	0.864	-	3.98 ¹³²
Fe-ZIF	0.98	0.85	-	4 ¹³³
Fe-N/C	0.861	0.735	55.6	3.98 ¹³⁴
Rh@NPCP	1.04	0.84	33	3.98 ¹³⁵
MOG(Fe)/CNT	0.92	0.72	66	3.92 ¹³⁶
CoP@NPCA	0.94	0.85	69.8	3.99 ¹³⁷
Co/N@PCS	-	0.87	-	.138

1.9 Direct Borohydride Fuel Cells

Direct borohydride fuel cells (DBFC) are alkaline fuel cells which utilizes NaBH_4 directly as a fuel to generate electricity. Most of the AFCs are fed with hydrogen at the anode and oxygen at the cathode. However, the main problem is related to the hydrogen production, storage and transport. Liquid fuels, alternative to ultra-pure H_2 , such as alcohols and borohydrides can be used in AFCs for easier storage and transport. Direct methanol fuel cell (DMFC) and ethanol fuel cell (DEFC) usually suffers from slow anode reaction kinetics, high catalyst loading, (usually noble metal based catalysts) and display small power densities. On the other hand, direct borohydride fuel cells (DBFCs) in which sodium borohydride (NaBH_4) is used as the fuel are gaining much attention due to high cell voltage (1.64 V), high theoretical specific capacity (5.7 Ah g^{-1}), high energy density (9.3 Wh g^{-1}), superior hydrogen storage (10.6 wt.%) and non-flammability. Furthermore, NaBH_4 is carbon-free, nontoxic and relatively stable in alkaline solution.¹³⁹⁻¹⁴⁰ The DBFC system was first proposed in the early 1960s.¹⁴¹ A practical demonstration of direct electricity generation from borohydride ions was reported by Indig and Snyder.¹⁴²

In DBFC, an aqueous base stabilized BH_4^- anion oxidises at the anode producing an environmentally benign, water soluble BO_2^- product which may be collected and recycled.¹⁴³⁻¹⁴⁵ This anodic borohydride oxidation reaction (BOR) involves the release of 8 electrons as shown in eq. 1. Eq. 2 shows the ORR occurring at the cathode. **Figure 1.23** shows the schematic representation of a direct borohydride fuel cell.

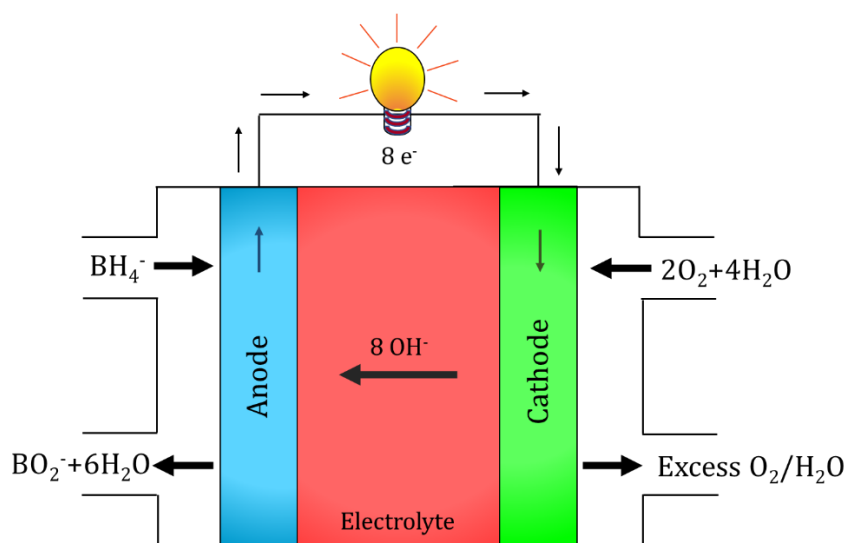
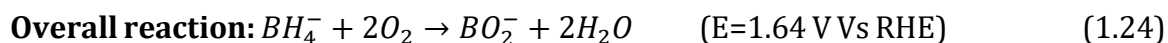
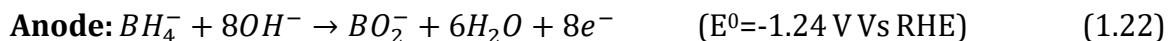


Figure 1.23 Schematic of a direct borohydride fuel cell.



The anodic BOR is a complex reaction and it is accompanied by several parasitic reactions like hydrogen evolution reaction (HER) and non-faradaic heterogeneous hydrolysis of BH_4^- . By virtue of these competing reactions, the number of released electrons is usually less than 8 indicating the inefficiency of the electrocatalysts.

There is another category of fuel cell that uses NaBH_4 indirectly and is named as indirect borohydride fuel cells (IBFC). The anodic fuel in IBFC is hydrogen which is released from NaBH_4 by hydrolysis. The difference between IBFC and DBFC is schematically represented in **Figure 1.24**.

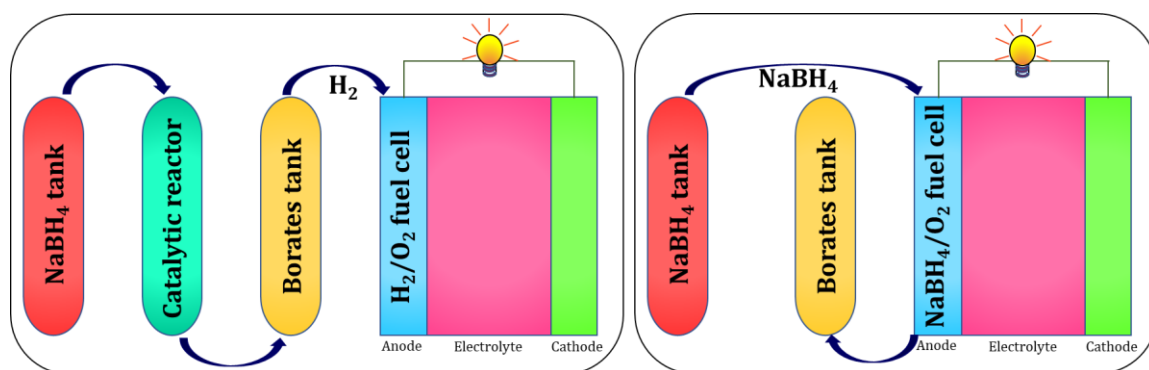


Figure 1.24 Schematic representation of (a) H_2/O_2 fuel cell fed by H_2 generated by hydrolysis of NaBH_4 (IBFC) and (b) direct borohydride fuel cell.

The competitions between the direct borohydride electrochemical oxidation and the hydrolysis pathway of BH_4^- anion is shown in **Figure 1.25**. The maximum output of energy and number of electrons will be resulting from the direct oxidation. Molecular hydrogen will be formed in the hydrolysis pathway resulting in a decrease in number of electron transfer. If the reaction follows a preferred hydrolysis route and the catalyst is capable of oxidising the generated molecular hydrogen, the anode will behave like a direct hydrogen fuel cell and there will be eight released electrons from the electrooxidation of four hydrogen molecules. The boron atoms here act like hydrogen carriers. Even though this route also involves eight electrons, it cannot be considered as efficient pathway since it wastes some of the chemical energy stored in

the fuel, due to the exothermic hydrolysis reaction. Therefore, anode catalysts with high performance and efficient utilization of BH_4^- are important for the practical application of DBFC.

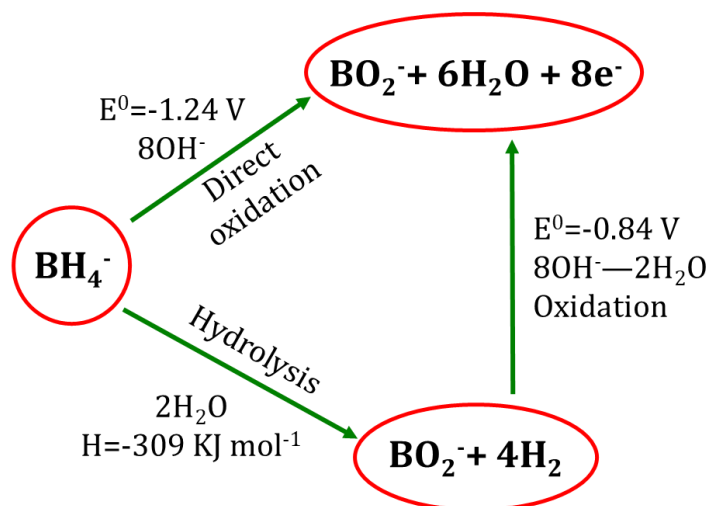


Figure 1.25 Schematic of the competition between the direct borohydride electrooxidation and the hydrolysis.

1.9.1 Electrocatalysts for BOR

1.9.1.1 Noble Metal Based Catalyst

The first study on BOR was reported in 1962 by Elder *et al.* where they had investigated the use of Pt electrode on the oxidation of borohydride.¹⁴⁶ Later many studies were carried out in which noble metals such as platinum, palladium and gold were most widely used.¹⁴⁷⁻¹⁴⁸ However, the increased ability of these noble metal catalyst towards breaking of B-H bond led to hydrogen gas production and hence less than 8 e- were collected for the conversion of every borohydride molecule.¹⁴⁹⁻¹⁵¹ This limits the overall stability of the fuel cell and therefore, it is highly demanded to develop catalysts that can selectively oxidize BH_4^- with negligible or no hydrogen evolution. Gyenge *et al.* reported the electrochemical oxidation of BH_4^- on Pt and Au electrodes where Pt catalyzed both the hydrolysis and direct oxidation of BH_4^- . The addition of thiourea inhibited the hydrolysis of BH_4^- and the H_2 evolution by the inhibiting effect of thiourea on the recombination of surface adsorbed hydrogen radicals. However, the issue of long-term anode performance, stability and poisoning in the presence of TU were not addressed.¹⁵² Au supported on high-surface area carbon silk catalyst for BOR was reported by Amendola *et al.* The number of electrons

utilized per molecule of BH_4^- oxidized was 6.9 implying efficient utilization of the BH_4^- oxidation.¹⁵³ However, Chatenet *et al.* later reported that Au is not an efficient electrocatalyst towards BOR mainly because of too high activation potentials.¹⁵⁴

1.9.1.2 Non-noble Metal Based Catalyst

From density functional theory, Janik *et al.* concluded that the activity for B-H bond dissociation determines the catalyst activity towards BOR.¹⁵⁵ Numerous types of research were conducted to develop low-cost transition metals such as Ni, Co, Fe, Cu based catalysts for BOR.¹⁵⁶⁻¹⁵⁷ Due to the high B-H bond-breaking ability of cobalt compared to other transition metals, cobalt-based materials can be used as a promising catalyst for BOR.¹⁵⁸⁻¹⁵⁹ However, there are only a few reports on cobalt based catalysts for BOR. Zhang *et al.* reported cobalt incorporated multiwalled carbon nanotubes with high catalytic activity and good stability for NaBH_4 electrooxidation. The hierarchical 3D network structure with dispersed Co nanoparticles increased the adsorption and electrooxidation of hydrogen during the reaction.¹⁶⁰ Alloying Co with other transition metals is also reported to be effective in improving the catalytic performance by the synergistic effect between the metals and special electron transfer path.^{159, 161} CNT supported CoBi,¹⁶² Ni-Co nanoparticles immobilized Ni foam¹⁶³ and NiB alloy decorated by Cu,¹⁶⁴ all exhibited good BOR activity and stability. Recently, Nagaiah *et al.* synthesized urchin-shaped cobalt tungstate catalyst with enhanced BOR performance.¹⁶⁵ Nevertheless, the catalytic activity of the current Co-based catalysts is still lower than those of noble metal catalysts and concerted efforts are essential to develop non-noble metal catalysts that can completely replace noble metal catalysts. List of some of the reported BOR catalysts and their electron transport number is shown in **Table 1.7**.

Table 1.7 Electron transfer number comparison of reported BOR catalysts

Sl. No	Sample	Electrolyte composition		n
1	AgY (Ag zeolites)	2 M NaOH	0.03 M NaBH_4	4.3 ¹⁶⁶
2	$\text{Pt}_{67}\text{Fe}_{33}/\text{C}$	3 M NaOH	0.1 M NaBH_4	4.9 ¹⁶⁷
3	$\text{Au}_2\text{-Ni}_1\text{-Cu}_1/\text{C}$	2 M NaOH	0.1 M NaBH_4	5.9 ¹⁶⁸

4	Cobalt tungstate	1 M NaOH	0.03 M NaBH ₄	7.2 ¹⁶⁵
5	Pd _x Au _{1-x} /C	2 M NaOH	0.013M NaBH ₄	6 ¹⁶⁹
6	Co-P/CF	1 M NaOH	0.1 M NaBH ₄	6 ¹⁵⁹
7	Au ₍₅₀₎ /Ni(OH) ₂₍₅₀₎ /C	3 M NaOH	0.1 M NaBH ₄	4.7 ¹⁷⁰
8	CuNiPd	2 M NaOH	0.1 M NaBH ₄	4.9 ¹⁵⁷
9	Ni-1	1 M NaOH	0.02 M NaBH ₄	7.02 ¹⁷¹
10	Ni ₁ @Ag ₁ /C	2 M NaOH	0.1 M NaBH ₄	4.8 ¹⁷²
11	NiBCu _x /C	2 M NaOH	0.1 M NaBH ₄	4.1 ¹⁶⁴
12	Ni _{1-x} Cu _x O	1 M KOH	0.01 M AB	5.9 ¹⁷³
13	Pd/rGO-Fe ₃ O ₄	2 M NaOH	0.03 M NaBH ₄	5.6 ¹⁷⁴
14	Pt-Ag	0.1 M NaOH	0.001 M NaBH ₄	5.7 ¹⁷⁵
15	PtSn/C	0.2 M KOH	0.001 M NaBH ₄	6.4 ¹⁷⁶
16	Au-NP@rGO	2M NaOH	0.4 M NaBH ₄	7.2 ¹⁵¹
17	CoAu/rGO	2M NaOH	0.03 M NaBH ₄	6.9 ¹⁷⁷
18	CoNi-NS/rGO	4M NaOH	0.5 M NaBH ₄	6.9 ¹⁷⁸

1.10 Definition of the Present Problem

After the detailed literature survey, it is understood that highly efficient and cost-effective electrocatalysts are necessarily required for the widespread use of the electrochemical energy conversion devices like fuel cells. The exorbitant price of the state-of-the-art Pt/C catalysts make fuel cells highly expensive and, thus, hinder its commercialization. Thus, it is important to develop non-noble electrocatalysts as substitutes for the state-of-the-art Pt/C catalyst. However, the multistep synthetic strategies, loss of nitrogen during high temperature pyrolysis (700-900 °C),

unavailability of the active sites due to relatively small pore sizes, low active site density and the low conductivity are considered major bottlenecks for the development of heteroatom doped carbon catalysts. Hence, a systematic study is needed for the development of heteroatom doped carbon by a careful design and selection of the precursors. This thesis is an effort to develop viable Pt-free electrocatalysts, mainly transition metal, N- co doped carbon, which can be used as replacements for Pt-based catalyst in alkaline fuel cell. The following scientific challenges are thus identified.

- Retention of the nitrogen content with appropriate pore characteristics after pyrolysis
- Generation of electrocatalytically active graphitic and pyridinic N with lower pyrrolic N content (electrocatalytically inactive)
- Improving the conductivity and active site density

Heteroporous carbon structures with enhanced N-doping are derived from MOG and a nitrogen precursor and its catalytic activity towards ORR is established. The role of Fe, N co-doping is also examined. Finally, trimetallic ZIF derived carbon alloy catalyst with high nitrogen content to aid the electrocatalysis of BOR is also examined. The specific work elements of the present thesis work are

- Development of heteroporous carbon structures with enhanced nitrogen content and conductivity from MOG and different nitrogen sources as ORR electrocatalyst.
- Synthesis of transition metal, N- co doped carbon from trimetallic ZIF and its electrochemical BOR studies.

References

1. Zou, X.; Zhang, Y. Noble Metal-Free Hydrogen Evolution Catalysts for Water Splitting. *Chem. Soc. Rev.* **2015**, *44* (15), 5148.
2. Gewirth, A. A.; Varnell, J. A.; DiAscro, A. M. Nonprecious Metal Catalysts for Oxygen Reduction in Heterogeneous Aqueous Systems. *Chem. Rev.* **2018**, *118* (5), 2313.
3. Winter, M.; Brodd, R. J. What are Batteries, Fuel Cells, and Supercapacitors? *Chem. Rev.* **2004**, *104* (10), 4245.

4. Staffell, I.; Scamman, D.; Abad, A. V.; Balcombe, P.; Dodds, P. E.; Ekins, P.; Shah, N.; Ward, K. R. The Role of Hydrogen and Fuel Cells in the Global Energy System. *Energy Environ. Sci.* **2019**, *12* (2), 463-491.
5. Reddy, T. B. Linden's Handbook of Batteries, *Mcgraw-hill New York*: **2011**; 4.
6. Ormerod, R. M. Solid Oxide Fuel Cells. *Chem. Soc. Rev.* **2003**, *32* (1), 17.
7. Choi, J. Y.; Hsu, R. S.; Chen, Z. Highly Active Porous Carbon-Supported Nonprecious Metal- N Electrocatalyst for Oxygen Reduction Reaction in PEM Fuel Cells. *J. Phys. Chem. C* **2010**, *114* (17), 8048.
8. Stambouli, A. B. Fuel cells: The Expectations for an Environmental-Friendly and Sustainable Source of Energy. *Renew. Sustain. Energy Rev.* **2011**, *15* (9), 4507.
9. Burke, K. In Fuel Cells for Space Science Applications, *1st International Energy Conversion Engineering Conference (IECEC)*, **2003**; 5938.
10. Chu, D.; Jiang, R.; Gardner, K.; Jacobs, R.; Schmidt, J.; Quakenbush, T.; Stephens, J. Polymer Electrolyte Membrane Fuel Cells for Communication Applications. *J. Power Sources* **2001**, *96* (1), 174.
11. Yu, W.; Sichuan, X.; Ni, H. Air Compressors for Fuel Cell Vehicles: An Systematic Review. *SAE Int. J. Altern. Powertrains* **2015**, *4* (1), 115.
12. Acha, S.; Le Brun, N.; Damaskou, M.; Fubara, T. C.; Mulgundmath, V.; Markides, C. N.; Shah, N. Fuel cells as Combined Heat and Power Systems in Commercial Buildings: A Case Study in the Food-Retail Sector. *Energy* **2020**, *206*, 118046.
13. Carrette, L.; Friedrich, K.; Stimming, U. Fuel Cells-Fundamentals and Applications. *Fuel cells* **2001**, *1*.
14. Nørskov, J. K.; Rossmeisl, J.; Logadottir, A.; Lindqvist, L.; Kitchin, J. R.; Bligaard, T.; Jonsson, H. Origin of the Overpotential for Oxygen Reduction at a Fuel-Cell Cathode. *J. Phys. Chem. B* **2004**, *108* (46), 17886.
15. Stacy, J.; Regmi, Y. N.; Leonard, B.; Fan, M. The Recent Progress and Future of Oxygen Reduction Reaction Catalysis: A Review. *Renew. Sustain. Energy Rev.* **2017**, *69*, 401.
16. Aricò, A. S.; Bruce, P.; Scrosati, B.; Tarascon, J.-M.; van Schalkwijk, W. Nanostructured Materials for Advanced Energy Conversion and Storage Devices. *Nature Materials* **2005**, *4* (5), 366.

17. Carrette, L.; Friedrich, K. A.; Stimming, U. Fuel Cells: Principles, Types, Fuels, and Applications. *ChemPhysChem* **2000**, *1* (4), 162.
18. Carrette, L.; Friedrich, K. A.; Stimming, U. Fuel Cells - Fundamentals and Applications. *Fuel Cells* **2001**, *1* (1), 5.
19. Ren, Q.; Wang, H.; Lu, X. F.; Tong, Y. X.; Li, G. R. Recent Progress on MOF-Derived Heteroatom-Doped Carbon-Based Electrocatalysts for Oxygen Reduction Reaction. *Adv. Sci.* **2018**, *5* (3), 1700515.
20. Cheng, N.; Ren, L.; Xu, X.; Du, Y.; Dou, S. X. Recent Development of Zeolitic Imidazolate Frameworks (ZIFs) Derived Porous Carbon Based Materials as Electrocatalysts. *Adv. Energy Mater.* **2018**, *8* (25), 1801257.
21. Shijina, K.; Illathvalappil, R.; Kurungot, S.; Nair, B. N.; Mohamed, A. P.; Yamaguchi, T.; Anilkumar, G. M.; Hareesh, U. S.; Sailaja, G. S. Chitosan Intercalated Metal Organic Gel as a Green Precursor of Fe Entrenched and Fe Distributed N-Doped Mesoporous Graphitic Carbon for Oxygen Reduction Reaction. *ChemistrySelect* **2017**, *2* (28), 8762.
22. Xu, H.; Shang, H.; Wang, C.; Du, Y. Ultrafine Pt-Based Nanowires for Advanced Catalysis. *Adv. Funct. Mater.* **2020**, *30* (28), 2000793.
23. Ren, X.; Lv, Q.; Liu, L.; Liu, B.; Wang, Y.; Liu, A.; Wu, G. Current progress of Pt and Pt-based electrocatalysts used for fuel cells. *Sustain. Energy Fuels* **2020**, *4* (1), 15.
24. Li, X.; Fang, Y.; Zhao, S.; Wu, J.; Li, F.; Tian, M.; Long, X.; Jin, J.; Ma, J. Nitrogen-Doped Mesoporous Carbon Nanosheet/Carbon Nanotube Hybrids as Metal-Free Bi-Functional Electrocatalysts for Water Oxidation and Oxygen Reduction. *J. Mater. Chem. A* **2016**, *4* (34), 13133.
25. Kissinger, P. T.; Heineman, W. R. Cyclic Voltammetry. *J. Chem. Educ.* **1983**, *60* (9), 702.
26. Elgrishi, N.; Rountree, K. J.; McCarthy, B. D.; Rountree, E. S.; Eisenhart, T. T.; Dempsey, J. L. A Practical Beginner's Guide to Cyclic Voltammetry. *J. Chem. Educ.* **2018**, *95* (2), 197.
27. Zhang, J. PEM Fuel Cell Electrocatalysts and Catalyst Layers: Fundamentals and Applications, *Springer Science & Business Media*: **2008**.
28. Lee, S. J.; Pyun, S. I.; Lee, S. K.; Kang, S. J. L. Fundamentals of Rotating Disc and Ring-Disc Electrode Techniques and their Applications to Study of the Oxygen

- Reduction Mechanism at Pt/C Electrode for Fuel Cells. *Isr. J. Chem.* **2008**, 48 (3-4), 215.
29. Yin, G.; Zhang, J. Rotating Electrode Methods and Oxygen Reduction Electrocatalysts, *Elsevier*: **2014**.
 30. Ananth, M. V.; Giridhar, V. V.; Renuga, K. Linear Sweep Voltametry Studies on Oxygen Reduction of Some Oxides in Alkaline Electrolytes. *Int. J. Hydrog. Energy* **2009**, 34 (2), 658.
 31. Du, C.; Sun, Y.; Shen, T.; Yin, G.; Zhang, J. Applications of RDE and RRDE Methods in Oxygen Reduction Reaction. *Rotating Electrode Methods and Oxygen Reduction Electrocatalysts* **2014**; 231.
 32. Jia, Z.; Yin, G.; Zhang, J. Rotating ring-disk electrode method. In *Rotating Electrode Methods and Oxygen Reduction Electrocatalysts*; Elsevier: **2014**; 199.
 33. Meek, S. T.; Greathouse, J. A.; Allendorf, M. D. Metal-Organic Frameworks: A Rapidly Growing Class of Versatile Nanoporous Materials. *Adv. Mater.* **2011**, 23 (2), 249.
 34. Kim, J.; Chen, B.; Reineke, T. M.; Li, H.; Eddaoudi, M.; Moler, D. B.; O'Keeffe, M.; Yaghi, O. M. Assembly of Metal-Organic Frameworks from Large Organic and Inorganic Secondary Building Units: New Examples and Simplifying Principles for Complex Structures. *J. Am. Chem. Soc.* **2001**, 123 (34), 8239.
 35. Zhou, H. C., Long, J. R., & Yaghi, O. M. Introduction to Metal-Organic Frameworks. *Chem. Rev.* **2012**, 112 (2), 673.
 36. Li, H.; Eddaoudi, M.; O'Keeffe, M.; Yaghi, O. M. Design and Synthesis of an Exceptionally Stable and Highly Porous Metal-Organic Framework. *Nature* **1999**, 402 (6759), 276.
 37. Yaghi, O. M.; O'Keeffe, M.; Ockwig, N. W.; Chae, H. K.; Eddaoudi, M.; Kim, J. Reticular Synthesis and the Design of New Materials. *Nature* **2003**, 423 (6941), 705.
 38. Eddaoudi, M.; Kim, J.; Rosi, N.; Vodak, D.; Wachter, J.; O'Keeffe, M.; Yaghi, O. M. Systematic Design of Pore Size and Functionality in Isoreticular MOFs and their Application in Methane Storage. *Science* **2002**, 295 (5554), 469.
 39. Chui, S. S. Y.; Lo, S. M. F.; Charmant, J. P.; Orpen, A. G.; Williams, I. D. A Chemically Functionalizable Nanoporous Material $[\text{Cu}_3(\text{TMA})_2(\text{H}_2\text{O})_3]_n$. *Science* **1999**, 283 (5405), 1148.

40. Furukawa, H.; Cordova, K. E.; O’Keeffe, M.; Yaghi, O. M. The Chemistry and Applications of Metal-Organic Frameworks. *Science* **2013**, *341* (6149), 1230444.
41. Baumann, A. E.; Burns, D. A.; Liu, B.; Thoi, V. S. Metal-Organic Framework Functionalization and Design Strategies for Advanced Electrochemical Energy Storage Devices. *Commun. Chem.* **2019**, *2* (1), 86.
42. Kandiah, M.; Nilsen, M. H.; Usseglio, S.; Jakobsen, S.; Olsbye, U.; Tilset, M.; Larabi, C.; Quadrelli, E. A.; Bonino, F.; Lillerud, K. P. Synthesis and Stability of Tagged UiO-66 Zr-MOFs. *Chem. Mater.* **2010**, *22* (24), 6632.
43. Cavka, J. H.; Jakobsen, S.; Olsbye, U.; Guillou, N.; Lamberti, C.; Bordiga, S.; Lillerud, K. P. A New Zirconium Inorganic Building Brick Forming Metal Organic Frameworks with Exceptional Stability. *J. Am. Chem. Soc.* **2008**, *130* (42), 13850.
44. Opelt, S.; Türk, S.; Dietzsch, E.; Henschel, A.; Kaskel, S.; Klemm, E. Preparation of Palladium Supported on MOF-5 and its Use as Hydrogenation Catalyst. *Catal. Commun.* **2008**, *9* (6), 1286.
45. Zorainy, M. Y.; Gar Alalm, M.; Kaliaguine, S.; Boffito, D. C. Revisiting the MIL-101 Metal-Organic Framework: Design, Synthesis, Modifications, Advances, and Recent Applications. *J. Mater. Chem. A* **2021**, *9* (39), 22159.
46. Feldblyum, J. I.; Wong-Foy, A. G.; Matzger, A. J. Non-Interpenetrated IRMOF-8: Synthesis, Activation, and Gas Sorption. *Chem. Commun.* **2012**, *48* (79), 9828.
47. Han, L.; Zhang, J.; Mao, Y.; Zhou, W.; Xu, W.; Sun, Y. Facile and Green Synthesis of MIL-53(Cr) and Its Excellent Adsorptive Desulfurization Performance. *Ind. Eng. Chem. Res.* **2019**, *58* (34), 15489.
48. Alhumaimess, M. S. Metal-Organic Frameworks and their Catalytic Applications. *J. Saudi Chem. Soc.* **2020**, *24* (6), 461.
49. Salehi, S.; Anbia, M. High CO₂ Adsorption Capacity and CO₂/CH₄ Selectivity by Nanocomposites of MOF-199. *Energy Fuels* **2017**, *31* (5), 5376.
50. Saha, D.; Bao, Z.; Jia, F.; Deng, S. Adsorption of CO₂, CH₄, N₂O, and N₂ on MOF-5, MOF-177, and Zeolite 5A. *Environ. Sci. Technol.* **2010**, *44* (5), 1820.
51. Foster, M. E.; Azoulay, J. D.; Wong, B. M.; Allendorf, M. D. Novel Metal-Organic Framework Linkers for Light Harvesting Applications. *Chem. Sci.* **2014**, *5* (5), 2081.

52. Huang, X.-C.; Lin, Y.-Y.; Zhang, J.-P.; Chen, X.-M. Ligand-Directed Strategy for Zeolite-Type Metal-Organic Frameworks: Zinc(II) Imidazolates with Unusual Zeolitic Topologies. *Angew. Chem. Int. Ed.* **2006**, *45* (10), 1557.
53. Liu, Y.; Kravtsov, V. C.; Larsen, R.; Eddaoudi, M. Molecular Building Blocks Approach to the Assembly of Zeolite-Like Metal-Organic Frameworks (ZMOFs) with Extra-Large Cavities. *Chem. Commun.* **2006**, (14), 1488.
54. Moggach, S. A.; Bennett, T. D.; Cheetham, A. K. The Effect of Pressure on ZIF-8: Increasing Pore Size with Pressure and the Formation of a High-Pressure Phase at 1.47 GPa. *Angew. Chem. Int. Ed.* **2009**, *48* (38), 7087.
55. Fairen-Jimenez, D.; Moggach, S. A.; Wharmby, M. T.; Wright, P. A.; Parsons, S.; Düren, T. Opening the Gate: Framework Flexibility in ZIF-8 Explored by Experiments and Simulations. *J. Am. Chem. Soc.* **2011**, *133* (23), 8900.
56. Wang, F.; Tan, Y. X.; Yang, H.; Zhang, H. X.; Kang, Y.; Zhang, J. A New Approach towards Tetrahedral Imidazolate Frameworks for High and Selective CO₂ Uptake. *Chem. Commun.* **2011**, *47* (20), 5828.
57. Chen, B.; Yang, Z.; Zhu, Y.; Xia, Y. Zeolitic Imidazolate Framework Materials: Recent Progress in Synthesis and Applications. *J. Mater. Chem. A* **2014**, *2* (40), 16811.
58. Wang, B.; Côté, A. P.; Furukawa, H.; O’Keeffe, M.; Yaghi, O. M. Colossal Cages in Zeolitic Imidazolate Frameworks as Selective Carbon Dioxide Reservoirs. *Nature* **2008**, *453* (7192), 207.
59. Gandara-Loe, J.; Bueno-Perez, R.; Missyul, A.; Fairen-Jimenez, D.; Silvestre-Albero, J. Molecular Sieving Properties of Nanoporous Mixed-Linker ZIF-62: Associated Structural Changes upon Gas Adsorption Application. *ACS Appl. Nano Mater.* **2021**, *4* (4), 3519.
60. Xue, W.; Zhou, Q.; Li, F.; Ondon, B. S. Zeolitic Imidazolate Framework-8 (ZIF-8) as Robust Catalyst for Oxygen Reduction Reaction in Microbial Fuel Cells. *J. Power Sources* **2019**, *423*, 9.
61. Lu, G.; Hupp, J. T. Metal-Organic Frameworks as Sensors: A ZIF-8 Based Fabry-Pérot Device as a Selective Sensor for Chemical Vapors and Gases. *J. Am. Chem. Soc.* **2010**, *132* (23), 7832.
62. Phan, A.; Doonan, C. J.; Uribe-Romo, F. J.; Knobler, C. B.; O’keeffe, M.; Yaghi, O. M. Synthesis, Structure, and Carbon Dioxide Capture Properties of Zeolitic Imidazolate Frameworks. **2009**.

63. Zou, D.; Liu, D.; Zhang, J. From Zeolitic Imidazolate Framework-8 to Metal-Organic Frameworks (MOF s): Representative Substance for the General Study of Pioneering MOF Applications. *Energy Environ. Mater.* **2018**, *1* (4), 209.
64. Duan, C.; Yu, Y.; Hu, H. Recent progress on synthesis of ZIF-67-Based Materials and their Application to Heterogeneous Catalysis. *Green Energy Environ.* **2020**.
65. Kouser, S.; Hezam, A.; Khadri, M.; Khanum, S. A. A Review on Zeolite Imidazole Frameworks: Synthesis, Properties, and Applications. *J. Porous Mater.* **2022**, *1*.
66. Pan, Y.; Liu, Y.; Zeng, G.; Zhao, L.; Lai, Z. Rapid Synthesis of Zeolitic Imidazolate Framework-8 (ZIF-8) Nanocrystals in an Aqueous System. *Chem. Commun.* **2011**, *47* (7), 2071.
67. Saliba, D.; Ammar, M.; Rammal, M.; Al-Ghoul, M.; Hmadeh, M. Crystal Growth of ZIF-8, ZIF-67, and their Mixed-Metal Derivatives. *J. Am. Chem. Soc.* **2018**, *140* (5), 1812.
68. Duan, C.; Yu, Y.; Hu, H. Recent Progress on Synthesis of ZIF-67-Based Materials and their Application to Heterogeneous Catalysis. *Green Energy Environ.* **2022**, *7* (1), 3.
69. Xia, W.; Mahmood, A.; Zou, R.; Xu, Q. Metal-Organic Frameworks and their Derived Nanostructures For Electrochemical Energy Storage and Conversion. *Energy Environ. Sci.* **2015**, *8* (7), 1837.
70. Kim, D.; Kim, D. W.; Hong, W. G.; Coskun, A. Graphene/ZIF-8 Composites with Tunable Hierarchical Porosity and Electrical Conductivity. *J. Mater. Chem. A* **2016**, *4* (20), 7710.
71. Wei, Q.; James, S. L. A Metal-Organic Gel Used as a Template for a Porous Organic Polymer. *Chem. Commun.* **2005**, (12), 1555.
72. Liu, Y. R.; He, L.; Zhang, J.; Wang, X.; Su, C. Y. Evolution of Spherical Assemblies to Fibrous Networked Pd(II) Metallogels from a Pyridine-Based Tripodal Ligand and Their Catalytic Property. *Chem. Mater.* **2009**, *21* (3), 557.
73. Fages, F. Metal Coordination To Assist Molecular Gelation. *Angew. Chem. Int. Ed.* **2006**, *45* (11), 1680.

74. Leong, W. L.; Tam, A. Y. Y.; Batabyal, S. K.; Koh, L. W.; Kasapis, S.; Yam, V. W. W.; Vittal, J. J. Fluorescence Enhancement of Coordination Polymeric Gel. *Chem. Commun.* **2008**, (31), 3628.
75. Wang, X.; McHale, R. Metal-Containing Polymers: Building Blocks for Functional (Nano)Materials. *Macromol. Rapid Commun.* **2010**, 31 (4), 331.
76. Cui, X. Y.; Gu, Z. Y.; Jiang, D. Q.; Li, Y.; Wang, H. F.; Yan, X. P. In situ Hydrothermal Growth of Metal-Organic Framework 199 Films on Stainless Steel Fibers for Solid-Phase Microextraction of Gaseous Benzene Homologues. *Anal. Chem.* **2009**, 81 (23), 9771.
77. Huang, J.; He, L.; Zhang, J.; Chen, L.; Su, C. Y. Dynamic Functionalised Metallogel: An Approach to Immobilised Catalysis with Improved Activity. *J. Mol. Catal. A Chem.* **2010**, 317 (1), 97.
78. Xing, B.; Choi, M.-F.; Xu, B. A Stable Metal Coordination Polymer Gel Based on a Calix[4]arene and its "Uptake" of Non-Ionic Organic Molecules from the Aqueous Phase. *Chem. Commun.* **2002**, (4), 362.
79. Nune, S. K.; Thallapally, P. K.; McGrail, B. P. Metal Organic Gels (MOGs): A New Class of Sorbents for CO₂ Separation Applications. *J. Mater. Chem.* **2010**, 20 (36), 7623.
80. Yin, J.; Yang, G.; Wang, H.; Chen, Y. Macroporous Polymer Monoliths Fabricated by Using a Metal-Organic Coordination Gel Template. *Chem. Commun.* **2007**, (44), 4614.
81. Krieg, E.; Weissman, H.; Shirman, E.; Shimoni, E.; Rybtchinski, B. A Recyclable Supramolecular Membrane for Size-Selective Separation of Nanoparticles. *Nat. Nanotechnol.* **2011**, 6 (3), 141.
82. Xia, W.; Qiu, B.; Xia, D.; Zou, R. Facile Preparation of Hierarchically Porous Carbons from Metal-Organic Gels and their Application in Energy Storage. *Sci. Rep.* **2013**, 3 (1), 1935.
83. Wei, S. C.; Pan, M.; Li, K.; Wang, S.; Zhang, J.; Su, C. Y. A multistimuli-Responsive Photochromic Metal-Organic Gel. *Adv. Mater.* **2014**, 26 (13), 2072.
84. Sharma, N.; Sharma, P. K.; Singh, Y.; Nagaraja, C. M. A Self-Healing Metal-Organic Gel (MOG) Exhibiting pH-Responsive Release of a Chemotherapeutic Agent, Doxorubicin: Modulation of Release Kinetics by Partial Dehydration of Matrix. *ACS Omega* **2019**, 4 (1), 1354.

85. Qiu, M.; Wu, H.; Cao, L.; Shi, B.; He, X.; Geng, H.; Mao, X.; Yang, P.; Jiang, Z. Metal-Organic Nanogel with Sulfonated Three-Dimensional Continuous Channels as a Proton Conductor. *ACS Appl. Mater. Interfaces* **2020**, *12* (17), 19788.
86. Li, L.; Xiang, S.; Cao, S.; Zhang, J.; Ouyang, G.; Chen, L.; Su, C. Y. A Synthetic Route to Ultralight Hierarchically Micro/Mesoporous Al(III)-Carboxylate Metal-Organic Aerogels. *Nat. Commun.* **2013**, *4* (1), 1774.
87. Qin, Z. S.; Dong, W. W.; Zhao, J.; Wu, Y. P.; Zhang, Q.; Li, D. S. A Water-Stable Tb(III)-Based Metal-Organic Gel (MOG) for Detection of Antibiotics and Explosives. *Inorg. Chem. Front.* **2018**, *5* (1), 120.
88. Li, B.; Zhou, X.; Liu, X.; Ye, H.; Zhang, Y.; Zhou, Q. Metal-Organic Gels Derived from Iron(III) and Pyridine Ligands: Morphology, Self-Healing and Catalysis for Ethylene Selective Dimerization. *Chem. Asian J.* **2019**, *14* (9), 1582.
89. Liu, L.; Zhang, J.; Fang, H.; Chen, L.; Su, C. Y. Metal-Organic Gel Material Based on UiO-66-NH₂ Nanoparticles for Improved Adsorption and Conversion of Carbon Dioxide. *Chem. Asian J.* **2016**, *11* (16), 2278.
90. Mallick, A.; Schön, E. M.; Panda, T.; Sreenivas, K.; Díaz, D. D.; Banerjee, R. Fine-Tuning the Balance Between Crystallization and Gelation and Enhancement of CO₂ Uptake on Functionalized Calcium Based MOFs and Metallogels. *J. Mater. Chem* **2012**, *22* (30), 14951.
91. Wu, Q.; He, L.; Jiang, Z. W.; Li, Y.; Zhao, T. T.; Li, Y. H.; Huang, C. Z.; Li, Y. F. One-Step Synthesis of Cu(II) Metal-Organic Gel as Recyclable Material for Rapid, Efficient and Size Selective Cationic Dyes Adsorption. *J. Environ. Sci.* **2019**, *86*, 203.
92. Shao, M.; Chang, Q.; Dodelet, J. P.; Chenitz, R. Recent Advances in Electrocatalysts for Oxygen Reduction Reaction. *Chem. Rev.* **2016**, *116* (6), 3594.
93. Tian, X.; Tang, H.; Luo, J.; Nan, H.; Shu, T.; Du, L.; Zeng, J.; Liao, S.; Adzic, R. R. High-Performance Core-Shell Catalyst with Nitride Nanoparticles as a Core: Well-Defined Titanium Copper Nitride Coated with an Atomic Pt Layer for the Oxygen Reduction Reaction. *ACS Catal.* **2017**, *7* (6), 3810
94. Nie, Y.; Li, L.; Wei, Z. Recent Advancements in Pt and Pt-Free Catalysts for Oxygen Reduction Reaction. *Chem. Soc. Rev.* **2015**, *44* (8), 2168.
95. Xiong, Y.; Shan, H.; Zhou, Z.; Yan, Y.; Chen, W.; Yang, Y.; Liu, Y.; Tian, H.; Wu, J.; Zhang, H.; Yang, D. Tuning Surface Structure and Strain in Pd-Pt Core-Shell

- Nanocrystals for Enhanced Electrocatalytic Oxygen Reduction. *Small* **2017**, *13* (7), 1603423.
96. Greeley, J.; Stephens, I. E. L.; Bondarenko, A. S.; Johansson, T. P.; Hansen, H. A.; Jaramillo, T. F.; Rossmeisl, J.; Chorkendorff, I.; Nørskov, J. K. Alloys of Platinum and Early Transition Metals as Oxygen Reduction Electrocatalysts. *Nat. Chem.* **2009**, *1* (7), 552.
97. Wang, C.; Chi, M.; Li, D.; van der Vliet, D.; Wang, G.; Lin, Q.; Mitchell, J. F.; More, K. L.; Markovic, N. M.; Stamenkovic, V. R. Synthesis of Homogeneous Pt-Bimetallic Nanoparticles as Highly Efficient Electrocatalysts. *ACS Catal.* **2011**, *1* (10), 1355.
98. Yano, H.; Kataoka, M.; Yamashita, H.; Uchida, H.; Watanabe, M. Oxygen Reduction Activity of Carbon-Supported Pt-M (M = V, Ni, Cr, Co, and Fe) Alloys Prepared by Nanocapsule Method. *Langmuir* **2007**, *23* (11), 6438.
99. Du, S.; Lu, Y.; Malladi, S. K.; Xu, Q.; Steinberger-Wilckens, R. A Simple Approach for PtNi-MWCNT Hybrid Nanostructures as High Performance Electrocatalysts for the Oxygen Reduction Reaction. *J. Mater. Chem. A* **2014**, *2* (3), 692.
100. Wang, R.; Higgins, D. C.; Hoque, M. A.; Lee, D.; Hassan, F.; Chen, Z. Controlled Growth of Platinum Nanowire Arrays on Sulfur Doped Graphene as High Performance Electrocatalyst. *Sci. Rep.* **2013**, *3* (1), 2431.
101. Ferrero, G. A.; Fuertes, A. B.; Sevilla, M.; Titirici, M.-M. Efficient Metal-Free N-Doped Mesoporous Carbon Catalysts for ORR by a Template-Free Approach. *Carbon* **2016**, *106*, 179.
102. Shijina, K.; Illathvalappil, R.; Sumitha, N. S.; Sailaja, G. S.; Kurungot, S.; Nair, B. N.; Peer Mohamed, A.; Anilkumar, G. M.; Yamaguchi, T.; Hareesh, U. S. Melamine Formaldehyde-Metal Organic Gel Interpenetrating Polymer Network Derived Intrinsic Fe-N-Doped Porous Graphitic Carbon Electrocatalysts for Oxygen Reduction Reaction. *New J. Chem.* **2018**, *42* (23), 18690.
103. Thomas, M.; Illathvalappil, R.; Kurungot, S.; Nair, B. N.; Mohamed, A. P.; Anilkumar, G. M.; Yamaguchi, T.; Hareesh, U. S. Morphological Ensembles of N-Doped Porous Carbon Derived from ZIF-8/Fe-Graphene Nanocomposites: Processing and Electrocatalytic Studies. *ChemistrySelect* **2018**, *3* (30), 8688.
104. Tian, H.; Wang, N.; Xu, F.; Zhang, P.; Hou, D.; Mai, Y.; Feng, X. Nitrogen-Doped Carbon Nanosheets and Nanoflowers with Holey Mesopores for Efficient Oxygen Reduction Catalysis. *J. Mater. Chem. A* **2018**, *6* (22), 10354.

105. Zhang, Z.; Sun, J.; Wang, F.; Dai, L. Efficient Oxygen Reduction Reaction (ORR) Catalysts Based on Single Iron Atoms Dispersed on a Hierarchically Structured Porous Carbon Framework. *Angew. Chem. Int. Ed.* **2018**, *57* (29), 9038.
106. Jiang, H.; Gu, J.; Zheng, X.; Liu, M.; Qiu, X.; Wang, L.; Li, W.; Chen, Z.; Ji, X.; Li, J. Defect-Rich and Ultrathin N Doped Carbon Nanosheets as Advanced Trifunctional Metal-Free Electrocatalysts for the ORR, OER and HER. *Energy Environ. Sci.* **2019**, *12* (1), 322.
107. Wang, N.; Lu, B.; Li, L.; Niu, W.; Tang, Z.; Kang, X.; Chen, S. Graphitic Nitrogen Is Responsible for Oxygen Electroreduction on Nitrogen-Doped Carbons in Alkaline Electrolytes: Insights from Activity Attenuation Studies and Theoretical Calculations. *ACS Catal.* **2018**, *8* (8), 6827.
108. Lu, X.; Wang, D.; Ge, L.; Xiao, L.; Zhang, H.; Liu, L.; Zhang, J.; An, M.; Yang, P. Enriched Graphitic N in Nitrogen-Doped Graphene as a Superior Metal-Free Electrocatalyst for the Oxygen Reduction Reaction. *New J. Chem.* **2018**, *42* (24), 19665.
109. Ning, X.; Li, Y.; Ming, J.; Wang, Q.; Wang, H.; Cao, Y.; Peng, F.; Yang, Y.; Yu, H. Electronic Synergism of Pyridinic- and Graphitic-Nitrogen on N-Doped Carbons for the Oxygen Reduction Reaction. *Chem. Sci.* **2019**, *10* (6), 1589.
110. Wang, X. R.; Liu, J. Y.; Liu, Z. W.; Wang, W. C.; Luo, J.; Han, X. P.; Du, X. W.; Qiao, S.-Z.; Yang, J. Identifying the Key Role of Pyridinic-N-Co Bonding in Synergistic Electrocatalysis for Reversible ORR/OER. *Adv. Mater.* **2018**, *30* (23), 1800005.
111. Quílez-Bermejo, J.; Melle-Franco, M.; San-Fabián, E.; Morallón, E.; Cazorla-Amorós, D. Towards Understanding the Active Sites for the ORR in N-Doped Carbon Materials through Fine-Tuning of Nitrogen Functionalities: An Experimental and Computational Approach. *J. Mater. Chem. A* **2019**, *7* (42), 24239.
112. Lv, Q.; Si, W.; He, J.; Sun, L.; Zhang, C.; Wang, N.; Yang, Z.; Li, X.; Wang, X.; Deng, W.; Long, Y.; Huang, C.; Li, Y. Selectively Nitrogen-Doped Carbon Materials as Superior Metal-Free Catalysts for Oxygen Reduction. *Nat. Commun.* **2018**, *9* (1), 3376.
113. Luo, Z.; Lim, S.; Tian, Z.; Shang, J.; Lai, L.; MacDonald, B.; Fu, C.; Shen, Z.; Yu, T.; Lin, J. Pyridinic N Doped Graphene: Synthesis, Electronic Structure, and Electrocatalytic Property. *J. Mater. Chem.* **2011**, *21* (22), 8038.

114. Morant, C.; Andrey, J.; Prieto, P.; Mendiola, D.; Sanz, J. M.; Elizalde, E. XPS Characterization of Nitrogen-Doped Carbon Nanotubes. *Phys. Status Solidi A* **2006**, *203* (6), 1069.
115. Yang, W.; Feller, T. P.; Antonietti, M. Efficient Metal-Free Oxygen Reduction in Alkaline Medium on High-Surface-Area Mesoporous Nitrogen-Doped Carbons Made from Ionic Liquids and Nucleobases. *J. Am. Chem. Soc.* **2011**, *133* (2), 206.
116. Salaberria, A. M.; Fernandes, S. C. M.; Diaz, R. H.; Labidi, J. Processing of α -Chitin Nanofibers by Dynamic High Pressure Homogenization: Characterization and Antifungal Activity Against *A. Niger*. *Carbohydr. Polym.* **2015**, *116*, 286.
117. Li, Y.; Zhang, H.; Liu, P.; Wang, Y.; Yang, H.; Li, Y.; Zhao, H. Self-Supported Bimodal-Pore Structured Nitrogen-Doped Carbon Fiber Aerogel as Electrocatalyst for Oxygen Reduction Reaction. *Electrochem. commun.* **2015**, *51*, 6.
118. Yuan, H.; Deng, L.; Cai, X.; Zhou, S.; Chen, Y.; Yuan, Y. Nitrogen-Doped Carbon Sheets Derived from Chitin as Non-Metal Bifunctional Electrocatalysts for Oxygen Reduction and Evolution. *RSC Adv.* **2015**, *5* (69), 56121.
119. Liu, Q.; Chen, C.; Pan, F.; Zhang, J. Highly Efficient Oxygen Reduction on Porous Nitrogen-Doped Nanocarbons Directly Synthesized from Cellulose Nanocrystals and Urea. *Electrochim. Acta* **2015**, *170*, 234.
120. Thomas, M.; Illathvalappil, R.; Kurungot, S.; Nair, B. N.; Mohamed, A. A. P.; Anilkumar, G. M.; Yamaguchi, T.; Hareesh, U. S. Graphene Oxide Sheathed ZIF-8 Microcrystals: Engineered Precursors of Nitrogen-Doped Porous Carbon for Efficient Oxygen Reduction Reaction (ORR) Electrocatalysis. *ACS Appl. Mater. Interfaces* **2016**, *8* (43), 29373.
121. Zhang, L.; Wilkinson, D. P.; Liu, Y.; Zhang, J. Progress in Nanostructured (Fe Or Co)/N/C Non-Noble Metal Electrocatalysts for Fuel Cell Oxygen Reduction Reaction. *Electrochim. Acta* **2018**, *262*, 326.
122. Ishihara, A.; Imai, H.; Ota, K. i. Transition Metal Oxides, Carbides, Nitrides, Oxynitrides, and Carbonitrides for O₂ Reduction Reaction Electrocatalysts for Acid PEM Fuel Cells. *Non-Noble Metal Fuel Cell Catalysts* **2014**, 183.
123. Transition Metal Chalcogenides for Oxygen Reduction Electrocatalysts in PEM Fuel Cells. *Non-Noble Metal Fuel Cell Catalysts* **2014** 157.
124. Jasinski, R. A New Fuel Cell Cathode Catalyst. *Nature* **1964**, *201* (4925), 1212.

125. Gupta, S.; Tryk, D.; Bae, I.; Aldred, W.; Yeager, E. Heat-Treated Polyacrylonitrile-Based Catalysts for Oxygen Electroreduction. *J. Appl. Electrochem.* **1989**, *19* (1), 19.
126. Jiang, Z.; Yu, J.; Huang, T.; Sun, M. Recent Advance on Polyaniline or Polypyrrole-Derived Electrocatalysts for Oxygen Reduction Reaction. *Polymers (Basel)* **2018**, *10* (12), 1397.
127. Borges Honorato, A. M.; Khalid, M.; Dai, Q.; Pessan, L. A. Nitrogen and Sulfur co-Doped Fibrous-Like Carbon Electrocatalyst Derived from Conductive Polymers for Highly Active Oxygen Reduction Catalysis. *Synth. Met.* **2020**, *264*, 116383.
128. Zhao, S. N.; Song, X. Z.; Song, S. Y.; Zhang, H. j. Highly Efficient Heterogeneous Catalytic Materials Derived from Metal-Organic Framework Supports/Precursors. *Coord. Chem. Rev.* **2017**, *337*, 80.
129. Xia, B. Y.; Yan, Y.; Li, N.; Wu, H. B.; Lou, X. W.; Wang, X. A Metal-Organic Framework-Derived Bifunctional Oxygen Electrocatalyst. *Nat. Energy* **2016**, *1*, 15006,
130. Meng, J.; Niu, C.; Xu, L.; Li, J.; Liu, X.; Wang, X.; Wu, Y.; Xu, X.; Chen, W.; Li, Q.; Zhu, Z.; Zhao, D.; Mai, L. General Oriented Formation of Carbon Nanotubes from Metal-Organic Frameworks. *J. Am. Chem. Soc.* **2017**, *139* (24), 8212.
131. Ye, G.; Zhao, K.; He, Z.; Huang, R.; Liu, Y.; Liu, S. Fe-N_x Sites Enriched Carbon Micropolyhedrons Derived from Fe-Doped Zeolitic Imidazolate Frameworks with Reinforced Fe-N Coordination for Efficient Oxygen Reduction Reaction. *ACS Sustain. Chem. Eng.* **2018**, *6* (11), 15624.
132. Deng, Y.; Chi, B.; Li, J.; Wang, G.; Zheng, L.; Shi, X.; Cui, Z.; Du, L.; Liao, S.; Zang, K.; Luo, J.; Hu, Y.; Sun, X. Atomic Fe-Doped MOF-Derived Carbon Polyhedrons with High Active-Center Density and Ultra-High Performance toward PEM Fuel Cells. *Adv. Energy Mater.* **2019**, *9* (13), 1802856.
133. Zhang, H.; Hwang, S.; Wang, M.; Feng, Z.; Karakalos, S.; Luo, L.; Qiao, Z.; Xie, X.; Wang, C.; Su, D.; Shao, Y.; Wu, G. Single Atomic Iron Catalysts for Oxygen Reduction in Acidic Media: Particle Size Control and Thermal Activation. *J. Am. Chem. Soc.* **2017**, *139* (40), 14143.
134. Lai, Q.; Zheng, L.; Liang, Y.; He, J.; Zhao, J.; Chen, J. Metal-Organic-Framework-Derived Fe-N/C Electrocatalyst with Five-Coordinated Fe-N_x Sites for Advanced Oxygen Reduction in Acid Media. *ACS Catal.* **2017**, *7* (3), 1655.

135. Huang, J.; Du, C.; Nie, J.; Zhou, H.; Zhang, X.; Chen, J. Encapsulated Rh Nanoparticles in N-Doped Porous Carbon Polyhedrons Derived from ZIF-8 for Efficient HER and ORR Electrocatalysis. *Electrochim. Acta* **2019**, *326*, 134982.
136. Wang, H.; Cheng, X.; Yin, F.; Chen, B.; Fan, T.; He, X. Metal-Organic Gel-Derived Fe-Fe₂O₃@Nitrogen-Doped-Carbon Nanoparticles Anchored on Nitrogen-Doped Carbon Nanotubes as a Highly Effective Catalyst for Oxygen Reduction reaction. *Electrochim. Acta* **2017**, *232*, 114.
137. Guo, H.; Feng, Q.; Xu, K.; Xu, J.; Zhu, J.; Zhang, C.; Liu, T. Self-Templated Conversion of Metallogel into Heterostructured TMP@Carbon Quasiasaerogels Boosting Bifunctional Electrocatalysis. *Adv. Funct. Mater.* **2019**, *29* (34), 1903660.
138. Zhu, T.; Feng, Q.; Liu, S.; Zhang, C. Metallogel-Derived 3D Porous Carbon Nanosheet Composites as an Electrocatalyst for Oxygen Reduction Reaction. *Compos. Commun.* **2020**, *20*, 100376.
139. Li, Z. P.; Liu, B. H.; Arai, K.; Asaba, K.; Suda, S. Evaluation of Alkaline Borohydride Solutions as the Fuel for Fuel Cell. *J. Power Sources* **2004**, *126* (1), 28.
140. Ma, X.; Ye, K.; Wang, G.; Duan, M.; Cheng, K.; Wang, G.; Cao, D. Facile Fabrication of Gold Coated Nickel Nanoarrays and its Excellent Catalytic Performance towards Sodium Borohydride Electrooxidation. *Appl. Surf. Sci.* **2017**, *414*, 353.
141. Jasinski, R. Fuel cell oxidation of alakali borohydrides. *Electrochem. Technol* **1965**, *3* (1-2), 40.
142. Indig, M. E.; Snyder, R. N. Closure to "Discussion of 'Sodium Borohydride, an Interesting Anodic Fuel' [M. E. Indig and R. N. Snyder, (pp. 1104–1106, Vol. 109, No. 11)]". *J. Electrochem. Soc.* **1963**, *110* (6), 592.
143. Wee, J. H. A Comparison of Sodium Borohydride as a Fuel for Proton Exchange Membrane Fuel Cells and for Direct Borohydride Fuel Cells. *J. Power Sources* **2006**, *155* (2), 329.
144. Züttel, A.; Wenger, P.; Rentsch, S.; Sudan, P.; Mauron, P.; Emmenegger, C. LiBH₄ A New Hydrogen Storage Material. *J. Power Sources* **2003**, *118* (1), 1.
145. Richardson, B. S.; Birdwell, J. F.; Pin, F. G.; Jansen, J. F.; Lind, R. F. Sodium Borohydride Based Hybrid Power System. *J. Power Sources* **2005**, *145* (1), 21.

146. Elder, J. P.; Hickling, A. Anodic Behaviour of the Borohydride Ion. *Transactions of the Faraday Society* **1962**, *58* (0), 1852.
147. Olu, P. Y.; Bonnefont, A.; Braesch, G.; Martin, V.; Savinova, E. R.; Chatenet, M. Influence of the Concentration of Borohydride towards Hydrogen Production and Escape for Borohydride Oxidation Reaction on Pt and Au Electrodes - Experimental and Modelling Insights. *J. Power Sources* **2018**, *375*, 300.
148. Braesch, G.; Bonnefont, A.; Martin, V.; Savinova, E. R.; Chatenet, M. Borohydride Oxidation Reaction Mechanisms and Poisoning Effects on Au, Pt and Pd Bulk Electrodes: From Model (Low) To Direct Borohydride Fuel Cell Operating (High) Concentrations. *Electrochim. Acta* **2018**, *273*, 483.
149. Pasqualetti, A. M.; Olu, P. Y.; Chatenet, M.; Lima, F. H. B. Borohydride Electrooxidation on Carbon-Supported Noble Metal Nanoparticles: Insights into Hydrogen and Hydroxyborane Formation. *ACS Catal.* **2015**, *5* (5), 2778.
150. Zadick, A.; Petit, J. F.; Martin, V.; Dubau, L.; Demirci, U. B.; Geantet, C.; Chatenet, M. Ubiquitous Borane Fuel Electrooxidation on Pd/C and Pt/C Electrocatalysts: Toward Promising Direct Hydrazine-Borane Fuel Cells. *ACS Catal.* **2018**, *8* (4), 3150.
151. Li, B.; Song, C.; Huang, X.; Ye, K.; Cheng, K.; Zhu, K.; Yan, J.; Cao, D.; Wang, G. A Novel Anode for Direct Borohydride-Hydrogen Peroxide Fuel Cell: Au Nanoparticles Decorated 3D Self-Supported Reduced Graphene Oxide Foam. *ACS Sustain. Chem. Eng.* **2019**, *7* (13), 11129.
152. Gyenge, E. Electrooxidation of Borohydride on Platinum and Gold Electrodes: Implications for Direct Borohydride Fuel Cells. *Electrochim. Acta* **2004**, *49* (6), 965.
153. Amendola, S. C.; Onnerud, P.; Kelly, M. T.; Petillo, P. J.; Sharp-Goldman, S. L.; Binder, M. A Novel High Power Density Borohydride-Air Cell. *J. Power Sources* **1999**, *84* (1), 130.
154. Chatenet, M.; Lima, F. H.; Ticianelli, E. A. Gold is not a Faradaic-Efficient Borohydride Oxidation Electrocatalyst: An Online Electrochemical Mass Spectrometry Study. *J. Electrochem. Soc.* **2010**, *157* (5), B697.
155. Rostamikia, G.; Janik, M. J. Direct Borohydride Oxidation: Mechanism Determination and Design of Alloy Catalysts Guided by Density Functional Theory. *Energy Environ. Sci.* **2010**, *3* (9), 1262.
156. Ye, K.; Ma, X.; Huang, X.; Zhang, D.; Cheng, K.; Wang, G.; Cao, D. The Optimal Design of Co Catalyst Morphology on a Three-Dimensional Carbon Sponge

- with Low Cost, Inducing Better Sodium Borohydride Electrooxidation Activity. *RSC Adv.* **2016**, 6 (47), 41608.
157. Song, C.; Wang, G.; Li, B.; Miao, C.; Ma, K.; Zhu, K.; Cheng, K.; Ye, K.; Yan, J.; Cao, D. A Novel Electrode of Ternary CuNiPd Nanoneedles Decorated Ni Foam and its Catalytic Activity toward NaBH₄ Electrooxidation. *Electrochim. Acta* **2019**, 299, 395.
158. Li, S.; Liu, Y.; Liu, Y.; Chen, Y. Study of CoO as an Anode Catalyst for a Membraneless Direct Borohydride Fuel Cell. *J. Power Sources* **2010**, 195 (21), 7202.
159. Zhang, J.; Zhang, D.; Cui, C.; Wang, H.; Jiao, W.; Gao, J.; Liu, Y. A Three-Dimensional Porous Co-P Alloy Supported on a Copper Foam as a New Catalyst for Sodium Borohydride Electrooxidation. *Dalton Trans.* **2019**, 48 (35), 13248.
160. Zhang, D.; Ye, K.; Cheng, K.; Cao, D.; Yin, J.; Xu, Y.; Wang, G. High Electrocatalytic Activity of Cobalt-Multiwalled Carbon Nanotubes-Cosmetic Cotton Nanostructures for Sodium Borohydride Electrooxidation. *Int. J. Hydrog. Energy* **2014**, 39 (18), 9651.
161. Martins, M.; Šljukić, B.; Metin, Ö.; Sevim, M.; Sequeira, C. A.; Şener, T.; Santos, D. M. Bimetallic PdM (M= Fe, Ag, Au) Alloy Nanoparticles Assembled on Reduced Graphene Oxide as Catalysts for Direct Borohydride Fuel Cells. *J. Alloys Compd.* **2017**, 718, 204.
162. Hansu, T. A.; Caglar, A.; Sahin, O.; Kivrak, H. Hydrolysis and Electrooxidation of Sodium Borohydride on Novel CNT Supported CoBi Fuel Cell Catalyst. *Mater. Chem. Phys.* **2020**, 239, 122031.
163. Guo, M.; Cheng, Y.; Yu, Y.; Hu, J. Ni-Co Nanoparticles Immobilized on a 3D Ni Foam Template as a Highly Efficient Catalyst for Borohydride Electrooxidation in Alkaline Medium. *Appl. Surf. Sci.* **2017**, 416, 439.
164. Yin, X.; Wang, Q.; Duan, D.; Liu, S.; Wang, Y. Amorphous NiB Alloy Decorated by Cu as the Anode Catalyst for a Direct Borohydride Fuel Cell. *Int. J. Hydrog. Energy* **2019**, 44 (21), 10971.
165. Tiwari, A.; Singh, V.; Nagaiah, T. C. Non-Noble Cobalt Tungstate Catalyst for Effective Electrocatalytic Oxidation of Borohydride. *ACS Appl. Mater. Interfaces* **2019**, 11 (24), 21465.
166. Milikić, J.; Oliveira, R. C.; Stoševski, I.; Krstić, J.; Hercigonja, R.; Miljanić, Š.; Santos, D. M.; Šljukić, B. Evaluation of Silver-Incorporating Zeolites as

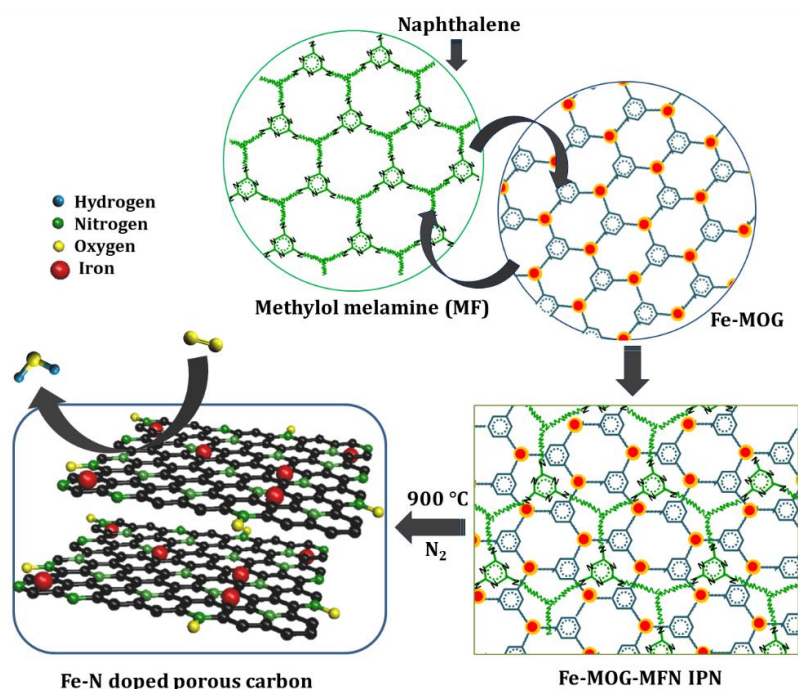
- Bifunctional Electrocatalysts for Direct Borohydride Fuel Cells. *New J. Chem.* **2019**, 43 (36), 14270.
167. Yi, L.; Yu, B.; Yi, W.; Zhou, Y.; Ding, R.; Wang, X. Carbon-Supported Bimetallic Platinum-Iron Nanocatalysts: Application in Direct Borohydride/Hydrogen Peroxide Fuel Cell. *ACS Sustain. Chem. Eng.* **2018**, 6 (7), 8142.
168. Duan, D.; Yin, X.; Wang, Q.; Liu, S.; Wang, Y. Performance Evaluation of Borohydride Electrooxidation Reaction with Ternary Alloy Au-Ni-Cu/C Catalysts. *J. Appl. Electrochem.* **2018**, 48 (7), 835.
169. Simões, M.; Baranton, S.; Coutanceau, C. Electrooxidation of Sodium Borohydride at Pd, Au, and Pd_xAu_{1-x} Carbon-Supported Nanocatalysts. *J. Phys. Chem. C* **2009**, 113 (30), 13369.
170. Yi, L.; Yu, B.; Fei, J.; Ding, Y.; Yang, C.; Wang, X. Carbon-Supported Ni(OH)₂ Nanospheres Decorated with Au Nanoparticles: A Promising Catalyst for BH₄⁻ Electrooxidation. *Ionics* **2019**, 25 (11), 5153.
171. Zolfaghari, M.; Arab, A.; Asghari, A. Surfactant-Assisted Electrodeposition of Nickel Nanostructures and Their Electrocatalytic Activities Toward Oxidation of Sodium Borohydride, Ethanol, and Methanol. *ChemistrySelect* **2019**, 4 (15), 4487.
172. Duan, D.; Wang, Q.; Liu, H.; You, X.; Liu, S.; Wang, Y. Investigation of Carbon-Supported Ni@Ag Core-Shell Nanoparticles as Electrocatalyst for Electrooxidation Of Sodium Borohydride. *J. Solid State Electrochem.* **2016**, 20 (10), 2699.
173. Wu, C.; Zhu, J.; Wang, H.; Wang, G.; Chen, T.; Tan, Y. Porous Ni_{1-x}Cu_xO Nanowire Arrays as Noble-Metal-Free High-Performance Catalysts for Ammonia-Borane Electrooxidation. *ACS Catal.* **2019**, 10 (1), 721.
174. Martins, M.; Metin, Ö.; Sevim, M.; Šljukić, B.; Sequeira, C. A.; Sener, T.; Santos, D. M. Monodisperse Pd Nanoparticles Assembled on Reduced Graphene Oxide-Fe₃O₄ Nanocomposites as Electrocatalysts for Borohydride Fuel Cells. *Int. J. Hydrog. Energy* **2018**, 43 (23), 10686.
175. Concha, B. M.; Chatenet, M. Direct Oxidation of Sodium Borohydride on Pt, Ag and Alloyed Pt-Ag Electrodes in Basic Media. Part I: Bulk Electrodes. *Electrochim. Acta* **2009**, 54 (26), 6119.
176. Bortoloti, F.; Angelo, A. C. Ordered PtSn/C electrocatalyst: A High Performance Material for the Borohydride Electrooxidation Reaction. *Catalysts* **2017**, 7 (7), 198.

-
177. Li, B.; Song, C.; Zhang, D.; Ye, K.; Cheng, K.; Zhu, K.; Yan, J.; Cao, D.; Wang, G. Novel Self-Supported Reduced Graphene Oxide Foam-Based CoAu Electrode: An Original Anode Catalyst for Electrooxidation of Borohydride in Borohydride Fuel Cell. *Carbon* **2019**, *152*, 77.
178. Li, B.; Yan, Q.; Song, C.; Yan, P.; Ye, K.; Cheng, K.; Zhu, K.; Yan, J.; Cao, D.; Wang, G. Reduced Graphene Oxide Foam Supported CoNi Nanosheets as an Efficient Anode Catalyst for Direct Borohydride Hydrogen Peroxide Fuel Cell. *Appl. Surf. Sci.* **2019**, *491*, 659.

Chapter 2

Melamine Formaldehyde-Metal Organic Gel Interpenetrating Polymer Network Derived Fe-N-doped Porous Carbon Electrocatalysts for Oxygen Reduction Reaction

Abstract



Fe, N doped porous graphitic carbon electrocatalyst (Fe-M-NC), obtained by the pyrolysis of an interpenetrating polymer network (IPN) comprising of melamine formaldehyde (MF as hard segment) and metal-organic gel (MOG as soft segment), exhibited significant oxygen reduction reaction (ORR) activity in alkaline medium. BET surface area analysis of Fe-M-NC showed high surface area ($821 \text{ m}^2 \text{ g}^{-1}$), while TEM, Raman and XPS results confirmed Fe and N co-doping. Furthermore, a modulated porous morphology with a higher degree of surface area ($950 \text{ m}^2 \text{ g}^{-1}$) has been accomplished for the system (Fe-MN-NC) when aided by a sublimable porogen, such as naphthalene. XPS results further demonstrated that these systems exhibited a better degree of distribution of graphitic N and an onset potential value of 0.91 V vs. RHE in 0.1 M KOH solution following an efficient four-electron ORR pathway. The electrocatalytic activity of Fe-MN-NC is superior to that of Fe-M-NC by virtue of its higher graphitic N content and surface area.

2.1 Introduction

The quest for high functional, cost-effective catalyst systems, as alternative to Pt-based systems, is primarily focused on the domain of heteroatom doped porous carbon structures.¹⁻³ Iron and Nitrogen (Fe, N) doping is widely pursued, as Fe, N-coordination on doped nitrogen induce implicit effects on enhancing the electrocatalytic properties due to the added positive charge density on neighboring carbon atoms.⁴⁻⁶ Fe/N/C catalysts with good stability are generally synthesized by high temperature treatment of a variety of precursors.⁷⁻¹⁰ Diverse methods such as pyrolysis,¹¹ chemical vapor deposition,¹² and template method¹³ are employed for the synthesis of porous carbons. Among these, pyrolysis of suitable carbon precursors such as metal organic framework (MOF) and zeolitic imidazolate framework (ZIF) accomplished significant interest specifically due to the flexibility in design, and improved morphology control.^{14,15} However, toxic solvents and tedious procedures are involved in the synthesis of these materials² and it is therefore necessary to develop new class of precursor materials with easy synthetic procedures and higher degree of porosity.

Metal organic gels (MOGs) are considered to be excellent precursors because of the high surface area with heteroporous nature. Moreover, the design flexibility and low-cost synthetic procedures using less toxic solvents are also favorable alternatives.^{16,17} N-doped carbon, for example, obtained by the pyrolytic treatment of Al-MOG doped with N-precursor offered electrode materials with high surface area and electron transfer capability.¹⁸ Porous carbon derived from Al-based metal-organic gels (MOGs) were developed by Zhang *et al.* was used as electrodes for capacitive deionization. The material having large specific surface area, large percentage of micropore, and a suitable pore size distribution showed a high salt removal rate and an excellent recycling stability.¹⁶ Bu *et al.* prepared flexible Fe_xO_y/nitrogen-doped carbon nanofiber films for lithium storage by facile electrospinning of Fe-based metal-organic gels and polyacrylonitrile (PAN) followed by high-temperature carbonization. The integration of MOGs and PAN enabled the even dispersion of hollow Fe_xO_y nanoparticles in the composite fibers, ensuring rapid electron and ion transport. The composite delivered a high specific capacity, outstanding rate performance, and great cycling stability for 500 cycles.¹⁹ A series of MOGs with various metal compositions

and tunable ratios were developed by Li *et al.* by simply mixing metal ions (Fe^{3+} , Co^{2+} , and Ni^{2+}) and the organic ligand 4,4',4''-[(1,3,5-triazine-2,4,6-triyl)tris(azanediyl)]tribenzoic acid (H_3TATAB) at room temperature. Spinel-type metal oxides with good electrocatalytic OER performance are then obtained by the pyrolysis of the as-prepared MOGs delivered remarkable catalytic activity with a low overpotential of 244 mV at a current density of 10 mA cm^{-2} and a small Tafel slope of 55.4 mV dec^{-1} in alkaline electrolyte, outperforming most recently reported electrocatalysts.²⁰ He *et al.* synthesized a urea/CNTs-decorated MOG(Fe) as the precursor for Fe- Fe_2O_3 nanoparticles anchored on N-doped carbon nanotubes for ORR electrocatalyst. The material exhibited a superior oxygen reduction catalyst with an onset and half-wave potential of 0.92V and 0.72V respectively. These results suggest that MOG is a promising material for electrocatalytic applications.²¹ However, the agglomeration of metal atoms into larger particles during pyrolysis hinder the accessibility of M-N/C active sites leading to activity loss.²² The stabilization of Fe atoms within the network structure is thus required to avoid Fe agglomeration during pyrolysis by creating strong network structure.

Inter penetrating network (IPN) with a minimum of two non-covalently bonded macromolecular networks each in independent network form, of which at least one is synthesized and cross linked in the immediate presence of the other, without any covalent bonds between them.^{23,24} It is difficult to separate the individual components as the IPN structures are very strong.²⁵ The reactivity of individual polymers can be modulated to accomplish desired physical and chemical stability.²⁶ Due to such attributes, IPN systems are employed as gas separation agents,²⁷ drug delivery systems,²⁸ artificial implants, dialysis membranes, burn dressings etc.²⁹⁻³³ IPN systems can work as precursors for porous carbon and are known to increase the phase stability of the final product and the thermodynamic incompatibility can be overcome due to permanent interlocking of the network segments.³⁴ **Figure 2.1** illustrates typical IPN formation.

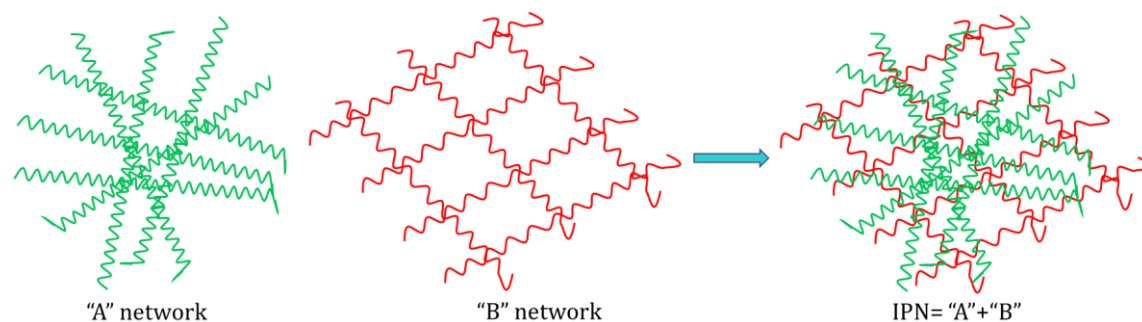


Figure 2.1 Schematic illustration of the formation of IPN.

Herein, Fe-N- doped IPN based porous carbon structures were synthesized from two individual networks without any covalent bond in between.^{34,35} By judicious selection of precursor materials, the resultant network topology could be modulated^{36,37} offering feasibility of designing new materials with controllable properties like porosity that primarily originates from its large interspace free volume.^{38,39} The Fe-N in situ integrated porous graphene structures presented here are derived from nitrogen abundant thermosetting polymer melamine formaldehyde (MF) and an iron containing MOG. The pre-polymer of MF when intercalated to the primary phase of iron-MOG, propagates simultaneously to generate the hard segment (MF) and soft segment (MOG) of the IPN. The introduction of MF pre-polymer into MOG precursor maximize the addition effect of the resulting polymer network and thereby improves its mechanical properties leading to a stable end product upon pyrolysis.⁴⁰ The strong covalently bonded organic polymer MF thus serves as a less expensive nitrogen enriched precursor of carbon. Even though melamine has been explored previously as a nitrogen resource,⁴¹⁻⁴³ neither of these studies explored the feasibility of MF based IPN systems.

2.2 Experimental

2.2.1 Materials

Anhydrous iron (III) chloride (FeCl_3), benzene-1,3,5-tricarboxylic acid (H_3BTC or trimesic acid), melamine ($\text{C}_3\text{H}_6\text{N}_6$) and formaldehyde were purchased from Sigma Aldrich Chemical Reagent Co. Ltd. Ethanol (99.9%) was procured from Jiangsu Huaxi International Trade Co-Ltd. China. Potassium hydroxide and tetrahydrofuran (THF) from Merck India and Naphthalene (C_{10}H_8) from TCI Chemicals, India Pvt. Ltd. were

used for the preparation of carbon precursor. All the reagents were used as received for the synthesis without any further purification.

2.2.2 Synthesis of Fe-MOG, Fe-MOG-MF and Fe-MOG-MFN IPNs

The Fe-MOG-MF IPN was prepared from Fe-MOG and MF pre-polymer. Fe-MOG (reactant A) was initially prepared by mixing ethanolic solutions of benzene-1,3,5-tricarboxylic acid and anhydrous FeCl₃ in the molar ratio of 1:3 at room temperature. Melamine formaldehyde (MF) pre-polymer (reactant B) was synthesized by reacting melamine and formaldehyde in the molar ratio of 1:3 at 70 °C. Upon mixing the reactants A and B, the individual networks are allowed to propagate simultaneously to generate the IPN at room temperature for overnight. In the alternative synthesis of Fe-MOG-MFN, naphthalene, a sublimable porogen (10%, w/w) was introduced to MF pre-polymer matrix as a solution in THF, which was subsequently added to the Fe-MOG. The individual networks of Fe-MOG and MF are allowed to propagate, as in the previous case, by keeping at room temperature for overnight. The IPNs formed were dried at 50 °C for 15 h followed by cross-linking of MF at 120 °C in an air oven for 48 h.

2.2.3 Synthesis of Fe-N Doped Porous Carbon

Fe-N-doped graphitic carbons from Fe-MOG, Fe-MOG-MF and Fe-MOG-MFN IPNs were derived by the pyrolysis of the corresponding precursors at 900 °C for 3h under N₂ atmosphere. Any unbound Fe present in the pyrolyzed samples were washed out with 1 M H₂SO₄ solution followed by rinsing with DI water for several times and dried at 50 °C. The samples derived were denoted as Fe-M-C, Fe-M-NC and Fe-MN-NC.

2.2.4 Structural Characterization

X-ray diffraction patterns were recorded using the diffractometer (PW1710 Philips, The Netherlands) employing Cu K α of 1.54 Å. The BET surface area and porosity analysis of the samples were performed with Micromeritics (Tristar 11, USA) surface area analyser using nitrogen adsorption at 77 K. The samples were degassed at 200 °C for 2 h in flowing N₂ before adsorption measurements. Raman spectra were obtained from a Confocal Raman microscope (alpha 300 R WITEC Germany) using 633 nm laser. The microstructure and morphology of the samples were observed

using scanning electron microscope (SEM Carl Zeiss, Germany). Elemental mapping was carried out using energy dispersive spectroscopy (EDS) measurements. Transmission electron micrographs of the samples were recorded on a FEI (Tecnai 30 G2 S-TWIN, The Netherlands) microscope. The rheological properties of the samples were measured using a Modular Compact Rheometer (MCR102, Anton Paar, India). XPS was investigated using a scanning X-ray microprobe (ULAC-PHI, Inc. PHI-4700 V, USA) with monochromated Al-K α X-ray source operating at 14 kV and 220 W.

2.2.5 Electrochemical Characterization

ORR measurements were carried out in a Bio-Logic Electrochemical Workstation (SP-300) using a three-electrode setup. The catalyst ink for ORR study was prepared by mixing 5 mg of the catalyst with 1 mL of DI water-isopropyl alcohol mixture (3:1) and 40 μ L of 5 wt. % nafion for 60 min in an ultrasonic bath. 10 μ L of this catalyst slurry was drop cast on the surface of a glassy carbon working electrode (0.196 cm²) using a micro syringe. The electrode was dried under an IR lamp for electrochemical analysis. Commercial Pt/C (40 wt. % from Johnson Matthey) was also studied for the comparison purpose. 0.1 M KOH was used as the electrolyte for the electrochemical measurements. Catalyst coated glassy carbon disc (0.196 cm² area, Pine Instruments, Inc.) was used as the working electrode. Hg/HgO was used as the reference electrode and graphite rod was used as the counter electrode. Cyclic voltammetry (CV) was performed at a scan rate of 50 mV s⁻¹ in both nitrogen and oxygen saturated 0.1 M KOH solution. Linear sweep voltammetry (LSV) was carried out by recording the voltammograms at a scan rate of 5 mV s⁻¹. The accelerated durability analysis of both Fe-MN-NC and Pt/C was carried out by running CV for 5000 cycles in a potential window of 0.97 to 0.57 V. All these measurements were carried out using a Rotating Disk Electrode (RDE, 0.196 cm², Pine Instruments). Hydrogen peroxide formation and number of electrons transferred during the oxygen reduction reaction were measured using a rotating ring disc electrode (RRDE, 0.2826 cm², Pine Instruments) in O₂ saturated 0.1 M KOH solution with a glassy carbon disc (0.2826 cm²) having a platinum ring as the working electrode, Hg/HgO as the reference electrode and graphite rod as the counter electrode. All potentials were converted into RHE by calibrating Hg/HgO in H₂ saturated 0.1 M KOH solution.⁴⁴

2.3 Results and Discussion

A simple and highly feasible method for the Fe-N-intrinsic doping via formation of IPN from an organic thermosetting polymer enriched with N and a metal (Fe)-organic gel network is developed. The competing growth of the propagating organic and inorganic chains lead to a stable network with soft and hard segments (Fe-MOG-MF), which upon pyrolysis undergo restructuring to generate highly porous graphitic sheets with firmly anchored Fe and N. The introduction of naphthalene in the MF polymer (Fe-MOG-MFN) has been examined as a strategy to enhance surface area of Fe-MOG-MFN. Upon pyrolysis, this material resulted in the formation of porous carbon with enhanced surface area due to the sublimation of the dissolved naphthalene. **Figure 2.2** illustrates the schematic illustration of formation of Fe-MN-NC.

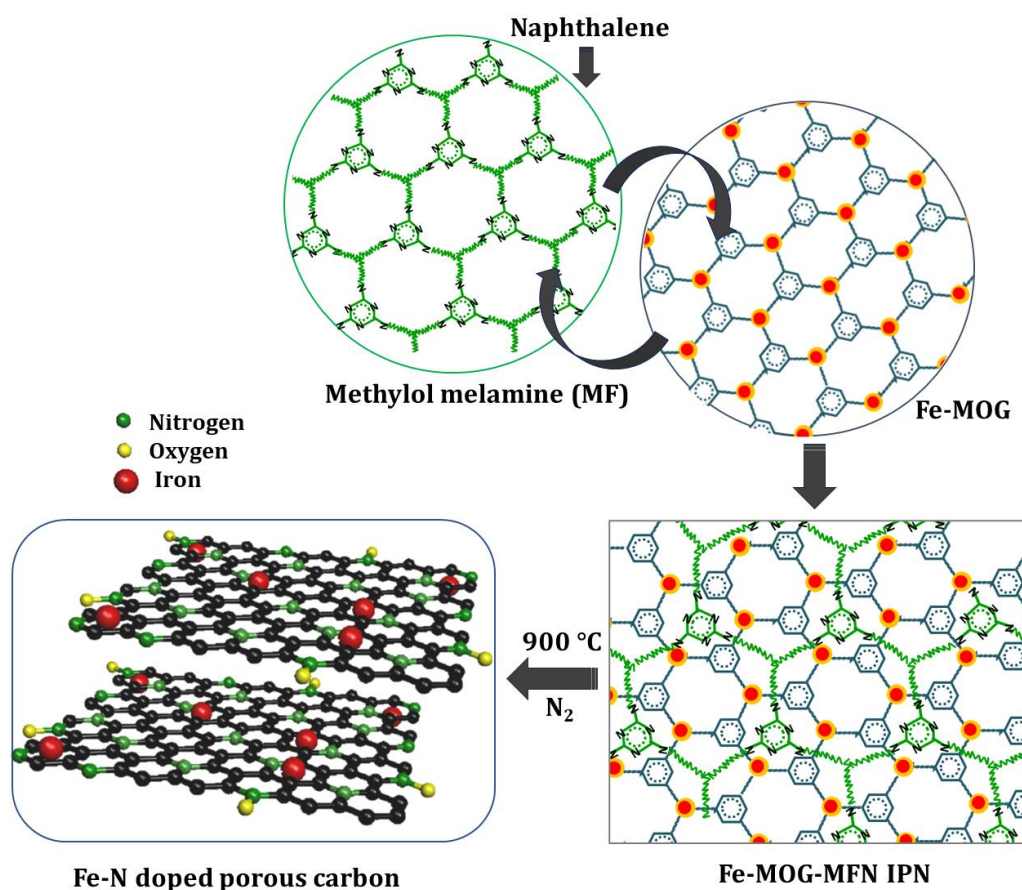


Figure 2.2 Schematic illustration for the formation of Fe-MN-NC.

2.3.1 Rheological Studies

The formation of Fe-MOG is characterized by rheological analysis. It was done using amplitude sweep test, where the strain percentage was kept between 0.01 to 10%. The storage modulus (G') and loss modulus (G'') were measured at a constant temperature of 25 °C and 10 rad/s frequency. **Figure 2.3** shows the range of viscoelastic properties of the gel as a function of strain. Fe-MOG exhibited values of G' higher than G'' upto a particular strain value indicating that the elasticity of the gel is higher than the viscous behavior, producing a well viscoelastic and stable gel. When G' and G'' approaches the crossover point, breaking down of gel network results. The cross over strain value for Fe-MOG is 5.95% indicating better stability of the formed gel network.

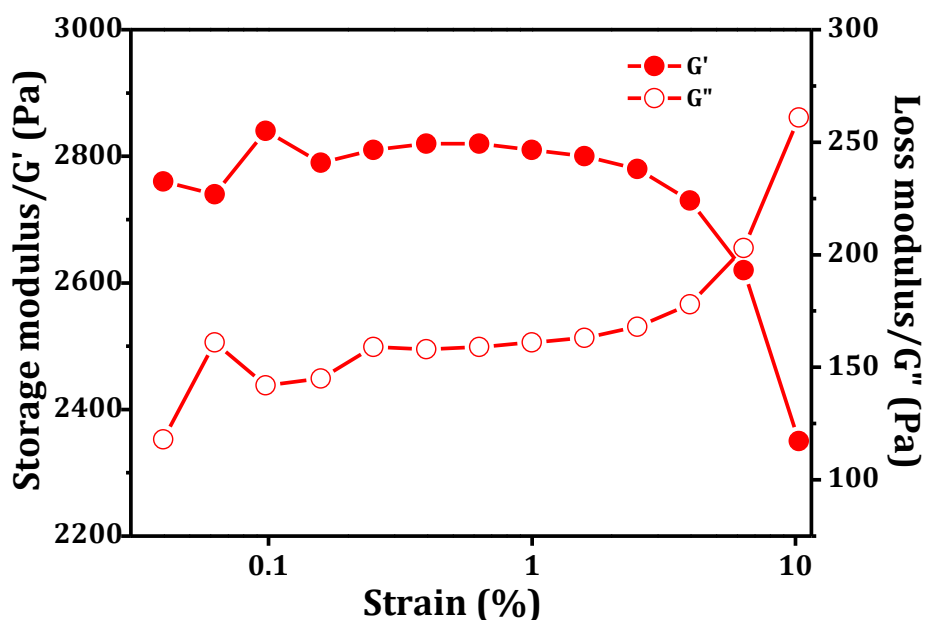


Figure 2.3 Amplitude sweep measurement of Fe-MOG. Solid and open symbol represent the storage and loss modulus respectively.

2.3.2 Morphology and Microstructure Analysis

The SEM image of the control sample (Fe-M-C) display a porous morphology (**Figure 2.4a & b**). The SEM images of Fe-M-NC (**Figure 2.4c & d**) and Fe-MN-NC (**Figure 2.4e & f**) indicate morphological diversity as a function of naphthalene content in the system. The sheet-like graphitized carbon structures are connected by elongated and better distributed pores in Fe-MN-NC (**Figure 2.4e & f**). For Fe-M-NC, only fewer pores are visible even though the macro-pores are evenly distributed, (**Figure 2.4c &**

d) demonstrating that naphthalene indigenously plays vital role in modulating the macro-porous structure and morphology of the system.

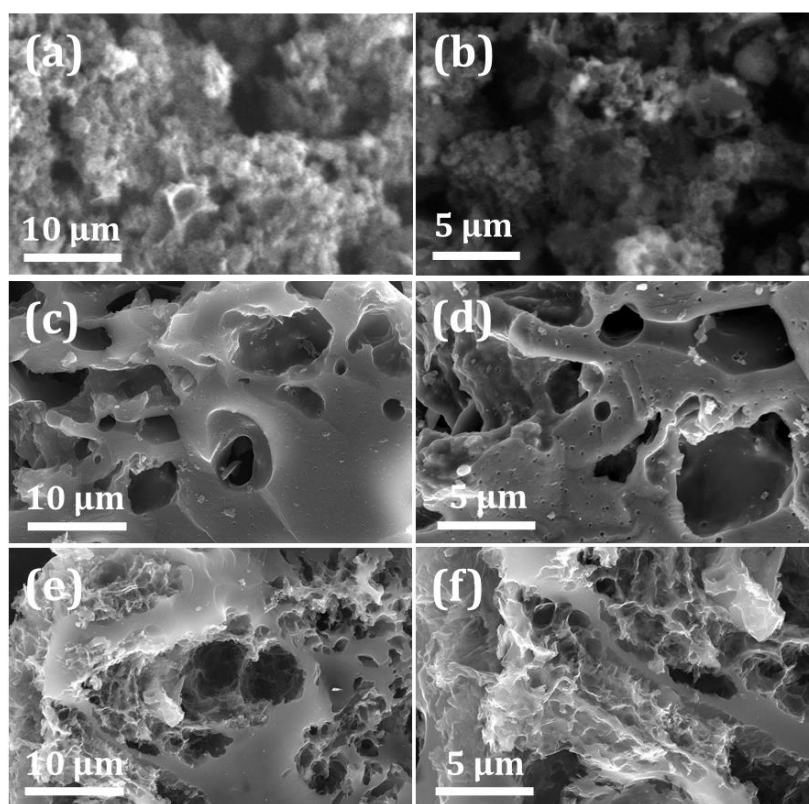


Figure 2.4 SEM images of (a, b) Fe-M-C, (c, d) Fe-M-NC and (e, f) Fe-MN-NC.

The presence of C, N, O and Fe can be clearly visualized in the elemental mapping shown in **Figure 2.5a & b**. The homogeneous distribution of N and Fe in the carbon framework is clearly seen from the corresponding elemental maps.

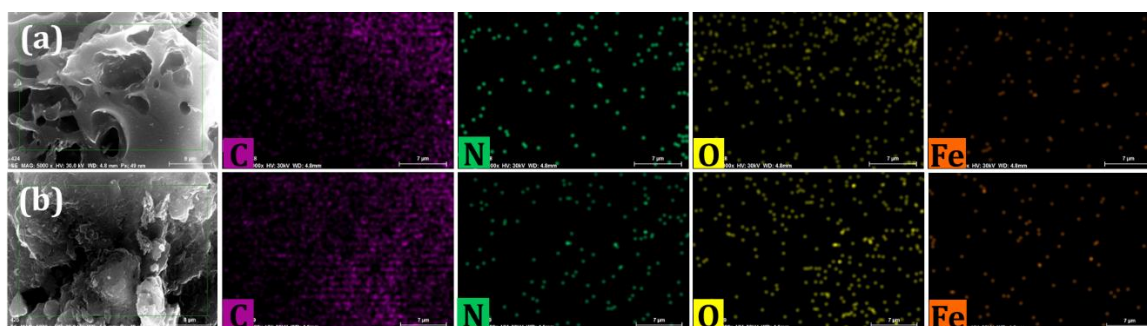


Figure 2.5 Elemental mapping of (a) Fe-M-NC and (b) Fe-MN-NC.

Further, TEM image of Fe-M-C showed sheet like carbon structure in which iron nanoparticles are distributed (**Figure 2.6**). The HRTEM images of Fe-M-NC and Fe-MN-NC (**Figure 2.7**) confirmed sheet-like graphitized carbon structures. Fe-M-NC

and Fe-MN-NC exhibited morphological diversity. Low magnification images of Fe-M-NC appeared as thin layered structures composed of interconnected, entangled chains (**Figure 2.7a**). The lattice spacing of 0.34 nm was consistent with (002) plane of graphitic carbon (**Figure 2.7b**).⁴⁵⁻⁴⁷ Nanoparticles with darker contrast were also clearly identified. The higher magnification image of the nanoparticle in **Figure 2.7c** displayed crystallized structure with a lattice spacing of 0.205 nm corresponding to the (220) plane of Fe₃C.^{48,49} Fe-MN-NC exhibited two phase morphology coherent to each other and consisted of star-like structures distributed well-over graphitic sheets of approximately 20 nm thick, with regular lattice arrangement at several regions (**Figure 2.7d & e**). This remarkable difference in the nano geometry is noticed upon the incorporation of naphthalene, and is apparent from the mixed structure of Fe-MN-NC given in **Figure 2.7d-f**. The well-defined interconnected network type organization shown by both Fe-M-NC and Fe-MN-NC at higher magnification demonstrated the structural features of the initial template and confirmed the generation of the proposed inter-penetrating network system, from which the carbon matrices were derived. It should also be noted here that; more diverse structure and a higher surface area is possessed by the graphitic sheets synthesized here as compared to the nano graphene sheets prepared by Peng *et al.* from the pyrolytic treatment of melamine and an iron precursor.⁴

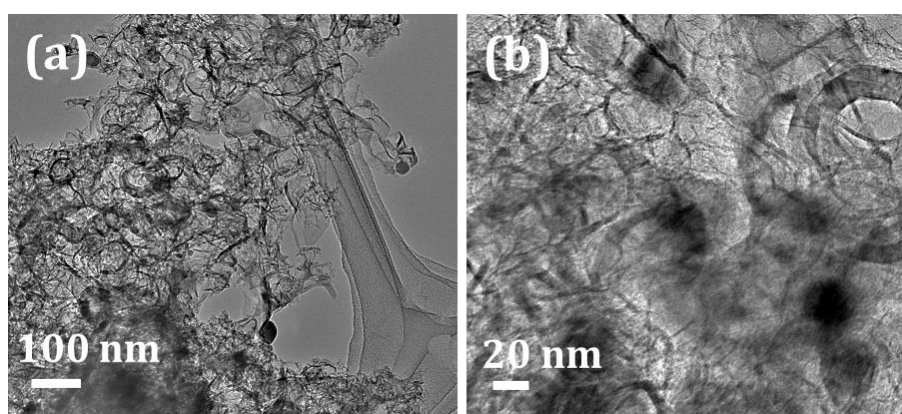


Figure 2.6 TEM images of Fe-M-C.

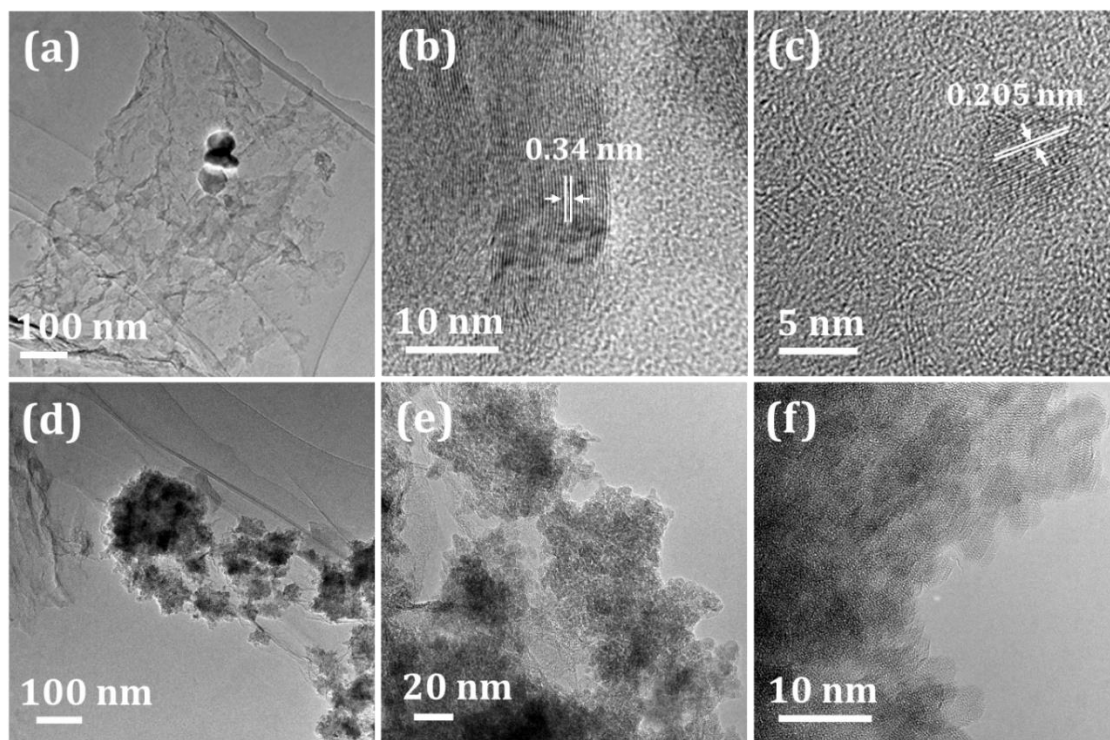


Figure 2.7 TEM images of (a, b, c) Fe-M-NC and (d, e, f) Fe-MN-NC.

2.3.3 Surface Area Analysis

The pore and textural characteristics of carbon samples were quantified from N_2 adsorption-desorption analysis (performed at 77 K). The carbon materials exhibited high surface area values of $347 \text{ m}^2 \text{ g}^{-1}$, $821 \text{ m}^2 \text{ g}^{-1}$ and $950 \text{ m}^2 \text{ g}^{-1}$ respectively for Fe-M-C, Fe-M-NC and Fe-MN-NC. Fe-M-C exhibited mesoporous structure whereas, the pore structure was predominantly microporous for Fe-M-NC and Fe-MN-NC (**Figure 2.8a**). The type II b isotherms having adsorption hysteresis indicated the presence of mesopores along with the micropores. The increased mesoporosity in Fe-M-NC sample compared to Fe-MN-NC can be clearly visible from the inset graph in **Figure 2.8a**. The increased microporosity observed for Fe-MN-NC sample was due to the sublimation of naphthalene. The cumulative pore volume measured from BJH was found to be $0.10 \text{ cm}^3 \text{ g}^{-1}$ and $0.07 \text{ cm}^3 \text{ g}^{-1}$ respectively for Fe-M-NC and Fe-MN-NC respectively (**Figure 2.8b**). The mesopore size distribution curve obtained from BJH method, shown in **Figure 2.8c**, has a pore size distribution within 2-12 nm for both the samples. Fe-M-NC sample seems to have slightly better pore size distribution. The micropore size distribution curves obtained from NLDFT analysis show the variation of micropore volume for the two samples (**Figure 2.8d**). Both the samples showed a

narrow pore size distribution within 0.5-2.0 nm with a slightly higher micropore volume for Fe-MN-NC sample.

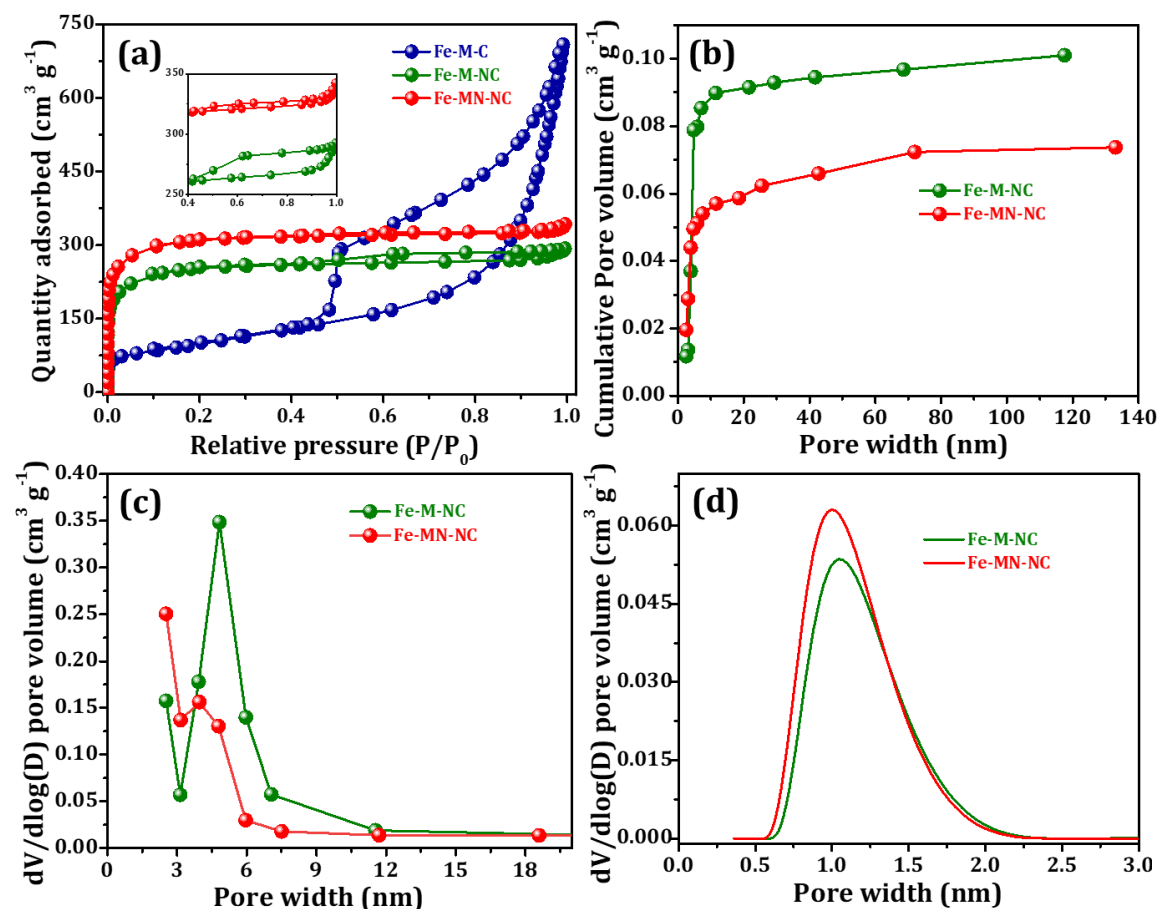


Figure 2.8 (a) N₂ adsorption-desorption isotherms of Fe-M-C, Fe-M-NC and Fe-MN-NC, (b) BJH cumulative pore volume and (c) pore size distribution of Fe-M-NC and Fe-MN-NC (d) NLDFT pore size distribution of Fe-M-NC and Fe-MN-NC.

2.3.4 Phase Analysis

Unlike Fe-M-C, both Fe-M-NC and Fe-MN-NC consisted of amorphous graphitized carbon, as confirmed from the XRD patterns (**Figure 2.9**). The increased amorphous nature was due to N-doping. Reflection peaks corresponding to 2θ values of 26° and 44° were indexed to (200) and (101) lattice of graphitic carbon respectively (JCPDS: 75-1621).^{50,51} It could be envisaged that for Fe-MN-NC, the broader peak (002) indicates increased degree of amorphous nature/ disorder in the structure⁵² derived due to the presence of naphthalene in the system which is further corroborated by Raman spectrum. No peak corresponding to Fe₃C was visible presumably due to the

disordered incorporation of iron atom in the carbon matrix and also due to its lower percentage in the carbon structure.

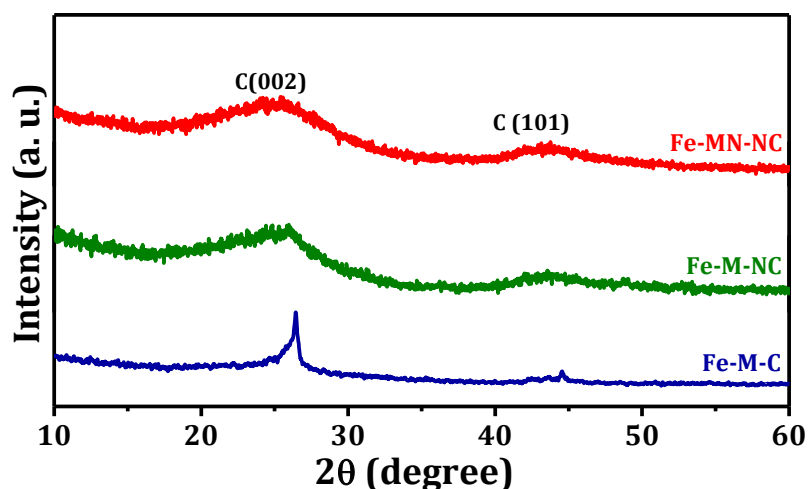


Figure 2.9 Powder X-ray diffraction patterns of Fe-M-NC and Fe-MN-NC.

2.3.5 Chemical Composition Analysis

Raman spectral interpretation is a standard tool endowed with important structural information of the graphitic, distorted, crystalline or amorphous carbon materials.⁵³ For Fe-M-NC (**Figure 2.10a**), the G band arising from the bond stretching of sp^2 hybridized carbon atoms of the hexagonal graphitic rings was observed at 1594 cm^{-1} while D band resulting from the disordered carbon frames on the defect sites was at 1344 cm^{-1} .⁵⁴⁻⁵⁶ For Fe-MN-NC Raman spectra indicated peaks at 1604 cm^{-1} corresponding to G band and 1352 cm^{-1} representing D band. The proportionality term I_D/I_G imparts insights into the degree of distortion of the carbon structure, as the distortion increases with increasing I_D/I_G ratio. Fe-M-NC has I_D/I_G ratio of 0.78, indicating higher degree of graphitization, whereas Fe-MN-NC displayed I_D/I_G ratio of 1.23 suggesting a greater disorder indicating increased nitrogen content. The increased disorder should be attributed to the structural changes occurring during the sublimation of naphthalene. In order to elucidate the influence of pyrolysis temperature on the nitrogen content and degree of graphitization, the precursor Fe-MOG-MFN was carbonized at 800 and 1000 °C for 3 h at a heating rate of 3 °C/min in N_2 atmosphere. The Raman spectra obtained for 800 and 1000 °C pyrolyzed samples shown in **Figure 2.10b** indicated an I_D/I_G ratio of 1.12 and 0.93 respectively for Fe-MN-NC-800 and Fe-MN-NC-1000. The ratio initially increased with temperature and

decreased after 900 °C, due to the removal of nitrogen at temperatures greater than 900 °C. Fe-MN-NC (pyrolyzed at 900 °C) is assumed to perform increased catalytic activity because of the increased graphitic N content. The influence of pyrolysis temperature on the ORR activity will be discussed later in the chapter.

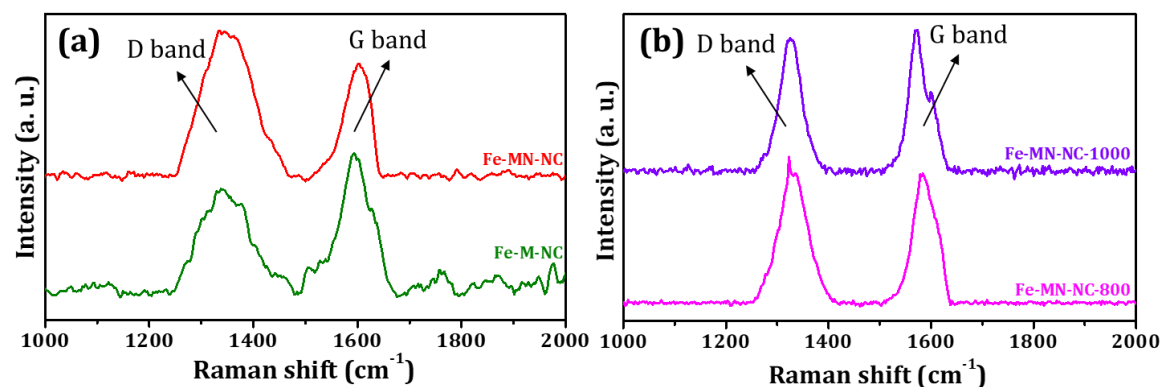


Figure 2.10 Raman spectra of (a) Fe-M-NC & Fe-MN-NC and (b) Fe-MN-NC-800 & Fe-MN-NC-1000.

The X-ray Photoelectron spectra (XPS) confirmed the chemical states of elements (C, Fe, N, O) in Fe-M-NC and Fe-MN-NC (**Figure 2.11**).

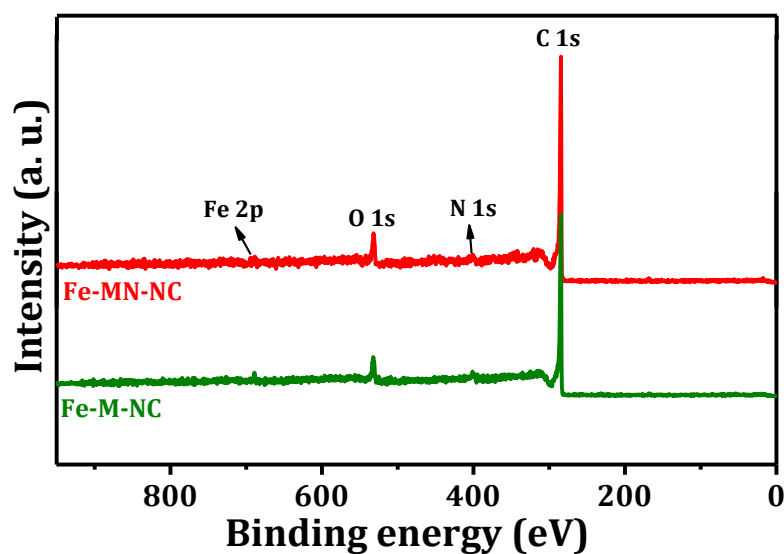


Figure 2.11 XPS survey scan spectrum of Fe-M-NC and Fe-MN-NC.

From the regional scan of N 1s spectrum (**Figure 2.12a**), three major N species, as pyridinic N (398.51 eV), graphitic N (400.90 eV) and oxidized N (403.70 eV) were noticed. No peak corresponding to pyrrolic N was observed owing to its very low concentration. The oxidized N was presumably formed as a result of the adsorption

of oxygen in air at the N-doped sites.^{57,58} In Fe-M-NC, graphitic N was the higher fraction (1.91 at.%) followed by pyridinic N (0.82 at.%). Since binding energies of N-Fe bond and pyridinic N were very close, the peak at 398.5 eV represent the form of nitrogen bonded to metal.⁵⁹⁻⁶¹ The higher fractions of graphitic and pyridinic N content influence the electrocatalytic activity of the carbon as the presence of appreciable amount of pyridinic and graphitic N is responsible for the catalytic performance.^{62,63} The deconvoluted N 1s spectrum of Fe-MN-NC (**Figure 2.12b**) showed the presence of pyridinic N (398.50 eV), graphitic N (401.11 eV) and oxidized N (404.71 eV). The percentage of different nitrogen species was different for the two samples. Fe-MN-NC with a higher graphitic nitrogen percentage (1.97 at.%) is expected to show good ORR activity.⁶² However, the doped Fe content was almost similar in both the samples (0.15 at.%).

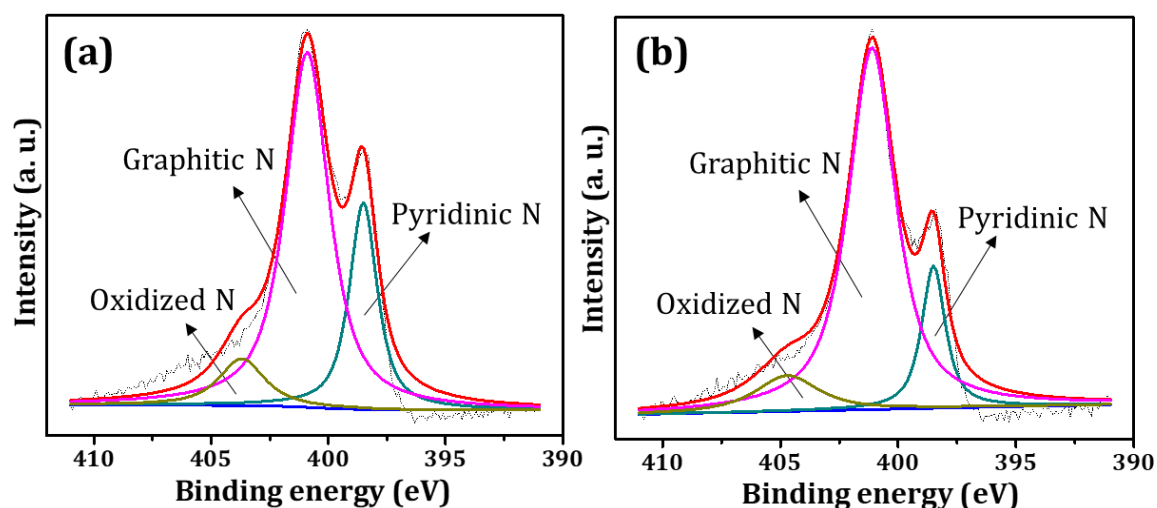


Figure 2.12 High resolution N 1s XPS spectra of (a) Fe-M-NC and (b) Fe-MN-NC.

The concentrations of different nitrogen species for the two samples are evaluated based on the integrated peak areas and the corresponding graph is shown in **Figure 2.13**.

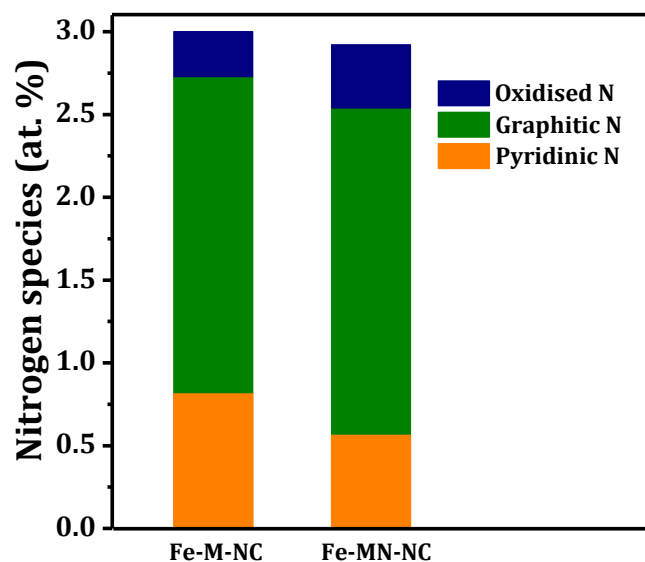


Figure 2.13 Concentration of various types of nitrogen (in atomic percentage) present in the Fe- doped carbon catalyst samples.

The nature of doped Fe was confirmed from Fe 2p XPS spectra (**Figure 2.14a & b**). The binding energies of Fe 2p_{3/2} and Fe 2p_{1/2} of Fe³⁺ ion were located at 711.5 and 724.7 eV respectively. The peak at 717.3 eV corresponded to Fe 2p_{3/2} satellite peak and was also an indication of the existence of iron oxide phase in the carbon structure.⁶⁴⁻⁶⁶

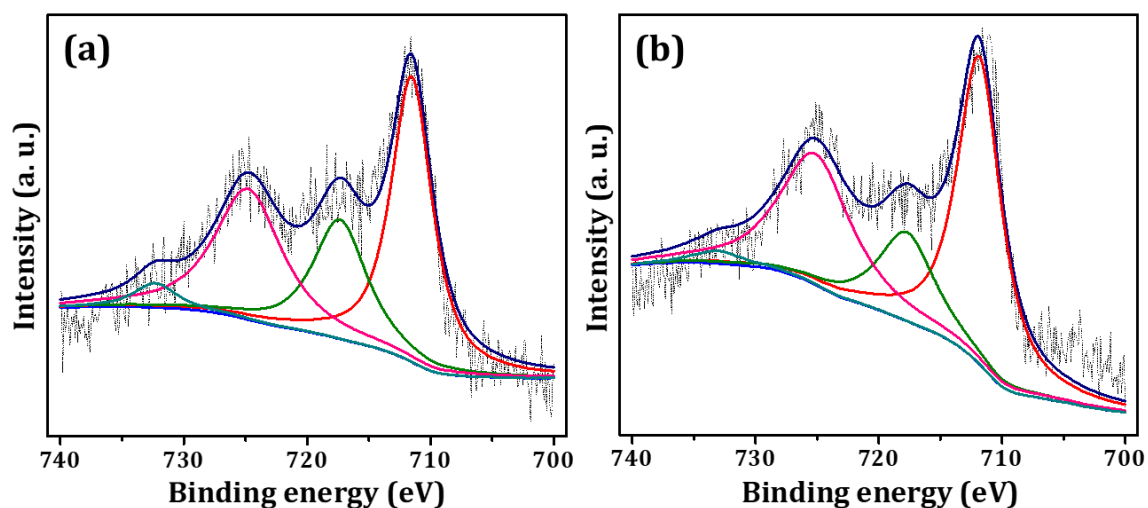


Figure 2.14 High resolution Fe 2p XPS spectra of (a) Fe-M-NC and (b) Fe-MN-NC.

The variation of N and Fe content with pyrolysis temperature was also studied with XPS analysis. The survey spectrum shown in **Figure 2.15** confirmed the presence of elements C, N, O and Fe. The deconvoluted N1s spectrum of Fe-MN-NC-800 showed a nitrogen content of 2 at.% while that of Fe-MN-NC-1000 was 0.5 at.% (**Figure 2.16**).

This data was in accordance with Raman results. The amount of graphitic N is 1.14 at.% for Fe-MN-NC-800 and 0.22 at.% for Fe-MN-NC-1000. No pyrrolic N was detected for Fe-MN-NC-1000 since, it is a thermally labile N species. The variation of concentration of different nitrogen species with pyrolysis temperature is shown in Table 2.1.

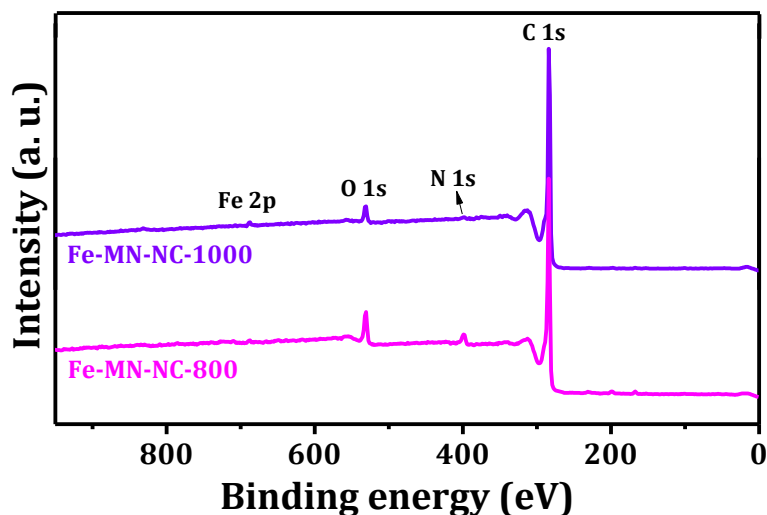


Figure 2.15 XPS survey scan spectrum of Fe-MN-NC-800 and Fe-MN-NC-1000.

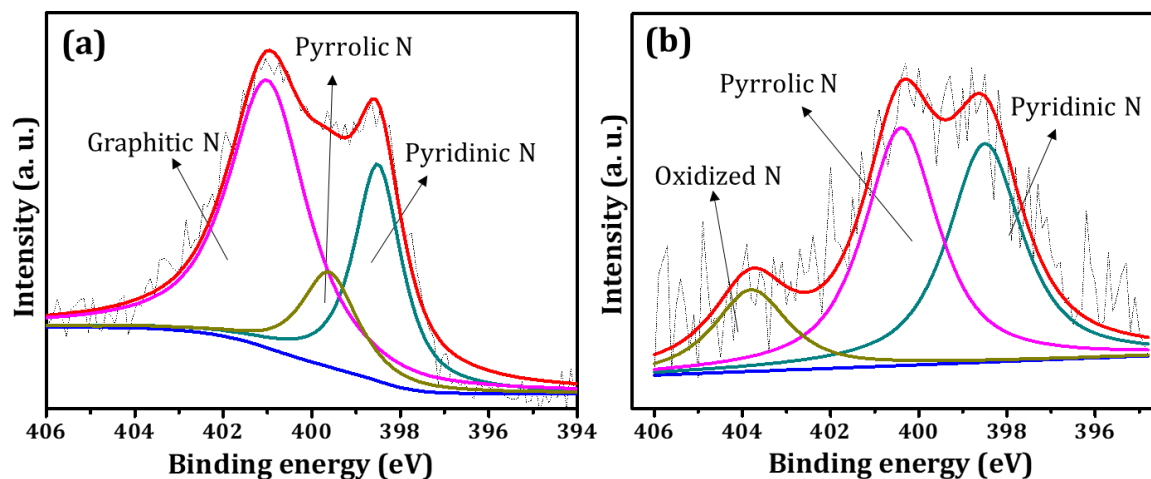


Figure 2.16 High resolution N 1s XPS spectra of (a) Fe-MN-NC-800 and (b) Fe-MN-NC-1000.

Table 2.1 Variation of concentration of different nitrogen species with pyrolysis temperature.

Sample	Elemental conc. (at.%)				N species (at.%)			
	C	O	N	Fe	Pyridinic	Pyrrolic	Graphitic	Oxidized
Fe-MN-NC-800	88.9	7.1	2	0.1	0.57	0.29	1.14	-
Fe-MN-NC-900	88.59	8.13	2.93	0.13	0.57	-	1.97	0.38
Fe-MN-NC-1000	96	3.5	0.5	<0.1	0.20	-	0.22	0.08

2.3.6 Electrochemical Analysis

The cyclic voltammograms of Fe-MN-NC and Pt/C in oxygen and nitrogen saturated 0.1 M KOH solution are presented in **Figure 2.17**. The measurements were performed at a typical scan rate of 50 mV s^{-1} at a rotation rate of 900 rpm in the potential window of 0.07 to 1.07 V vs RHE. No well-defined peak in N_2 saturated electrolyte was observed. On oxygen purging, the cathodic current increased indicating the reduction of oxygen.

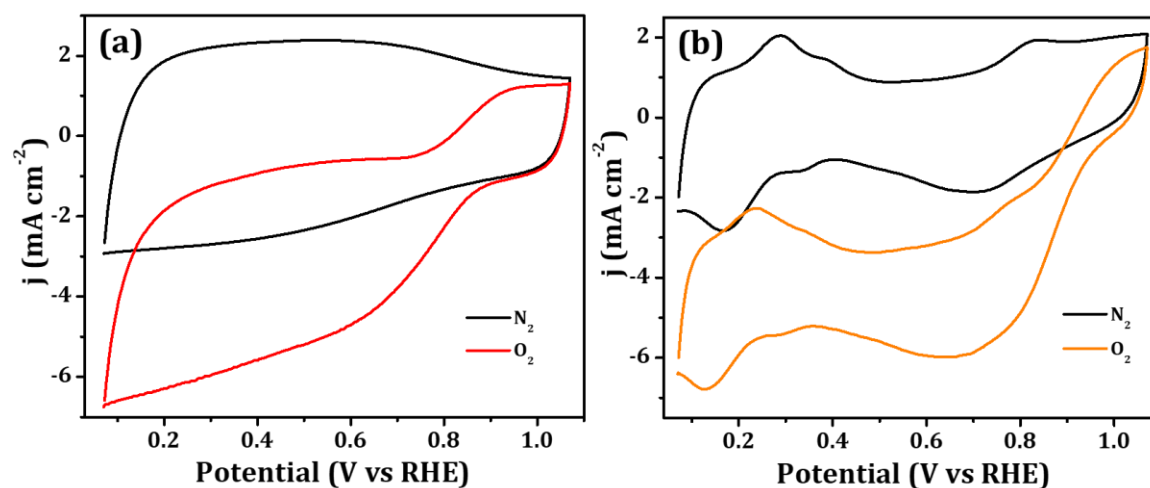


Figure 2.17 Cyclic voltammograms of (a) Fe-MN-NC and (b) Pt/C in 0.1 M KOH solution measured at a scan rate of 50 mV s^{-1} at 900 rpm.

Figure 2.18a shows the comparison of LSVs of Fe-M-C, Fe-M-NC and Fe-MN-NC in oxygen saturated 0.1 M KOH solution at a rotation rate of 1600 rpm. Both Fe-M-NC and Fe-MN-NC samples exhibited an onset potential of 0.91 V and that of Pt/C is 1 V. Even though the onset potentials of Fe-M-NC and Fe-MN-NC samples are the same, the limiting current value was higher for Fe-MN-NC, which was attributed to the increased surface area and graphitic nitrogen content. The onset potential for the control sample is 0.81 V, which was much lower than the above N-doped samples, which corroborated the role of nitrogen species in enhancing the ORR catalytic activity. The effect of pyrolysis temperature on the ORR activity was analyzed by plotting LSVs of Fe-MOG-MFN sample pyrolyzed at temperatures of 800, 900 and 1000 °C (**Figure 2.18b**). The onset potential of Fe-MN-NC 800 and Fe-MN-NC-900 were 0.91 V, but the limiting current density was higher for 900 °C pyrolyzed sample (-4.5 mA cm^{-2}), which was due to the increased graphitic N content. For 1000 °C pyrolyzed sample, the lower nitrogen content resulted in low onset potential (0.85 V) and limiting current density (-3.8 mA cm^{-2}).

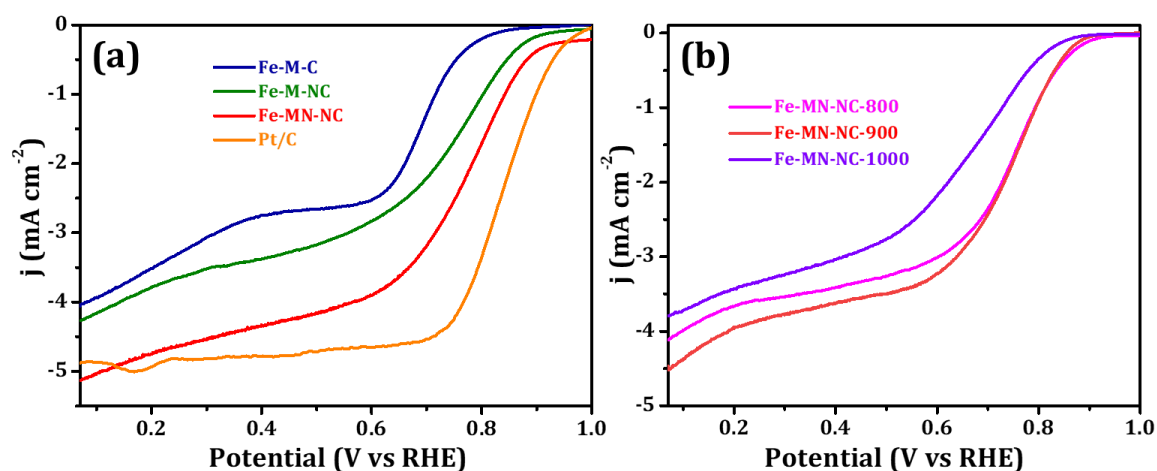


Figure 2.18 (a) Linear Sweep voltammogram (LSV) comparison of (a) Fe-M-C, Fe-M-NC, Fe-MN-NC & Pt/C and (b) Fe-MN-NC pyrolyzed at temperatures 800, 900 & 1000 °C in O₂ saturated 0.1 M KOH solution measured at a scan rate of 5 mV s⁻¹ at 1600 rpm.

The LSVs of all the samples at different working electrode rotations was also studied and the result showed increased limiting current value with increased electrode rotation because of the enhanced diffusion of electrolyte and mass transfer (**Figure 2.19**).

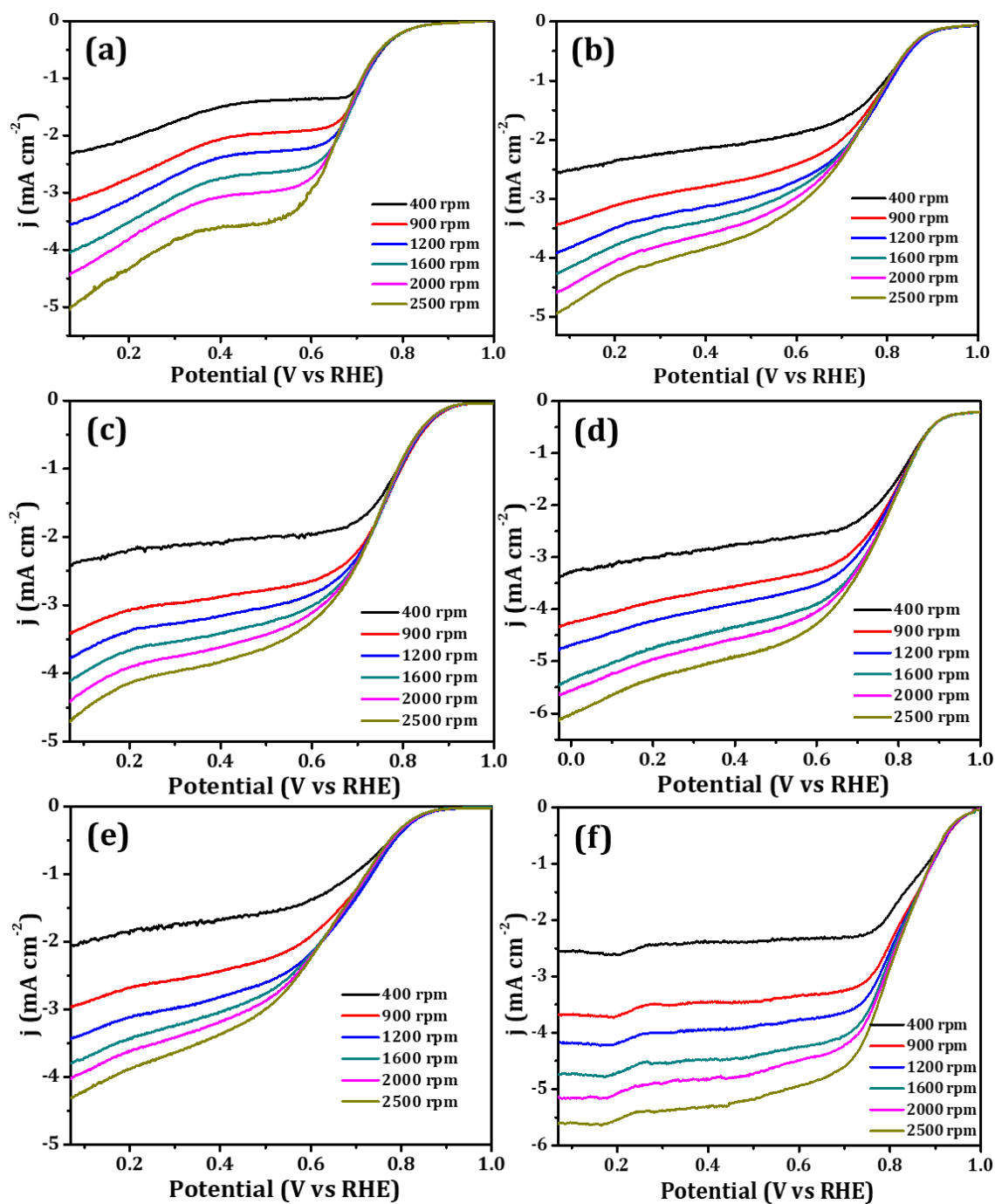


Figure 2.19 LSVs of (a) Fe-M-C, (b) Fe-M-NC, (c) Fe-MN-NC-800, (d) Fe-MN-NC (e) Fe-MN-NC-1000 and (f) Pt/C in O₂ saturated 0.1 M KOH solution measured at different rotation rates at a scan rate of 5 mV s⁻¹.

The kinetic parameters of the ORR can be analyzed on the basis of the Koutecky-Levich (K-L) equation. and the K-L equation can be represented as,

$$\frac{1}{j} = \frac{1}{j_d} + \frac{1}{j_k} \quad (2.1)$$

$$\frac{1}{j} = \frac{1}{0.62nFAC_0^*D_0^{2/3}v^{-1/6}\omega^{1/2}} + \frac{1}{nFAkC_0^*} \quad (2.2)$$

where, 'j' is the measured current density, 'j_d' is the diffusion-limiting current density, 'j_k' is the kinetic current density, 'w' is the angular rotation ($w=2\pi f/60$, f is the rotation speed), 'n' is the number of transferred electrons during ORR, 'F' is the Faraday's constant (96480 C), 'C₀^{*}' is the bulk concentration of O₂ (1.22×10^{-6} mol cm⁻³), 'D₀' is the diffusion coefficient of O₂ (1.9×10^{-5} cm² s⁻¹), 'ν' is the kinematic viscosity of the electrolyte (0.01 cm² s⁻¹) and 'k' is the electron transfer rate constant. K-L slopes obtained by plotting inverse of current density (1/j) against inverse of square root of angular density (1/ω^{1/2}). K-L plot of different samples are shown in **Figure 2.20**. Good linearity was obtained for all the samples. A linear relationship between current density and square root of the rotation speed is obtained for all the samples. The obtained slope is constant at different potentials suggesting similar electron transfer number over this potential range.

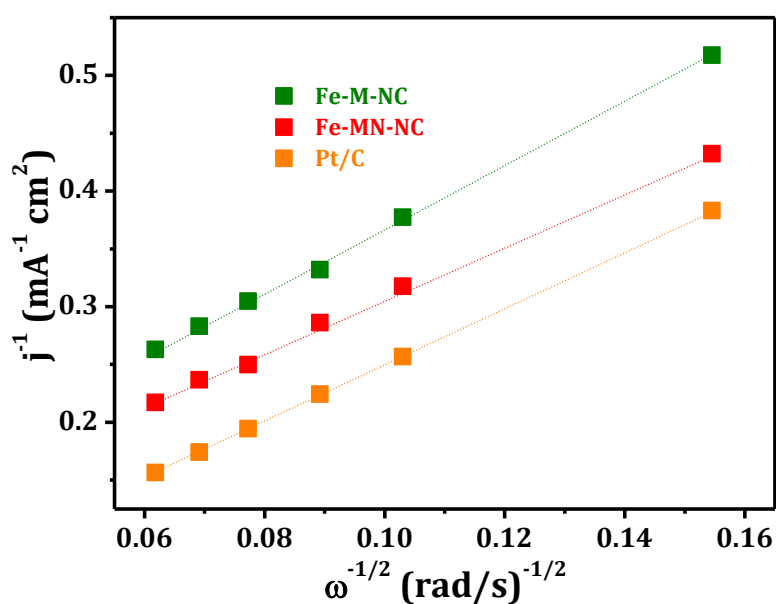


Figure 2.20 Comparison of the Koutecky-Levich (K-L) plots of Fe-M-C, Fe-M-NC, Fe-MN-NC and Pt/C.

RRDE measurements were carried out to investigate the number of electron transfer and the amount of peroxide generated during ORR. Following equations have been used to calculate the percentage of H₂O₂ produced and the number of electron transferred during ORR.

$$H_2O_2\% = 200X \frac{I_r}{I_d + \frac{I_r}{N}} \quad (2.3)$$

$$n = 4X \frac{I_d}{I_d + \frac{I_r}{N}} \quad (2.4)$$

where 'I_r' and 'I_d' are the Faradaic ring and disc current, respectively. 'N' is the collection efficiency of the ring electrode (0.37) and the 'n' is the number of the transferred electron.

The electron transfer number calculated from RRDE for all the samples are presented in **Figure 2.21a**. Fe-MN-NC showed an electron transfer number of 3.6 proves that the preferred ORR kinetics involved a major contribution from the direct reduction of oxygen into water in the system. The increased electron transfer number for Fe-MN-NC compared to Fe-M-NC is attributed to the increased surface area and graphitic N content. The amount of H₂O₂ has been quantified by analyzing the ring current of the RRDE result. If the amount of peroxide produced is less, the ring current becomes lower since less amount of peroxide reaches the Pt ring electrode. A comparison of percentage of peroxide produced over different catalysts is presented in **Figure 2.21b**. The peroxide yield on Fe-MN-NC was estimated to be 20 % which was significantly lower than that of Fe-M-NC. The Pt/C sample was calculated to produce 5 % H₂O₂.

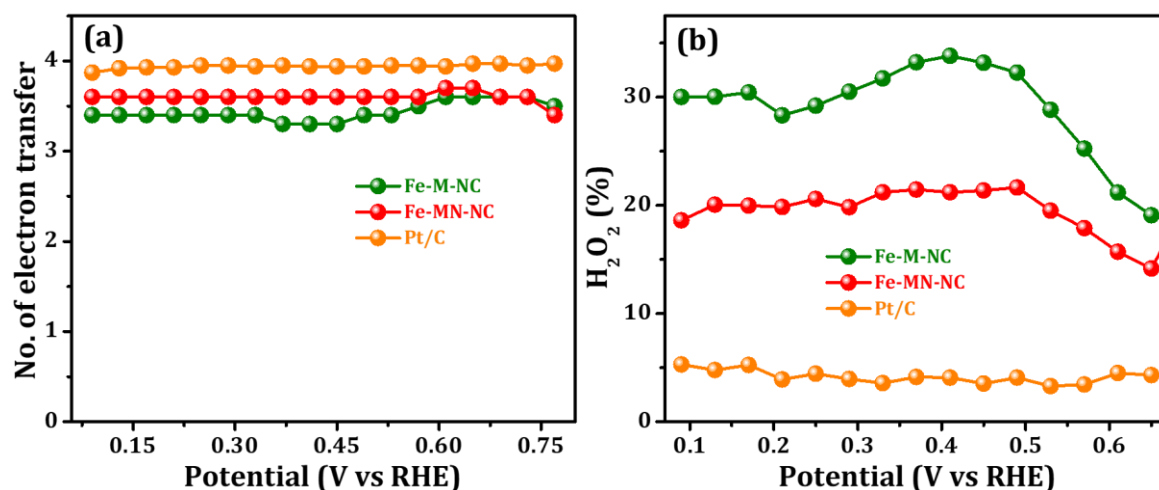


Figure 2.21 Comparison of (a) number of electron transfer and (b) hydrogen peroxide yield at different potentials obtained from the RRDE experiment.

Tafel slope for Fe-MN-NC is 83.4 mV dec⁻¹ and was comparatively lower than Fe-M-NC indicating faster ORR kinetics (**Figure 2.22**).

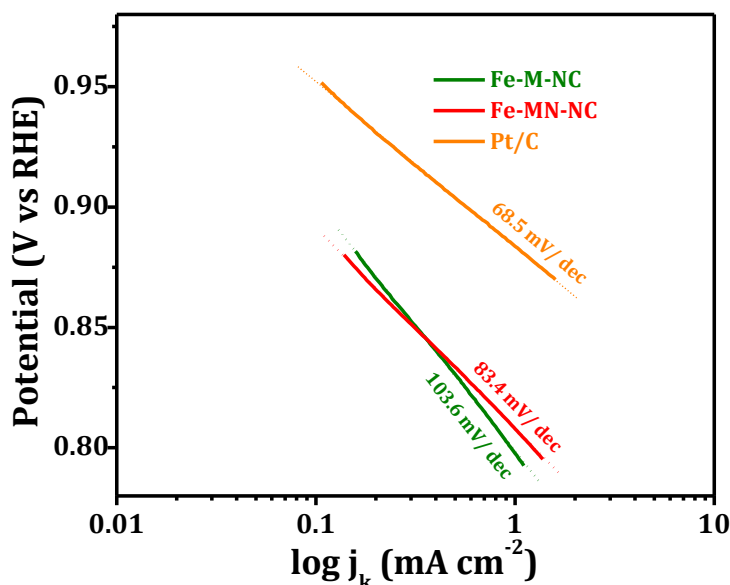


Figure 2.22 Tafel slope comparison of Fe-M-NC and Fe-MN-NC with Pt/C.

In addition to the improved ORR activity, it is important to check the stability of the catalyst under the electrochemical environment. Hence accelerated durability test (ADT) was carried out to compare the stability of the catalyst with respect to Pt/C. The ADT was performed at room temperature in oxygen-saturated 0.1 M KOH at a scan rate of 100 mV s⁻¹ for 5000 cycles. Initially, the LSV of Fe-MN-NC was taken at 1600 rpm to envisage its original ORR performance. After 5000 cycles, LSV was repeated again and degradation in activity was quantified by comparing the half wave potential of the catalyst before and after the ADT test (**Figure 2.23a**). The potential drop after 5000 cycles was 31 mV which was lower compared to that of Pt/C, with a shift of 34 mV (**Figure 2.23b**). **Table 2.2** summarizes the electrocatalytic performance of the prepared samples.

Table 2.2 Comparison of electrocatalytic performance of the samples

Sample	E _{onset} (V vs RHE)	n	H ₂ O ₂ (%)	Tafel slop (mV dec ⁻¹)
Fe-M-NC	0.91	3.4	35	103.6
Fe-MN-NC	0.91	3.6	20	83.4
Pt/C	1.00	3.9	4	68.5

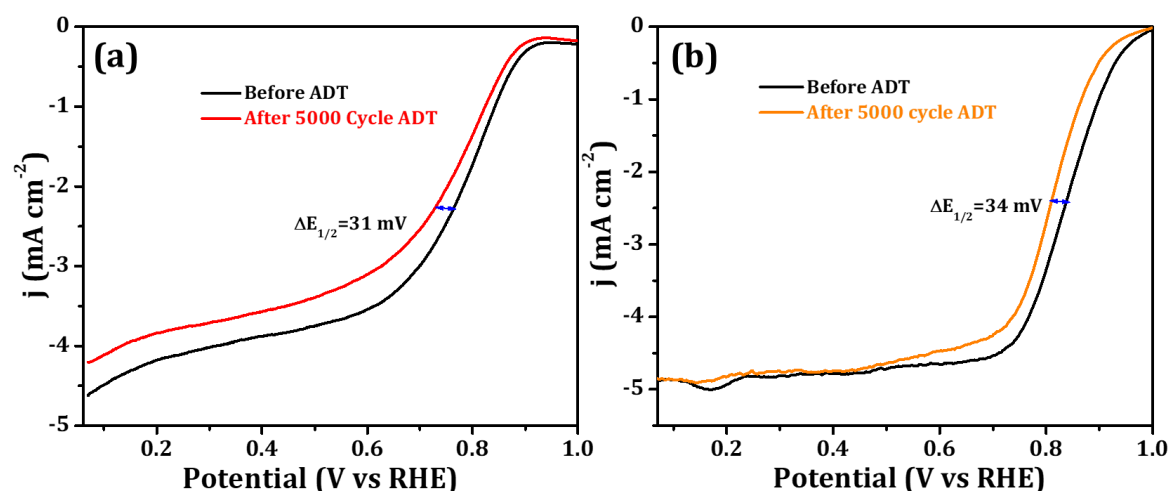


Figure 2.23 (a) LSV recorded before and after 5000 cycles ADT analysis for (a) Fe-MN-NC and (b) Pt/C in O₂ saturated 0.1 M KOH solution with electrode rotation of 1600 rpm.

It is implicit that, the design of carbon catalysts with an optimum combination of higher surface area, pore structure, amount of doped heteroatoms, pore and dopants distribution and degree of graphitization contribute positively in accomplishing better electrocatalytic activity. It is therefore difficult to specify a single parameter as the governing factor for improved ORR performance of carbon electrocatalysts. The catalysts proposed here were synthesized as high purity hetero-atom (Fe and N) decorated carbon with high surface area, in an economically beneficial route based on a gel-polymer IPN system by using less-expensive melamine formaldehyde as the nitrogen source. Here, we have adopted the technique of intrinsic doping and in situ synthesis for realizing carbon with both Fe and N as intrinsic part of their composition. The addition of porogen (naphthalene) influenced the material characteristics such as morphology and surface area, as seen from the XRD, TEM, BET analysis and ORR performance. The increased microporosity accounts for the pore generation associated with naphthalene sublimation. Fe-MN-NC contained higher amount of doped graphitic N (1.97) with higher I_D/I_G ratio in the Raman spectrum. It has helped in improving the ORR catalytic activity in Fe-MN-NC. ORR onset potential was same in both the samples (0.91 V) while the limiting current is higher in Fe-MN-NC due to the higher surface area. Besides all these properties, a good durability of 5000 cycles also makes Fe-MN-NC a good ORR catalyst.

2.4. Conclusions

A simple synthetic procedure for the preparation of Fe-N intrinsically doped porous graphitic carbon electrocatalysts from inter penetrating network (IPN) of in situ polymerized melamine formaldehyde (hard segment) and metal-organic gel (soft segment) is developed. Raman spectroscopic analysis and XPS analysis revealed the successful doping of nitrogen and iron in the graphitic carbon network. The deconvoluted N 1s spectra clearly showed the presence of more amount of nitrogen in the form of graphitic nitrogen as the active site for enhanced ORR activity. No detectable amount of pyrrolic nitrogen was observed. Moreover, high surface area of $950 \text{ m}^2 \text{ g}^{-1}$ also contributed towards the improved ORR activity. The catalyst displayed enhanced electrocatalytic properties with an onset potential of 0.91 V and an electron transfer number of 3.6. The electrocatalyst showed only 31 mV shift in the onset $E_{1/2}$ for the tested 5000 cycles, whereas, the commercial Pt/C sample showed a reduction of 32 mV in $E_{1/2}$ after 5000 cycles in alkaline conditions. The results further demonstrated the feasibility to derive extended versions of in situ Fe-N doped porous carbon structures with better ORR activity from IPN based structures via systemic modulations of synthetic protocols and inclusion of porogens.

References

1. Liang, H. W.; Wei, W.; Wu, Z. S.; Feng, X.; Müllen, K. Mesoporous Metal-Nitrogen-Doped Carbon Electrocatalysts for Highly Efficient Oxygen Reduction Reaction. *J. Am. Chem. Soc.* **2013**, *135* (43), 16002.
2. Xia, W.; Qiu, B.; Xia, D.; Zou, R. Facile Preparation of Hierarchically Porous Carbons from Metal-Organic Gels and Their Application in Energy Storage. *Sci. Rep.* **2013**, *3*, 1935.
3. Jalilov, A. S.; Ruan, G.; Hwang, C. C.; Schipper, D. E.; Tour, J. J.; Li, Y.; Fei, H.; Samuel, E. L. G.; Tour, J. M. Asphalt-Derived High Surface Area Activated Porous Carbons for Carbon Dioxide Capture. *ACS Appl. Mater. Interfaces* **2015**, *7* (2), 1376.
4. Peng, H.; Mo, Z.; Liao, S.; Liang, H.; Yang, L.; Luo, F.; Song, H.; Zhong, Y.; Zhang, B. High Performance Fe- and N- Doped Carbon Catalyst with Graphene Structure for Oxygen Reduction. *Sci. Rep.* **2013**, *3*, 1765.

5. Liang, J.; Zhou, R. F.; Chen, X. M.; Tang, Y. H.; Qiao, S. Z. Fe–N Decorated Hybrids of CNTs Grown on Hierarchically Porous Carbon for High-Performance Oxygen Reduction. *Adv. Mater.* **2014**, *26* (35), 6074.
6. He, C.; Zhang, T.; Sun, F.; Li, C.; Lin, Y. Fe/N co-doped Mesoporous Carbon Nanomaterial as an Efficient Electrocatalyst for Oxygen Reduction Reaction. *Electrochim. Acta* **2017**, *231*, 549.
7. Li, J. C.; Zhao, S. Y.; Hou, P. X.; Fang, R. P.; Liu, C.; Liang, J.; Luan, J.; Shan, X. Y.; Cheng, H. M. A Nitrogen-Doped Mesoporous Carbon Containing an Embedded Network of Carbon Nanotubes as a Highly Efficient Catalyst for the Oxygen Reduction Reaction. *Nanoscale* **2015**, *7* (45), 19201.
8. Unni, S. M.; Anilkumar, G. M.; Matsumoto, M.; Tamaki, T.; Imai, H.; Yamaguchi, T. Direct Synthesis of a Carbon Nanotube Interpenetrated Doped Porous Carbon Alloy as a Durable Pt-Free Electrocatalyst for the Oxygen Reduction Reaction in an Alkaline Medium. *Sustain. Energy Fuels* **2017**, *1* (7), 1524.
9. Meng, F. L.; Wang, Z. L.; Zhong, H. X.; Wang, J.; Yan, J. M.; Zhang, X. B. Reactive Multifunctional Template-Induced Preparation of Fe-N-Doped Mesoporous Carbon Microspheres Towards Highly Efficient Electrocatalysts for Oxygen Reduction. *Adv. Mater.* **2016**, *28* (36), 7948.
10. Li, J. C.; Hou, P. X.; Shi, C.; Zhao, S. Y.; Tang, D. M.; Cheng, M.; Liu, C.; Cheng, H. M. Hierarchically Porous Fe-N-Doped Carbon Nanotubes as Efficient Electrocatalyst for Oxygen Reduction. *Carbon* **2016**, *109*, 632.
11. Choi, C. H.; Park, S. H.; Woo, S. I. N-Doped Carbon Prepared by Pyrolysis of Dicyandiamide with Various $\text{MeCl}_2 \cdot x\text{H}_2\text{O}$ (Me = Co, Fe, and Ni) Composites: Effect of Type and Amount of Metal Seed on Oxygen Reduction Reactions. *Appl. Catal. B* **2012**, *119-120*, 123.
12. Zhang, R.; He, S.; Lu, Y.; Chen, W. Fe, Co, N-Functionalized Carbon Nanotubes in situ Grown on 3D Porous N-Doped Carbon Foams as a Noble Metal-Free Catalyst for Oxygen Reduction. *J. Mater. Chem. A* **2015**, *3* (7), 3559.
13. Chen, M.; Wu, P.; Chen, L.; Yang, S.; Yu, L.; Ding, Y.; Zhu, N.; Shi, Z.; Liu, Z. Three-Dimensional Multi-Doped Porous Carbon/Graphene Derived from Sewage Sludge with Template-Assisted Fe-pillared Montmorillonite for Enhanced Oxygen Reduction Reaction. *Sci. Rep.* **2017**, *7* (1), 4158.
14. Li, A.; Mu, X.; Li, T.; Wen, H.; Li, W.; Li, Y.; Wang, B. Formation of Porous Cu Hydroxy Double Salts Nanoflowers Derived from Metal-Organic Frameworks with Efficient Peroxidase-Like Activity for Label-Free Detection of Glucose. *Nanoscale* **2018**, *10*, 11948.

15. Li, Y.; Kim, J.; Wang, J.; Liu, N. I.; Bando, Y.; Alshehri, A. A.; Yamauchi, Y.; Hou, C.-H.; Wu, K. C. W. High Performance Capacitive Deionization using Modified ZIF-8 Derived, N-doped Porous Carbon with Improved Conductivity. *Nanoscale* **2018**, 10, 14852.
16. Wang, Z.; Yan, T.; Chen, G.; Shi, L.; Zhang, D. High Salt Removal Capacity of Metal–Organic Gel Derived Porous Carbon for Capacitive Deionization. *ACS Sustain. Chem. Eng.* **2017**, 5 (12), 11637.
17. Li, L.; Xiang, S.; Cao, S.; Zhang, J.; Ouyang, G.; Chen, L.; Su, C.-Y. A Synthetic Route to Ultralight Hierarchically Micro/Mesoporous Al(III)-Carboxylate Metal–Organic Aerogels. *Nat. Commun.* **2013**, 4, 1774.
18. Cui, L.; Wu, J.; Ju, H. Nitrogen-Doped Porous Carbon Derived from Metal–Organic Gel for Electrochemical Analysis of Heavy-Metal Ion. *ACS Appl. Mater. Interfaces* **2014**, 6 (18), 16210.
19. Yang, D. H.; Kong, L.; Zhong, M.; Zhu, J.; Bu, X. H. Metal–Organic Gel-Derived Fe_xO_y/Nitrogen-Doped Carbon Films for Enhanced Lithium Storage. *Small* **2019**, 15 (3), 1804058.
20. Cao, Z.; Jiang, Z.; Li, Y.; Huang, C.; Li, Y. Metal–Organic Gel-Derived Multimetal Oxides as Effective Electrocatalysts for the Oxygen Evolution Reaction. *ChemSusChem* **2019**, 12 (11), 2480.
21. Wang, H.; Cheng, X.; Yin, F.; Chen, B.; Fan, T.; He, X. Metal–Organic Gel-Derived Fe-Fe₂O₃@Nitrogen-Doped-Carbon Nanoparticles Anchored on Nitrogen-Doped Carbon Nanotubes as a Highly Effective Catalyst for Oxygen Reduction Reaction. *Electrochim. Acta* **2017**, 232, 114-122.
22. Miao, Z.; Wang, X.; Tsai, M.-C.; Jin, Q.; Liang, J.; Ma, F.; Wang, T.; Zheng, S.; Hwang, B.-J.; Huang, Y.; Guo, S.; Li, Q. Atomically Dispersed Fe-N_x/C Electrocatalyst Boosts Oxygen Catalysis via a New Metal–Organic Polymer Supramolecule Strategy. *Adv. Energy Mater.* **2018**, 8 (24), 1801226.
23. Dragan, E. S. Design and Applications of Interpenetrating Polymer Network Hydrogels. A Review. *Chem. Eng. J.* **2014**, 243, 572.
24. Sperling, L. H. Interpenetrating Polymer Networks: An Overview. In *Interpenetrating Polymer Networks*; *Am. Chem. Soc.*: **1994**; Chapter 1, pp 3-38.
25. Haque, M. A.; Kurokawa, T.; Gong, J. P. Super Tough Double Network Hydrogels and Their Application as Biomaterials. *Polymer* **2012**, 53 (9), 1805.
26. Zhang, Y.; Liu, J.; Huang, L.; Wang, Z.; Wang, L. Design and Performance of a Sericin-Alginate Interpenetrating Network Hydrogel for Cell and Drug Delivery. *Sci. Rep.* **2015**, 5, 12374.

27. Saimani, S.; Kumar, A. Semi-IPN Asymmetric Membranes Based on Polyether Imide (ULTEM) and Polyethylene Glycol Diacrylate for Gaseous Separation. *J. Appl. Polym. Sci.* **2008**, 110 (6), 3606.
28. Banerjee, S.; Chaurasia, G.; Pal, D.; Ghosh, A. K.; Ghosh, A.; Kaity, S. Investigation on Crosslinking Density for Development of Novel Interpenetrating Polymer Network (IPN) Based Formulation. *J. Sci. Ind. Res.* **2010**, 69, 777.
29. Zhang, Q.; Fang, Z.; Cao, Y.; Du, H.; Wu, H.; Beuerman, R.; Chan-Park, M. B.; Duan, H.; Xu, R. High Refractive Index Inorganic-Organic Interpenetrating Polymer Network (IPN) Hydrogel Nanocomposite Toward Artificial Cornea Implants. *ACS Macro Lett.* **2012**, 1 (7), 876.
30. Hande, P. E.; Kamble, S.; Samui, A. B.; Kulkarni, P. S. Chitosan-Based Lead Ion-Imprinted Interpenetrating Polymer Network by Simultaneous Polymerization for Selective Extraction of Lead(II). *Ind. Eng. Chem. Res.* **2016**, 55 (12), 3668.
31. Fathi, A.; Lee, S.; Zhong, X.; Hon, N.; Valtchev, P.; Dehghani, F. Fabrication of Interpenetrating Polymer Network to Enhance the Biological Activity of Synthetic Hydrogels. *Polymer* **2013**, 54 (21), 5534.
32. Zhao, J.; Zhao, X.; Guo, B.; Ma, P. X. Multifunctional Interpenetrating Polymer Network Hydrogels Based on Methacrylated Alginate for the Delivery of Small Molecule Drugs and Sustained Release of Protein. *Biomacromolecules* **2014**, 15 (9), 3246.
33. Shen, C.; Li, Y.; Wang, H.; Meng, Q. Mechanically Strong Interpenetrating Network Hydrogels for Differential Cellular Adhesion. *RSC Adv.* **2017**, 7 (29), 18046.
34. Blatov, V. A.; Carlucci, L.; Ciani, G.; Proserpio, D. M. Interpenetrating Metal-Organic and Inorganic 3D Networks: A Computer-Aided Systematic Investigation. Part I. Analysis of the Cambridge Structural Database. *CrystEngComm* **2004**, 6 (65), 377.
35. Vendamme, R.; Onoue, S.-Y.; Nakao, A.; Kunitake, T. Robust Free-Standing Nanomembranes of Organic/Inorganic Interpenetrating Networks. *Nat. Mater.* **2006**, 5 (6), 4941.
36. Batten, S. R.; Harris, A. R.; Jensen, P.; Murray, K. S.; Ziebell, A. Copper (I) Dicyanamide Coordination Polymers: Ladders, Sheets, Layers, Diamond-Like Networks and Unusual Interpenetration. *J. Chem. Soc., Dalton Trans.* **2000**, (21), 3829.
37. Zhang, C.; Ding, S.; Li, J.; Xu, H.; Sun, L.; Wei, W.; Li, C.; Liu, J.; Qu, X.; Lu, Y. Interpenetration Network (IPN) Assisted Transcription of Polymeric Hollow

- Spheres: A General Approach Towards Composite Hollow Spheres. *Polymer* **2008**, 49 (13), 3098.
38. Reineke, T. M.; Eddaoudi, M.; Moler, D.; O'keeffe, M.; Yaghi, O. Large Free Volume in Maximally Interpenetrating Networks: The Role of Secondary Building Units Exemplified by $Tb_2(ADB)_3[(CH_3)_2SO]_{4.16}[(CH_3)_2SO]^1$. *J. Am. Chem. Soc.* **2000**, 122 (19), 4843.
39. Kondo, M.; Shimamura, M.; Noro, S.-i.; Minakoshi, S.; Asami, A.; Seki, K.; Kitagawa, S. Microporous Materials Constructed from the Interpenetrated Coordination Networks. Structures and Methane Adsorption Properties. *Chem. Mater.* **2000**, 12 (5), 1288.
40. Kim, E. H.; Jung, Y. G.; Jo, C. Y. Microstructure and Mechanical Properties of Heterogeneous Ceramic-Polymer Composite Using Interpenetrating Network. *J. Nanomater.* **2012**, 2012, 23.
41. Wang, L.; Gao, Z.; Chang, J.; Liu, X.; Wu, D.; Xu, F.; Guo, Y.; Jiang, K. Nitrogen-Doped Porous Carbons as Electrode Materials for High-Performance Supercapacitor and Dye-Sensitized Solar Cell. *ACS Appl. Mater. Interfaces* **2015**, 7 (36), 20234.
42. Tiwari, D.; Goel, C.; Bhunia, H.; Bajpai, P. K. Melamine-Formaldehyde Derived Porous Carbons for Adsorption of CO₂ Capture. *J. Environ. Manage.* **2017**, 197, 415.
43. Li, K.; Xie, X.; Zhang, W. D. Porous Graphitic Carbon Nitride Derived from Melamine-Ammonium Oxalate Stacking Sheets with Excellent Photocatalytic Hydrogen Evolution Activity. *ChemCatChem* **2016**, 8 (12), 2128.
44. Li, Y.; Zhou, W.; Wang, H.; Xie, L.; Liang, Y.; Wei, F.; Idrobo, J.-C.; Pennycook, S. J.; Dai, H. An Oxygen Reduction Electrocatalyst Based on Carbon Nanotube-Graphene Complexes. *Nat. Nanotechnol.* **2012**, 7 (6), 394.
45. Chen, M.; Wu, P.; Chen, L.; Yang, S.; Yu, L.; Ding, Y.; Zhu, N.; Shi, Z.; Liu, Z. Three-Dimensional Multi-Doped Porous Carbon/Graphene Derived from Sewage Sludge with Template-Assisted Fe-pillared Montmorillonite for Enhanced Oxygen Reduction Reaction. *Sci. Rep.* **2017**, 7, 4158.
46. Hu, E.; Yu, X. Y.; Chen, F.; Wu, Y.; Hu, Y.; Lou, X. W. Graphene Layers-Wrapped Fe/Fe₅C₂ Nanoparticles Supported on N-doped Graphene Nanosheets for Highly Efficient Oxygen Reduction. *Adv. Energy Mater.* **2018**, 8 (9), 1702476.
47. Li, X.; Fang, Y.; Zhao, S.; Wu, J.; Li, F.; Tian, M.; Long, X.; Jin, J.; Ma, J. Nitrogen-Doped Mesoporous Carbon Nanosheet/Carbon Nanotube Hybrids as Metal-Free Bi-Functional Electrocatalysts for Water Oxidation and Oxygen Reduction. *J. Mater. Chem. A* **2016**, 4 (34), 13133.

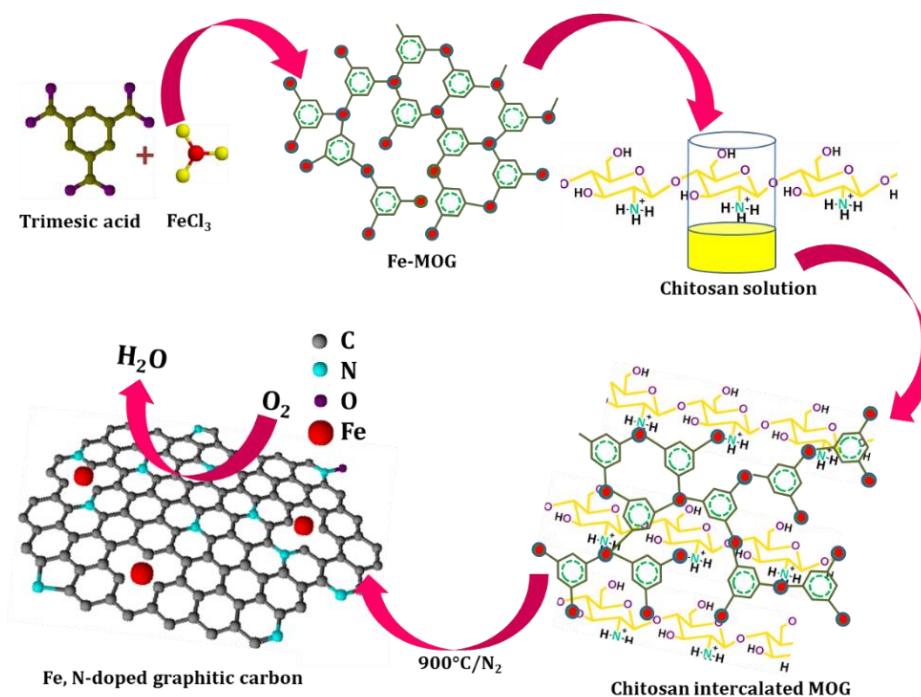
48. Ren, G.; Lu, X.; Li, Y.; Zhu, Y.; Dai, L.; Jiang, L. Porous Core-Shell Fe₃C Embedded N-Doped Carbon Nanofibers as an Effective Electrocatalysts for Oxygen Reduction Reaction. *ACS Appl. Mater. Interfaces* **2016**, 8 (6), 4118.
49. Zhou, T.; Zhou, Y.; Ma, R.; Liu, Q.; Zhu, Y.; Wang, J. Achieving Excellent Activity and Stability for Oxygen Reduction Electrocatalysis by Hollow Mesoporous Iron-Nitrogen-Doped Graphitic Carbon Spheres. *J. Mater. Chem. A* **2017**, 5 (24), 12243.
50. Qiao, X.; Jin, J.; Fan, H.; Li, Y.; Liao, S. In situ Growth of Cobalt Sulfide Hollow Nanospheres Embedded in Nitrogen and Sulfur Co-Doped Graphene Nanoholes as a Highly Active Electrocatalyst for Oxygen Reduction and Evolution. *J. Mater. Chem. A* **2017**, 5 (24), 12354.
51. Chaudhari, N. K.; Song, M. Y.; Yu, J.-S. Heteroatom-Doped Highly Porous Carbon from Human Urine. *Sci. Rep.* **2014**, 4, 5221.
52. Kashyap, V.; Singh, S. K.; Kurungot, S. Cobalt Ferrite Bearing Nitrogen-Doped Reduced Graphene Oxide Layers Spatially Separated with Microporous Carbon as Efficient Oxygen Reduction Electrocatalyst. *ACS Appl. Mater. Interfaces* **2016**, 8 (32), 20730.
53. Wang, B.; Xu, L.; Liu, G.; Zhang, P.; Zhu, W.; Xia, J.; Li, H. Biomass Willow Catkins-Derived Co₃O₄/N-Doped Hollow Hierarchical Porous Carbon Microtubes as the Effective Tri-Functional Electrocatalyst. *J. Mater. Chem. A* **2017**, 5, 20170.
54. Ni, Y.; Yao, L.; Wang, Y.; Liu, B.; Cao, M.; Hu, C. Construction of Hierarchically Porous Graphitized Carbon-Supported NiFe Layered Double Hydroxides with a Core-Shell Structure as an Enhanced Electrocatalyst for the Oxygen Evolution Reaction. *Nanoscale* **2017**, 9 (32), 11596.
55. Zhu, J.; Zhou, H.; Zhang, C.; Zhang, J.; Mu, S. Dual Active Nitrogen Doped Hierarchical Porous Hollow Carbon Nanospheres as an Oxygen Reduction Electrocatalyst for Zinc-Air Batteries. *Nanoscale* **2017**, 9, 13257.
56. Thomas, M.; Illathvalappil, R.; Kurungot, S.; Nair, B. N.; Mohamed, A. A. P.; Anilkumar, G. M.; Yamaguchi, T.; Hareesh, U. S. Graphene Oxide Sheathed ZIF-8 Microcrystals: Engineered Precursors of Nitrogen-Doped Porous Carbon for Efficient Oxygen Reduction Reaction (ORR) Electrocatalysis. *ACS Appl. Mater. Interfaces* **2016**, 8 (43), 29373.
57. Thanh, T. D.; Chuong, N. D.; Balamurugan, J.; Van Hien, H.; Kim, N. H.; Lee, J. H. Porous Hollow-Structured LaNiO₃ Stabilized N, S-Codoped Graphene as an Active Electrocatalyst for Oxygen Reduction Reaction. *Small* **2017**, 13, 1701884.

58. Illathvalappil, R.; Dhavale, V. M.; Bhang, S. N.; Kurungot, S. Nitrogen-Doped Graphene Anchored with Mixed Growth Patterns of CuPt Alloy Nanoparticles as a Highly Efficient and Durable Electrocatalyst for the Oxygen Reduction Reaction in an Alkaline Medium. *Nanoscale* **2017**, 9 (26), 9009.
59. Jiang, W. J.; Gu, L.; Li, L.; Zhang, Y.; Zhang, X.; Zhang, L. J.; Wang, J. Q.; Hu, J. S.; Wei, Z.; Wan, L. J. Understanding the High Activity of Fe-N-C Electrocatalysts in Oxygen Reduction: Fe/Fe₃C Nanoparticles Boost the Activity of Fe-N_x. *J. Am. Chem. Soc.* **2016**, 138 (10), 3570.
60. Zhang, C.; Liu, J.; Ye, Y.; Aslam, Z.; Brydson, R.; Liang, C. Fe-N-Doped Mesoporous Carbon with Dual Active Sites Loaded on Reduced Graphene Oxides for Efficient Oxygen Reduction Catalysts. *ACS Appl. Mater. Interfaces* **2018**, 10 (3), 2423.
61. Zhu, C.; Fu, S.; Song, J.; Shi, Q.; Su, D.; Engelhard, M. H.; Li, X.; Xiao, D.; Li, D.; Estevez, L. Self-Assembled Fe-N-Doped Carbon Nanotube Aerogels with Single-Atom Catalyst Feature as High-Efficiency Oxygen Reduction Electrocatalysts. *Small* **2017**, 13 (15), 1603407.
62. Li, O. L.; Chiba, S.; Wada, Y.; Panomsuwan, G.; Ishizaki, T. Synthesis of Graphitic-N And Amino-N in Nitrogen-Doped Carbon via a Solution Plasma Process and Exploration of Their Synergic Effect for Advanced Oxygen Reduction Reaction. *J. Mater. Chem. A* **2017**, 5 (5), 2073.
63. Li, X. F.; Lian, K. Y.; Liu, L.; Wu, Y.; Qiu, Q.; Jiang, J.; Deng, M.; Luo, Y. Unraveling the Formation Mechanism of Graphitic Nitrogen-Doping in Thermally Treated Graphene with Ammonia. *Sci. Rep.* **2016**, 6, 23495.
64. Huang, X.; Yang, Z.; Dong, B.; Wang, Y.; Tang, T.; Hou, Y. In situ Fe₂N@N-Doped Porous Carbon Hybrids as Superior Catalysts for Oxygen Reduction Reaction. *Nanoscale* **2017**, 9 (24), 8102.
65. Zhou, L.; Yang, C.; Wen, J.; Fu, P.; Zhang, Y.; Sun, J.; Wang, H.; Yuan, Y. Soft-Template Assisted Synthesis of Fe/N-Doped Hollow Carbon Nanospheres as Advanced Electrocatalysts for the Oxygen Reduction Reaction in Microbial Fuel Cells. *J. Mater. Chem. A* **2017**, 5 (36), 19343.
66. Shijina, K.; Illathvalappil, R.; Kurungot, S.; Nair, B. N.; Mohamed, A. P.; Yamaguchi, T.; Anilkumar, G. M.; Hareesh, U. S.; Sailaja, G. S. Chitosan Intercalated Metal Organic Gel as a Green Precursor of Fe Entrenched and Fe Distributed N-Doped Mesoporous Graphitic Carbon for Oxygen Reduction Reaction. *ChemistrySelect* **2017**, 2 (28), 8762.

Chapter 3

Chitosan Intercalated Metal Organic Gel as a Green Precursor of Fe, N co-doped Mesoporous Graphitic Carbon for Oxygen Reduction Reaction

Abstract



A metal-organic gel intercalated with chitosan is used as a precursor for the synthesis of intrinsic N-doped Fe distributed mesoporous graphitic carbon structures for application as oxygen reduction reaction (ORR) catalyst in alkaline medium. Modulation of the synthetic protocol as a function of reaction kinetics and gelation time improved the microstructure, surface area and Fe distribution of the graphitic structures (Fe-MCS-NCM). A high specific surface area value of 565 m²g⁻¹ and a higher percentage of graphitic N was apparent from the XPS data validated that the modified synthetic method favored creation of more graphitic N sites contributing to better ORR performance. Fe-MCS-NCM catalyst exhibited comparable electrocatalytic activity with that of the commercially available Pt/C via an efficient four-electron-dominant ORR pathway with a positive onset potential value of 0.925 V vs RHE. Good durability after 5000 cycles further confirmed the prospects of MOG-chitosan and the feasibility to be used as a potential catalyst for ORR.

3.1 Introduction

In the previous chapter, the pore characteristics, N-doping, and conductivity of the Fe, N-doped carbon derived from metal organic gel-melamine formaldehyde was discussed. In this chapter an earth abundant natural polymer chitosan was chosen as the nitrogen source instead of melamine formaldehyde since, it contains high nitrogen content (~7 wt.%) due to the presence of nitrogen containing functional groups (amine and acetamide) in its structure.¹ These structural functional groups are responsible for the nontoxic, biocompatible, and biodegradable properties of chitosan making it as a green precursor for N-doped carbon materials.²

The doped nitrogen provides basic sites on porous carbon surface with increased polarity, imparting better adsorption and electrochemical capabilities, enabling them to be employed for separation and catalysis.³ When a combination of metal species is introduced as active additives in porous carbon structures, enhancement of ORR activity is effected both in terms of activity and stability. This is primarily accomplished due to the generation of higher number of active sites, from MN_xC_y clusters (M= Fe or Co) during pyrolysis, that eventually enhances adsorption.^{4,5} Fe plays a vital role in creating active site for ORR⁶ while Fe-N combination (Fe-N-C) amplifies the ORR activity theoretically due to the interactions between the Fe and N species on the carbon substrates.⁷⁻⁹ Besides Fe doped carbon, N-doped Co_3O_4 nanowires¹⁰ and Co_3O_4 nanoparticle embedded N rich carbon¹¹ are also reported as good ORR electrocatalyst. Even though N dopant could improve the conductivity and O_2 adsorption capability, excess N doping would lead to deterioration of the reaction kinetics because these excess N atom and defects are capable of functioning as scattering centers that hinder the electron or hole transport.¹¹

Conventional doping procedures relying upon post-synthesis procedures through dopant sources encounter significant drawbacks due to difficulties in controlling doping level and reproducibility.¹² Intrinsic doping approaches for synthesizing advanced functional porous carbon structures employ precursor sources, that contain N and other preferred heteroatoms as part of the molecular structure to eliminate the challenges associated with the post-doping procedures.¹³ Novel synthesis routes utilizing less expensive precursors are actively pursued in the quest for Pt-alternative catalysts with similar or higher activity compared to that of Pt/C for ORR.

Porous carbons derived from metal organic frameworks (MOFs) and zeolitic imidazolate frameworks (ZIFs) are vital components of renewable energy conversion technologies for application as electrodes in energy storage devices, electrocatalysis,^{14,15} photocatalytic water splitting, heterogeneous catalysis, and biofuels.^{16,17} While there are several approaches for the synthesis, the template approach acquired significance as an efficient processing route to produce porous carbon materials with tunable structures. Pore textures with regular and controlled morphology in the nano and micron-scale could be realized through appropriate precursor formulations.^{18,19} Recent reports demonstrate the excellent potential of MOFs; 3D network structures having high surface area, controllable structures and abundant metal species^{20,21} as interesting templates/precursors for constructing porous carbons within their networks.^{22,23} However, it is also envisaged that many of these building-up processes are expensive and time-consuming, besides the involvement of several toxic and teratogenic solvents.¹⁸

Metal organic gels (MOGs), the extended versions of MOF structures find great potential in catalysis, gas storage and separation due to their abundant Lewis acid sites and porous gel structures.^{24,25} In contrast to MOFs, MOGs are amorphous, with a less elucidated structure, but they are more environmentally benign and their modes of synthesis are indigenously less expensive and much easier than MOFs.²⁶ Hence, MOG based carbon structures derived from less expensive carbon-precursors would be a highly promising approach for realizing doping of relevant elements.

Chitosan, the N rich (6.89%) naturally abundant polysaccharide has attracted much interest as metal binding/extraction system owing to its inherent chelating properties.²⁷ Chitosan is a derivative compound of chitin obtained by partial deacetylation (**Figure 3.1**).²⁸ Chitin and chitosan are a family of linear polysaccharides composed of varying amounts of (β 1 \rightarrow 4) linked residues of N-acetyl-2-amino-2-deoxy-D-glucose (glucosamine, GlcN) and 2-amino-2-deoxy-D-glucose (N-acetyl-glucosamine, GlcNAc). Chitin is a very abundant biopolymer found in invertebrates like insects, shrimps, crabs, algae and in the cell wall of fungi. In contrast to chitin, chitosan is soluble in aqueous acidic media via primary amine protonation. Being soluble in aqueous acidic solutions, chitosan is largely used in different applications as solutions, gels, or films and fibers.²⁹ In addition, its N enriched

structure was further explored as a resource for the development of N-doped carbon with improved conductivity and capacitance for supercapacitor electrodes.^{30,31}

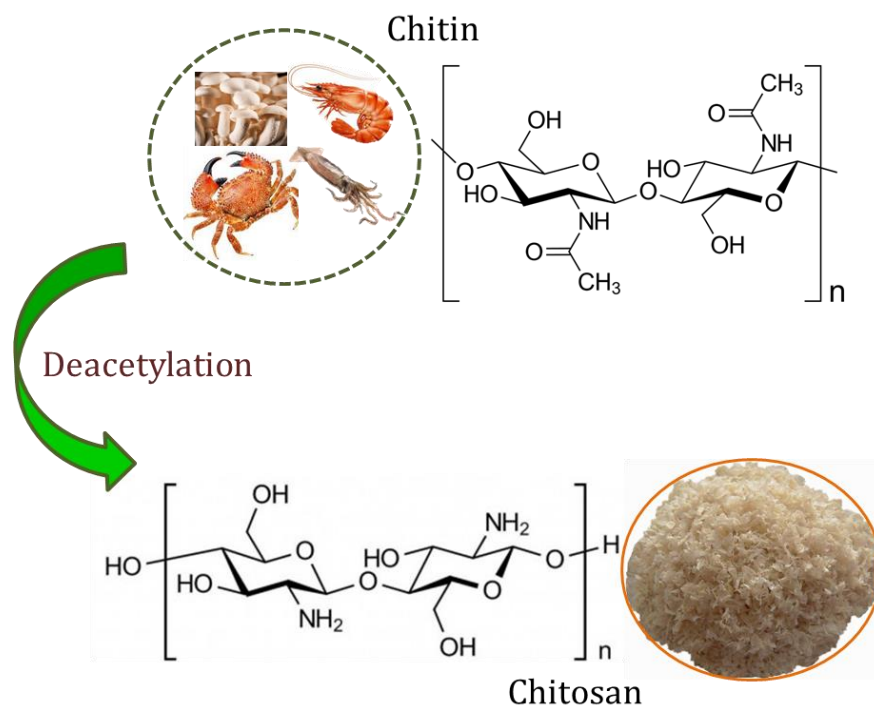


Figure 3.1 The conversion of chitin to chitosan by deacetylation.

Recent attempts to understand ORR catalytic activity of chitosan based systems mainly employed simple mixing of other nitrogen rich sources such as urea and melamine into chitosan followed by pyrolysis. However, ORR performance of the pyrolyzed chitosan-urea³² and N-doped carbon from chitosan-melamine³³ systems were found to be not satisfactory enough to be proposed as a good catalyst. Hydrothermal carbonization of chitosan alone also yielded graphitic carbon nanoparticulate ORR electrocatalyst.³⁴ But the synthetic procedure involved tedious hydrothermal treatment at 180 °C for 12 h before pyrolysis. An alternate approach employed incorporation of transition metal salts like cobalt into chitosan followed by direct pyrolysis.³⁵ Fe₃C nanocrystals doped graphitic carbon nanocomposites, reported by Wu *et al.*, exhibited good ORR activity in alkaline media owing to the synergistic role of Fe₃C nanocrystals.³⁶ Even though the low-cost and earth-abundant biomass was used, the use of additional processing chemicals and the 24 h UV irradiation time limited its wide spread application. **Table 3.1** summarizes the comparison of ORR performance of chitosan derived catalysts.

Table 3.1 Comparison of the ORR performance of chitosan derived catalysts.

Catalyst	Precursors	Preparation method	ORR performance
NCN	chitosan/urea	Pyrolysis	$E_{\text{onset}} = -0.03$ V vs Ag/AgCl, $n = 3.67$ ³²
CH-mel	chitosan, melamine	Pyrolysis	$E_{\text{onset}} = 0.761$ V vs RHE, $E_{1/2} = 0.595$ ³³
N-GCNP	chitosan	Hydrothermal followed by pyrolysis	$E_{\text{onset}} = -0.07$ V vs Ag/AgCl, $n = 3.9$ ³⁴
CoNC	chitosan and Co salt	Pyrolysis	$E_{\text{onset}} = -0.105$ V vs vs Ag/AgCl, $n = 3.98$ ³⁵
Fe ₃ C@NGC	Chitosan, Fe salt	24 h UV irradiation of chitosan, pyrolysis	$E_{\text{onset}} = -0.09$ V vs Ag/AgCl, $n = 3.6$ ³⁶

A novel, less expensive, green precursor system based on MOG intercalated with chitosan is thus designed to arrive at N-doped Fe entrenched (Fe-MCS-NC) and Fe distributed mesoporous graphitic carbon structures (Fe-MCS-NCM) with high specific surface area and good ORR activity. The functional properties of the earth abundant polysaccharide are better explored in the present study and the simple green system based on MOG-chitosan is reported for the first time to yield a unique heterogeneous and mesoporous product that favorably contributes for improved ORR activity.

3.2 Experimental

3.2.1 Materials

Chitosan (medium molecular weight, 190,000-310,000 Da.) and benzene-1,3,5-tricarboxylic acid (H₃BTC or trimesic acid) were purchased from Sigma-Aldrich. Ferric chloride hexahydrate (FeCl₃·6H₂O) and 100 % glacial acetic acid (CH₃COOH) were purchased from Merck India Ltd. All the reagents were used as received for the synthesis without any further purification.

3.2.2 Synthesis of Chitosan-Fe Complex Mediated MOG (Fe-MCS)

100 mL of 1 wt. % chitosan solution prepared in acetic acid was reacted with 0.1 M $\text{FeCl}_3 \cdot 6\text{H}_2\text{O}$ solution under mechanical stirring for 1 h to form chitosan Fe complex. To this, 0.03 M alcoholic solution of trimesic acid was added and the reaction was continued for another 4 h at room temperature to complete complexation and gelation. The gel microparticles formed were centrifuged, washed with DI water several times to remove excess reagents and subsequently lyophilized to obtain Fe-MCS powder sample.

3.2.3 Synthesis of Chitosan Intercalated Fe-MOG (Fe-MCS-M)

$\text{FeCl}_3 \cdot 6\text{H}_2\text{O}$ and trimesic acid were reacted in the molar ratio of 3:1 and kept undisturbed for 30 min. Fe-MOG thus formed was mixed with 100 mL of 1 wt. % chitosan solution under stirring for 15 min to form chitosan intercalated Fe-MOG network. The obtained gel was subsequently washed with DI water several times for the removal of excess reagents present and then lyophilized to remove any water molecule trapped inside the pores to obtain Fe-MCS-M sample.

3.2.4 Synthesis of Porous Carbon

Carbonization of the lyophilized samples was performed at 900 °C for 3h (at the rate of 5 °C/min) under N_2 atmosphere. The products obtained were washed with 1 M H_2SO_4 solution to remove any uncoordinated Fe, followed by multiple rinsing with DI water and drying at 50 °C. After carbonization, the samples derived from chitosan-Fe complex mediated MOG and chitosan intercalated Fe-MOG were denoted as Fe-MCS-NC and Fe-MCS-NCM respectively.

3.2.5 Structural Characterization

X-ray diffraction patterns were recorded in the 2θ range of 10-60° using the $\text{Cu K}\alpha$ ($\lambda_{\text{Cu}}=1.542 \text{ \AA}$) radiation using PW1710 Philips (The Netherlands) instrument. Raman spectroscopy measurements were performed using a Confocal Raman Microscope Alpha 300 R WITec Germany with 633 laser. The specific surface area and porosity of the samples were measured using a Micromeritics (Tristar 11, USA) surface area analyzer using nitrogen adsorption at 77 K after degassing the powders in flowing N_2 at 200 °C for 2 h. Thermogravimetric analysis (Perkin Elmer STA 6000, USA) was done

at a heating rate of 10 °C/min up to 1000 °C in N₂ atmosphere. The morphology and microstructure of the samples were obtained from a Scanning Electron Microscope (SEM, Carl Zeiss, Germany) after sputter coating the samples with gold under argon atmosphere. Transmission Electron Micrographs (TEM) of the samples were recorded on an FEI (Tecnai 30 G2 S-TWIN, The Netherlands) microscope operating at an accelerating voltage of 300 kV. X-ray Photoelectron Spectroscopy (XPS) analysis was performed to analyze the elements present and their chemical state in the samples. The XPS spectra were recorded by a scanning X-ray Microprobe (ULAC-PHI, Inc. PHI-4700 V, USA) with monochromated Al-K α X-ray source operating at 14 kV and 220 W. The bulk Fe content in the samples was obtained by ICP-MS analysis (Thermo Electron IRIS Intrepid II XSP DUO).

3.2.6 Electrochemical Characterization

All the electrochemical measurements were carried out in a Biologic Electrochemical Workstation (SP-300) using a three-electrode setup. An aqueous solution of 0.1 M KOH was used as the electrolyte for the electrochemical measurements. Catalyst coated glassy carbon and Hg/HgO were used as the working electrode and reference electrode respectively, whereas a graphite rod was used as the counter electrode. Catalyst slurry was prepared by ultrasonically mixing 5 mg of the catalyst in 1 mL of isopropyl alcohol-DI water mixture (1:3), followed by 40 μ L of 5 wt. % nafion solution for 60 min. Subsequently, 10 μ L of the prepared slurry was dropped on the surface of the glassy carbon working electrode (0.196 cm²) with the help of a microsyringe. The electrode thus obtained was dried under an IR lamp for 3 h. For the comparison purpose, the electrochemical analysis was also carried out using commercial 40 wt. % Pt/C catalyst (Johnson Matthey) with the same catalyst loading. The number of electrons transferred during ORR was measured using a Rotating Ring Disc Electrode (RRDE, 0.2826 cm², Pine Instruments) in O₂ saturated 0.1 M KOH solution with a glassy carbon disc (0.2826 cm²) having a platinum ring as the working electrode, Hg/HgO as the reference electrode and graphite rod as the counter electrode. The accelerated durability test (ADT) was carried out to check the durability of the catalyst in O₂ saturated 0.1 M KOH solution by running the CV for 5000 cycles at a scan rate of 100 mV s⁻¹ in the potential window of 0.57 to 0.97 V. The LSVs before and

after ADT were analyzed. All potentials were converted into RHE by calibrating Hg/HgO in H₂ saturated 0.1 M KOH solution.

3.3 Results and Discussion

Synthesis of both Fe-MCS-NC and Fe-MCS-NCM involves two steps. In Fe-MCS-NC, Fe(III) ion initially coordinates with cationic amino groups of chitosan forming Fe-chitosan complex. However, it is plausible for Fe(III) to form hexacoordinated structure. In the second stage, reaction proceeds with trimesic acid leading to gelation. In Fe-MCS-NCM, chitosan is intercalated during the process of Fe-MOG gelation. Chitosan gets entrapped in the three dimensional network of Fe-MOG which further provide stronger electrostatic interaction of cationic N sites of chitosan with Fe(III). An additional reactive cross-linking is thus established to the intrinsic Fe-MOG 3D cross-linked structure facilitating stronger binding with Fe in Fe-MCS-NCM. In both cases pyrolysis procedure remains the same. In both the cases, Fe acts as a catalyst for the graphitization of the pyrolyzed product. The schematic illustration of formation Fe, N co-doped carbon structure is shown in **Figure 3.2**.

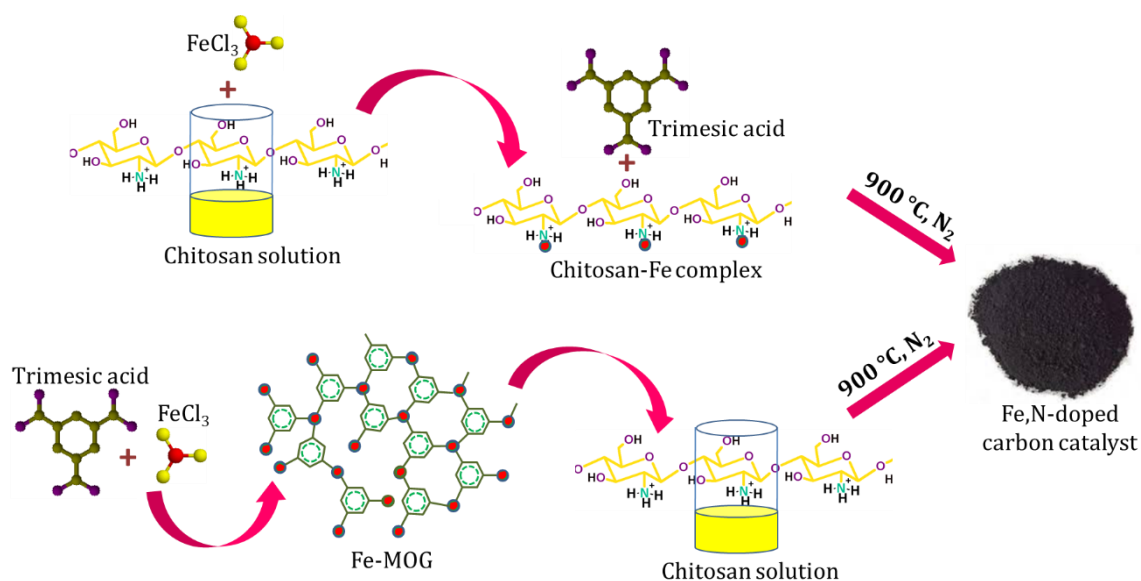


Figure 3.2 Schematic illustration of the formation of Fe, N co-doped carbon.

3.3.1 Thermogravimetric Analysis

The weight changes of the precursors during the pyrolysis were recorded using thermogravimetric analysis under N₂ atmosphere (**Figure 3.3**). The decomposition profile supports the nature of the gel structure formation. The stronger Fe-MCS-M gel, decomposed gradually in a near single step profile extending from 200 to 900 °C. On the contrary, the weaker Fe-MCS gel was pyrolyzed in three stages corresponding to the temperature regions of 175-420, 420-520 and 550-620 °C. Carbonization was more or less completed by 900 °C in both the samples. After the heat treatment at 1000 °C, both the samples retained 24.5 wt. % of residual weight.

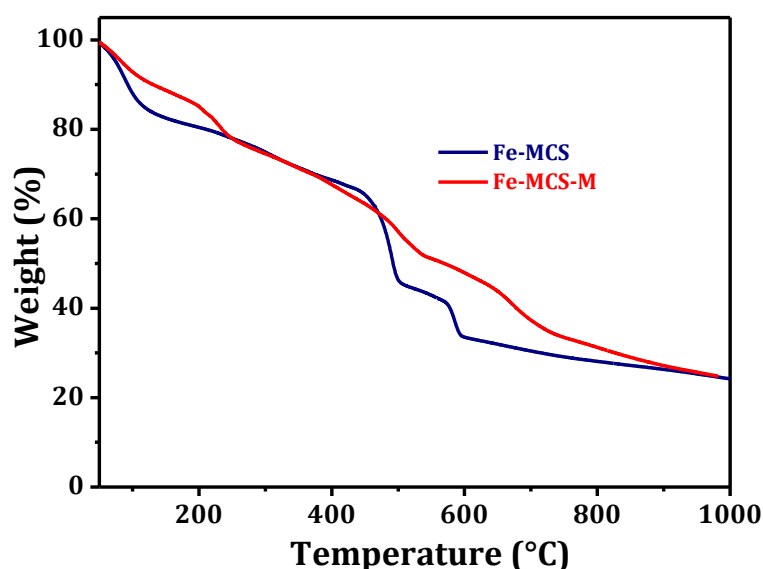


Figure 3.3 TGA patterns of Fe-MCS and Fe-MCS-M in nitrogen atmosphere.

3.3.2 Morphology and Microstructure Analysis

The overall microstructural configuration of Fe-MCS-NC and Fe-MCS-NCM elucidated from scanning electron microscopy (**Figure 3.4**) indicated porous morphology with homogeneously distributed micron sized spherical pores for Fe-MCS-NC (**Figure 3.4a & b**). The presence of chitosan should have played a vital role in providing the lucid porous spherical microglobular structures. However, the morphology was interestingly transformed to a more finely distributed mesoporous structure for Fe-MCS-NCM (**Figure 3.4c & d**).

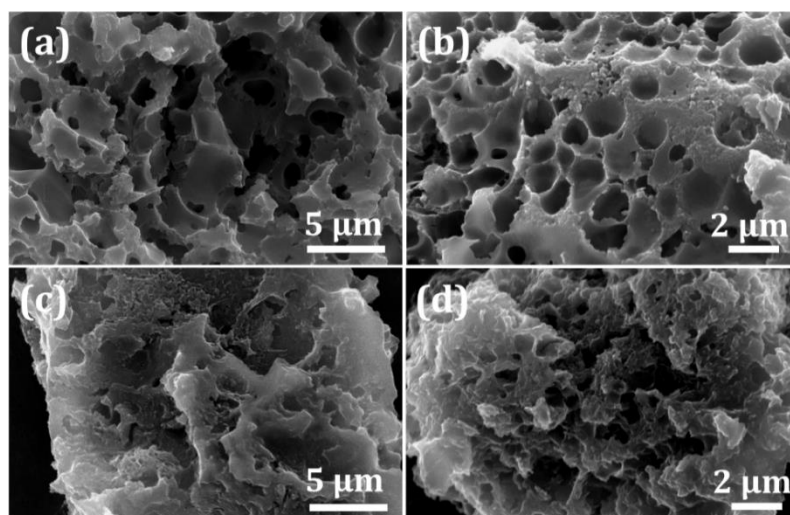


Figure 3.4 SEM images of (a, b) Fe-MCS-NC and (c, d) Fe-MCS-NCM.

The TEM images presented in **Figure 3.5** provide detailed features of Fe-MCS-NC (**Figure 3.5a-c**). A morphologically distinct configuration of N-doped carbon cages that homogeneously encircle the Fe nanoparticles are seen in these samples (**Figure 3.5c**). During pyrolysis, structural distortion of the carbon framework occurs generating Fe entrenched carbon nanocapsules. The carbon cages are identified with graphite-like layers. From **Figure 3.5c**, it can be said that the typical size of the Fe nanoparticle is 15-20 nm with carbon shell thickness of ~5 nm. There are reports confirming that the inner Fe₃C with outside C form synergetic active sites to enhance ORR activity.³⁷ Fe-MCS-NCM resembled graphitic sheet-like structure (**Figure 3.5d-f**) with amplified surface area. It could be envisaged that chitosan intercalation and modulated gelation resulted a rigid MOG network formation. Good graphitic sheetlike structure with uniformly distributed Fe nanoparticles was obtained without any structural alteration during pyrolysis. It is presumed that these Fe nanoparticles have a key role in the formation of graphitic structure in Fe-MCS-NCM.

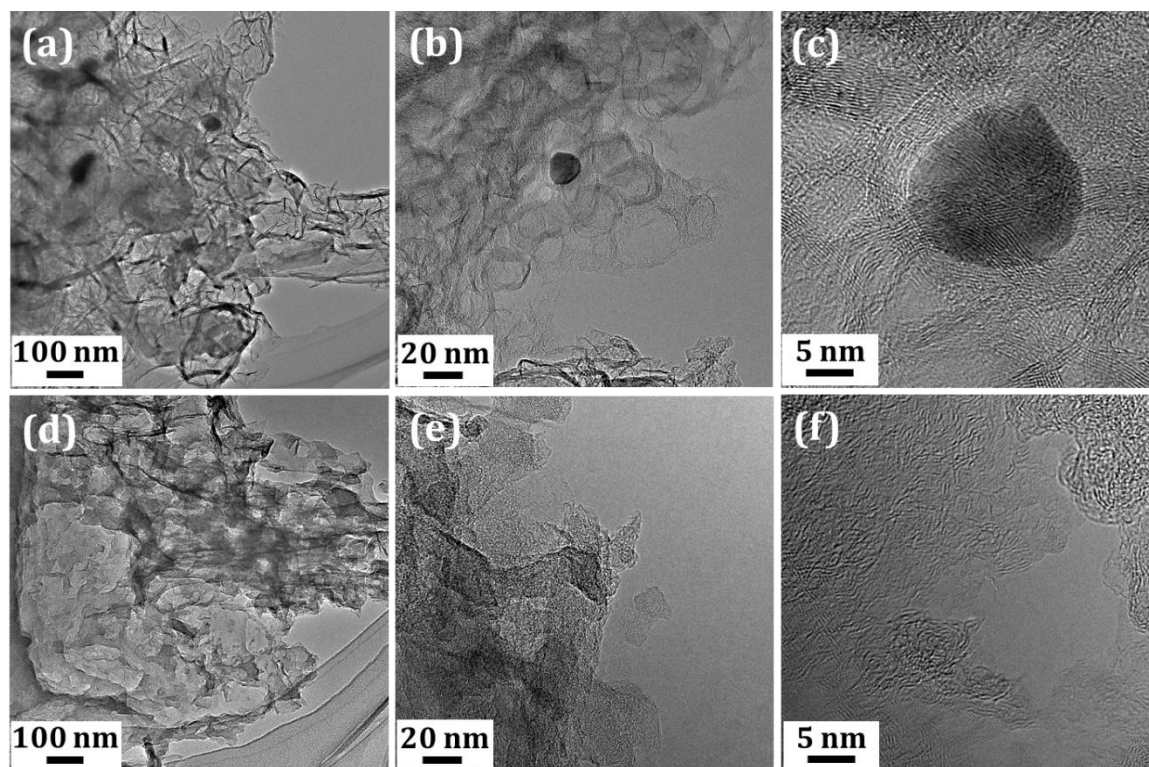


Figure 3.5 TEM images of (a-c) Fe-MCS-NC and (d-f) Fe-MCS-NCM.

The elemental mapping of Fe-MCS-NC (**Figure 3.6a**) and Fe-MCS-NCM (**Figure 3.6b**) evidenced the presence of C, N, O and Fe in both the samples. While N is homogeneously distributed within the carbon matrix, Fe signals were less abundant but better distributed in Fe-MCS-NC. Elemental mapping further demonstrated the presence of O and corroborated that Fe nanoparticles presumably formed bonds with adjacent C or N. Results shown in **Figure 3.6** indicate that Fe-MCS-NCM has smaller sized Fe nanoparticles with coherent distribution (**Figure 3.6b**) and is therefore expected to provide the active sites for ORR.

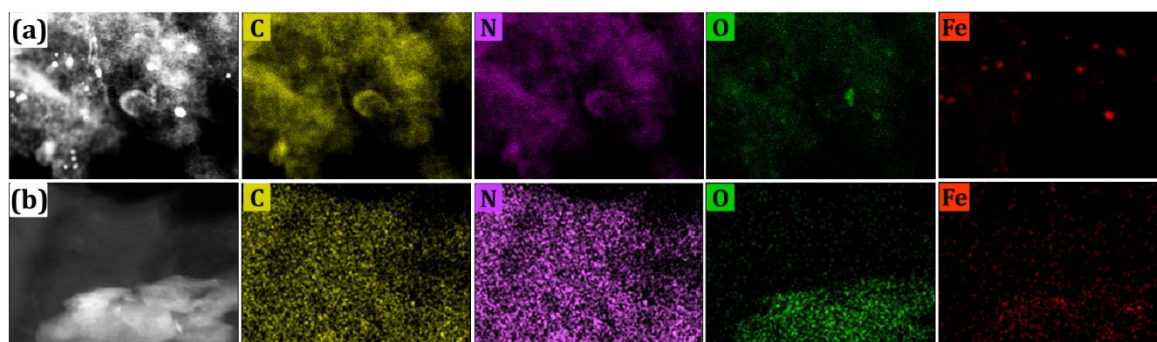


Figure 3.6 C-K α , N-K α , O-K α , Fe-K α map of (a) Fe-MCS-NC and (b) Fe-MCS-NCM.

3.3.3 Surface Area Analysis

N₂ adsorption isotherms of the samples Fe-MCS-NC_{unwashed} and Fe-MCS-NCM_{unwashed} (before acid washing) shown in **Figure 3.7a**, clearly established the differences in porous structure of the two samples. Fe-MCS-NCM_{unwashed} sample showed larger N₂ adsorption values in the low P/P₀ (corresponding to micropores) as well as in the high P/P₀ (mesopores and larger ones) regions of the isotherms. The specific surface area values (BET) for Fe-MCS-NC_{unwashed} and Fe-MCS-NCM_{unwashed} were calculated as 93 m² g⁻¹ and 247 m² g⁻¹ respectively from the N₂ adsorption isotherms. The rapid decomposition of a weak gel structure in Fe-MCS resulted in a carbon of relatively lower surface area while the stronger gel network of Fe-MCS-M produced carbon of higher surface area.

Fe-MCS-NCM sample showed larger N₂ adsorption values in the low (corresponding to micropores) as well as in the high P/P₀ (mesopores and larger ones) regions of the isotherms (**Figure 3.7b**). The specific surface area (BET) values for Fe-MCS-NC and Fe-MCS-NCM 381 m² g⁻¹ were and 565 m² g⁻¹ respectively, and were more than two-fold higher compared to the corresponding unwashed sample. The pore structure formation in these materials can be explained based on carbonization as well as on the removal of unbound Fe trapped inside the carbon network by acid leaching. In Fe-MCS-NC, the weaker interaction of chitosan and Fe led to the formation of an intangible complex with a weak gel structure. The decomposition of this poorly formed network yielded porous carbon with a fairly low surface area. Moreover, the caged structure also influenced the surface area compared to the sheet-like structure. In Fe-MCS-NCM, the presence of stronger and extensive gel network formed due to the better interaction with the chitosan matrix, presumably helped in significant increase in surface area compared to the Fe-MCS-NC sample.

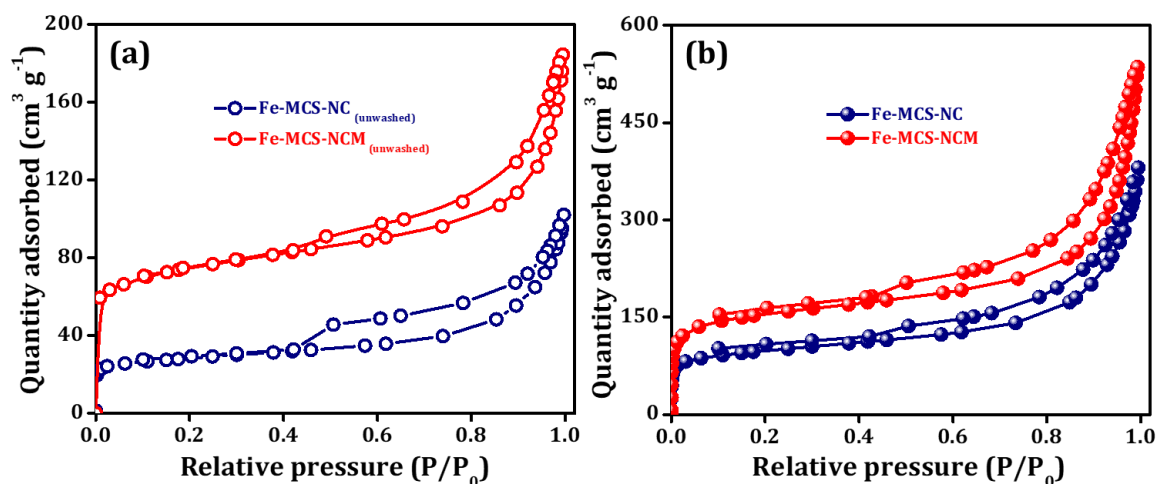


Figure 3.7 Nitrogen adsorption-desorption isotherms of (a) Fe-MCS-NC_{unwashed} & Fe-MCS-NCM_{unwashed} and (b) Fe-MCS-NC & Fe-MCS-NCM.

The pore size analysis results shown in **Figure 3.8a & b** quantitatively established the variation of porosity (cumulative pore volume) and pore size of the two samples. The cumulative pore volume of Fe-MCS-NCM was $0.7 \text{ cm}^3 \text{ g}^{-1}$ compared to the value of $0.51 \text{ cm}^3 \text{ g}^{-1}$ measured for the Fe-MCS-NC. In addition, the pore size values clearly established that Fe-MCS-NCM has a significant pore volume in the mesoporous range ($< 50 \text{ nm}$ pore size). Further, the micropore volume (t-plot) of Fe-MCS-NCM ($0.075 \text{ cm}^3 \text{ g}^{-1}$) was found larger than the value of $0.07 \text{ cm}^3 \text{ g}^{-1}$ measured for Fe-MCS-NC. In other words, chitosan intercalation adapted for Fe-MCS-NCM helped to realize porous materials with larger microporosity as well as mesoporosity. This micro/mesopore architecture is expected to impart better catalytic activity by virtue of its higher surface area as well as better interaction between the diffusing molecules and catalyst surface.

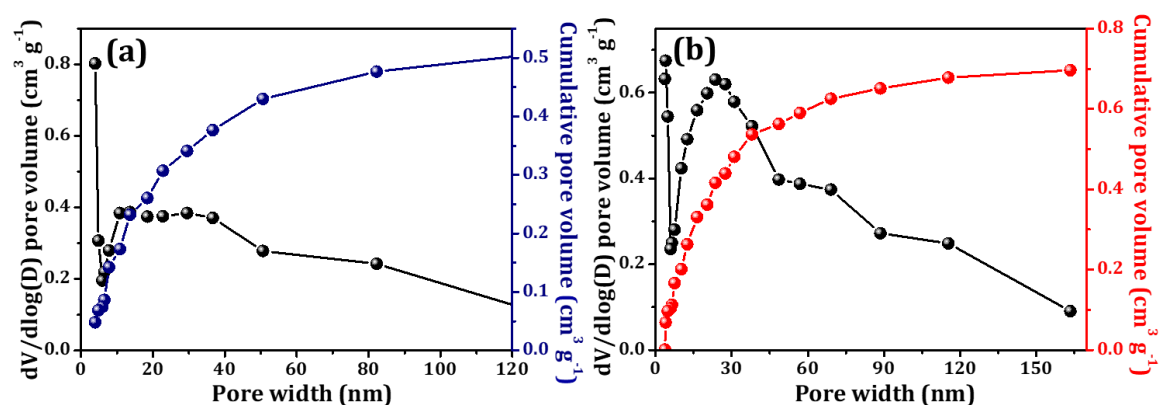


Figure 3.8 BJH pore volume and pore size distribution of (a) Fe-MCS-NC and (b) Fe-MCS-NCM.

3.3.4 Phase Analysis

XRD analysis imparted insights into the phase characterization of the porous carbon structures (**Figure 3.9**). Fe-MCS-NC and Fe-MCS-NCM samples showed distinctive peak at two theta value of 49.2° corresponding to the (024) plane of $\alpha\text{-Fe}_2\text{O}_3$ (JCPDS number 79-1741). However, (122) plane of Fe_3C also has a peak at the same two theta value (JCPDS number 06-0688). It is also possible that these two phases coexist in the carbon rich matrix as reported elsewhere.³⁸ The typical graphitic carbon peak visible at the 2θ value of 26° in Fe-MCS-NC was found broadened and shifted towards a lower 2θ value (23.8°) for the sample Fe-MCS-NCM. The d-spacing increased from 0.34 to 0.37 nm. This lower shift in the G (002) diffraction peaks in Fe-MCS-NCM suggested enhanced nitrogen retention as reported earlier.³⁹ The peak at 44° is also a characteristic carbon peak corresponding to the diffraction from the (100) plane.

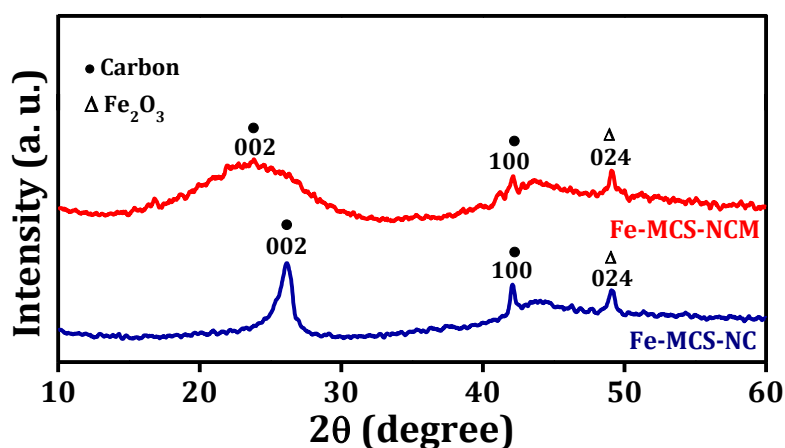


Figure 3.9 XRD patterns of Fe-MCS-NC and Fe-MCS-NCM.

3.3.5 Chemical Composition Analysis

Raman spectral measurements were carried out to further assess the graphitic structure. Raman spectra analysis of Fe-MCS-NC and Fe-MCS-NCM provide basic information on the structure of the porous carbon and the associated defects. The spectra of both the samples indicated the typical G and D bands at 1585 cm^{-1} and 1330 cm^{-1} (**Figure 3.10**) respectively. The G band signified the vibrational mode (E_{2g}) of the sp^2 hybridized hexagonally bonded graphitic carbon while the D band resulted from the structurally disordered carbon atoms.⁴⁰ The intensity ratios (I_D/I_G) of Fe-MCS-NC and Fe-MCS-NCM were found to be 0.85 and 1.31 respectively. The high intensity ratio indicated a higher degree of disorder in the structure of Fe-MCS-NCM and can be

assigned to the increased nitrogen content in the sample as a result of improved gelation properties during the MOG formation.

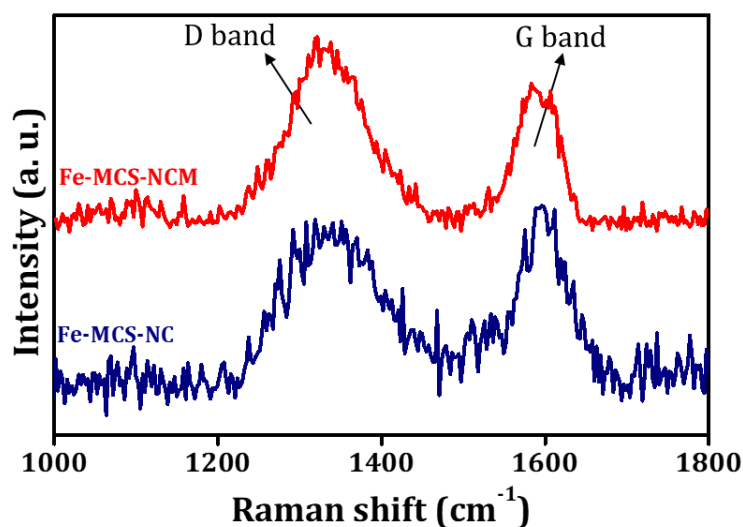


Figure 3.10 Raman spectra of Fe-MCS-NC and Fe-MCS-NCM.

The chemical composition and oxidation states of Fe and type of N present in Fe-MCS-NC and Fe-MCS-NCM were analyzed from the XPS data. **Figure 3.11** represents the corresponding survey scan spectrum with characteristic spectra of C 1s, N 1s, Fe 2p and O 1s confirming the presence of N and Fe in the sample. The total N content in Fe-MCS-NC and Fe-MCS-NCM was found to be 0.16 and 1.58 atomic % respectively with corresponding Fe contents of 0.06 and 0.01 atomic % (**Table 3.2**). However, from ICP analysis, the bulk Fe content was estimated to be 0.15 atomic % for Fe-MCS-NCM, which was higher than the XPS results as ICP analysis also detected the Fe in the carbon capsules.

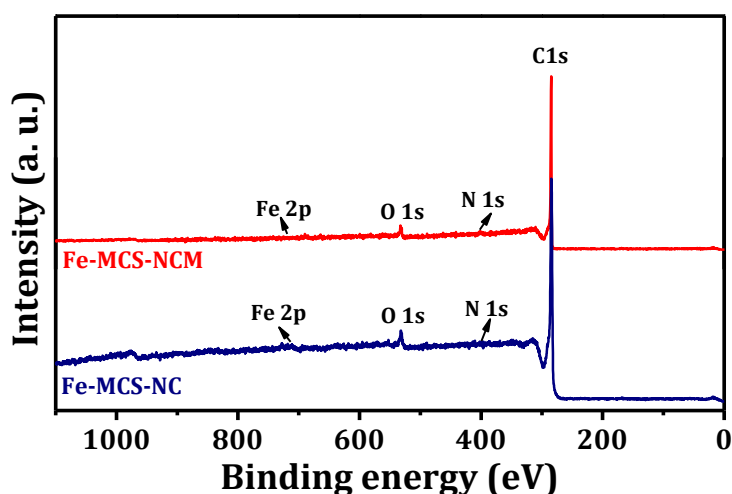


Figure 3.11 XPS survey spectra of Fe-MCS-NC and Fe-MCS-NCM.

The high resolution N 1s spectra showed four different signals at binding energies of 398.55, 400.54, 401.64 and 404.73 eV corresponding to the pyridinic, pyrrolic, graphitic and oxidized nitrogen⁴¹ respectively for Fe-MCS-NC (**Figure 3.12a**) and at 398.62, 401.31 and 403.95 eV corresponding to the pyridinic, graphitic and oxidized nitrogen respectively for Fe-MCS-NCM (**Figure 3.12b**). The two main nitrogen species providing the active sites of ORR are the pyridinic and graphitic N.⁴² Unlike the pyrrolic N, the lone pair of electrons in the pyridinic and graphitic N does not take part in delocalization, and are available for bonding with oxygen, thereby weakening the O-O bond and facilitating the reduction of O₂.⁴³

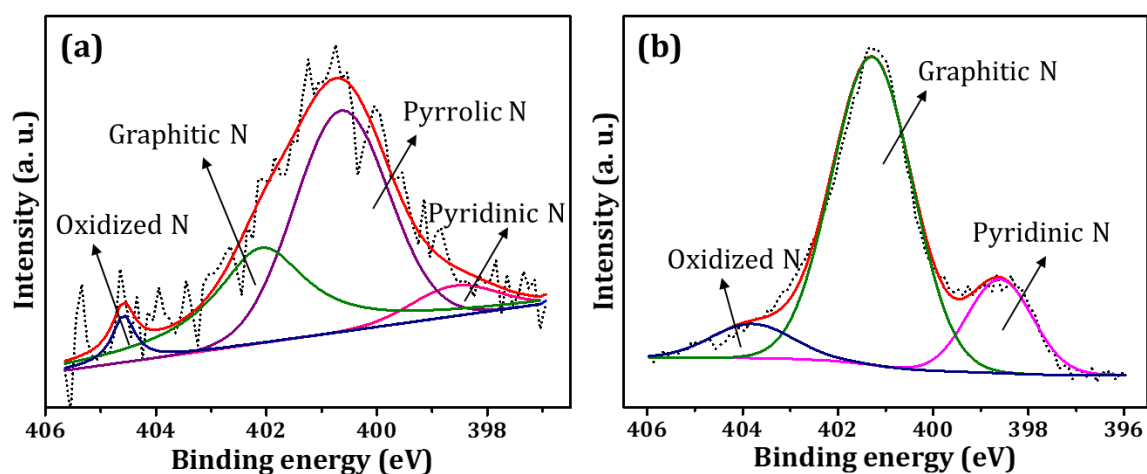


Figure 3.12 High-resolution N 1s XPS spectra of (a) Fe-MCS-NC and (b) Fe-MCS-NCM.

The existence of Fe³⁺ ions in both the samples were evidenced from the high-resolution Fe 2p spectra recorded. The Fe 2p spectrum of Fe-MCS-NC sample shown in **Figure 3.13a** could be deconvoluted into five main peaks at 711.7, 714.7, 719.8, 724.8 and 727.2 eV. The peak at 711.7 eV corresponded to the binding energy of 2p_{3/2} of the Fe (III) ion and the peak at 724.8 eV was assigned to the binding energy of 2p_{1/2} of the Fe (III) ion.⁴⁴ The peak at 719.8 eV was identified as a satellite peak corresponding to Fe 2p_{3/2}. The presence of extra peaks at 714.3 and 727.2 eV provided information of the existence of iron carbide and oxidized species.³⁸ The peak at 711.7 eV in the Fe 2p_{3/2} spectrum suggested that Fe is coordinated to N. However, in the case of Fe-MCS-NCM sample, the Fe 2p spectrum (**Figure 3.13b**) was difficult to deconvolute probably owing to the very low concentration of Fe in the sample as shown in **Table 3.2** below.

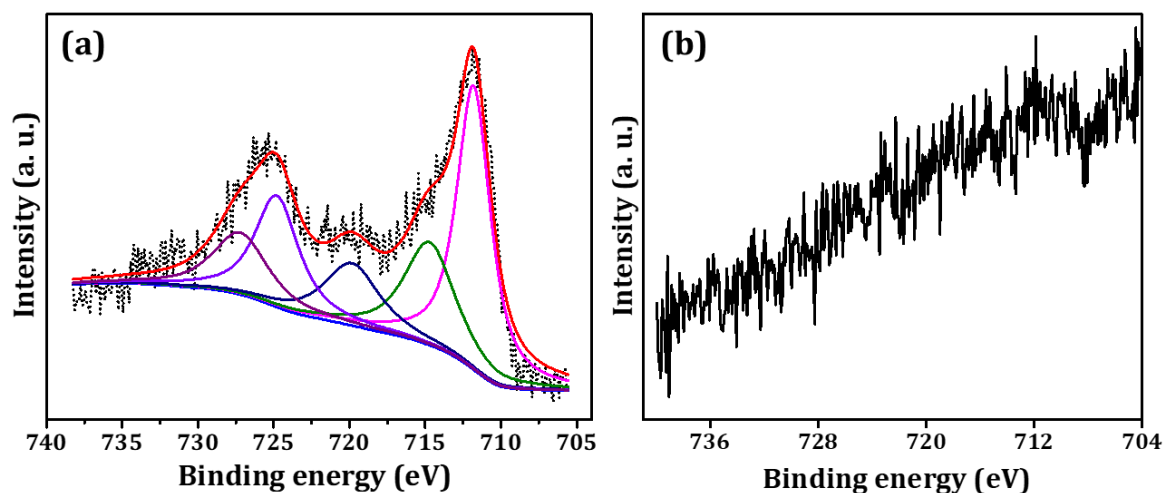


Figure 3.13 High-resolution Fe 2p XPS spectra of (a) Fe-MCS-NC and (b) Fe-MCS-NCM.

Table 3.2 Atomic % values of C, N, and Fe of Fe-MCS-NC and Fe-MCS-NCM measured from XPS analysis.

Sample	C (at.%)	N (at.%)	Fe (at.%)
Fe-MCS-NC	97.67	0.16	0.06
Fe-MCS-NCM	94.57	1.58	0.01

The C 1s spectra presented in **Figure 3.14** can be deconvoluted into 4 peaks where the major peak at 284.7 corresponded to the sp^2 carbon. The peaks at 285.1, and 285.7 eV indicated C-N and different modes of C-O respectively.

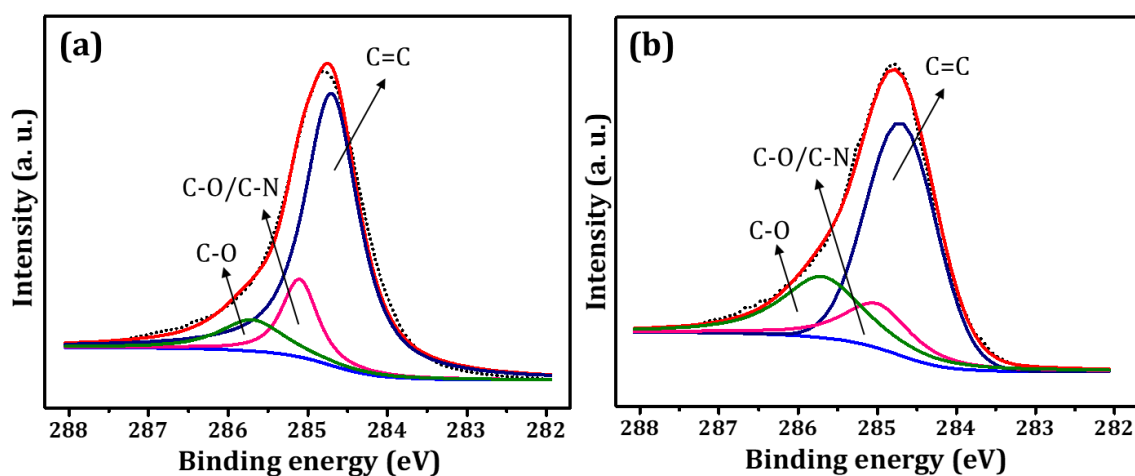


Figure 3.14 Deconvoluted C 1s spectra of (a) Fe-MCS-NC and (b) Fe-MCS-NCM.

XPS analyses indicated that the overall N content in Fe-MCS-NCM was very high compared to Fe-MCS-NC whereas the amount of Fe was lower. The increased N content in Fe-MCS-NCM is expected to induce a crucial role in improving the ORR activity and therefore the composition based on nitrogen species was evaluated (**Figure 3.15**). The implication of these results will be discussed later in the chapter.

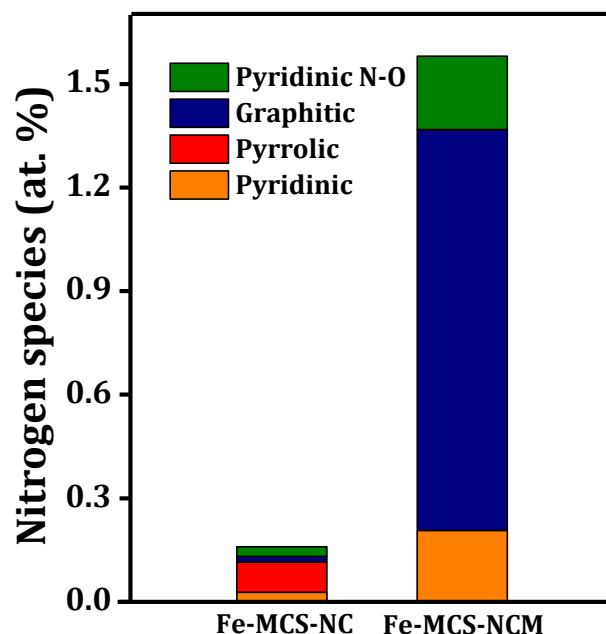


Figure 3.15 Percentage of different nitrogen species present in Fe-MCS-NC and Fe-MCS-NCM.

3.3.6 Electrochemical Analysis

The ORR activity of the catalyst was measured using linear sweep voltammetry (LSV) measurements using a rotating disc electrode (RDE) in oxygen saturated 0.1 M KOH solution at a rotation speed of 1600 rpm and at a scan rate of 5 mV s⁻¹. A commercial 40 wt. % Pt/C (Johnson Matthey) was also tested for comparison. The detailed cyclic voltammetry (CV) measurements of Fe-MCS-NC and Fe-MCS-NCM samples both in N₂ and O₂ saturated 0.1 M KOH solution were conducted with a rotation speed of 900 rpm (**Figure 3.16a & b**). In the N₂ saturated 0.1 M KOH solution, there was no characteristic peak for ORR. However, the presence of more active sites in the catalyst was indicated by an increase in the cathodic current during oxygen purging, which was a measure of its ORR potential.

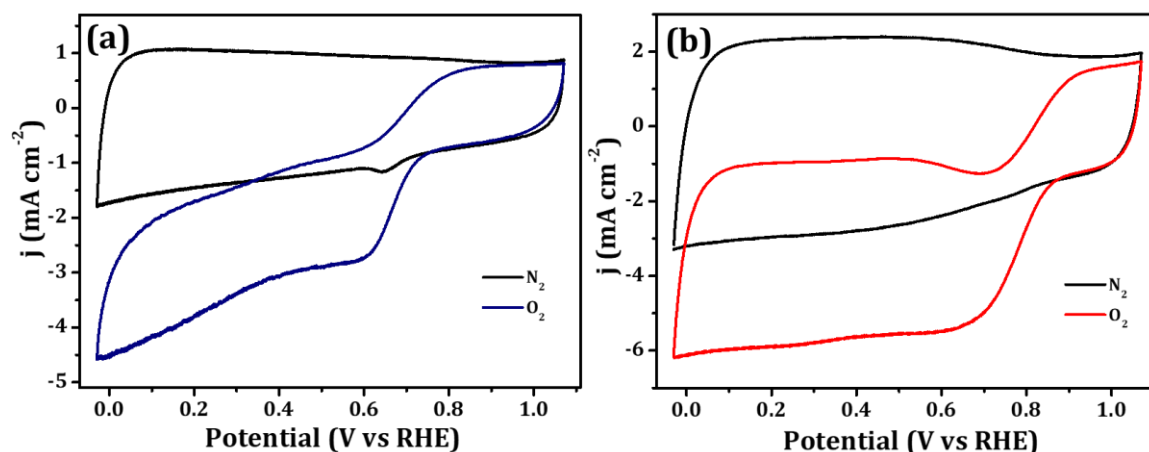


Figure 3.16 Cyclic voltammograms of (a) Fe-MCS-NC and (b) Fe-MCS-NCM 0.1 M KOH solution measured at a scan rate of 50 mV s^{-1} at 900 rpm.

Figure 3.17 displays the comparative LSVs of Fe-MCS-NC, Fe-MCS-NCM, and Pt/C. The onset potential of Fe-MCS-NC was 0.782 V while the chitosan modified Fe-MCS-NCM showed an onset potential of 0.925 V, which was 143 mV higher than that of Fe-MCS-NC and only 75 mV lower than the state-of-the-art catalyst Pt/C (1 V vs RHE).

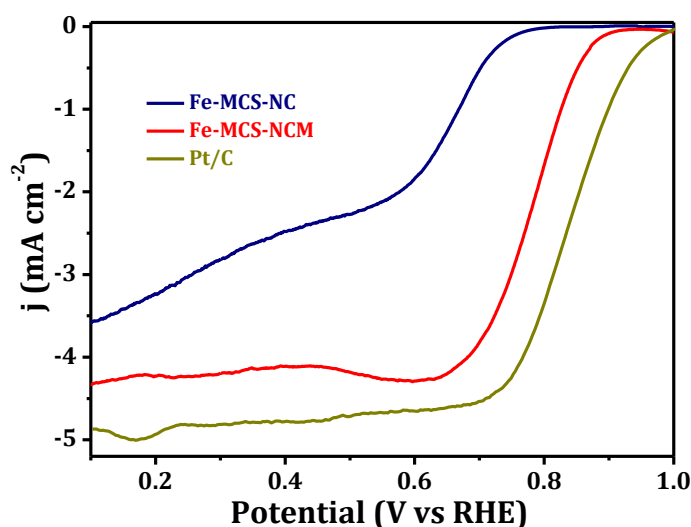


Figure 3.17 (a) Linear Sweep voltammogram (LSV) comparison of Fe-MCS-NC, Fe-MCS-NCM & Pt/C in O_2 saturated 0.1 M KOH solution measured at a scan rate of 5 mV s^{-1} at 1600 rpm.

The half-wave potentials ($E_{1/2}$) of Fe-MCS-NC and Fe-MCS-NCM were respectively 0.61 V and 0.78 V while that of Pt/C was 0.83 V. The 50 mV difference in $E_{1/2}$ of Fe-MCS-NCM from Pt/C reflected that the performance of the modified sample is comparable with Pt/C in terms of the $E_{1/2}$. The onset potential values also suggested

the enhancement of activity with increase in the graphitic N content and surface to volume ratio upon synthetic modification.

LSVs of Fe-MCS-NC and Fe-MCS-NCM at different rotation speeds of 400, 900, 1200, 1600, 2000 and 2500 rpm are presented in **Figure 3.18 a & b**. During the rotation of the working electrode, the current density increased due to the enhanced electrolyte diffusion and the mass transfer characteristics arising due to the heteroporous nature of the material.

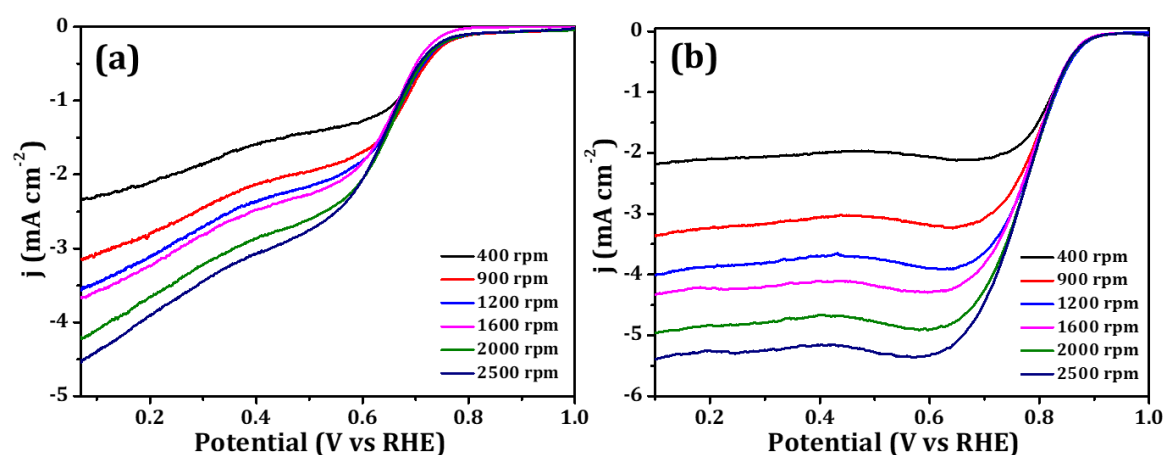


Figure 3.18 LSVs of (a) Fe-MCS-NC and (b) Fe-MCS-NCM in O_2 saturated 0.1 M KOH solution measured at different rotation rates at a scan rate of 5 mV s^{-1} .

The K-L plots for the different samples presented in **Figure 3.19** were found to be linear with similar slopes at different potentials. This constant slope suggested similar oxygen reduction kinetics in the given range of potentials.

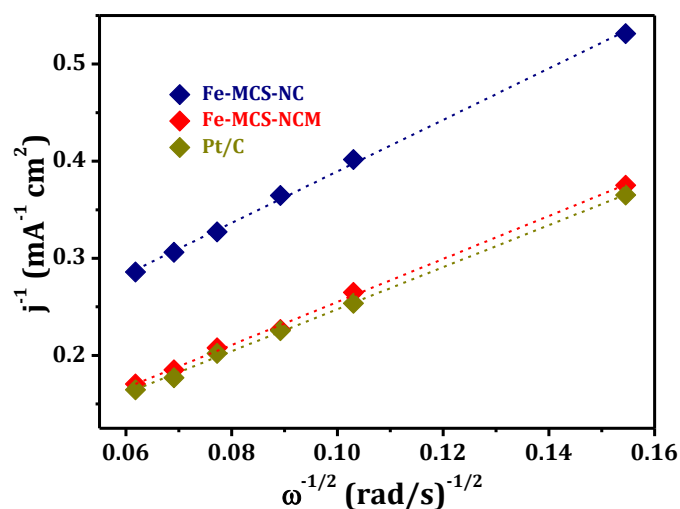


Figure 3.19 Comparison of the Koutecky-Levich (K-L) plots of Fe-MCS-NC, Fe-MCS-NCM and Pt/C.

RRDE analysis was performed to quantify the amount of H_2O_2 generated during the oxygen reduction (**Figure 3.20a**). The yield of H_2O_2 was found to be 7.8 to 13.8% for Fe-MCS-NCM, 18 to 39% for Fe-MCS-NC and 2.3-4.4% for Pt/C catalyst under the same conditions of measurement. The number of electron transfer (n) as calculated from H_2O_2 %, at 0.6 V for Fe-MCS-NCM was 3.8, which confirmed that Fe-MCS-NCM followed a four-electron reduction pathway to produce water directly rather than the two-electron pathway with the production of peroxide intermediate in alkaline conditions (**Figure 3.20b**). This improved activity of Fe-MCS-NCM in comparison to Fe-MCS-NC may be attributed to the increased amount of doped N and its strong interaction with Fe.

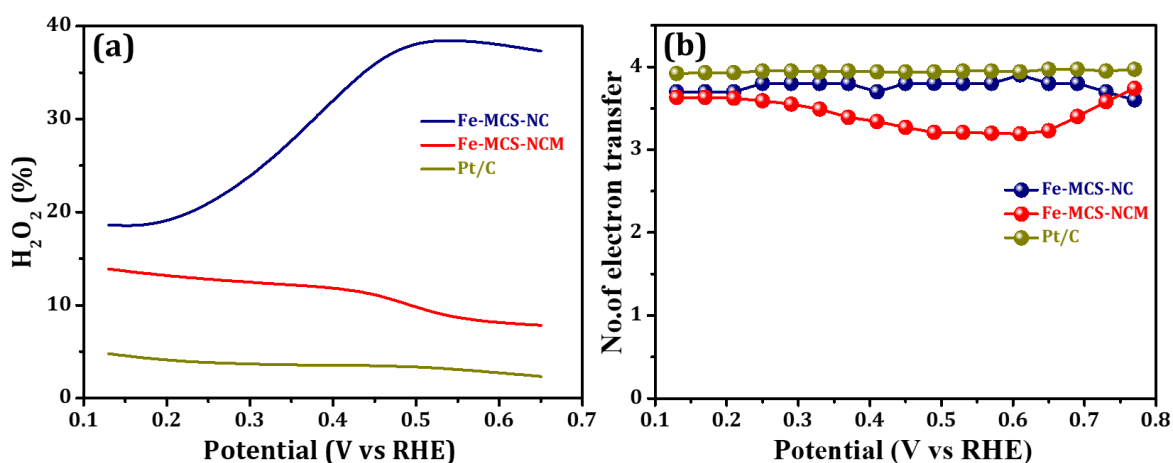


Figure 3.20 Comparison of (a) hydrogen peroxide yield and (b) number of electron transfer at different potentials obtained from the RRDE experiment.

Tafel plot is another useful method for the ORR kinetic analysis. The Tafel plots were derived by plotting the mass transport corrected kinetic current density against the overpotential. 65% i_R compensation was done during the plotting of $\log j_k$ against the overpotential and the corresponding plots are presented in **Figure 3.21**. The Tafel slope for Fe-MCS-NC was estimated to be 99.4 mV dec^{-1} and the corresponding value for Fe-MCS-NCM was 90.9 mV dec^{-1} . The comparatively lower Tafel slope for Fe-MCS-NCM indicated its faster kinetics and hence better performance towards ORR. The corresponding value estimated for Pt/C is 68.5 mV dec^{-1} .⁴⁵ **Table 3.3** summarizes the electrocatalytic performance of the prepared samples.

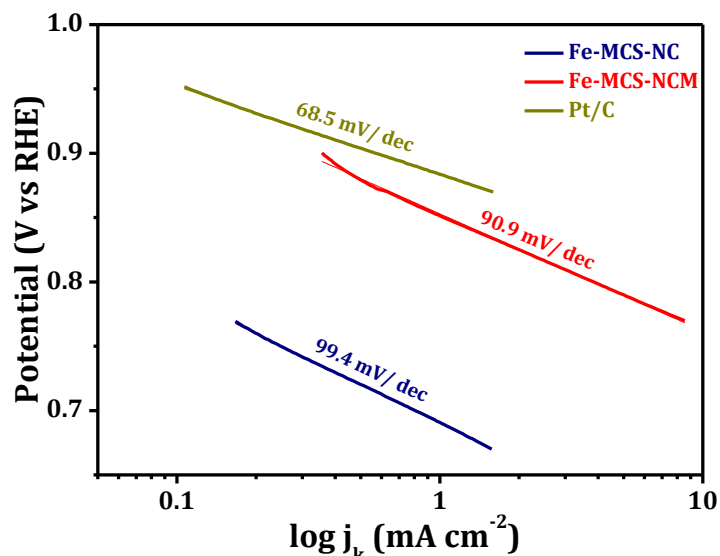


Figure 3.21 Tafel slope comparison of Fe-MCS-NC and Fe-MCS-NCM with Pt/C.

Table 3.3 Comparison of electrocatalytic performance of the samples.

Sample	E_{onset} (V vs RHE)	$E_{1/2}$ (V vs RHE)	n	H_2O_2 (%)	Tafel slop (mV dec^{-1})
Fe-MCS-NC	0.782	0.61	3.7	39	99.4
Fe-MCS-NCM	0.925	0.78	3.8	13	90.9
Pt/C	1.00	0.83	3.9	4	68.5

Accelerated Durability Test (ADT) was carried out to determine the stability of the catalyst. Fe-MCS-NCM was subjected to ADT in O_2 saturated 0.1 M KOH solution with a cycling scan rate of 100 mV s^{-1} . LSV was taken before and after 5000 cycles. The results presented in **Figure 3.22a** demonstrated a slightly negative shift in $E_{1/2}$ (24 mV) after 5000 cycles while the onset potential remained almost unchanged. Pt/C with a negative shift of 30 mV in $E_{1/2}$ indicated lower durability in alkaline medium. The results implied that the intrinsic activity of Fe-MCS-NCM towards ORR remained unaltered even after ADT, compared to the performance of Pt/C as shown in **Figure 3.22b**.

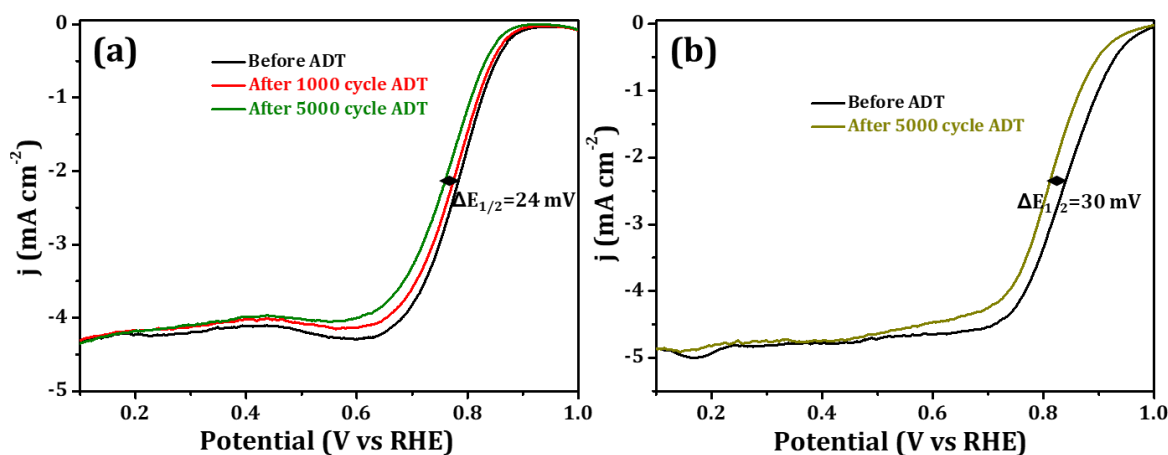


Figure 3.22 (a) LSV recorded before and after 5000 cycles ADT analysis for (a) Fe-MCS-NC and (b) Pt/C in O₂ saturated 0.1 M KOH solution with electrode rotation of 1600 rpm.

Fe-MCS-NCM exhibited high amount of doped N (1.58%) and the XPS analysis distinctly showed the existence of N species corresponding to the pyridinic (398.62 eV), graphitic (401.3 eV) and oxidized (403.95 eV) N structures. However, it contained very less amount of Fe (0.01%) as well-defined peaks in the high-resolution Fe 2p XPS spectrum were absent. Compared to Fe-MCS-NC, Fe-MCS-NCM showed far better ORR catalytic performance. It may be inferred that very low doping of Fe is sufficient for better ORR while the extent and type of N as well as its bonding play crucial roles. Literature substantiates that, the type of N present and the N-bonding configuration of Fe are dominant factors determining the catalytic activity of Fe-N-C catalysts.⁴⁶ The presence of the pyridinic as well as graphitic nitrogen was found to have a greater ability to act as active sites.^{42,47} The percentage of the graphitic N that contributed more to the catalytic performance was greater in Fe-MCS-NCM compared to Fe-MCS-NC, where the pyrrolic N was prevalent than the others (**Figure 3.15**). In Fe-MCS-NC, as a result of poor gelation arising from the weak Fe-N bonding, pyrolysis of the gel network yielded a graphitic carbon structure with lesser amounts of N and Fe, due to the disintegration of the network at the Fe-N sites. Hence, the amount of the graphitic N will be less and N at the edges of the carbon skeleton was in the form of pyrrolic N. In the case of Fe-MCS-NCM, the stronger gel network formed as a result of the stronger Fe-N interaction did not disintegrate at the Fe-N sites. It can be therefore anticipated that the adopted chitosan intercalation favored the creation of more graphitic N. Fe-MCS-NCM exhibited exceptionally good ORR activity and stability comparable to the

values reported in some of the recent publications (**Table 3.4**). This performance should be attributed to its peculiar Fe distributed N-doped graphitic structure and the morphology arising from the stronger precursor gel network structure. This distinctive structure with more number of active sites could be accounted for the increased limiting current and onset potential in Fe-MCS-NCM. The Fe and N-doping in the graphitic carbon layers led to loss of electroneutrality resulting in asymmetrical charge distribution. This caused changes in charge and spin densities around the carbon atom,⁴⁸ facilitating the adsorption of oxygen as the first step of ORR and subsequently enhancing the ORR activity. In addition, a higher surface area with micro-mesoporous structure and good graphitic nitrogen content helped in the enhancement of the ORR activity of Fe-MCS-NCM to values comparable to Pt/C under our testing conditions.

Table 3.4 Comparison of ORR activity of Fe-MCS-NCM catalyst with reported non precious metal catalysts in alkaline medium.

Sl. No.	Sample	E_{onset} (V vs RHE)	$E_{1/2}$ (V vs RHE)	Tafel slope (mV dec ⁻¹)	n	Reference
1	FeGNT	1	0.85	84.84	3.90	1
2	Fe-N-CC	0.94	0.83	Undefined	3.7	2
3	Fe-N-C	0.95	0.84	59	3.4	3
4	Fe-N _x	0.98	0.85	Undefined	4	4
5	Fe-N/MCN	0.95	0.85	Undefined	4	5
6	Fe-Fe ₂ O ₃ /NGR	0.94	0.75	Undefined	3.8	6
7	Fe ₃ C@NCNF-900	0.97	0.88	81	3.8	7
8	Fe ₁₅ -N-C1000	0.99	0.85	63	3.98	8
9	Fe/N/G	0.98	0.84	90	3.9	9
10	Fe-MCS-NCM	0.92	0.78	90.9	3.9	Present study
11	40 wt.% Pt/C	1	0.83	68.5	3.9	Present study

3.4 Conclusions

N-doped mesoporous graphitic carbon structures, Fe entrenched (Fe-MCS-NC) and Fe distributed (Fe-MCS-NCM), were synthesized from the green precursor of Fe-MOG intercalated with chitosan. The MOG-Chitosan favorably contributed towards the microstructure, surface area and ORR activity of the graphitic structures. Moreover, modulation in the synthesis procedures resulted in a catalyst with improved surface area ($565 \text{ m}^2\text{g}^{-1}$) and a significantly higher graphitic N (1.26 at.%) that coordinately binds to lower concentrations of Fe with a better distribution. The higher amount of graphitic N was due to the stronger gel network formation as a result of the stronger Fe-N interaction, which prevented the disintegration at the Fe-N sites. Fe-MCS-NCM owns high activity towards ORR in terms of the onset potential (0.925 V), half-wave potential (0.78 V), and Tafel slope (90.9 mV dec^{-1}). RDE and RRDE experiments showed that ORR proceeds through a four-electron reaction pathway with good durability profile. The present study is, therefore, a promising approach for the synthesis of a highly feasible new candidate (Fe-MCS-NCM) as a sustainable catalyst for ORR.

References

1. Kumar, M. N. R. A Review of Chitin and Chitosan Applications. *React. Funct. Polym.* **2000**, 46 (1), 1.
2. Kumar, M. R.; Muzzarelli, R. A.; Muzzarelli, C.; Sashiwa, H.; Domb, A. Chitosan Chemistry and Pharmaceutical Perspectives. *Chem. Rev.* **2004**, 104 (12), 6017.
3. Lopez-Salas, N.; Gutierrez, M. C.; Ania, C. O.; Fierro, J. L. G.; Luisa Ferrer, M.; Monte, F. d. Efficient Nitrogen-Doping and Structural Control of Hierarchical Carbons Using Unconventional Precursors in the Form of Deep Eutectic Solvents. *J. Mater. Chem. A* **2014**, 2 (41), 17387.
4. Liang, H. W.; Wei, W.; Wu, Z. S.; Feng, X.; Müllen, K. Mesoporous Metal-Nitrogen-Doped Carbon Electrocatalysts for Highly Efficient Oxygen Reduction Reaction. *J. Am. Chem. Soc.* **2013**, 135 (43), 16002.
5. Choi, J. Y.; Hsu, R. S.; Chen, Z. Highly Active Porous Carbon-Supported Nonprecious Metal-N Electrocatalyst for Oxygen Reduction Reaction in PEM Fuel Cells. *J. Phys. Chem. C* **2010**, 114 (17), 8048.

6. Lefèvre, M.; Proietti, E.; Jaouen, F.; Dodelet, J. P. Iron-Based Catalysts with Improved Oxygen Reduction Activity in Polymer Electrolyte Fuel Cells. *Science* **2009**, 324 (5923), 71.
7. Peng, H.; Mo, Z.; Liao, S.; Liang, H.; Yang, L.; Luo, F.; Song, H.; Zhong, Y.; Zhang, B., High Performance Fe- and N- Doped Carbon Catalyst with Graphene Structure for Oxygen Reduction. *Sci. Rep.* **2013**, 3, 1765.
8. Liang, J.; Zhou, R. F.; Chen, X. M.; Tang, Y. H.; Qiao, S. Z. Fe-N Decorated Hybrids of CNTs Grown on Hierarchically Porous Carbon for High-Performance Oxygen Reduction. *Adv. Mater.* **2014**, 26 (35), 6074.
9. Tang, H.; Zeng, Y.; Zeng, Y.; Wang, R.; Cai, S.; Liao, C.; Cai, H.; Lu, X.; Tsiakaras, P., Iron-Embedded Nitrogen Doped Carbon Frameworks as Robust Catalyst for Oxygen Reduction Reaction in Microbial Fuel Cells. *Appl. Catal. B* **2017**, 202, 550.
10. Zheng, D.; Zhu, L.; Feng, H.; Yu, M.; Lu, X.; Tong, Y., Co₃O₄@ Co Nanoparticles Embedded Porous N-Rich Carbon Matrix for Efficient Oxygen Reduction. *Part. Part. Syst. Charact.* **2017**, 34 (6), 1700074.
11. Yu, M.; Wang, Z.; Hou, C.; Wang, Z.; Liang, C.; Zhao, C.; Tong, Y.; Lu, X.; Yang, S., Nitrogen-Doped Co₃O₄ Mesoporous Nanowire Arrays as an Additive-Free Air-Cathode for Flexible Solid-State Zinc-Air Batteries. *Adv. Mater.* **2017**, 29 (15), 1602868.
12. Liang, J.; Jiao, Y.; Jaroniec, M.; Qiao, S. Z., Sulfur and Nitrogen Dual-Doped Mesoporous Graphene Electrocatalyst for Oxygen Reduction with Synergistically Enhanced Performance. *Angew. Chem. Int. Ed.* **2012**, 51 (46), 11496.
13. Aghabarari, B.; Martinez-Huerta, M. V.; Ghiaci, M.; Fierro, J. L. G.; Pena, M. A. Hybrid Chitosan Derivative-Carbon Support for Oxygen Reduction Reactions. *RSC Adv.* **2013**, 3 (16), 5378.
14. Khan, I. A.; Qian, Y.; Badshah, A.; Nadeem, M. A.; Zhao, D., Highly Porous Carbon Derived from MOF-5 as a Support of ORR Electrocatalysts for Fuel Cells. *ACS Appl. Mater. Interfaces* **2016**, 8 (27), 17268.
15. Thomas, M.; Illathvalappil, R.; Kurungot, S.; Nair, B. N.; Mohamed, A. A. P.; Anilkumar, G. M.; Yamaguchi, T.; Hareesh, U. S. Graphene Oxide Sheathed ZIF-8 Microcrystals: Engineered Precursors of Nitrogen-Doped Porous Carbon for Efficient Oxygen Reduction Reaction (ORR) Electrocatalysis. *ACS Appl. Mater. Interfaces* **2016**, 8 (43), 29373.
16. Chaikittisilp, W.; Ariga, K.; Yamauchi, Y. A New Family of Carbon Materials: Synthesis of MOF-Derived Nanoporous Carbons and their Promising Applications. *J. Mater. Chem. A* **2013**, 1 (1), 14.

17. Zhang, P.; Sun, F.; Shen, Z.; Cao, D. ZIF-Derived Porous Carbon: A Promising Supercapacitor Electrode Material. *J. Mater. Chem. A* **2014**, 2 (32), 12873.
18. Xia, W.; Qiu, B.; Xia, D.; Zou, R. Facile Preparation of Hierarchically Porous Carbons from Metal-Organic Gels and their Application in Energy Storage. *Sci. Rep.* **2013**, 3, 1935.
19. He, C.; Wu, S.; Zhao, N.; Shi, C.; Liu, E.; Li, J. Carbon-Encapsulated Fe₃O₄ Nanoparticles as a High-Rate Lithium Ion Battery Anode Material. *ACS Nano* **2013**, 7 (5), 4459.
20. Janiak, C.; Vieth, J. K., MOFs, MILs and More: Concepts, Properties and Applications for Porous Coordination Networks (PCNs). *New J. Chem.* **2010**, 34 (11), 2366.
21. Yang, S. J.; Kim, T.; Im, J. H.; Kim, Y. S.; Lee, K.; Jung, H.; Park, C. R., MOF-Derived Hierarchically Porous Carbon with Exceptional Porosity and Hydrogen Storage Capacity. *Chem. Mater.* **2012**, 24 (3), 464.
22. Liu, B.; Shioyama, H.; Jiang, H.; Zhang, X.; Xu, Q. Metal-Organic Framework (MOF) as a Template for Syntheses of Nanoporous Carbons as Electrode Materials for Supercapacitor. *Carbon* **2010**, 48 (2), 456.
23. Jiang, H. L.; Liu, B.; Lan, Y. Q.; Kuratani, K.; Akita, T.; Shioyama, H.; Zong, F.; Xu, Q. From Metal-Organic Framework to Nanoporous Carbon: Toward a Very High Surface Area and Hydrogen Uptake. *J. Am. Chem. Soc.* **2011**, 133 (31), 11854.
24. Cui, L.; Wu, J.; Ju, H. Nitrogen-Doped Porous Carbon Derived from Metal-Organic Gel for Electrochemical Analysis of Heavy-Metal Ion. *ACS Appl. Mater. Interfaces* **2014**, 6 (18), 16210.
25. Zhang, L.; Marzec, B.; Clerac, R.; Chen, Y.; Zhang, H.; Schmitt, W. Supramolecular Approaches to Metal-Organic Gels Using 'Chevrel-Type' Coordination Clusters as Building Units. *Chem. Commun.* **2013**, 49 (1), 66.
26. Li, L.; Xiang, S.; Cao, S.; Zhang, J.; Ouyang, G.; Chen, L.; Su, C. Y. A Synthetic Route to Ultralight Hierarchically Micro/Mesoporous Al(III)-Carboxylate Metal-Organic Aerogels. *Nat. Commun.* **2013**, 4, 1774.
27. Chandy, T.; Sharma, C. P. Chitosan-as a biomaterial. *Biomater. Artif. Organs* **1990**, 18 (1), 1.
28. No, H. K.; Meyers, S. P. Preparation and Characterization of Chitin and Chitosan-A Review. *J. Aquat. Food Prod. Technol.* **1995**, 4 (2), 27.
29. Bhattarai, N.; Gunn, J.; Zhang, M. Chitosan-Based Hydrogels for Controlled, Localized Drug Delivery. *Adv. Drug Deliv. Rev.* **2010**, 62 (1), 83.

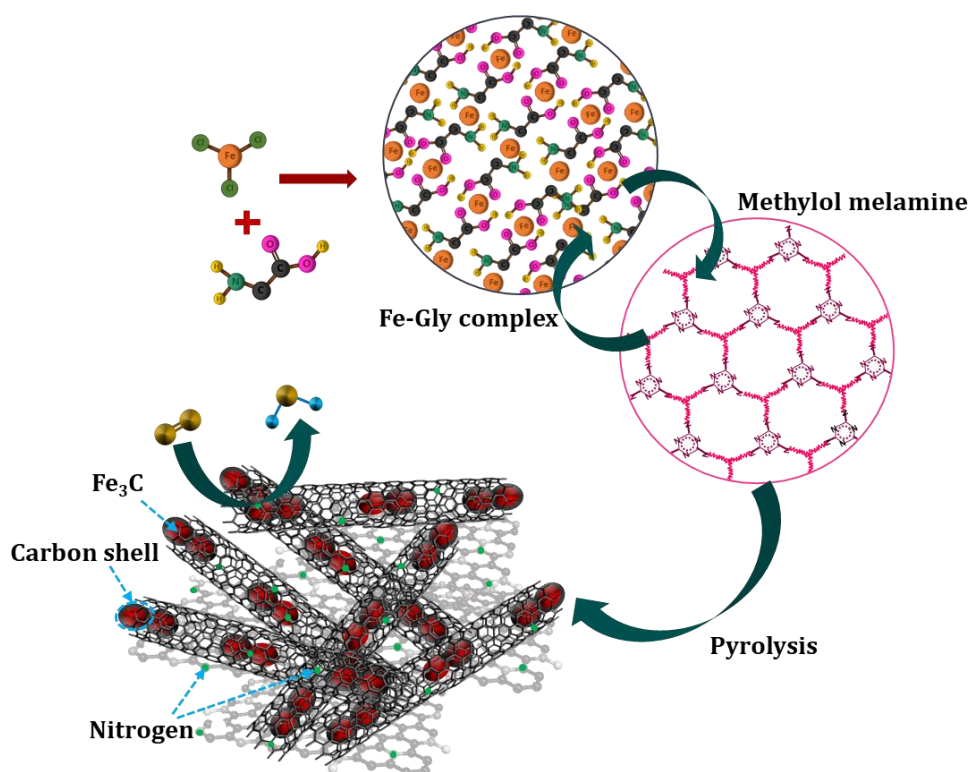
30. Śliwak, A.; Díez, N.; Miniach, E.; Gryglewicz, G. Nitrogen-Containing Chitosan-Based Carbon as an Electrode Material for High-Performance Supercapacitors. *J. Appl. Electrochem.* **2016**, 46 (6), 667.
31. Gao, F.; Qu, J.; Zhao, Z.; Wang, Z.; Qiu, J. Nitrogen-Doped Activated Carbon Derived from Prawn Shells for High-Performance Supercapacitors. *Electrochim. Acta* **2016**, 190, 1134.
32. Liu, Q.; Duan, Y.; Zhao, Q.; Pan, F.; Zhang, B.; Zhang, J. Direct Synthesis of Nitrogen-Doped Carbon Nanosheets with High Surface Area and Excellent Oxygen Reduction Performance. *Langmuir* **2014**, 30 (27), 8238.
33. Rybarczyk, M. K.; Lieder, M.; Jablonska, M. N-Doped Mesoporous Carbon Nanosheets Obtained by Pyrolysis of a Chitosan-Melamine Mixture for the Oxygen Reduction Reaction in Alkaline Media. *RSC Adv.* **2015**, 5 (56), 44969.
34. Wu, T. X.; Wang, G. Z.; Zhang, X.; Chen, C.; Zhang, Y. X.; Zhao, H. J. Transforming Chitosan into N-doped Graphitic Carbon Electrocatalysts. *Chem. Commun.* **2015**, 51 (7), 1334.
35. Xie, S.; Huang, S.; Wei, W.; Yang, X.; Liu, Y.; Lu, X.; Tong, Y. Chitosan Waste-Derived Co and N Co-doped Carbon Electrocatalyst for Efficient Oxygen Reduction Reaction. *ChemElectroChem* **2015**, 2 (11), 1806.
36. Wu, T.; Zhang, H.; Zhang, X.; Zhang, Y.; Zhao, H.; Wang, G. A low-Cost Cementite (Fe₃C) Nanocrystal@N-doped Graphitic Carbon Electrocatalyst for Efficient Oxygen Reduction. *Phys. Chem. Chem. Phys.* **2015**, 17 (41), 27527.
37. Zhong, G.; Wang, H.; Yu, H.; Peng, F., Nitrogen Doped Carbon Nanotubes with Encapsulated Ferric Carbide as Excellent Electrocatalyst for Oxygen Reduction Reaction in Acid and Alkaline Media. *J. Power Sources* **2015**, 286, 495.
38. Wu, Z. Y.; Xu, X. X.; Hu, B. C.; Liang, H. W.; Lin, Y.; Chen, L. F.; Yu, S. H., Iron Carbide Nanoparticles Encapsulated in Mesoporous Fe-N-Doped Carbon Nanofibers for Efficient Electrocatalysis. *Angew. Chem. Int. Ed.* **2015**, 54 (28), 8179.
39. Dhavale, V. M.; Singh, S. K.; Nadeema, A.; Gaikwad, S. S.; Kurungot, S. Nanocrystalline Fe-Fe₂O₃ Particle-Deposited N-Doped Graphene as an Activity-Modulated Pt-Free Electrocatalyst for Oxygen Reduction Reaction. *Nanoscale* **2015**, 7 (47), 20117.
40. Sun, M.; Liu, H.; Liu, Y.; Qu, J.; Li, J. Graphene-Based Transition Metal Oxide Nanocomposites for the Oxygen Reduction Reaction. *Nanoscale* **2015**, 7 (4), 1250.
41. Yuan, H.; Hou, Y.; Wen, Z.; Guo, X.; Chen, J.; He, Z. Porous Carbon Nanosheets Codoped with Nitrogen and Sulfur for Oxygen Reduction Reaction in Microbial Fuel Cells. *ACS Appl. Mater. Interfaces* **2015**, 7 (33), 18672-18678.

-
42. Lai, L.; Potts, J. R.; Zhan, D.; Wang, L.; Poh, C. K.; Tang, C.; Gong, H.; Shen, Z.; Lin, J.; Ruoff, R. S. Exploration of the Active Center Structure of Nitrogen-Doped Graphene-Based Catalysts for Oxygen Reduction Reaction. *Energy Environ. Sci.* **2012**, 5 (7), 7936.
 43. Feng, L.; Yang, L.; Huang, Z.; Luo, J.; Li, M.; Wang, D.; Chen, Y. Enhancing Electrocatalytic Oxygen Reduction on Nitrogen-Doped Graphene by Active Sites Implantation. *Sci. Rep.* **2013**, 3, 3306.
 44. Guo, Z.; Ren, G.; Jiang, C.; Lu, X.; Zhu, Y.; Jiang, L.; Dai, L., High Performance Heteroatoms Quaternary-Doped Carbon Catalysts Derived from *Shewanella* Bacteria for Oxygen Reduction. *Sci. Rep.* **2015**, 5, 17064.
 45. Zhou, R.; Qiao, S. Z. An Fe/N Co-Doped Graphitic Carbon Bulb for High-Performance Oxygen Reduction Reaction. *Chem. Commun.* **2015**, 51 (35), 7516.
 46. Yang, L.; Su, Y.; Li, W.; Kan, X. Fe/N/C Electrocatalysts for Oxygen Reduction Reaction in PEM Fuel Cells Using Nitrogen-Rich Ligand as Precursor. *J. Phys. Chem. C* **2015**, 119 (21), 11311.
 47. Zhang, C.; Hao, R.; Liao, H.; Hou, Y. Synthesis of Amino-Functionalized Graphene as Metal-Free Catalyst and Exploration of the Roles of Various Nitrogen States in Oxygen Reduction Reaction. *Nano Energy* **2013**, 2 (1), 88.
 48. Zhang, L.; Xia, Z. Mechanisms of Oxygen Reduction Reaction on Nitrogen-Doped Graphene for Fuel Cells. *J. Phys. Chem. C* **2011**, 115 (22), 11170.

Chapter 4

Fe₃C Encapsulated Pod like Carbon Structures for Efficient Oxygen Reduction Reaction

Abstract



Iron carbide (Fe₃C) encapsulated hierarchical pod-like porous graphitic carbon structures were prepared by a simple pyrolysis of Fe-glycine complex integrated melamine formaldehyde resin precursor. The unique structure and stronger network of the resulting thermosetting resin facilitated the formation of porous carbon nanosheets while Fe catalyzed the formation of carbon nanotubes. The best catalyst among the ones studied, Fe-G2-NC, possessed high degree of graphitization with enhanced surface area (205 m² g⁻¹) and porosity (0.54 cm³ g⁻¹). The XPS results confirmed the presence of high degree of graphitic N. The catalyst with optimized Fe content (Fe-G2-NC) exhibited high ORR activity with an onset potential of 0.95 V and a half-wave potential ($E_{1/2}$) of 0.80 V vs RHE in alkaline media through the four-electron reduction pathway. Moreover, the catalyst exhibited excellent long-term durability with good methanol tolerance.

4.1 Introduction

From the previous chapters it is identified that the heteroatom doping in carbon matrix enhances the electrocatalytic activity by breaking the electroneutrality and creating large number of active sites for O₂ adsorption. The heteroatoms mainly include non-metallic elements like B, N, P, S etc.¹⁻³ Out of these non-metallic dopants, N is the most preferred one owing to its similar size with that of C and its high electronegativity. Moreover, N-doping induces the creation of positive charge densities on the adjacent carbon atoms producing greater number of active sites for oxygen adsorption.^{4,5}

Besides N-doping, transition metal (Fe, Co, Ni, Cu, Mn etc.) doping is also pursued owing to their abundant reserves, economic applicability and their potential catalytic activity comparable to noble metals.⁶⁻⁸ The synergetic effects between the nitrogen-doped carbon and transition metals could significantly increase the number of active sites and boost the catalytic behavior.⁹⁻¹² M-N_x/C where, nitrogen coordinated with a metal is considered to be the best among the doped carbon catalyst.^{13,14} Metal/metal carbide nanoparticles encapsulated in carbon nanostructures, where, the graphitic carbon shells are activated by the encapsulated nanoparticles have emerged to be efficient catalysts for ORR.^{15,16} Among the various metal carbides-based catalysts, attention has been focused on the Fe based catalyst which exhibit superior electrocatalytic ORR.¹⁷⁻¹⁹ Wang *et al.* constructed Fe₃C nanoparticles encapsulated 3D N-doped graphene carbon nanotubes. The catalyst with bamboo like structure displayed excellent bifunctional ORR/OER activity with a potential difference of only 0.84 V in alkaline media.²⁰ Hu and *et al.* used a protective silica shell as template where, polypyrrole coated carbon nanofibers were embedded which upon pyrolysis with iron salt yielded Fe-N doped carbon. The catalyst exhibited superior ORR activity in acidic media ($E_{1/2}=0.74$ V).²¹ These synthetic procedures involved a harsh etching step to remove silica template and hence raises environmental issues on scale-up production. Xin and *et al.* synthesized Fe₃C encapsulated hollow carbon nano spindles using a reactive hard template approach. Fe₂O₃ not only acted as source for doped iron, but also acted as a hard reactive template. Even though, the catalyst exhibited high ORR activity and long-term stability, the synthetic method involved the use of irritant chemicals like tris(hydroxymethyl)aminomethane and 48 h hydrothermal

treatment.²² Therefore, developing a simple and efficient strategy for the synthesis of Fe₃C-encapsulated mesoporous N-doped carbon catalysts is highly demanded.

In this study, we have synthesized Fe encapsulated pod like graphitic carbon sheet structure by the carbonization of a hybrid thermosetting network structure formed by an optimized compositional mixing of Fe-glycine complex and melamine formaldehyde (MF). We expect that the presence of Fe in the reaction mixture will also help in the formation of interesting structures by playing an active role in the chemical synthesis process. The stronger MF network structure should assist in the formation of graphitic N rich catalyst with high surface area leading to the formation of doped carbon catalysts exhibiting good ORR activity along with long term cyclic stability and methanol tolerance.²³

4.2 Experimental

4.2.1 Materials

Anhydrous iron (III) chloride (FeCl₃), melamine (C₃H₆N₆) and formaldehyde were purchased from Sigma Aldrich Chemical Reagent Co. Ltd. Glycine (C₂H₅NO₂) and potassium hydroxide were obtained from Merck India.

4.2.2 Synthesis of Fe-G-MF IPN

In a typical synthesis procedure 13.5 g glycine and 3.2 g FeCl₃ were separately dissolved in 80 mL deionized water. The two solutions were mixed and stirred overnight. A reddish-brown precipitate of Fe-glycine complex was obtained, labelled as component A.

In another synthesis, 8.3 mL formaldehyde was added to 2.7 g melamine and 0.1 M KOH was added to maintain alkaline pH. The mixture was stirred at 70 °C to form a clear solution of methylol melamine, which is labelled as component B. Component B was carefully introduced into component A and stirred for 15 min and allowed to complete polymerization at room temperature. The product obtained was freeze dried (denoted as Fe-G1-MF). Similarly, Fe-G2-MF and Fe-G3-MF were synthesized by changing the amount of Fe as 4.8 g and 9.6 g respectively.

4.2.3 Synthesis of Fe, N Doped Porous Carbon

Pyrolysis of Fe-G-MFs with varying Fe-Glycine ratio was done in a tubular furnace at 900 °C for 3 h under N₂ gas flow. The obtained black products were treated with 1 M H₂SO₄ at 70 °C for 4 h followed by washing with deionized water to remove any unreacted Fe species present. The dried samples were named as Fe-G1-NC, Fe-G2-NC and Fe-G3-NC.

4.2.4 Structural Characterization

Microstructural and morphological analysis of the samples were done with a scanning electron microscope (SEM Carl Zeiss, Germany). Transmission electron microscopic images of samples were obtained using an FEI (Tecnai 30 G2 S-TWIN, The Netherlands) microscope. BET surface area and porosity analysis of the samples were performed with Micromeritics (Tristar 11, USA) surface area analyzer using nitrogen adsorption at 77 K. Degassing of the samples were done at 200 °C in flowing N₂ before adsorption analysis. X-ray diffraction patterns were recorded with a PW1710 Philips, (The Netherlands) instrument using Cu K α radiation (1.5 Å). Raman spectra were obtained from a Confocal Raman microscope (alpha 300 R WITEC Germany) using 633 nm laser. XPS was investigated using a scanning X-ray microprobe (ULAC-PHI, Inc. PHI-4700 V, USA) with a monochromated Al-K α X-ray source operating at 14 kV and 220 W.

4.2.5 Electrochemical Characterization

Electrochemical analysis was carried out in a Bio logic electrochemical work station (sp-300) using a three-electrode set up in which glassy carbon electrode was used as the working electrode, Hg/HgO as the reference electrode and graphite rod as the counter electrode. For the catalyst ink preparation, 5 mg of the sample was weighed and transferred into a vial and mixed with 1 mL solution of 3:1 water: isopropyl alcohol mixture. 40 μ L of 5 wt.% nafion solution was added to this and the entire mixture was ultrasonicated for 60 min to obtain a uniform dispersion. 10 μ L of the slurry was then drop cast on the glassy carbon electrode surface (0.196 cm²) using a micropipette and dried under IR lamp. For comparison, commercial 40 wt.% Pt/C (Johnson Matthey) was also tested with the same catalyst loading. Cyclic voltammetric analysis (CV) were performed both in nitrogen and oxygen saturated 0.1 M KOH

solution at a scan rate of 50 mV s⁻¹ with a working electrode rotation of 900 rpm. Linear sweep voltammetric (LSV) measurements were carried out at a scan rate of 5 mV s⁻¹ with different working electrode rotations. The durability of the catalyst was checked using accelerated durability test (ADT) in which CV analysis was carried out for 5000 cycles in O₂ saturated 0.1 M KOH at a scan rate of 100 mV s⁻¹ in the potential window of 0.57 to 0.97 V. The LSVs before and after ADT was performed and compared.

The number of electrons transferred and percentage of H₂O₂ produced during ORR were measured using rotating ring disc electrode technique (RRDE, Pine Instruments) in oxygen saturated 0.1 M KOH solution at a scan rate of 10 mV s⁻¹ with a working electrode rotation of 1600 rpm. The glassy carbon disc with a platinum ring was used as the working electrode, Hg/HgO as the reference electrode and graphite rod as the counter electrode. All the potentials were converted to RHE by calibrating the reference Hg/HgO electrode in hydrogen saturated 0.1 M KOH solution.²⁴

4.3 Results and Discussion

Figure 4.1 shows the synthesis of Fe-G-NC catalyst. In the initial step, Fe forms a strong coordinated complex with glycine which subsequently reacted with methylol melamine to form a cross-linked 3D structure. The complex formation occurred when Fe³⁺ gets bonded to glycine through chelation between hydrophilic -COOH and -NH₂ groups of glycine. The complex thus formed contained dispersed Fe³⁺ ions. Addition of methylol melamine resulted in a highly cross-linked 3D structure that effectively reduced the agglomeration of iron particles by virtue of its strong interaction with the complex. Thus Fe³⁺ was stabilized within the network resulting in the formation of N-doped porous graphitic carbon structure with uniform iron carbide dispersion. The Fe species also aided the transformation of nearby graphitic carbon sheets into tubes, thereby getting entrapped into a pod like structure.

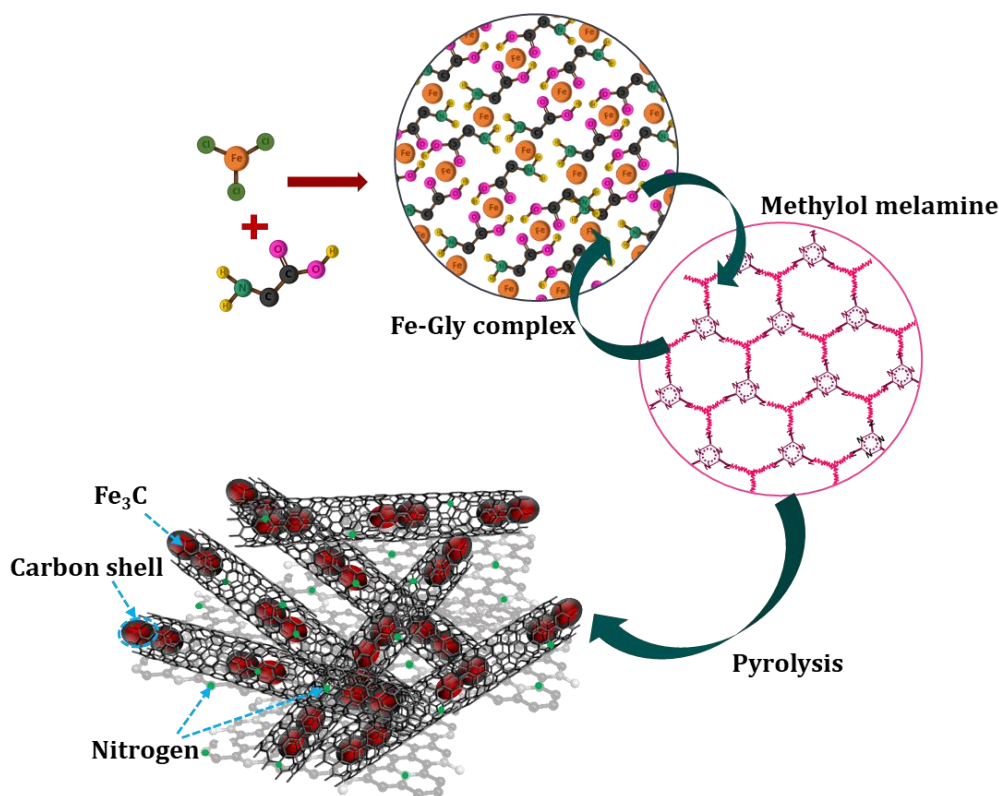


Figure 4.1 Schematic illustration of the formation of Fe-G-NC.

4.3.1 Phase Analysis

XRD patterns recorded for the samples are presented in **Figure 4.2**. All the three samples showed a peak at 25.8° corresponding to the (002) plane of the graphitic carbon. Another peak at 42° also corresponded to the (100) plane of the graphitic carbon (JCPDS: 75-1621).^{25, 26} Fe-G1-NC sample exhibited less intense peak of the Fe species since the amount of Fe added during the preparation of the sample was lower. Only a single Fe₃C peak was visible at the 2θ value of 49.1° for this sample. Upon increasing the amount of Fe, as in the case of Fe-G2-NC and Fe-G3-NC, more number of Fe₃C peaks appeared at the 2θ values of 43.6° and 51° corresponding to the (102) and (122) planes, respectively (JCPDS:77-0255).²⁷ More intense less broader graphitic carbon peaks of Fe-G2-NC indicated its higher crystallinity and degree of graphitization.

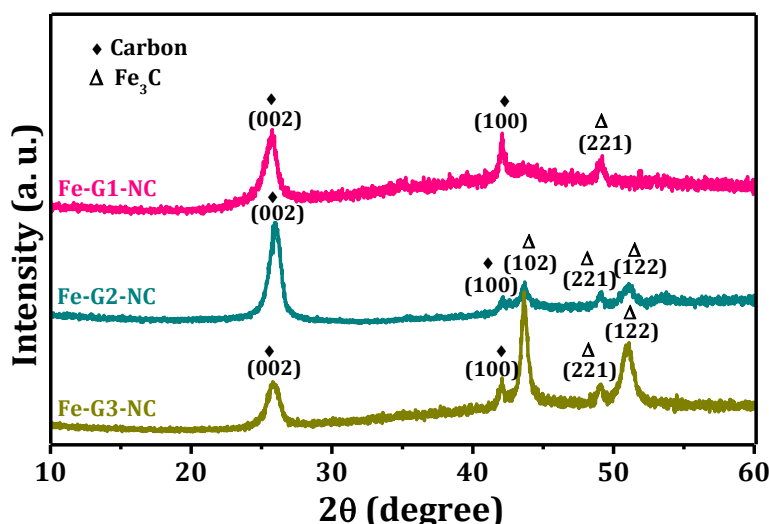


Figure 4.2 Powder X-ray diffraction patterns of Fe-G1-NC, Fe-G2-NC and Fe-G3-NC.

The information about the extent of defects, the ordered and disordered structures and the graphitic nature were obtained from Raman spectroscopy. **Figure 4.3** represents the comparison of the Raman spectra of the samples with different molar composition of Fe and glycine. All the samples showed two main peaks at 1360 and 1580 cm^{-1} corresponding to the D and G bands, respectively. The D band was indicative of the disordered graphite structure, whereas the G band indicated the presence of crystalline graphitic carbon. The extent of disorder within the samples can be estimated by the intensity ratio of the D and G bands (I_D/I_G).^{28,29} The I_D/I_G ratio increased from 0.94 to 0.99 to 1.03 respectively for Fe-G1-NC, Fe-G2-NC and Fe-G3-NC. Increased Fe content caused a decrease in the degree of graphitization since the graphitic structure of the resultant carbon gets deformed by the inclusion of Fe particles in the carbon lattice upon carbonization. Thus, the Fe-G3-NC sample having the highest Fe content appeared to be more disordered in the Raman spectra. Fe-G1-NC sample with enhanced graphitization degree may have increased electrical conductivity which is beneficial for the electron transport during ORR. Despite that, the decreased Fe content caused a reduction in the electrocatalytic active sites leading to reduced ORR activity. Thus, Fe-G2-NC with moderate Fe content and good graphitization was presumed to show better ORR activity.

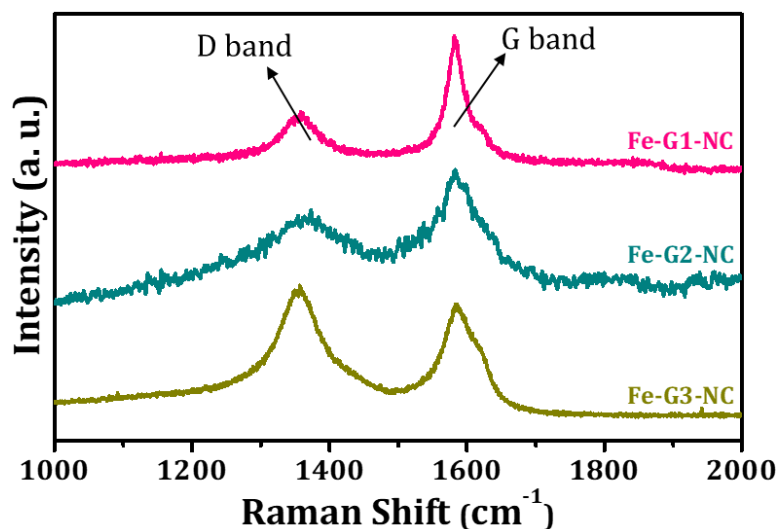


Figure 4.3 Raman spectra of Fe-G1-NC, Fe-G2-NC and Fe-G3-NC.

4.3.2 Morphology and Microstructure Analysis

The morphological and microstructural analysis were obtained from SEM microscopy. **Figure 4.4** shows the SEM micrographs of all the three samples with different Fe-Gly ratios. All the samples exhibited tube like morphology typically arising from the glycine-melamine formaldehyde precursor upon carbonization at 900 °C. Fe-G1-NC appeared to have aggregated tubular structure (**Figure 4.4a & b**) and a similar structure was also observed for Fe-G3-NC sample (**Figure 4.4e & f**). Interestingly, darker particles enclosed within hollow tubes was observed for Fe-G2-NC sample and the nanotubes appeared overlapped with one another (**Figure 4.4c & d**). Such a structure is believed to assist in the enhancement of the kinetics of the electrocatalysis process by improving the mass and electron transport.²¹ The AFM images of Fe-G2-NC sample presented in **Figure 4.5** also evidenced a tubular morphology.

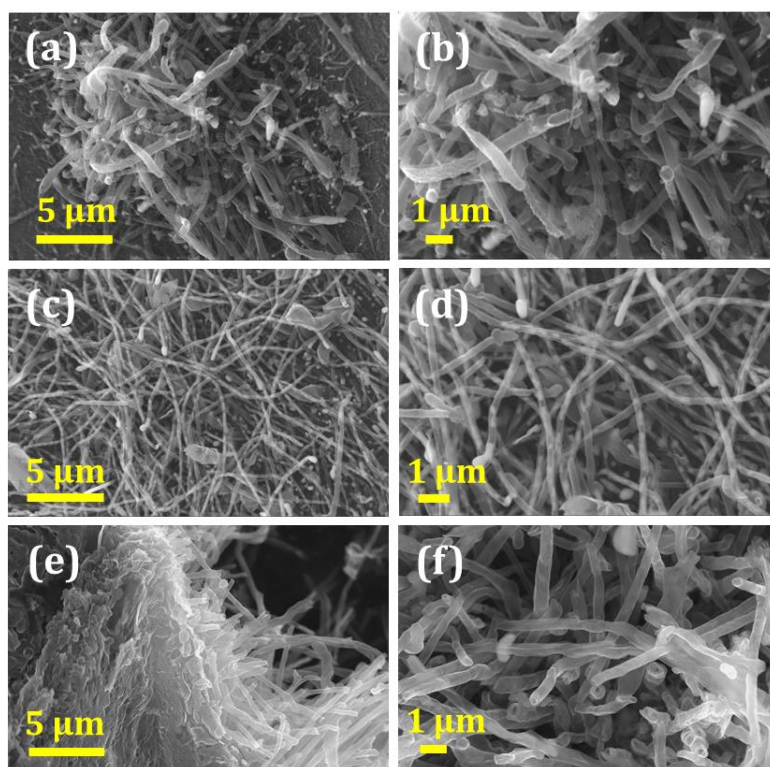


Figure 4.4 SEM images of (a, b) Fe-G1-NC (c, d) Fe-G2-NC and (e, f) Fe-G3-NC.

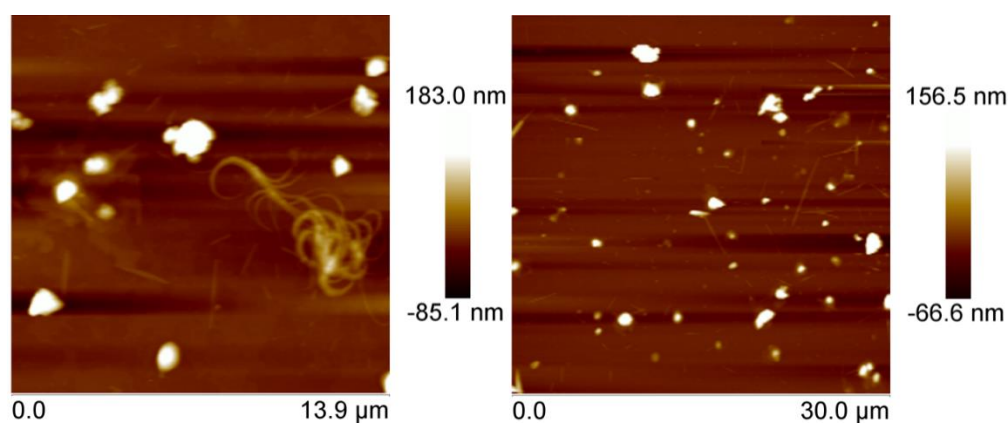


Figure 4.5 AFM images of Fe-G2-NC.

The EDAX spectrum confirmed the presence of C, N, O and Fe (**Figure 4.6**), while the elemental mapping presented in **Figure 4.7** indicated the homogeneous dispersion of N and Fe in the carbon matrix. Fe-G2-NC sample especially showed good amount of N and Fe as seen in **Figure 4.7b**.

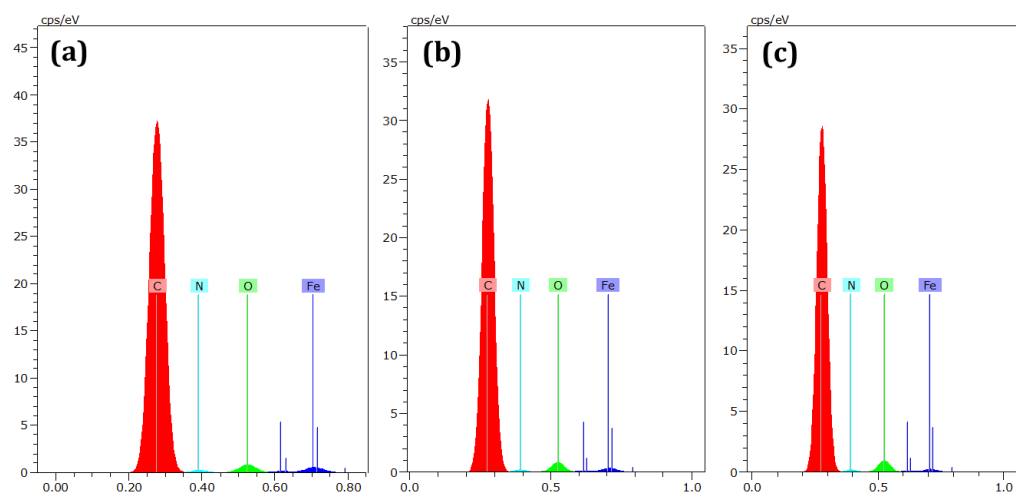


Figure 4.6 EDAX spectra of (a) Fe-G1-NC, (b) Fe-G2-NC and (c) Fe-G3-NC.

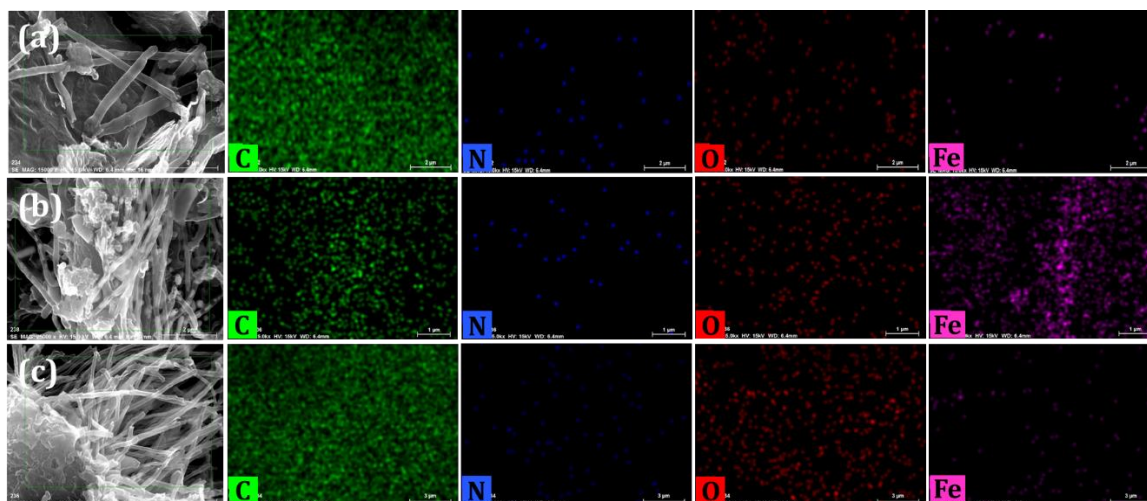


Figure 4.7 Elemental mapping of (a) Fe-G1-NC, (b) Fe-G2-NC and (c) Fe-G3-NC.

A closer look on the sample morphology was obtained from TEM analysis. **Figure 4.8a, c & i** showed a mixture of sheet like and tubular morphologies for all the carbonized samples. The darker particles seen were iron species and their phases were previously identified from XRD as Fe₃C. The sheets and tubes observed are composed of graphitic carbon. The HR-TEM images (**Figure 4.8b, d & j**) and the corresponding SAED patterns shown in the inset are consistent with the (002) plane of the graphitic carbon with a d-spacing of 0.34 nm.^{30,31} It should be noted that the presented TEM images were all after acid washing of the samples to remove the soluble iron. Unlike the other two samples, there was a slight difference in the morphology for Fe-G2-NC sample where, tubular hollow graphitic carbon (pod-like structure) enclosed with darker particles were observed. Even though lesser amount of Fe was added for the preparation of Fe-G2-NC compared to Fe-G3-NC, the TEM

image of Fe-G2-NC contained more amount of Fe species (**Figure 4.8c**). The increased amount of Fe addition during the synthesis of Fe-G3-NC presumably caused agglomeration of Fe species upon pyrolysis and hence were washed off easily on acid washing resulting in lesser Fe content in the catalyst microstructure. The formation of pod-like morphology in Fe-G2-NC was ascribed to the creation of a strong 3D network structure with optimized Fe/glycine ratio and stabilized Fe³⁺ ions. The stabilization of Fe³⁺ ions not only reduced its agglomeration during pyrolysis but also catalyzed the tube formation of the nearby carbon resulting in pod like carbon with embedded Fe₃C species. By virtue of the occupation of the Fe₃C particles inside the pod like carbon structure, it is protected from acid attack. Occasionally, the Fe₃C particles were seemed protruding out of the tube (**Figure 4.8e**), and can thus function as additional ORR active sites. The carbon tube, (**Figure 4.8c**) has around 250 nm diameter and a wall thickness of around 8 nm (**Figure 4.8d**). The entrapped Fe₃C particles possessed an elongated morphology with a length of about 450 nm and a width of about 110 nm (**Figure 4.8f**). HR-TEM image of the Fe₃C particle presented in **Figure 4.8g** showed a graphitic carbon shell of thickness about 8 nm. The HR-TEM image shown in **Figure 4.8h** had a d-spacing of 0.34 nm, confirming the graphitic carbon structure surrounding the Fe₃C particle.

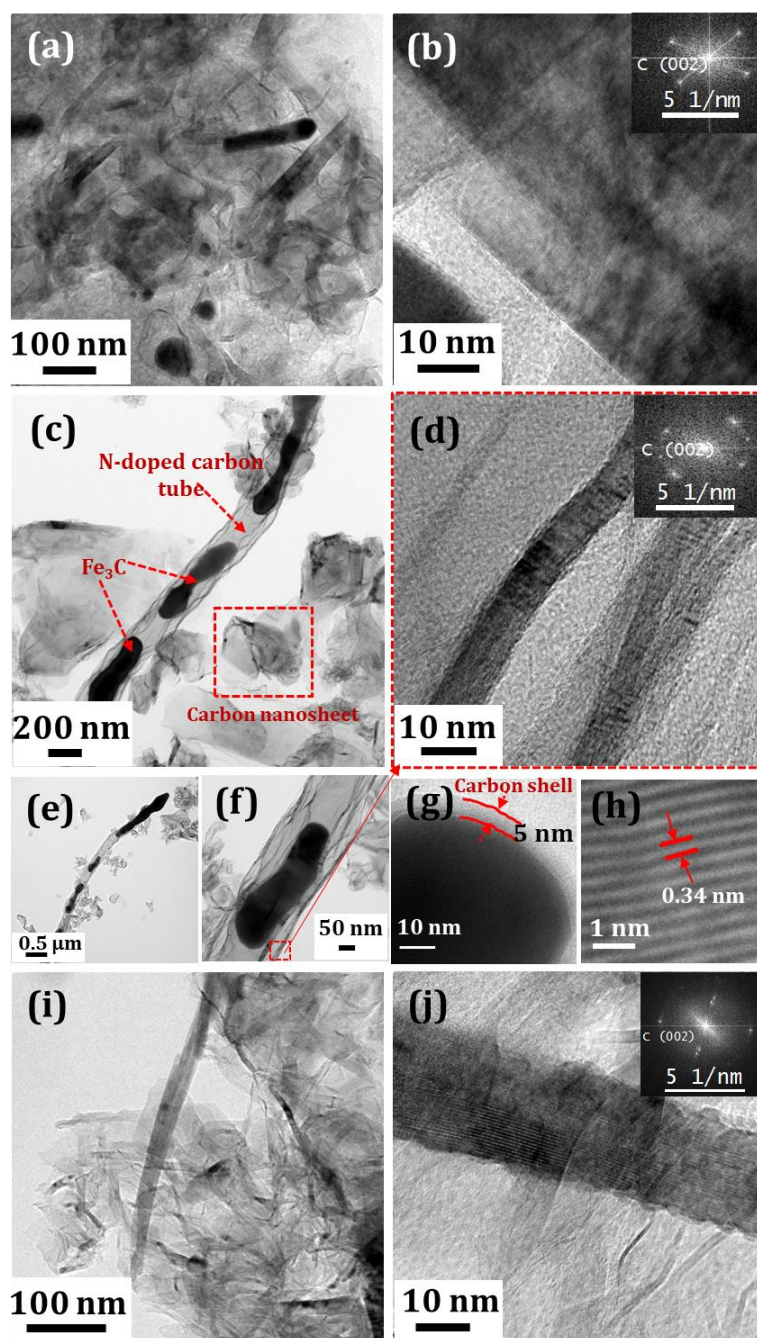


Figure 4.8 TEM images of (a, b) Fe-G1-NC (c, d, e, f, g, h) Fe-G2-NC and (i, j) Fe-G3-NC.

4.3.3 Surface Area Analysis

The BET surface area and pore characteristics of the carbonized samples were analyzed from N₂ adsorption-desorption analysis (performed at 77 K). All the three samples had almost similar surface area (as also reflected by identical isotherms below $P/P_0 < 0.3$) of 205 m² g⁻¹. The surface area of the sample was found not to be dependent on the amount of Fe in it. The isotherms appeared to be similar to Type II

with H3 Hysteresis loop (Ref: IUPAC technical report 2015). However, the well-defined inflection point and significant adsorption at low P/P₀ values indicated that at least some part of the constituent particles is small enough to form a microporous structure. The H3 hysteresis indicated a structure with the presence of non-rigid aggregation of plate-like particles (**Figure 4.9a**). The pore size distribution curve obtained from NLDFT analysis shown in **Figure 4.9b** also indicated the heteroporosity in the samples. The cumulative pore volume measured from BJH was found to be 0.45 cm³ g⁻¹, 0.52 cm³ g⁻¹ and 0.58 cm³ g⁻¹, respectively for Fe-G1-NC, Fe-G2-NC and Fe-G3-NC (**Figure 4.9c**).

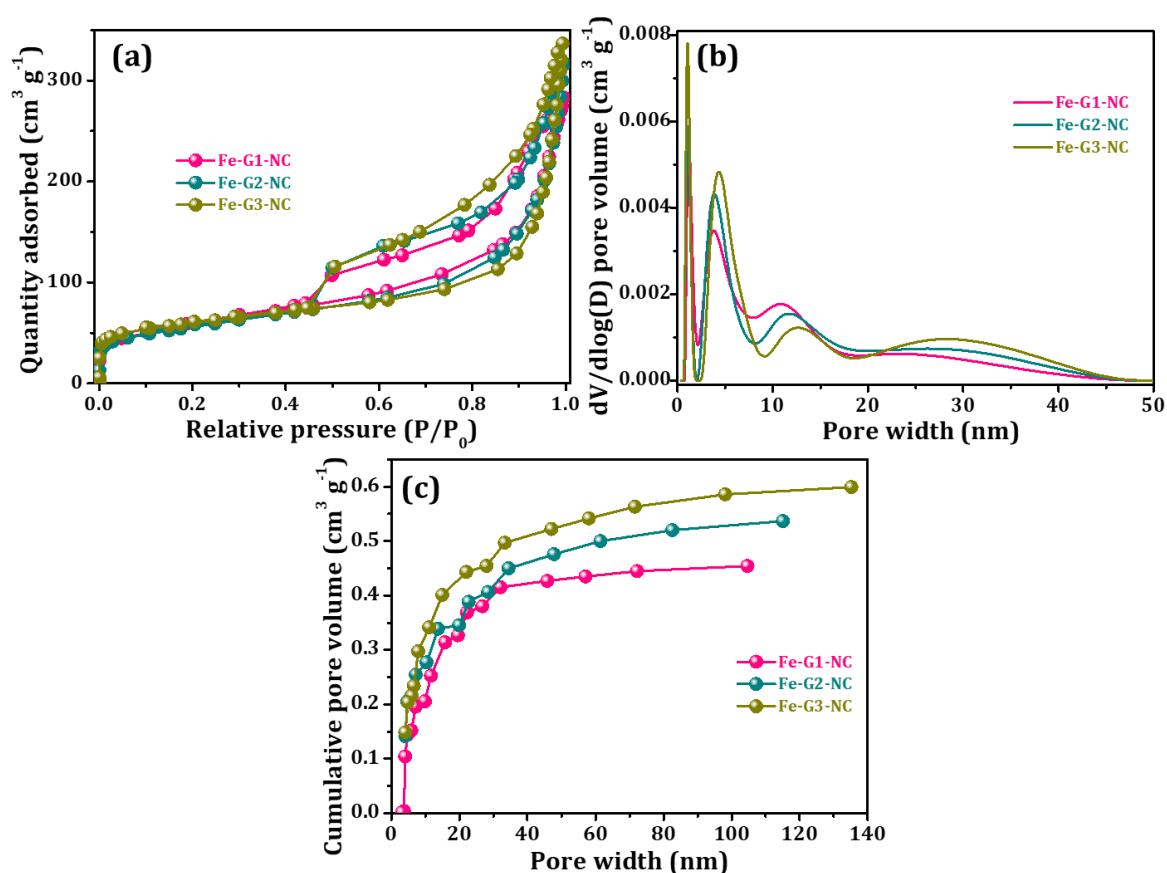


Figure 4.9 (a) N₂ adsorption-desorption isotherms and (b) NLDFT pore size distribution curves and (c) BJH cumulative pore volume of Fe-G1-NC, Fe-G2-NC and Fe-G3-NC.

4.3.4 Chemical Compositional Analysis

The surface chemical composition and the extent of N doping were confirmed using XPS analysis. **Figure 4.10** represents the survey spectrum of the three samples which showed peaks corresponding to elements C, N, and Fe. Furthermore, a peak at 534 eV

designated the existence of the doped or surface adsorbed O. The intensity of the O peak is the highest for Fe-G3-NC among the three samples resulting increased defects on the carbon structure. This could also be the reason for the enhanced I_D/I_G ratio obtained in the Raman spectra.

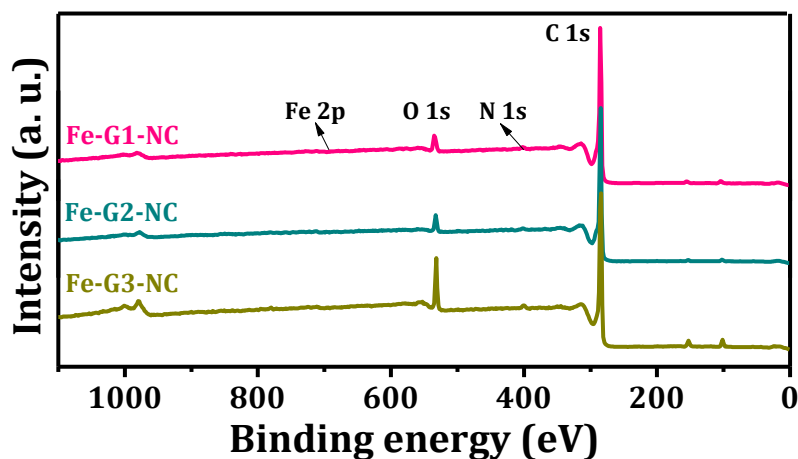


Figure 4.10 XPS survey spectrum of Fe-G1-NC, Fe-G2-NC and Fe-G3-NC.

The atomic percentages of the elements present in the samples obtained from XPS are summarized in **Table 4.1**. The sample with the lowest amount of added FeCl₃, Fe-G1-NC, has the lowest atomic percentage of N (1.0 at. %). For Fe-G2-NC, the atomic percentage of N increased to a higher value of 1.8 at. %, probably due to the enhanced Fe-N coordination with increased Fe content. However, further increase in Fe addition, i.e., in the case of Fe-G3-NC, caused a reduction of the N content (1.1 at. %). The percentage of the Fe content on the other hand, increased from Fe-G1-NC to Fe-G3-NC. Even though the TEM images of Fe-G2-NC obviously showed higher amount of the Fe species inside the tubes, the atomic percentage of Fe detected from XPS was low (0.2 at.%). This was not totally unexpected as XPS analysis was limited to the surface of the sample only. Moreover, the Fe atoms from the particles inside the carbon nanotubes were obviously not reflected in the XPS count, as the nanotube shield would have protected the Fe species from the incident X-ray photons. Atomic percentage of N should have varied along with the Fe addition, but it was also clear that the presence of higher N content was indirectly promoted by the formation of unique tubular morphology owing to the optimum Fe/Gly ratio, which obviously helped to retain more N atoms during pyrolysis.

Table 4.1 Atomic percentages of C, O, N and Fe of various samples obtained from XPS

Sample	C (at.%)	O (at.%)	N (at.%)	Fe (at.%)
Fe-G1-NC	93.9	5.1	1.0	<0.1
Fe-G2-NC	93.5	4.5	1.8	0.2
Fe-G3-NC	88.3	10.3	1.1	0.3

In addition to the amount of N, the type of N species also had impact on the ORR activity. The deconvoluted N 1s spectra of all the samples are presented in **Figure 4.11** and their percentages are also quantified. Two types of N species namely pyridinic N (398.6 eV) and graphitic N (401.5 eV) were identified from the N 1s spectra. Since the binding energy of the Fe-N bond was also near to that of the pyridinic N, the peak at 398.6 eV represented the Fe-N bond also.³²

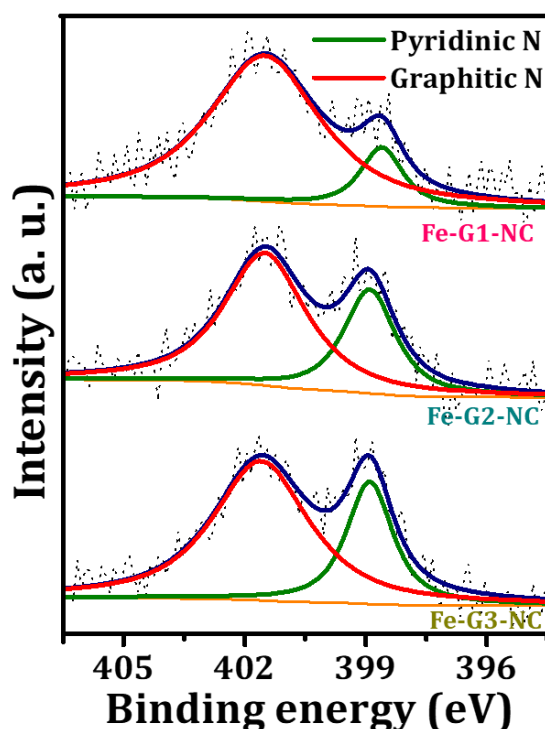


Figure 4.11 Deconvoluted N 1s spectra of Fe-G1-NC, Fe-G2-NC and Fe-G3-NC.

The fraction of the graphitic N was found to be higher in all the samples as shown in **Figure 4.12** and was attributed to the strong network structure of the precursors resulting in stronger Fe-N interaction. The strong network upon pyrolysis ultimately led to the formation of entrapped N in the carbon matrix (graphitic N) rather than

edge N species (pyridinic and pyrrolic). Due to the existence of greater amount of the pyridinic and graphitic N in Fe-G2-NC, the sample is expected to display good catalytic activity.

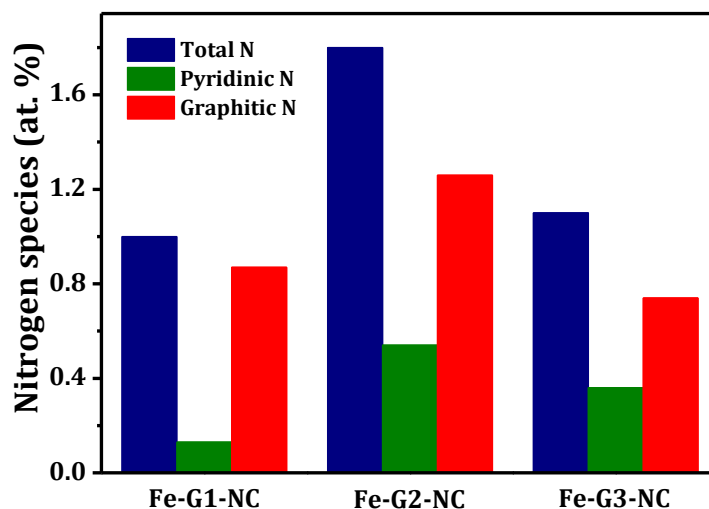


Figure 4.12 Atomic percentage of different types of N species present in Fe-G1-NC, Fe-G2-NC and Fe-G3-NC.

The high-resolution Fe 2p spectra presented in **Figure 4.13** indicated two main peaks at 711.6 and 725 eV for all the three samples, representing the binding energies of Fe 2p_{3/2} and Fe 2p_{1/2} of Fe³⁺ ion, respectively.³³ Further deconvolution of the peaks was found difficult as the percentage of Fe was very low.

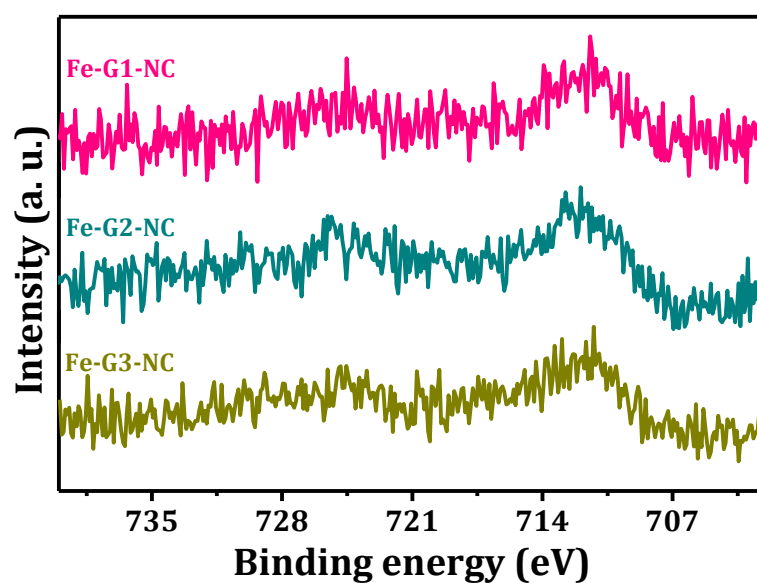


Figure 4.13 High resolution Fe 2p XPS spectra of Fe-G1-NC, Fe-G2-NC and Fe-G3-NC.

The high-resolution C 1s spectra (**Figure 4.14**) can be deconvoluted into two major peaks with the primary peak at 284.8 eV corresponding to the sp² carbon. The peak at 285.7 eV corresponded to the C-N bond. An additional peak at low binding energy was detected for Fe-G3-NC representing the Fe-C bonding.³⁴

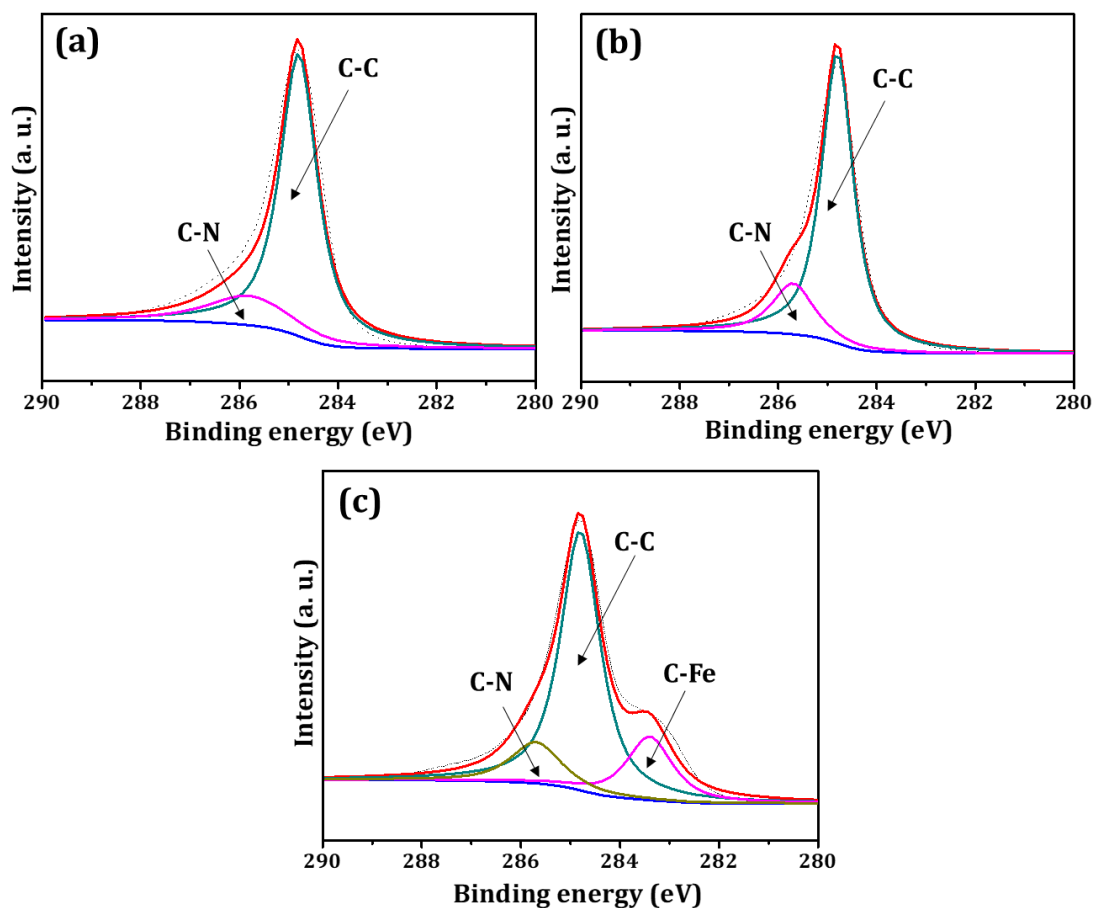


Figure 4.14 Deconvoluted C 1s spectra of (a) Fe-G1-NC, (b) Fe-G2-NC and (c) Fe-G3-NC.

4.3.5 Electrochemical Analysis

The electrochemical analyses of the samples were carried out using a rotating disc electrode (RDE) set up. The cyclic voltammetry (CV) recorded for Fe-G1-NC, Fe-G2-NC, Fe-G3-NC and the commercial Pt/C samples in N₂ and O₂ saturated 0.1 M KOH solution are given in **Figure 4.15 a-d**. In N₂ saturated KOH solution, the CV curve is devoid of any characteristic peak indicating the absence of any Faradaic reactions. After oxygen saturation, there was a rapid increase in current density in the cathodic direction owing to the reduction of oxygen molecules.

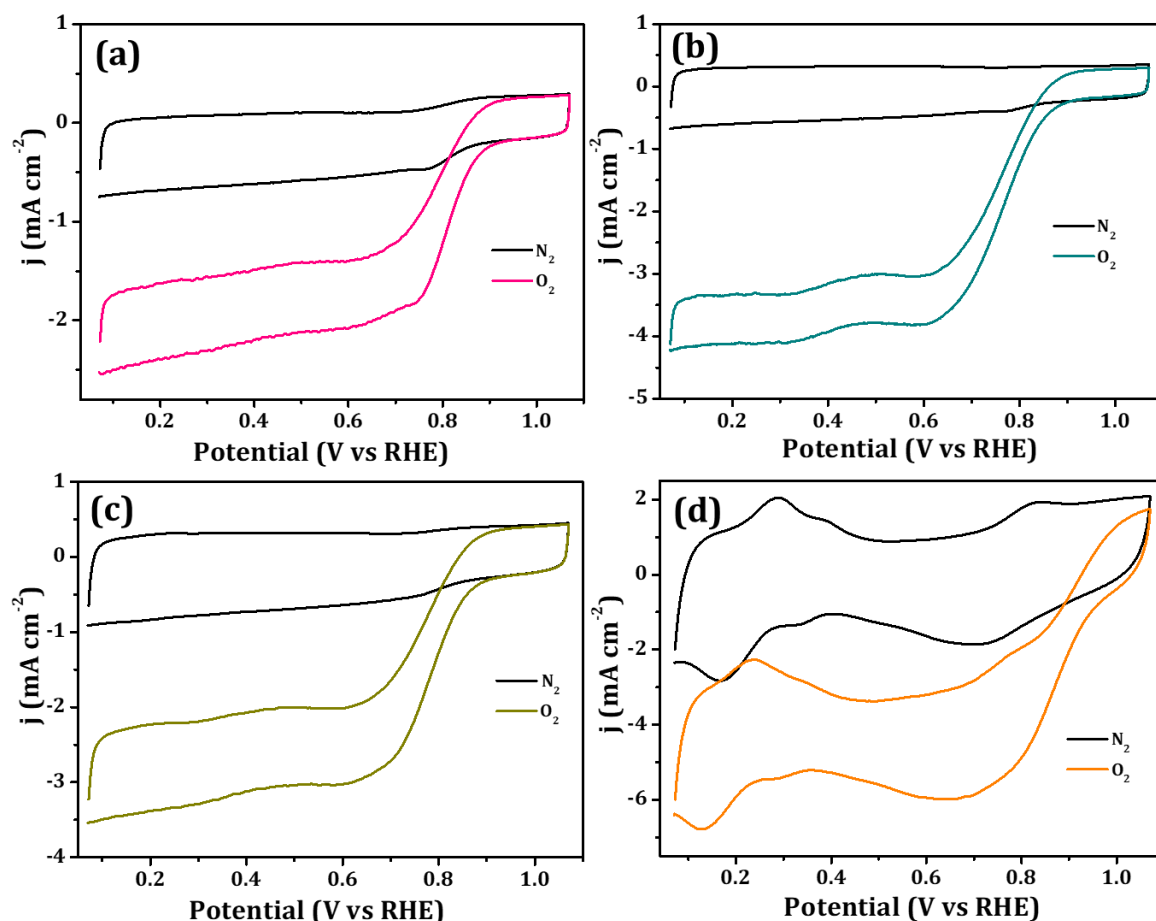


Figure 4.15 Cyclic voltammograms of (a) Fe-G1-NC, (b) Fe-G2-NC, (c) Fe-G3-NC and (d) Pt/C in N₂ and O₂ saturated 0.1 M KOH solution measured at a scan rate of 50 mV s⁻¹ at 900 rpm.

Linear sweep voltammetry (LSV) was done for a better understanding of the ORR activity of the catalysts. The LSV was conducted at a scan rate of 10 mV s⁻¹ with a working electrode rotation speed of 1600 rpm. **Figure 4.16** shows the LSV curves of the synthesized samples in comparison with the commercial 40 wt. % Pt/C (Johnson Matthey) sample. The ORR onset potential of the samples Fe-G1-NC and Fe-G3-NC were found to be 0.92 V which is 80 mV lower than that of Pt/C, whereas that of Fe-G2-NC was 0.95 V which is only 50 mV lower than Pt/C. The $E_{1/2}$ for Fe-G1-NC and Fe-G3-NC were 0.76 and 0.74 V, respectively, whereas it was higher for Fe-G2-NC (0.80 V). There is only 30 mV difference in the $E_{1/2}$ value of Fe-G2-NC compared to Pt/C. In addition to the enhanced onset and half wave potentials, Fe-G2-NC also possessed a high limiting current density of -4.5 mA cm⁻². These factors make the sample a potential ORR electrocatalyst. Though there are various theoretical and experimental studies conducted for a better understanding of the origin of electrocatalytic activity

of the Fe, N-doped catalysts, the exact mechanism is still unclear. The presence of the Fe/Fe₃C particles with Fe-N coordination is reported to show enhanced ORR performance. Moreover, the existence of pyridinic and graphitic N influences the ORR pathway.

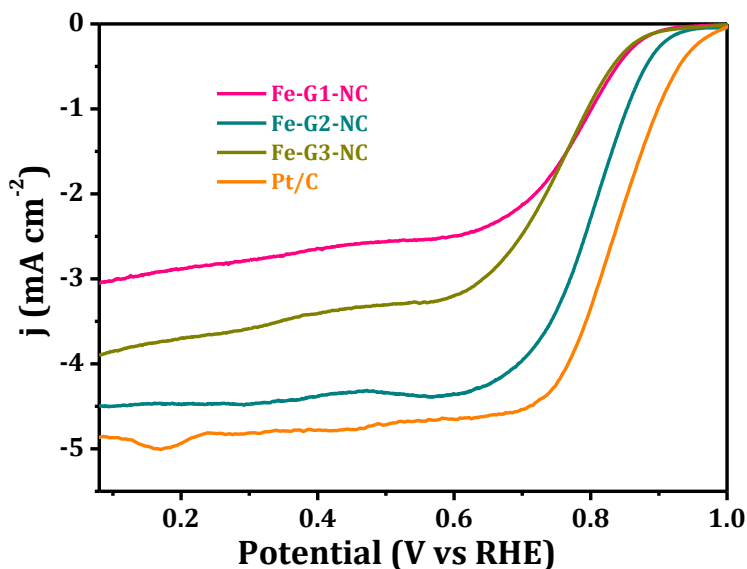


Figure 4.16 Linear sweep voltammogram comparison of Fe-G1-NC, Fe-G2-NC, Fe-G3-NC and Pt/C in O₂ saturated 0.1 M KOH solution measured at a scan rate of 10 mV s⁻¹ at 1600 rpm.

The LSV recorded for Fe-G1-NC, Fe-G2-NC, Fe-G3-NC and Pt/C at different working electrode rotation speeds are shown in **Figure 4.17a-d**. The limiting current density increased with increase in rotation speed due to the enhancement in the mass transfer and electrolyte diffusion.

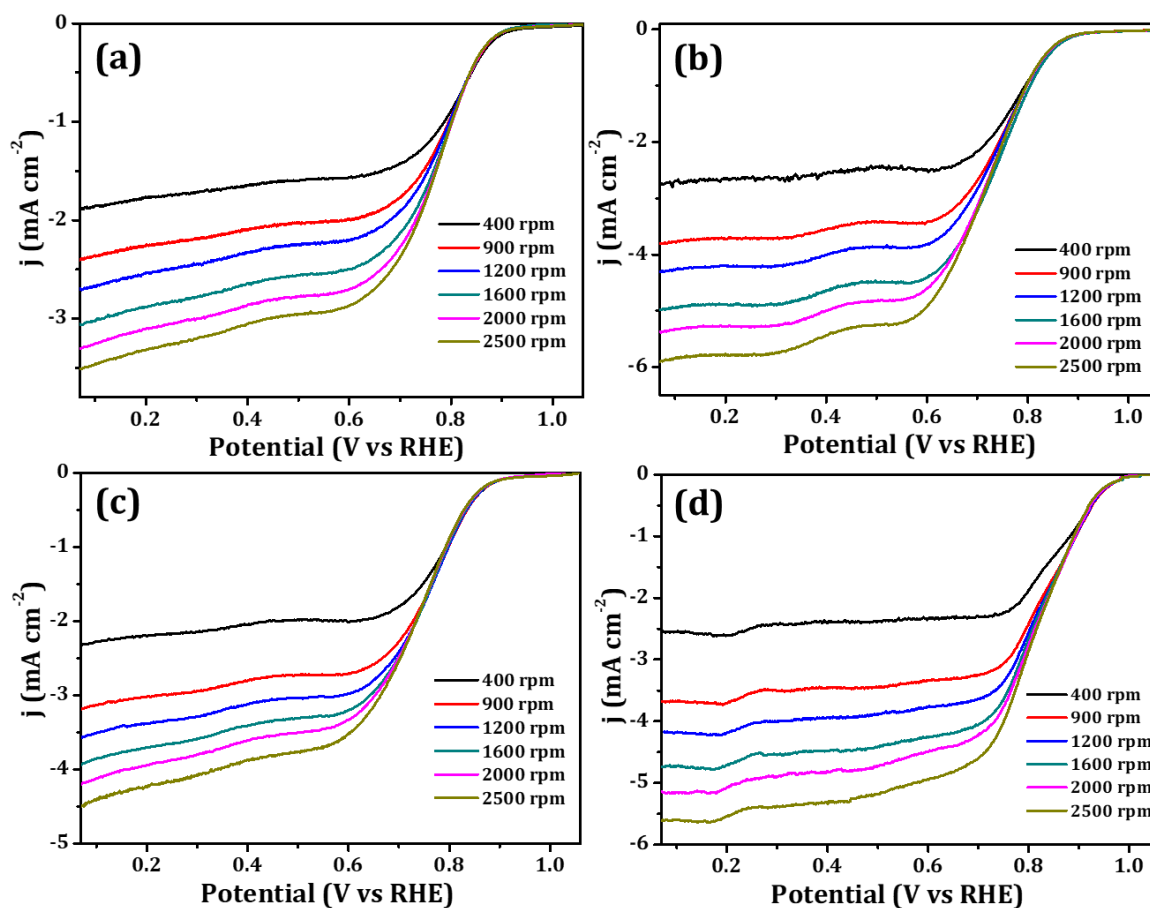


Figure 4.17 LSVs of (a) Fe-G1-NC (b) Fe-G2-NC (c) Fe-G3-NC and (d) Pt/C in O₂ saturated 0.1 M KOH solution measured at different rotation speeds at a scan rate of 10 mV s⁻¹ at 1600 rpm.

The K-L plots were obtained by plotting $1/j$ against $1/\omega^{1/2}$. From the slope, the number of electron transfer was calculated according to the following equation.³⁵

$$\frac{1}{j} = \frac{1}{j_d} + \frac{1}{j_k} \quad (4.1)$$

$$\frac{1}{j} = \frac{1}{0.62nFAC_0^*D_0^{2/3}\nu^{-1/6}\omega^{1/2}} + \frac{1}{nFAkC_0^*} \quad (4.2)$$

where, j is the measured current density, j_d is the diffusion-limiting current density, j_k is the kinetic current density, ω is the angular rotation ($\omega=2\pi f/60$, f is the rotation speed), n is the number of transferred electrons during ORR, F is the Faraday's constant (96480 C), C_0^* is the bulk concentration of O₂ (1.22×10^{-6} mol cm⁻³), D_0 is the diffusion coefficient of O₂ (1.9×10^{-5} cm² s⁻¹), ν is the kinematic viscosity of the electrolyte (0.01 cm² s⁻¹) and k is the electron transfer rate constant

The K-L plots of all the samples have appeared linear indicating first order ORR kinetics (**Figure 4.18**).

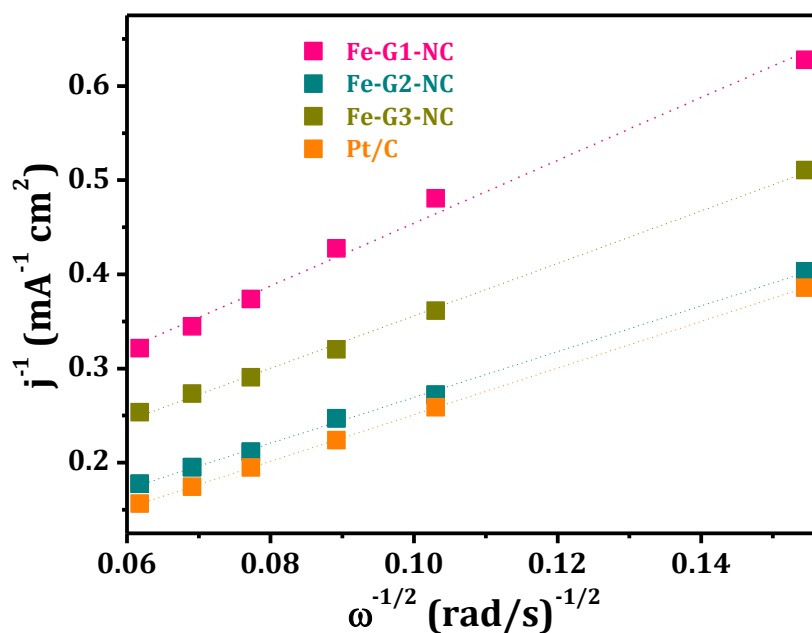


Figure 4.18 Comparison of the Koutecky-Levich (K-L) plots of Fe-G1-NC, Fe-G2-NC, Fe-G3-NC and Pt/C.

Figure 4.19a gives the number of electrons transferred (n) during the ORR process for all the samples. For Fe-G1-NC, Fe-G2-NC and Pt/C, n appeared to be almost constant at all the potentials whereas slight deviation was observed in the case of Fe-G3-NC, indicating its poor consistency. The average values of n obtained are 3.7, 3.8, 3.3 and 3.9 respectively for Fe-G1-NC, Fe-G2-NC, Fe-G3-NC and Pt/C. The amount of peroxide generated was also quantified in percentages and the values for Fe-G1-NC, Fe-G2-NC, Fe-G3-NC and Pt/C were respectively 15, 10, 33 and 4% (**Figure 4.19b**). From the value of n and % H₂O₂, Fe-G2-NC was identified as the catalyst with appreciable ORR catalytic activity.

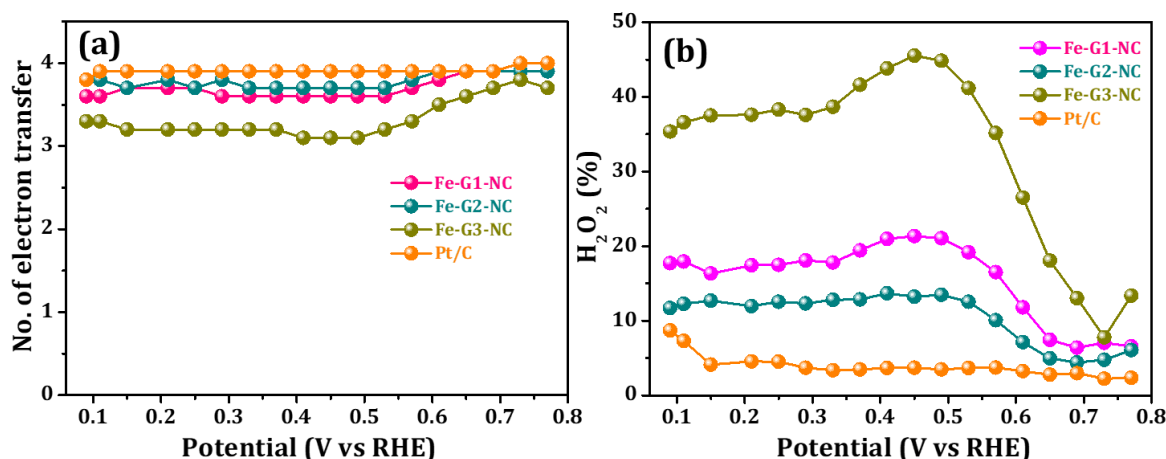


Figure 4.19 Comparison of (a) number of electrons transferred and (b) hydrogen peroxide yield at different potentials obtained from the RRDE experiment.

Further information about the ORR kinetics was obtained from Tafel plot by plotting logarithm of the kinetic current density (in the onset region of the LSV curve measured at 1600 rpm) against the corresponding potential (**Figure 4.20**). To eliminate possible contributions from ohmic polarization, 65 % iR compensation was applied while plotting. The Tafel plots of the samples are calculated to be 84, 73, 87 and 60 mV dec⁻¹, respectively, for Fe-G1-NC, Fe-G2-NC, Fe-G3-NC and Pt/C. The lower the Tafel slope, faster will be the ORR kinetics. The relatively closer values of the Tafel slope for Fe-G2-NC with Pt/C indicate similar ORR mechanisms. **Table 4.2** summarizes the electrocatalytic performance of the prepared samples.

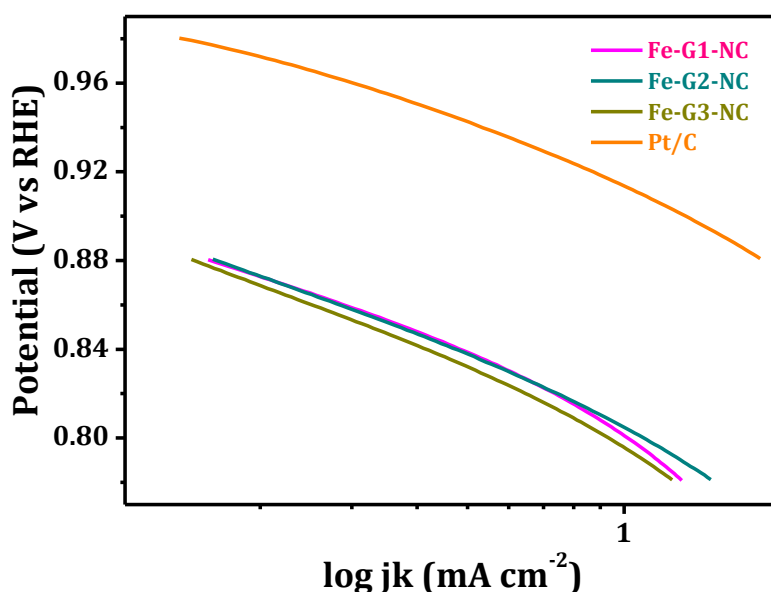
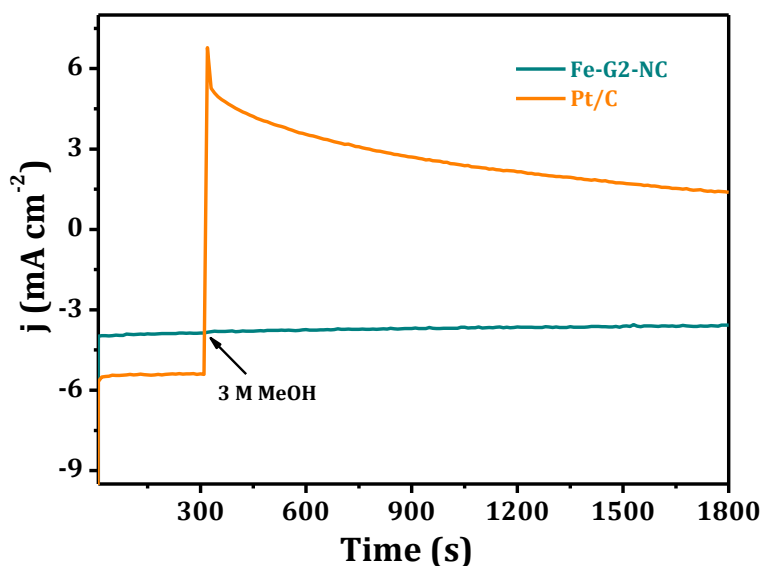


Figure 4.20 Comparison of Tafel slopes of Fe-G1-NC, Fe-G2-NC, Fe-G3-NC and Pt/C.

Table 4.2 Comparison of electrocatalytic performance of the samples

Sample	E _{onset} (V vs RHE)	E _{1/2} (V vs RHE)	n	H ₂ O ₂ (%)	Tafel slop (mV dec ⁻¹)
Fe-G1-NC	0.92	0.76	3.7	15	84
Fe-G2-NC	0.95	0.80	3.8	10	73
Fe-G3-NC	0.92	0.74	3.3	33	87
Pt/C	1.00	0.83	3.9	4	60

Methanol poisoning test was performed by the chronoamperometric method in 0.1 M KOH at a rotation speed of 1600 rpm for Fe-G2-NC, and the result was compared with that of Pt/C (**Figure 4.21**). The test was carried out for 2000 s and 3 M methanol was added during the initial stage (300 s) of analysis. The addition of methanol resulted in a rapid decrease in the cathodic current when Pt/C was coated on the working electrode, indicating its significant intolerance towards methanol. This was due to the methanol oxidation on the surface of Pt which ultimately leads to its poisoning. The current density generated by Fe-G2-NC on the other hand appeared to be intact, signifying its excellent methanol tolerance.

**Figure 4.21** Methanol tolerance study of Fe-Gly-2 MF-C in comparison with Pt/C.

The stability of the catalyst was investigated using ADT in O₂ saturated 0.1 M KOH. From the LSVs recorded before and after 5000 cycles of ADT, the shift in the E_{1/2} value

was calculated (**Figure 4.22**). The catalyst Fe-G2-NC exhibited excellent durability with only a slight shift in $E_{1/2}$ (10 mV) whereas Pt/C exhibited poor durability with a 30 mV shift in $E_{1/2}$. All these results indicated that the synthesized Fe-G2-NC sample was a potential electrocatalyst towards ORR by virtue of its excellent activity, durability and methanol tolerance.

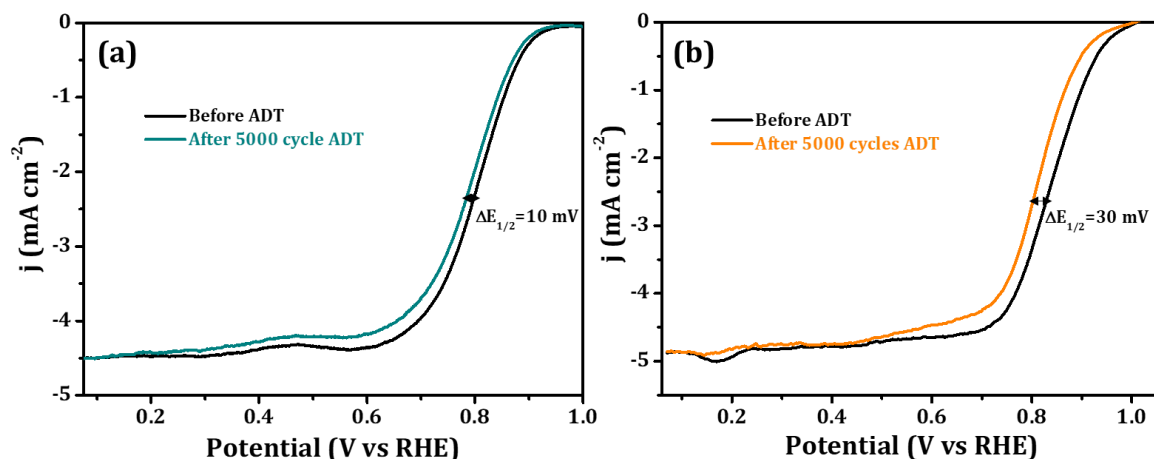


Figure 4.22 LSVs recorded before and after the 5000 cycle ADT analysis of (a) Fe-G2-NC and (b) Pt/C in O₂ saturated 0.1 M KOH solution with a working electrode rotation of 1600 rpm.

The enhanced electrocatalytic performance of Fe-G2-NC could be ascribed to many reasons. The unique pod-like morphology of the catalyst played a vital role. The projection of catalytically active Fe₃C species outwards the hollow carbon aided greater exposure and allowing its utilization towards ORR activity. Furthermore, the overlapped tubular structure could also enhance the kinetics by improved mass transportation during the ORR process. Additionally, the heteroporous architecture with high surface area provided more sites for O₂ adsorption and the mesopores promoted faster diffusion of O₂. High degree of graphitization with I_b/I_G ratio of 0.99 imparted good electrical conductivity and facilitated the electron transfer. The presence of high atomic percentage of N alters the electronic structure of carbon thereby providing large number of active sites for O₂ adsorption. The high fraction of pyridinic and graphitic N species boosts the electrical conductivity and hydrophilicity. A combination of such useful attributes rendered the Fe-G2-NC with enhanced electrocatalytic activity towards oxygen reduction.

4.4 Conclusions

Fe, N-doped, heteroporous, tubular graphitic carbon was successfully synthesized through the simple pyrolysis of a hybrid thermosetting network structure formed by mixing Fe-glycine complex and melamine formaldehyde (MF). The stronger network of MF resin resulted in the formation of heteroporous carbon containing predominantly of catalytically active graphitic and pyridinic N without the formation of any measurable pyrrolic N. The optimized composition, Fe-G2-NC, exhibited appreciable electrocatalytic behavior with an onset potential of 0.95 V along with excellent stability and methanol tolerance. The micro/meso porous architecture with pod like morphologies and the presence of encapsulated Fe/Fe₃C particle in carbon nanostructure contributed towards the enhanced catalytic activity. The present study thus provides an easy synthetic method for the development of Fe, N-doped heteroporous carbon with outstanding electro-catalytic properties.

References

1. Ge, X.; Sumboja, A.; Wu, D.; An, T.; Li, B.; Goh, F. W. T.; Hor, T. S. A.; Zong, Y.; Liu, Z., Oxygen Reduction in Alkaline Media: From Mechanisms to Recent Advances of Catalysts. *ACS Catal.* **2015**, 5 (8), 4643.
2. Paraknowitsch, J. P.; Thomas, A., Doping Carbons Beyond Nitrogen: An Overview of Advanced Heteroatom Doped Carbons with Boron, Sulphur and Phosphorus for Energy Applications. *Energy Environ. Sci.* **2013**, 6 (10), 2839.
3. Dong, F.; Cai, Y. X.; Liu, C.; Liu, J. Y.; Qiao, J. L., Heteroatom (B, N and P) Doped Porous Graphene Foams for Efficient Oxygen Reduction Reaction Electrocatalysis. *Int. J. Hydrogen Energy* **2018**, 43 (28), 12661.
4. Tian, H.; Wang, N.; Xu, F.; Zhang, P.; Hou, D.; Mai, Y.; Feng, X., Nitrogen-Doped Carbon Nanosheets and Nanoflowers with Holey Mesopores for Efficient Oxygen Reduction Catalysis. *J. Mater. Chem. A* **2018**, 6 (22), 10354.
5. Singh, S. K.; Takeyasu, K.; Nakamura, J., Active Sites and Mechanism of Oxygen Reduction Reaction Electrocatalysis on Nitrogen-Doped Carbon Materials. *Adv. Mater.* **2019**, 31 (13), 1804297.
6. Liu, Y.; Jiang, H.; Zhu, Y.; Yang, X.; Li, C., Transition Metals (Fe, Co, and Ni) Encapsulated in Nitrogen-Doped Carbon Nanotubes as Bi-Functional Catalysts for Oxygen Electrode Reactions. *J. Mater. Chem. A* **2016**, 4 (5), 1694.

7. Singh, S. K.; Kashyap, V.; Manna, N.; Bhangre, S. N.; Soni, R.; Boukherroub, R.; Szunerits, S.; Kurungot, S., Efficient and Durable Oxygen Reduction Electrocatalyst Based on CoMn Alloy Oxide Nanoparticles Supported Over N-Doped Porous Graphene. *ACS Catal.* **2017**, 7 (10), 6700.
8. Li, T.; Deng, H.; Liu, J.; Jin, C.; Song, Y.; Wang, F., First-Row Transition Metals and Nitrogen Co-Doped Carbon Nanotubes: The Exact Origin of the Enhanced Activity for Oxygen Reduction Reaction. *Carbon* **2019**, 143, 859.
9. Stoyanov, S. R.; Titov, A. V.; Král, P. Transition Metal and Nitrogen Doped Carbon Nanostructures. *Coord. Chem. Rev.* **2009**, 253 (23), 2852.
10. Masa, J.; Xia, W.; Muhler, M.; Schuhmann, W. On the Role of Metals in Nitrogen-Doped Carbon Electrocatalysts for Oxygen Reduction. *Angew. Chem. Int. Ed.* **2015**, 54 (35), 10102.
11. Wu, G.; Zelenay, P. Nanostructured Nonprecious Metal Catalysts for Oxygen Reduction Reaction. *Acc. Chem. Res.* **2013**, 46 (8), 1878.
12. Jaouen, F.; Proietti, E.; Lefèvre, M.; Chenitz, R.; Dodelet, J. P.; Wu, G.; Chung, H. T.; Johnston, C. M.; Zelenay, P. Recent Advances in Non-Precious Metal Catalysis for Oxygen-Reduction Reaction in Polymer Electrolyte Fuel Cells. *Energy Environ. Sci.* **2011**, 4 (1), 114.
13. Liu, D. X.; Wang, B.; Li, H. G.; Huang, S. F.; Liu, M. M.; Wang, J.; Wang, Q. J.; Zhang, J. J.; Zhao, Y. F., Distinguished Zn, Co-N_x-C-S_y Active Sites Confined in Dentric Carbon for Highly Efficient Oxygen Reduction Reaction and Flexible Zn-Air Batteries. *Nano Energy* **2019**, 58, 277.
14. Qian, Y.; Khan, I. A.; Zhao, D., Electrocatalysts Derived from Metal-Organic Frameworks for Oxygen Reduction and Evolution Reactions in Aqueous Media. *Small* **2017**, 13 (37), 1701143.
15. Li, M.; Liu, Y.; Han, L.; Xiao, J.; Zeng, X.; Zhang, C.; Xu, M.; Dong, P.; Zhang, Y., A Novel Strategy for Realizing High Nitrogen Doping in Fe₃C-Embedded Nitrogen and Phosphorus-Co-Doped Porous Carbon Nanowires: Efficient Oxygen Reduction Reaction Catalysis in Acidic Electrolytes. *J. Mater. Chem. A* **2019**, 7 (30), 17923.
16. Feng, W.; Liu, M.; Liu, J.; Song, Y.; Wang, F., Well-Defined Fe, Fe₃C, and Fe₂O₃ Heterostructures on Carbon Black: A Synergistic Catalyst for Oxygen Reduction Reaction. *Catal. Sci. Technol.* **2018**, 8 (19), 4900.
17. Liu, M.; Guo, X.; Hu, L.; Yuan, H.; Wang, G.; Dai, B.; Zhang, L.; Yu, F., Fe₃O₄/Fe₃C@Nitrogen-Doped Carbon for Enhancing Oxygen Reduction Reaction. *ChemNanoMat* **2019**, 5 (2), 187.

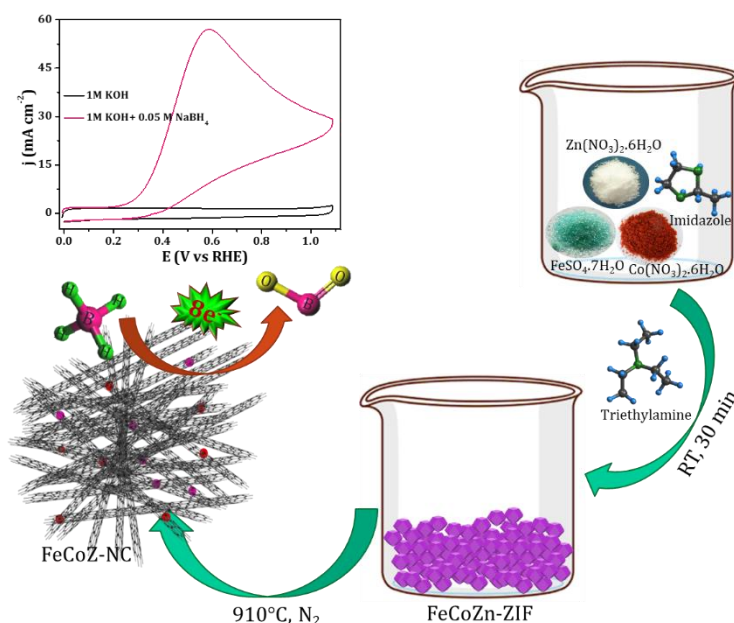
18. Kim, D.; Zussblatt, N. P.; Chung, H. T.; Becwar, S. M.; Zelenay, P.; Chmelka, B. F., Highly Graphitic Mesoporous Fe,N-Doped Carbon Materials for Oxygen Reduction Electrochemical Catalysts. *ACS Appl. Mater. Interfaces* **2018**, 10 (30), 25337.
19. Lai, Y.; Jiao, Y.; Song, J.; Zhang, K.; Li, J.; Zhang, Z., Fe/Fe₃C@Graphitic Carbon Shell Embedded in Carbon Nanotubes Derived from Prussian Blue as Cathodes for Li–O₂ Batteries. *Mater. Chem. Front.* **2018**, 2 (2), 376.
20. Lv, Q.; Si, W.; He, J.; Sun, L.; Zhang, C.; Wang, N.; Yang, Z.; Li, X.; Wang, X.; Deng, W.; Long, Y.; Huang, C.; Li, Y., Selectively Nitrogen-Doped Carbon Materials as Superior Metal-Free Catalysts for Oxygen Reduction. *Nat. Commun.* **2018**, 9 (1), 3376.
21. Hu, B. C.; Wu, Z. Y.; Chu, S. Q.; Zhu, H. W.; Liang, H. W.; Zhang, J.; Yu, S. H., SiO₂-Protected Shell Mediated Templating Synthesis of Fe-N-Doped Carbon Nanofibers and their Enhanced Oxygen Reduction Reaction Performance. *Energy Environ. Sci.* **2018**, 11 (8), 2208.
22. Xin, X.; Qin, H.; Cong, H. P.; Yu, S. H., Templating Synthesis of Mesoporous Fe₃C-Encapsulated Fe-N-Doped Carbon Hollow Nanospindles for Electrocatalysis. *Langmuir* **2018**, 34 (17), 4952.
23. Shijina, K.; Illathvalappil, R.; Sumitha, N. S.; Sailaja, G. S.; Kurungot, S.; Nair, B. N.; Peer Mohamed, A.; Anilkumar, G. M.; Yamaguchi, T.; Hareesh, U. S., Melamine Formaldehyde-Metal Organic Gel Interpenetrating Polymer Network Derived Intrinsic Fe-N-Doped Porous Graphitic Carbon Electrocatalysts for Oxygen Reduction Reaction. *New J. Chem.* **2018**, 42 (23), 18690.
24. Illathvalappil, R.; Dhavale, V. M.; Bhanke, S. N.; Kurungot, S. Nitrogen-Doped Graphene Anchored with Mixed Growth Patterns of CuPt Alloy Nanoparticles as a Highly Efficient and Durable Electrocatalyst for the Oxygen Reduction Reaction in an Alkaline Medium. *Nanoscale* **2017**, 9 (26), 9009.
25. Zhang, R.; Huang, K.; Wang, D.; Hussain, N.; Zhang, A.; Wei, H.; Ou, G.; Zhao, W.; Zhang, C.; Wu, H., Ultrafine Fe/Fe₃C Nanoparticles on Nitrogen-Doped Mesoporous Carbon by Low-Temperature Synthesis for Highly Efficient Oxygen Reduction. *Electrochim. Acta* **2019**, 313, 255.
26. Tian, Y.; Xu, L.; Qian, J.; Bao, J.; Yan, C.; Li, H.; Li, H.; Zhang, S., Fe₃C/Fe₂O₃ Heterostructure Embedded in N-Doped Graphene as a Bifunctional Catalyst for Quasi-Solid-State Zinc-Air Batteries. *Carbon* **2019**, 146, 763.
27. Deng, Y.; Wang, G.; Sun, K.; Chi, B.; Shi, X.; Dong, Y.; Zheng, L.; Zeng, J.; Li, X.; Liao, S., Highly Effective and Stable Doped Carbon Catalyst with Three-Dimensional

- Porous Structure and Well-Covered Fe₃C Nanoparticles Prepared with C₃N₄ and Tannic Acid as Template/Precursors. *J. Power Sources* **2019**, 417, 117.
28. Li, Z.; Gao, Q.; Qian, W.; Tian, W.; Zhang, H.; Zhang, Q.; Liu, Z., Ultrahigh Oxygen Reduction Reaction Electrocatalytic Activity and Stability over Hierarchical Nanoporous N-doped Carbon. *Sci. Rep.* **2018**, 8 (1), 2863.
29. Jiang, H.; Gu, J.; Zheng, X.; Liu, M.; Qiu, X.; Wang, L.; Li, W.; Chen, Z.; Ji, X.; Li, J., Defect-Rich and Ultrathin N Doped Carbon Nanosheets as Advanced Trifunctional Metal-Free Electrocatalysts for the ORR, OER and HER. *Energy Environ. Sci.* **2019**, 12 (1), 322.
30. Zhao, P.; Nie, H.; Yu, J.; Wang, J.; Cheng, G., A Facile Synthesis of Porous N-Doped Carbon with Hybridization of Fe₃C Nanoparticle-Encased CNTS for an Advanced Oxygen Reduction Reaction Electrocatalyst. *Inorg. Chem. Front.* **2018**, 5 (10), 2546.
31. Miao, Z.; Wang, X.; Tsai, M. C.; Jin, Q.; Liang, J.; Ma, F.; Wang, T.; Zheng, S.; Hwang, B. J.; Huang, Y.; Guo, S.; Li, Q. Atomically Dispersed Fe-N_x/C Electrocatalyst Boosts Oxygen Catalysis via a New Metal-Organic Polymer Supramolecule Strategy. *Adv. Energy Mater.* **2018**, 8 (24), 1801226.
32. Li, Q.; Zhao, J.; Wu, M.; Li, C.; Han, L.; Liu, R., Hierarchical Porous N-doped Carbon Nanofibers Supported Fe₃C/Fe Nanoparticles as Efficient Oxygen Electrocatalysts for Zn-Air Batteries. *ChemistrySelect* **2019**, 4 (2), 722.
33. Yang, Z.; Zhao, T.; Huang, X.; Chu, X.; Tang, T.; Ju, Y.; Wang, Q.; Hou, Y.; Gao, S., Modulating the Phases of Iron Carbide Nanoparticles: From a Perspective of Interfering with the Carbon Penetration of Fe@Fe₃O₄ by Selectively Adsorbed Halide Ions. *Chem. Sci.* **2017**, 8 (1), 473.
34. Wang, H.; Yin, F. X.; Liu, N.; Kou, R. H.; He, X. B.; Sun, C. J.; Chen, B. H.; Liu, D. J.; Yin, H. Q., Engineering Fe-Fe₃C@Fe-N-C Active Sites and Hybrid Structures from Dual Metal-Organic Frameworks for Oxygen Reduction Reaction in H₂-O₂ Fuel Cell and Li-O₂ Battery. *Adv. Funct. Mater.* **2019**, 29 (23), 1901531.
35. Ananth, M. V.; Giridhar, V. V.; Renuga, K. Linear Sweep Voltametry Studies on Oxygen Reduction of Some Oxides in Alkaline Electrolytes. *Int. J. Hydrogen Energy* **2009**, 34 (2), 658.

Chapter 5

Zeolitic Imidazole Framework Derived Bimetallic Carbon Alloy Catalyst for the Electrocatalytic Borohydride Oxidation Reaction

Abstract



Direct borohydride fuel cells show interesting performances for mobile applications owing to the use of sodium borohydride (NaBH₄) as the fuel. The complete electrooxidation of NaBH₄ proceeds via an eight-electron pathway. However, due to the inevitable hydrolysis of borohydride at the electrode, the released electrons are usually less than 8. The use of anode catalysts with good performance and high utilization of BH₄⁻ is therefore imperative for practical applications. In this work, we report the development of an anode catalyst, derived from trimetallic zeolitic imidazolate framework (ZIF) with M-N_x active centers and enhanced porous features created by Zn evaporation on pyrolysis. XPS studies revealed the presence of pyridinic N, graphitic N and Co-N_x active centers on the catalyst surface. The nanotubular structure of the formed carbon assists faster electron transport and the oxidation current density reached 56.5 mA cm⁻² at 0.61 V in 0.05 M NaBH₄+ 1 M KOH. The enhanced electrocatalytic performance induced by the morphological and textural features of the porous carbon catalysts enabled NaBH₄ electrooxidation via an eight-electron transfer indicating its potential as a promising catalyst for BOR.

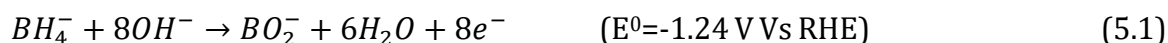
5.1 Introduction

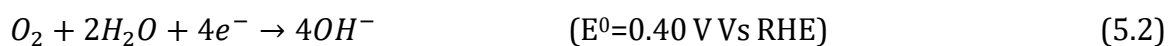
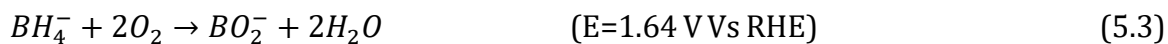
The high demand for clean, sustainable, and renewable energy arising out of the depletion of fossil fuels as well as due to the alarming increase of environmental pollution has prompted researchers worldwide to explore the options of highly efficient fuel cells, batteries and supercapacitors. Fuel cells are considered a breakthrough in the field of clean energy production owing to its salient features like high efficiency, high reliability reduced greenhouse gas emissions etc.¹ Solid alkaline fuel cells (SAFCs) in particular exhibit advantages over proton exchange membrane fuel cells (PEMFCs) such as the use of liquid fuels and lower fuel cross-over.^{2,3} Also, most of the metals are stable in the alkaline medium compared to the acidic medium and hence non-noble electrocatalysts can be used in SAFCs with superior stability. Most of the SAFCs are fed with hydrogen at the anode and oxygen at the cathode. However, the main problem is related to hydrogen production, storage, and transport. Liquid fuels alternative to ultra-pure H₂, such as alcohols, formate, and borohydrides can be used in SAFCs, which makes easier storage and transport.⁴

Direct borohydride fuel cells (DBFCs) with sodium borohydride (NaBH₄) as fuel is currently attracting much attention due to high cell voltage (1.64 V), high theoretical specific capacity (5.7 Ah g⁻¹), high energy density (9.3 Wh g⁻¹), superior hydrogen storage (10.6 wt.%) and non-flammability. Also, NaBH₄ is carbon-free, non-toxic, and relatively stable in alkaline solution.^{5,6} Furthermore, DBFCs have low operating temperature (70°C) and easily recyclable non-toxic products. However, it is difficult to achieve the cell voltage of 1.64 V in practice due to the slow kinetics of borohydride oxidation reaction (BOR). Besides direct oxidation of borohydride, the competing reactions of hydrolysis of borohydride and hydrogen electrooxidation also occur, resulting in a mixed BOR potential.

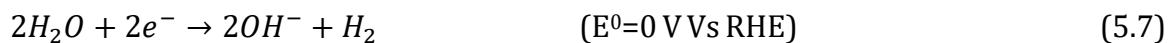
Generally, the borohydride oxidation reaction (BOR) at the anode involves the release of 8 electrons as shown in eq. 5.1 and the corresponding oxygen reduction reaction (ORR) takes place at the cathode (eq. 5.2).⁷

Anode



Cathode**Overall reaction**

As mentioned earlier, the anodic BOR is a complex reaction normally accompanied by several parasitic reactions like heterogeneous hydrolysis of BH_4^- (eq. 5.4-5.6)⁸ and, the competing faradaic hydrogen evolution reaction (HER) (eq. 5.7), causing the evolution of H_2 , and resulting in a low fuel conversion efficiency.



By virtue of these competing reactions, the number of released electrons is usually less than eight reflecting on the inefficiency of the catalysts. As the BOR proceeds, hydrogen evolution occurs which ultimately reduces the effectiveness of the borohydride. Moreover, the hydrogen bubbles that are entrapped at the anode resist charge carrier migration.⁹ Therefore, anode catalysts with high performance and efficient utilization of BH_4^- are important for the practical application of DBFC.

Noble metals like Pt, Pd, Au, Ag, etc. have been extensively studied for BOR owing to their superior catalytic activity.^{10,11} However, these catalysts, especially Pt and Pd, cause severe hydrolysis of borohydride (eq. 5.4-5.7).¹²⁻¹⁴ Therefore, it is highly demanded to develop catalysts that can selectively oxidize BH_4^- with very negligible or no hydrogen evolution.

From density functional theory, Janik *et al.* concluded that the B-H bond dissociation determines the catalyst activity towards BOR.¹⁵ Numerous efforts were thus conducted to develop low-cost transition metals such as Ni, Co, Fe, Cu based catalysts for BOR.^{16,17} Due to the high B-H bond-breaking ability of cobalt compared to other transition metals, cobalt-based materials can be promising catalysts for BOR.^{18,19} Nevertheless, there are only a few reports on cobalt based catalysts for BOR. Zhang *et*

al. reported cobalt incorporated multiwalled carbon nanotubes with high catalytic activity and good stability for NaBH₄ electrooxidation. The hierarchical 3D network structure with dispersed Co nanoparticles increased the adsorption and electrooxidation of hydrogen during the reaction.²⁰ Alloying Co with other transition metals is also reported to be effective in improving the catalytic performance by the synergistic effect between the metals and the special electron transfer path.^{19,21} CNT supported CoBi,²² Ni-Co nanoparticles immobilized Ni foam²³ and NiB alloy decorated by Cu,²⁴ all exhibited good BOR activity and stability. Recently, Nagaiah *et al.* synthesized urchin-shaped cobalt tungstate catalyst with enhanced BOR performance.²⁵ Nevertheless, the catalytic activity of the current Co-based catalysts is still lower than those of noble metal catalysts and concerted efforts are essential to develop non-noble metal catalysts that can completely replace noble metal catalysts.

It is well known that catalyst with large specific surface area, porosity, large number of active sites and good conductivity is advantageous for better electrocatalytic performance by facilitating the flow of electrons and reagents. Thus, high surface area carbon supported catalysts with strong interaction between catalyst and the support are preferred.²⁶ Metal-organic frameworks (MOF) are attractive precursors for the development of metal-doped carbon catalysts with high surface area and porosity.^{27,28} Liu *et al.* investigated MOF-5 derived high surface area nanoporous carbon (NPC) as the anode catalyst support in DBFC. NPC-supported Pt catalyst showed a 36% increase in current density for borohydride oxidation compared to the Vulcan XC-72 carbon supported Pt. The enhancement in the activity was attributed solely to the supporting effect of the NPC.²⁹ Tiwari *et al.* reported mesoporous nitrogen rich carbon as a metal free catalyst for BOR. The catalyst exhibited high current density of 27.43 mA cm⁻² in 0.1 M NaBH₄ + 1.0 M aqueous NaOH electrolyte. The enhanced activity is attributed to the presence of quaternary and pyridinic nitrogen sites present in the catalyst.³⁰ It is expected that the combined effect of N-doped carbon with other metallic species further enhances the activity towards borohydride oxidation.

A high surface area N- doped carbon catalyst from a precursor having a framework structure with high fraction of microporosity and with nitrogen as a coordination element is expected to have high BOR activity. Thus, zeolitic imidazolate frameworks (ZIF) were chosen as the precursor to develop the catalyst. ZIFs are ideal precursors

which can undergo structural transformation to N and metal-doped microporous graphitic carbon during pyrolysis under inert condition.³¹⁻³³ ZIF-8 can produce high surface area carbon with high nitrogen content. However, it cannot give M-N_x active sites due to the evaporation of Zn during pyrolysis. Co-based ZIF-67, which is isostructural to ZIF-8, can produce Co-N_x active sites, but the carbon thus formed suffers from low surface area and porosity. Doping ZIF-8 with suitable metals is found to be an effective strategy to enhance the surface area as well as M-N_x active centers. Recently, Lu *et al.* reported ZIF-derived Fe and N co-doped porous carbon supported Au nanoparticles (Au/FeNPC-40) as electrocatalyst for BOR. They have obtained a BOR peak current density up to 45.4 mA cm⁻² with a high electron transfer number of 7.0.³⁴ In another report, Lu *et al.* synthesized Co, N co-doped porous carbon-supported Au nanoparticles from ZIF precursor. The catalyst acquired a BOR peak current density of 48.4 mA cm⁻² with an electron transfer number of 7.5.³⁵ Even though these catalysts showed high efficiency towards BOR, large scale synthesis is limited due to the use of noble metal Au.

This work details the development of non-noble metal doped carbon with enhanced BOR activity. A fast synthesis strategy was adopted to prepare trimetallic ZIF (Fe, Co, Zn) through an aqueous wet chemical approach. The resulting product formed in high yields, showed nanometer-sized ZIF particles with different metal centers.³⁶ The *in situ* porosity creation due to Zn evaporation, Fe catalyzed nanotube formation, and the synergistic effect of Co and Fe are favorable attributes contributing towards enhanced BOR activity and stability of the developed catalyst.

5.2 Experimental

5.2.1 Materials

2-Methylimidazole, zinc nitrate hexahydrate (99%), cobalt nitrate hexahydrate (99.5%), and iron sulfate heptahydrate (99%) were purchased from Sigma Aldrich. Triethylamine (TEA) was purchased from Wako pure chemical Industries (Japan). All chemicals were used as received.

5.2.2 Synthesis of Trimetallic ZIF

In a typical synthesis, 3.242 g of 2-methyl imidazole was dissolved in 50 ml DI water. 4 g TEA was added to this solution and stirred for 5 min. 50 mL aqueous solution containing 0.55 g zinc nitrate, 0.089 g cobalt nitrate, and 0.085 g iron sulfate were prepared separately and added to the imidazole-TEA mixture under stirring. The stirring was continued at room temperature for 30 min. The precipitate obtained was washed with deionized water several times by centrifugation and dried at 90 °C overnight. The resulting ZIF contains 75% Zn, and a (1:1) molar ratio of Co and Fe (25%). Similarly, bimetallic and monometallic ZIFs with different metal ions were also synthesized using the same procedure.

5.2.3 Synthesis of Carbon Alloy Catalyst

Carbon alloy catalysts were synthesized by the carbonization of ZIFs at a temperature of 910 °C for 1 h under nitrogen atmosphere. The sample details are presented in **Table 5.1**.

Table 5.1 Details of various ZIF samples with different metal percentages

Catalyst	ZIF	Percentage of metal present in ZIF
Z-NC	Zn-ZIF (ZIF-8)	100% Zn
Co-NC	Co-ZIF (ZIF-67)	100% Co
CoZ-NC	CoZn-ZIF	25% Co, 75% Zn
FeZ-NC	FeZn-ZIF	25% Fe, 75% Zn
FeCoZ-NC	FeCoZn-ZIF	25%Fe & Co (1:1), 75% Zn

5.2.4 Structural Characterization

Phase identification of the synthesized samples was performed at a scan rate of 3° min⁻¹ using an Ultima IV X-ray Diffractometer (Rigaku, Japan) with a Cu K α ($\lambda=1.5406$ Å) X-ray source operating at 40 kV and 40 mA. Raman spectra were obtained from a LabRAM HR Evolution Raman spectrometer using a visible laser beam of wavelength 532 nm. The morphological characterization was carried out using a scanning electron microscope (S-4800, Hitachi High-Technologies Corporation) and the HR-TEM images were captured using a TOPCON EM-002BF-J system (Japan) operating at

an accelerating voltage of 200 kV and equipped with a twin EDS facility for the elemental distribution of the catalysts. The BET surface area and porosity were calculated with Micromeritics (Tristar 11, USA) surface area analyzer using nitrogen adsorption at 77 K. The samples were initially degassed at 200 °C for 2 h in flowing N₂. The surface elemental composition and oxidation states of the metal species present in the catalyst were studied using a Quantum 2000 (ULVAC-PHI Inc., Japan) X-ray photoelectron spectrometer fitted with a twin-anode X-ray source using Al K α radiation ($h\nu = 1486.58$ eV).

5.2.5 Electrochemical Characterization

An electrochemical workstation (HD HOKUTO DENKO), was used for the borohydride oxidation reaction (BOR) activity measurements. A three-electrode setup in which the catalyst coated glassy carbon electrode with a surface area of 0.196 cm² was used as the working electrode. Hg/HgO and Pt were used as the reference and counter electrode respectively. Cyclic voltammetry (CV) and linear sweep voltammetry (LSV) measurements were carried out in N₂ saturated 1 M KOH solution containing different concentrations of NaBH₄. All potentials were converted into RHE by calibrating Hg/HgO in H₂ saturated 0.1 M KOH solution. The catalyst ink was prepared by ultrasonically mixing 5 mg of the catalyst with 860 μ L deionized water, 100 μ L isopropyl alcohol, and 40 μ L 5 wt.% Nafion solution, followed by sonicating it for 2h. 10 μ L of this catalyst slurry was drop cast on the polished glassy carbon working electrode using a microsyringe. The catalyst loading was maintained as 0.25 mg cm⁻² for all samples. The number of electron transfer was calculated using a rotating ring disc electrode (RRDE) in N₂ saturated 1 M KOH containing 0.05 M NaBH₄ at a scan rate of 10 mV s⁻¹ and an electrode rotation of 1600 rpm. A glassy carbon disc (0.126 cm²) with a gold ring was used as a sensor to monitor the H₂ produced during the hydrolysis of NaBH₄ by the catalysts. Hg/HgO was used as the reference electrode, and Pt wire was used as the counter electrode. The catalyst loading was maintained as 0.04 mg cm⁻². The stability of the catalyst was analyzed using chronoamperometry measurements in 0.05 M NaBH₄+ 1 M KOH solution at different potentials.

5.3 Results and Discussion

Trimetallic ZIF was synthesized by mixing aqueous metal salts (Fe, Co, and Zn salt) with aqueous imidazole-TEA for 30 min. TEA deprotonates the imidazole ligand and allows the faster formation of ZIF at room temperature with good yield. Through this method, Fe and Co can be easily doped into the ZIF-8 framework upon carbonization at 910 °C under N₂ atmosphere. The combination of Fe and Co is expected to give high catalytic activity by the generation of more active sites and Zn evaporation during pyrolysis enhances the porous nature of the doped carbon samples.

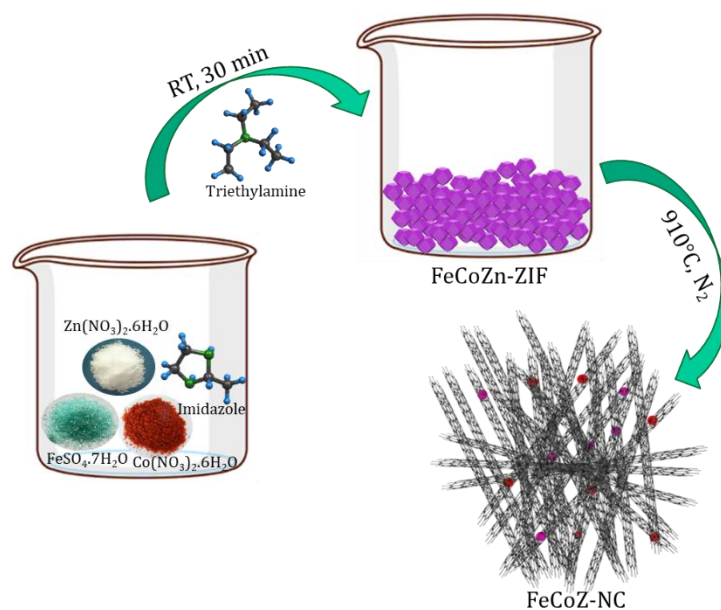


Figure 5.1 Schematic illustration of the formation of FeCoZ-NC.

5.3.1 Phase Analysis

X-ray diffraction patterns of the synthesized ZIF samples are presented in **Figure 5.2a**. All the samples exhibited similar peaks indicating that the addition of metals did not alter the structural features and crystallinity of the derived ZIFs while maintaining the sodalite crystal structure.³⁷ After carbonization, all the samples exhibited a peak at the 2θ value of $\sim 26^\circ$ corresponding to the (002) plane of graphitic carbon (**Figure 5.2b**). Z-NC exhibited only graphitic carbon peak since the element Zn was volatilized on heating at 910 °C. The XRD patterns of samples Co-NC and CoZ-NC indicated presence of metallic cobalt as well as cobalt oxide phases. The presence of oxide phases of iron (Fe_2O_3 and Fe_3O_4), carbide (Fe_3C), and metallic Fe phase were also identified in the XRD pattern of sample FeZ-NC. The trimetallic ZIF derived

carbon sample FeCoZ-NC exhibited an intense peak of metallic Fe/Co at the 2θ value of 44.8° in addition to the oxide phases of cobalt and iron.

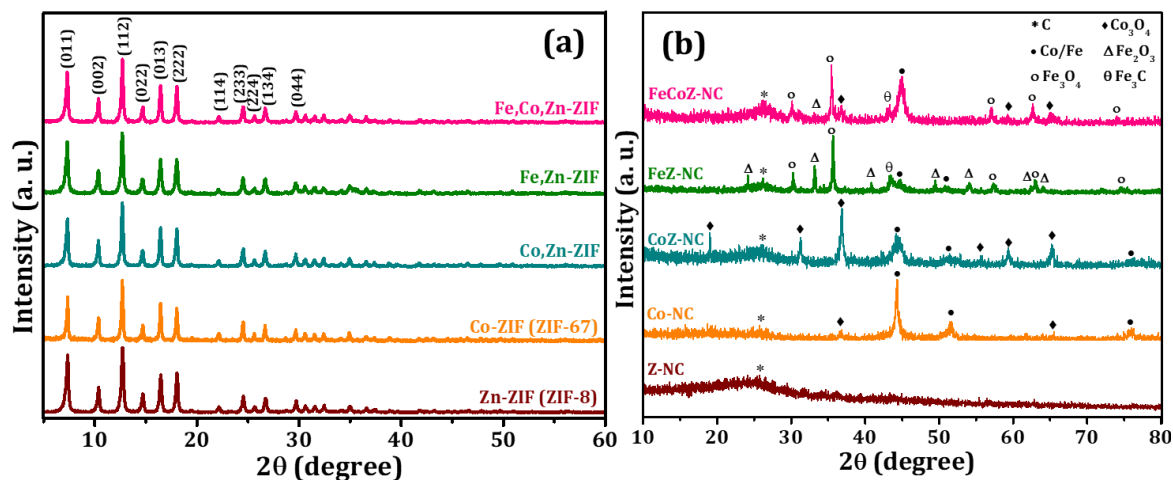


Figure 5.2 X-ray diffraction patterns of (a) precursor ZIFs (b) derived carbons.

The graphitic nature of the ZIF-derived samples was revealed by Raman spectra. Raman spectra displayed in **Figure 5.3** consisted of two major peaks at 1350 and 1590 cm^{-1} corresponding to the D band and G band respectively. The D band with A_{1g} vibration mode, was due to the in-plane imperfections in the carbon lattice, and was an indicator of the extent of defects and heteroatoms doping. The G band was indicative of the graphitic carbon form with E_{2g} vibration mode.³⁷ The value I_D/I_G was used to compare the extent of disorder/modifications occurring in the sample during carbonization. The I_D/I_G ratio of the catalysts Z-NC and CoZ-NC was found to be 1.06 and 1.03, respectively, whereas, Co-NC and FeCoZ-NC exhibited similar I_D/I_G values (0.99). The lower I_D/I_G value for Co-NC and FeCoZ-NC was a clear indication of the dominance of the graphitic phase in these catalysts, leading to enhanced electrical conductivity. The Raman spectra of FeZ-NC appeared noisy with multiple peaks of low intensity and the I_D/I_G ratio could not be obtained. The catalyst appeared to be the least graphitic of all compositions. The presence of a substantial amount of Fe may also been one of the reasons for the lower graphitization in this sample.

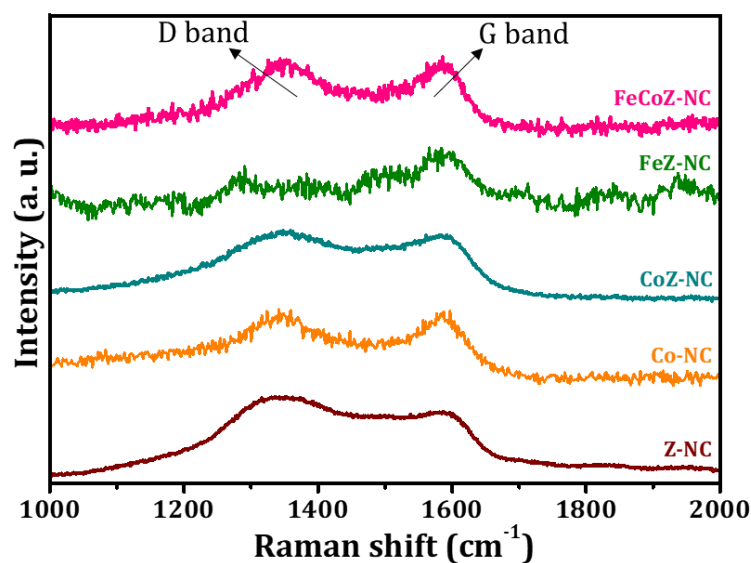


Figure 5.3 Raman spectra of Z-NC, Co-NC, CoZ-NC, FeZ-NC and FeCoZ-NC.

5.3.2 Morphology and Microstructure Analysis

The SEM images of trimetallic ZIF (FeCoZn-ZIF) displayed in **Figure 5.4** show an average particle size of around 80 nm. The carbonization resulted in the collapse of the morphological features of ZIF. Z-NC and CoZ-NC have an average particle size of around 50 nm (**Figure 5.5a & b**). The iron added samples showed a complete transformation of the precursor morphology to a tubular structure (**Figure 5.5c & d**). The detailed morphological analysis was further attempted using transmission electron microscopy.

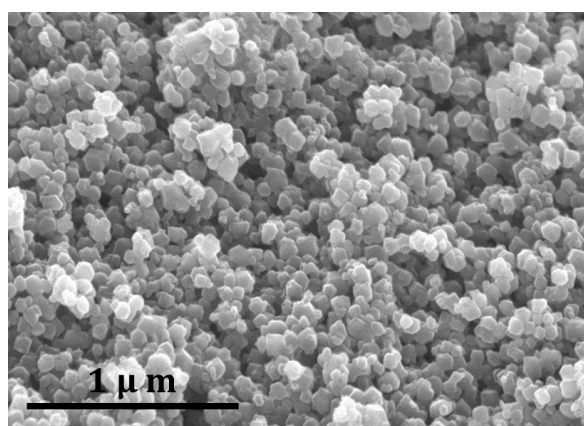


Figure 5.4 SEM image of FeCoZn-ZIF.

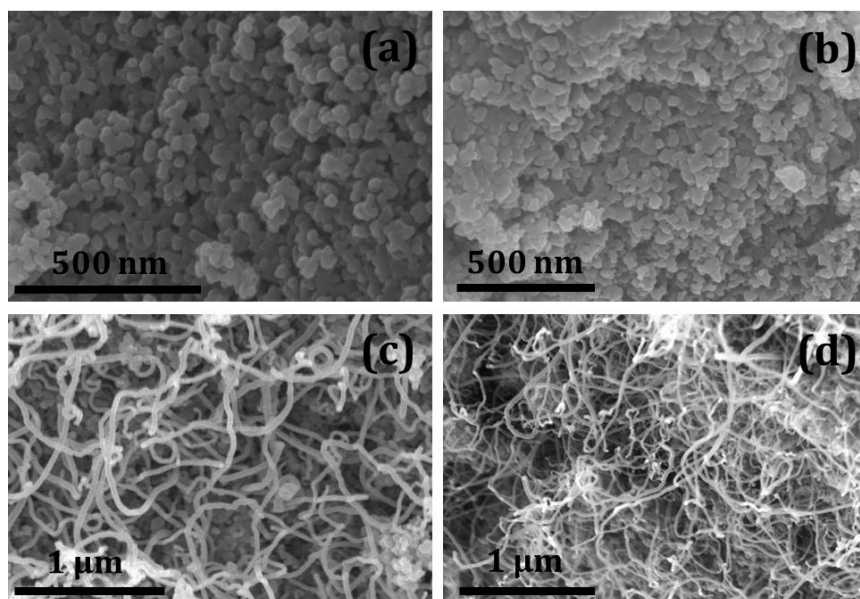


Figure 5.5 SEM images of (a) Z-NC, (b) CoZ-NC, (c) FeZ-NC and (d) FeCoZ-NC.

The TEM images of Z-NC shown in **Figure 5.6** appeared to be consisting of distorted hexagonal particles. The inset of the high-resolution image shown in **Figure 5.6c** indicated the (002) phase of graphitic carbon with a d-spacing of 0.34 nm. The elemental mapping given in **Figure 5.7** confirmed the uniform nitrogen doping in the sample.

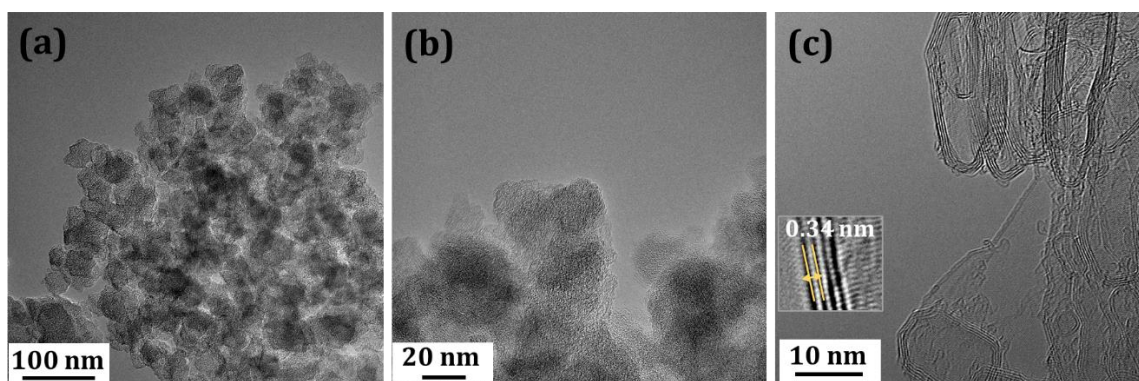


Figure 5.6 TEM images of Z-NC at different magnifications (a) 100 kX, (b) 300 kX, and (c) 1 mX. HR-TEM image is shown in the inset of (c).

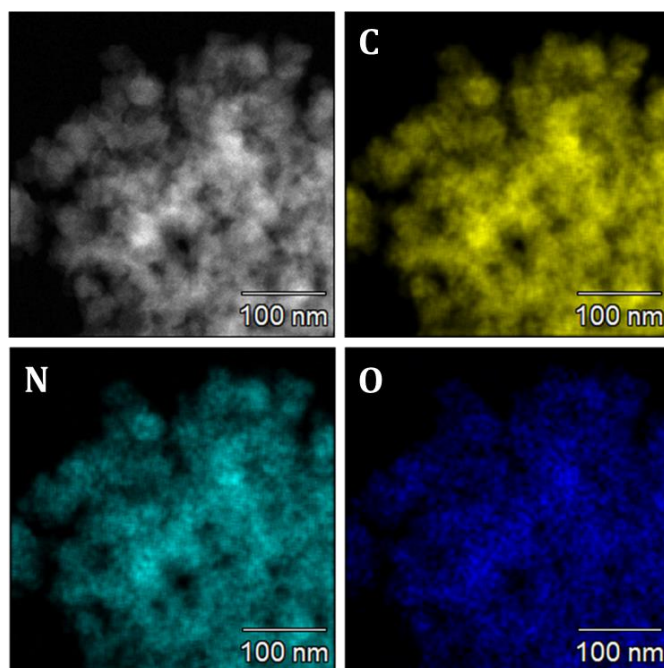


Figure 5.7 Elemental mapping of Z-NC.

Sheet-like structures, identified to be graphitic carbon, having a d-spacing of 0.34 nm with uniformly distributed particles are seen for Co-NC (**Figure 5.8**) sample. The FFT image of the selected particle shown in the inset indicated the (111) and (220) phases of metallic Co. This was in accordance with the XRD pattern (**Figure 5.2**), where metallic Co was confirmed through peaks at 2 theta value of 44.8° . The particles were having an average size of around 10 nm. The elemental mapping of this sample shown in **Figure 5.9** confirmed the uniform distribution of Co over the graphitic carbon sheets.

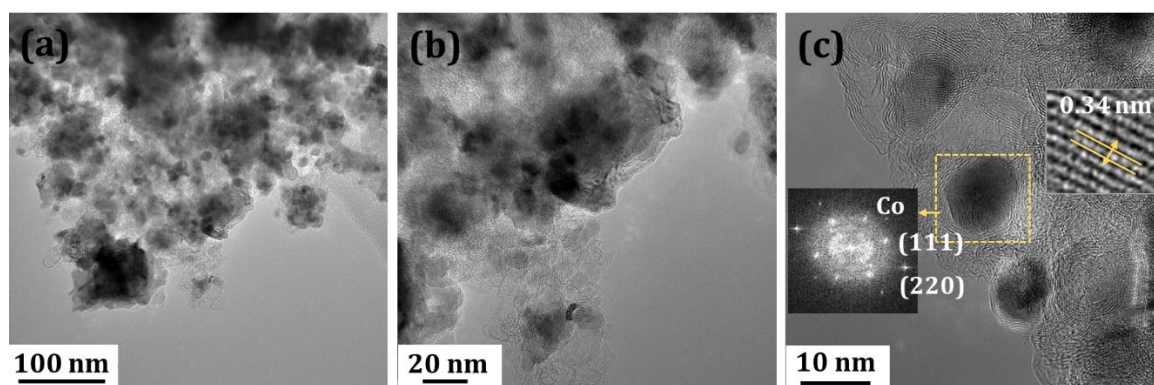


Figure 5.8 TEM images of Co-NC at different magnifications (a) 120 kX, (b) 300 kX, and (c) 1 mX. HR-TEM and FFT are shown in the inset of (c).

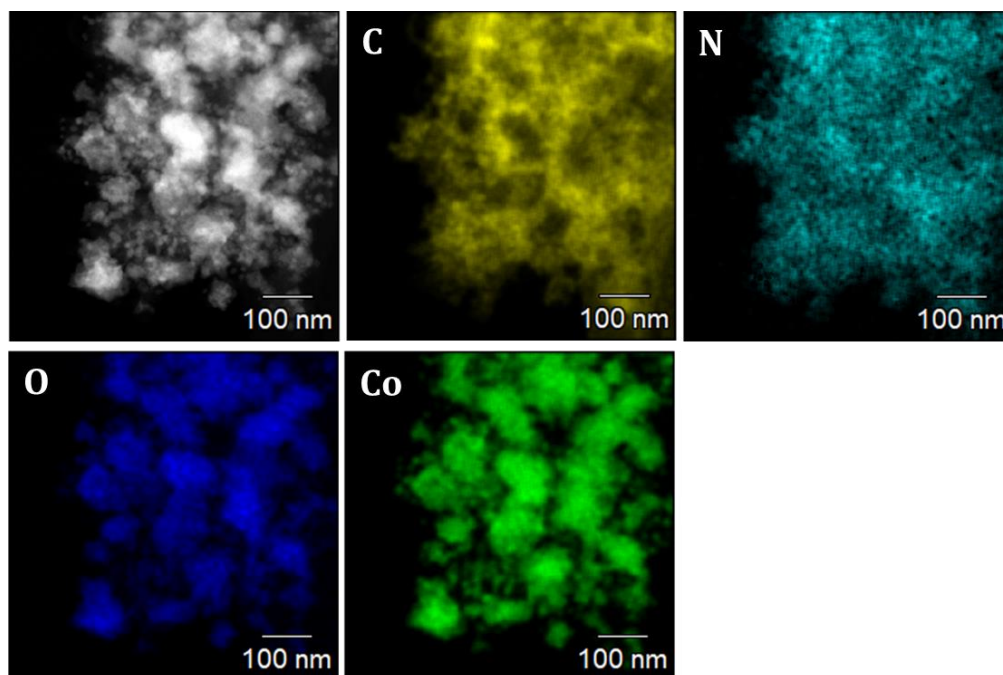


Figure 5.9 Elemental mapping of Co-NC.

TEM images of CoZ-NC exhibited similar morphology as that of Co-NC (**Figure 5.10**) and from the HR-TEM image, these particles were identified to be Co_3O_4 particles with the size of 7-10 nm. Unlike Co-NC, the major phase in CoZ-NC was the oxide phase of cobalt, as confirmed by the (311) plane of Co_3O_4 in the FFT image shown in the inset of **Figure 5.10c**. This was also in accordance with the corresponding XRD pattern where the major phase of Co was identified to be the oxide phase. The elemental mapping shown in **Figure 5.11** clearly showed the distribution of Co_3O_4 over the N-doped graphitic carbon sheets.

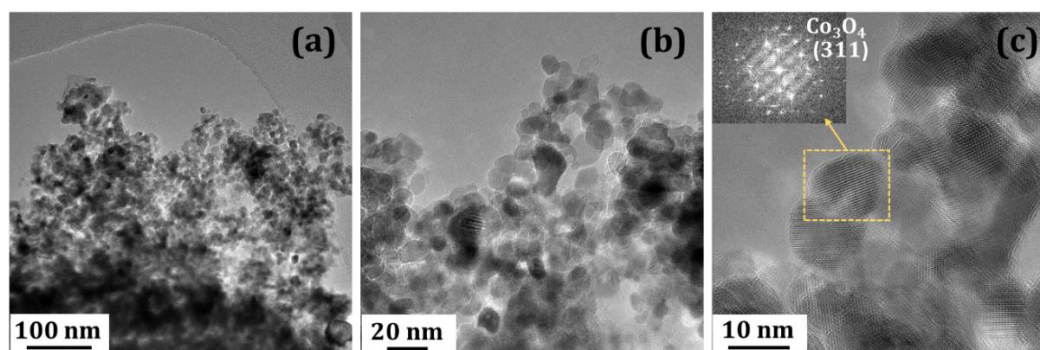


Figure 5.10 TEM images of CoZ-NC at different magnifications (a) 100 kX, (b) 300 kX, and (c) 1 mX. FFT is shown in the inset of (c).

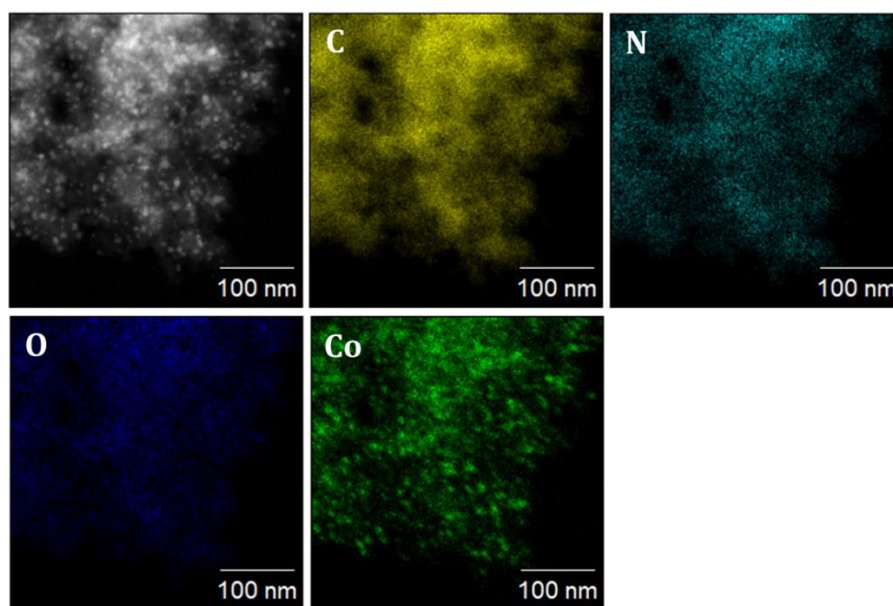


Figure 5.11 Elemental mapping of CoZ-NC.

The sample FeZ-NC exhibited a tube-like structure with distributed particles (**Figure 5.12**). The tubes were composed of N-doped graphitic carbon with a d-spacing of 0.34 nm (inset of **Figure 5.12c**). Metallic Fe particles were identified from the FFT image (102 plane). The corresponding elemental mapping shown in **Figure 5.13** indicated uniform distribution of doped elements.

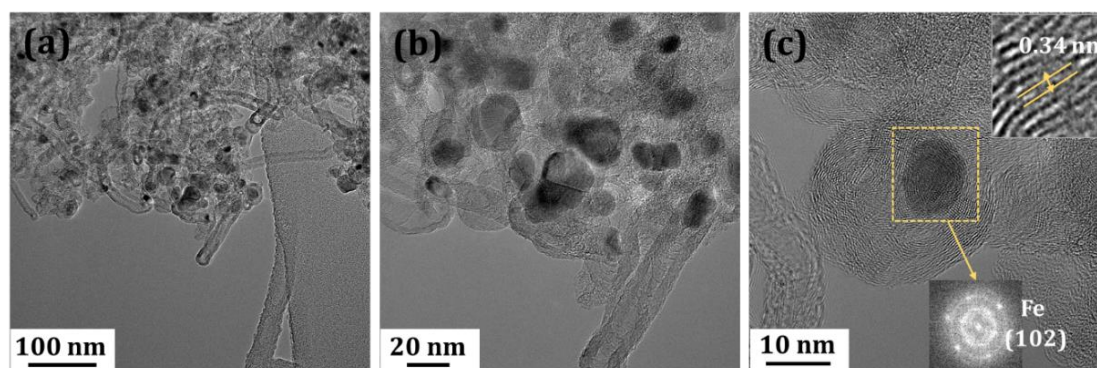


Figure 5.12 TEM images of FeZ-NC at different magnifications (a) 100 kX, (b) 300 kX, and (c) 1 mX. HR-TEM image and FFT are shown in the inset of (c).

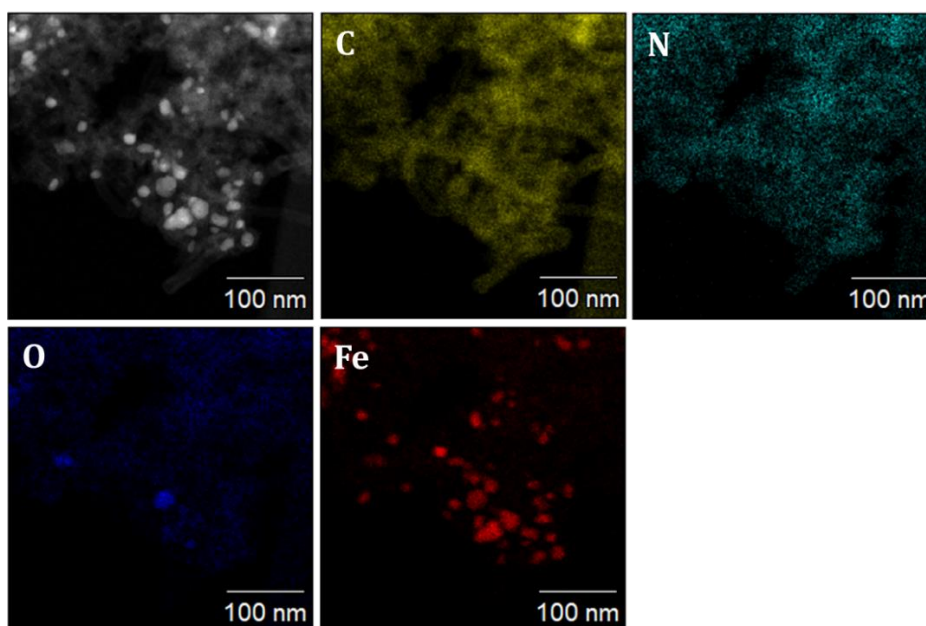


Figure 5.13 Elemental mapping of FeZ-NC.

The morphology of FeCoZ-NC was similar to FeZ-NC, where tube-like structures with uniformly distributed particles were seen (**Figure 5.14**). The formation of tubular structure observed in both these samples was due to the presence of Fe, which catalyzed the sheet-to-tube transformation of carbon. The tubes were composed of graphitic carbon as confirmed by its d-spacing value of 0.34 nm (shown in the inset of **Figure 5.14c**). From the HR-TEM image shown in **Figure 5.14c**, the particle having a size of around 10 nm was identified as metallic Co in (111) plane. In addition to the metallic Co, the HR-TEM imaging also confirmed the presence of 20 nm sized metallic Fe (**Figure 5.14d**). The inset shows the FFT image of Fe particle in 102 plane. It is reported that carbon nanotubes can store hydrogen electrochemically and the stored hydrogen can be electrooxidized.³⁸ Thus the *in situ* formation of carbon nanotubes in Fe doped catalysts enables good electrical conductivity and hydrogen storage, consequently minimizing H₂ evolution. From **Figures 5.14a & b**, it was clear that the metallic particles were interconnected by the tube structures, resulting in an enhancement in the electrical conductivity. Furthermore, the particle surfaces can be easily accessed to the reactants via diffusion through the carbon nanotube network, enabling higher catalytic activity. The encapsulation of metal nanoparticles in carbon structures are expected to promote corrosion resistance.

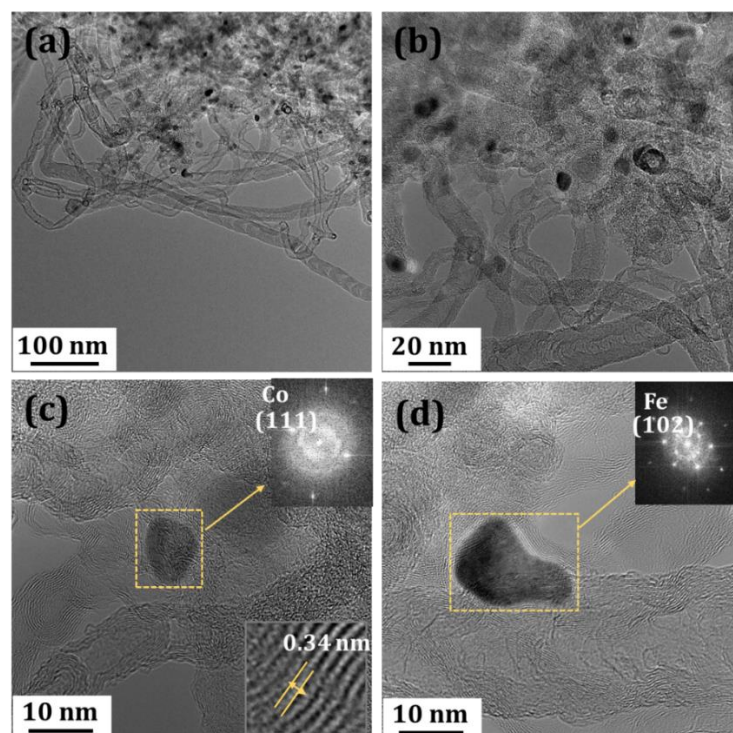


Figure 5.14 TEM images of FeCoZ-NC at different magnifications (a) 100 kX, (b) 300 kX, and (c and d) 1 mX. HR-TEM image and FFT are shown in the inset of (c & d).

The elemental mapping shown in **Figure 5.15** indicated that almost equal amounts of Fe and Co are present in the sample. Fe and Co are located at the same positions indicating the probability of alloy formation.

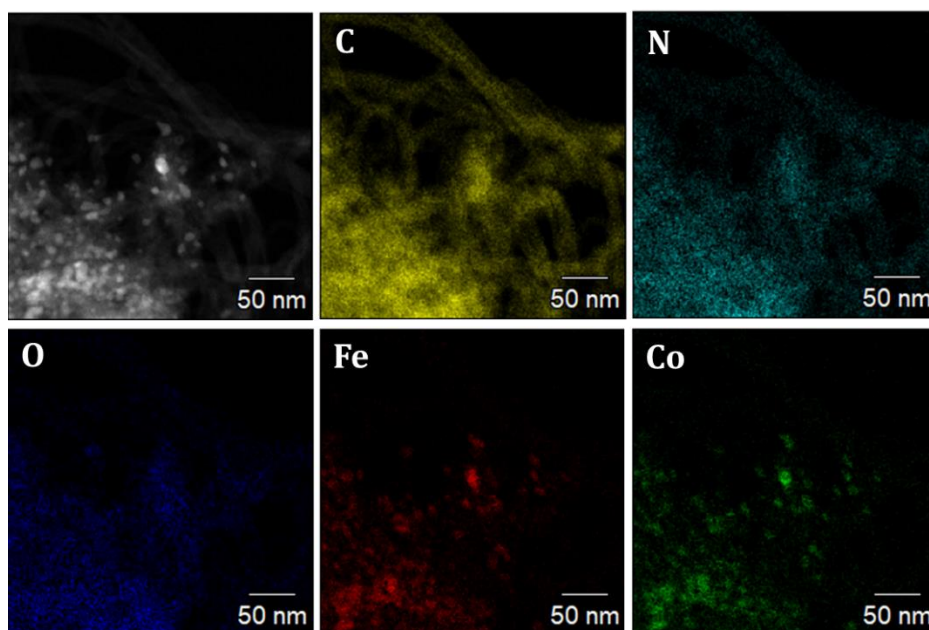


Figure 5.15 Elemental mapping of FeCoZ-NC.

The weight percentage of metal present in each sample obtained from EDS analysis is given in **Table 5.2**. The sample Z-NC contained no Zn indicating the complete evaporation of it during the carbonization process. After the carbonization of Co,Zn-ZIF, the resulting catalyst exhibited very less amount (3.22%) of Zn. On the other hand, Fe,Zn-ZIF yielded a catalyst with zero Zn content upon carbonization. The trimetallic ZIF (Fe,Co,Zn-ZIF) derived carbon contained a slightly higher amount of Fe (52.87%) compared to Co (46.4%). In addition to this, trace amounts of Zn (0.73%) were also seen indicating that > 99% of Zn was evaporated during carbonization.

Table 5.2 Weight percentage of metals obtained from EDS.

Sample	Zn	Fe	Co
	(weight %)		
Z-NC	0	0	0
Co-NC	0	0	100
CoZ-NC	3.22	0	96.78
FeZ-NC	0	100	0
FeCoZ-NC	0.73	52.87	46.4

5.3.3 Surface Area Analysis

The surface area and pore characteristics of the samples were quantified using N₂ adsorption-desorption analysis. The isotherms obtained from the analysis, shown in **Figure 5.16a**, resembled the Type I, characteristic of microporous materials. As expected, the surface area and micropore volume exhibited by Z-NC were the highest (792 m² g⁻¹) compared to all the other samples and were ascribed to the Zn evaporation during carbonization. Co-NC showed the least surface area due to the presence of cobalt which was not volatilized during carbonization. The other catalysts (CoZ-NC, FeZ-NC, and FeCoZ-NC) exhibited surface area values in between Co-NC and Z-NC. The evaporation of Zn in these samples helped the enhancement of surface area compared to Co-NC having no Zn in its precursor. Among these catalysts, FeZ-NC and FeCoZ-NC exhibited almost similar surface areas (323 and 321 m² g⁻¹ respectively), whereas CoZ-NC exhibited a slightly higher surface area (417 m² g⁻¹). This was ascribed to the differences in structural features as evidenced from TEM analysis. The

physical and chemical interactions of the electroactive materials at the interface depend on the surface energy as well as surface chemistry of the catalyst. The enhanced surface area of the catalyst provides the BOR intermediates a longer lifetime at the catalyst sites, leading to the completion of the reaction, thereby enhancing the faradaic efficiency.

The high specific surface area and dual metal doping in FeCoZ-NC are expected to provide a large number of active sites and are also helpful for greater contact with sodium borohydride. The variation in the micropore volume for the samples was obtained from the NLDFT analysis shown in **Figure 5.16b**. The samples exhibited a narrow pore size distribution within 0.6-1.8 nm.

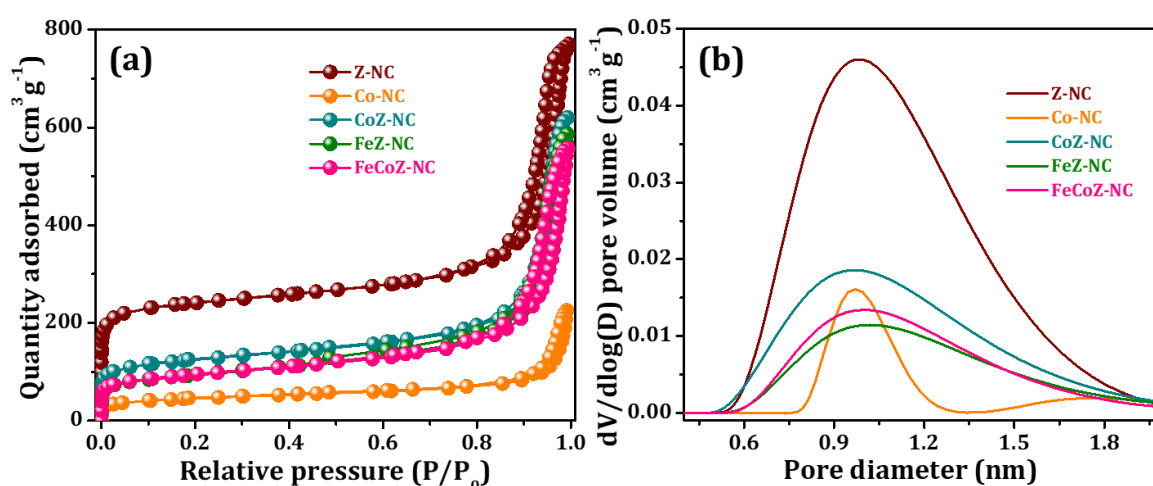


Figure 5.16 (a) N₂ adsorption-desorption isotherms and (b) NLDFT pore size distribution of Z-NC, Co-NC, CoZ-NC, FeZ-NC, and FeCoZ-NC.

5.3.4 Chemical Compositional Analysis

X-ray photoelectron spectroscopy was used to estimate the surface elemental composition and their chemical environment. All the samples showed the presence of carbon, nitrogen, and oxygen. Z-NC, CoZ-NC, and FeCoZ-NC showed the presence of traces of Zn, indicating its incomplete evaporation (**Figure 5.17**). The presence of cobalt was detected in Co-NC, CoZ-NC, and FeCoZ-NC while the existence of iron was observed in FeZ-NC and FeCoZ-NC.

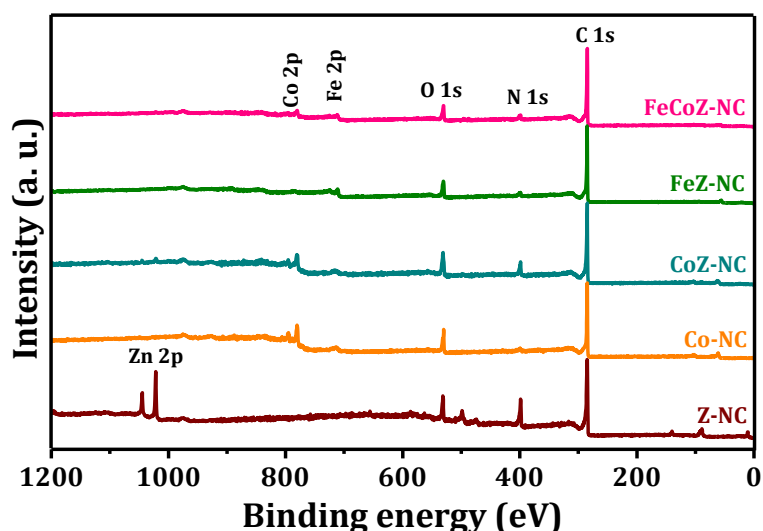


Figure 5.17 XPS survey spectrum of Z-NC, Co-NC, CoZ-NC, FeZ-NC, and FeCoZ-NC.

The high-resolution Zn 2p spectra (**Figure 5.18**) of Z-NC showed two distinct peaks at 1021.7 eV and 1044.7 eV corresponding to the binding energies of Zn 2p_{3/2} and Zn 2p_{1/2} respectively. A slight red shift was observed for both Zn 2p_{3/2} and Zn 2p_{1/2} peaks (1021.4 eV and 1044.4 eV respectively) in CoZ-NC and FeCoZ-NC indicating that Fe and/Co were successfully doped in these catalysts. The less intense and noisy Zn 2p spectrum in CoZ-NC and FeCoZ-NC, compared to Z-NC, indicated that the presence of Zn in these samples was indeed very low.

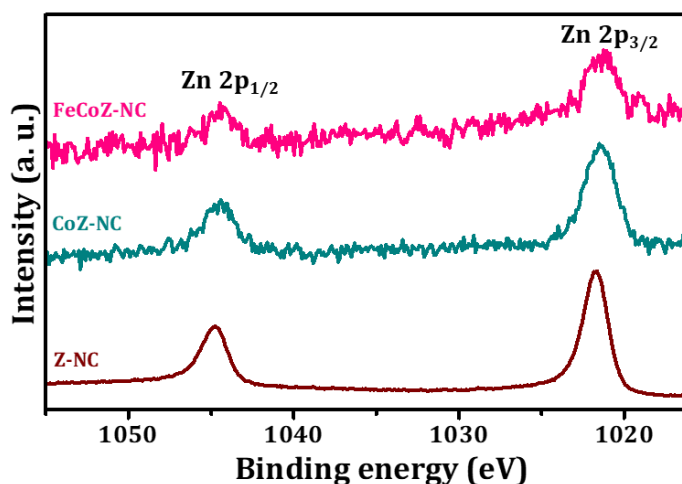


Figure 5.18 Deconvoluted Zn 2p XPS spectrum Z-NC, CoZ-NC, and FeCoZ-NC.

The deconvoluted Co 2p spectra of Co-NC, CoZ-NC, and FeCoZ-NC are shown in **Figure 5.19**. The peak at 778.5 eV corresponded to metallic cobalt. The broad Co 2p_{3/2} and Co 2p_{1/2} peaks consisted of two pairs of peaks. The XPS spectrum of Co 2p_{3/2} consisted of two peaks at 779.9 and 781.9 eV, whereas Co 2p_{1/2} comprised peaks at 795.1 and

796.8 eV. The peaks at 781.9 and 796.8 eV corresponded to the Co^{2+} oxidation state, while the Co^{3+} oxidation state was indicated by the peaks 779.9 and 795.1 eV. Interestingly, Co-N_x peaks were also present in the XPS spectra which were believed to be the active site for the BOR. Co has a partial positive charge and is therefore more favorable for the adsorption of negatively charged BH_4^- leading to an enhanced electrooxidation process.

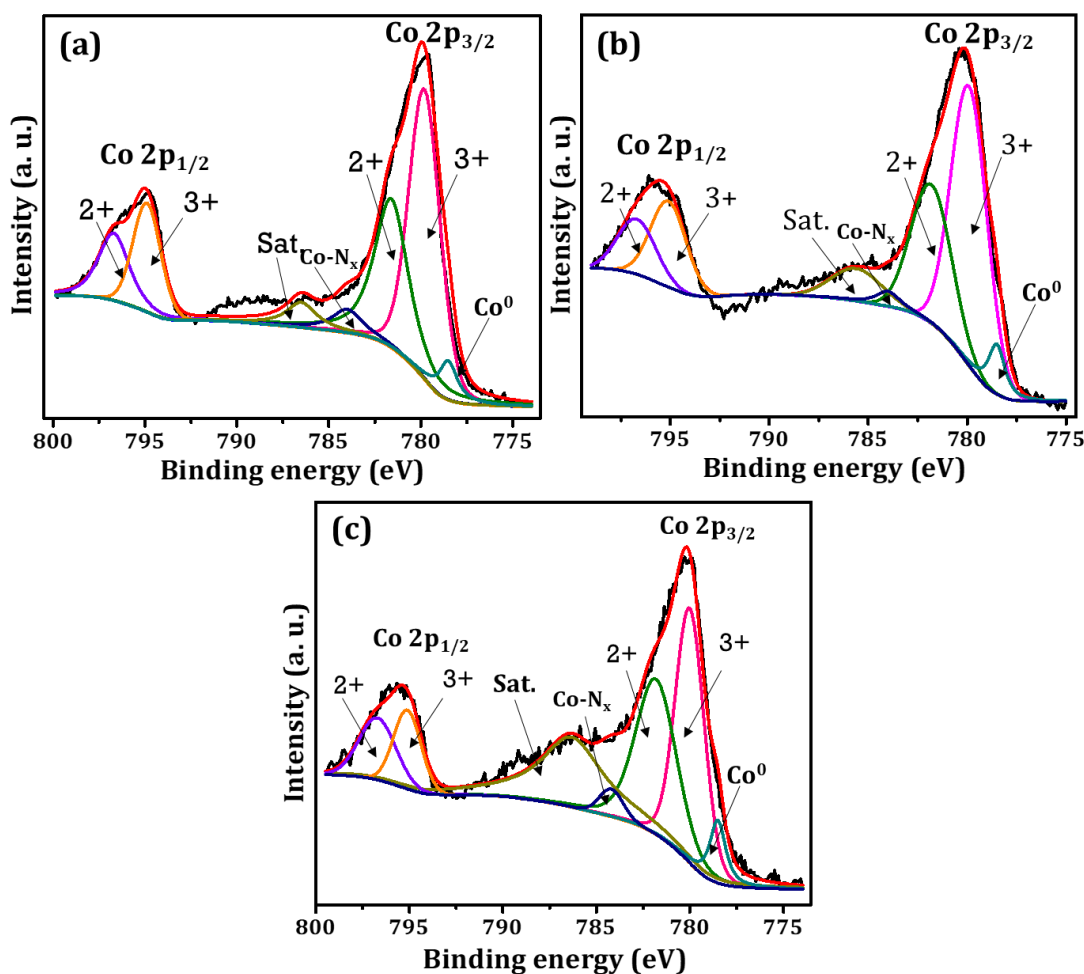


Figure 5.19 Deconvoluted Co2p spectrum of (a) Co-NC, (b) CoZ-NC and (b) FeCoZ-NC.

The deconvoluted Fe 2p spectrum of FeZ-NC and FeCoZ-NC shown in **Figure 5.20** was similar to Co 2p spectra, where bimodal pairs for Fe $2p_{3/2}$ and Fe $2p_{1/2}$ were seen. The peaks at 710.2 and 723.7 eV corresponded to $2p_{3/2}$ and $2p_{1/2}$ orbitals of Fe (II) and the peaks at 711.8 and 725.9 eV corresponded to $2p_{3/2}$ and $2p_{1/2}$ orbitals of Fe (III). The existence of peaks at binding energies of 707.7 and 714.7 eV respectively indicated the presence of Fe-O and Fe- N_x centers.

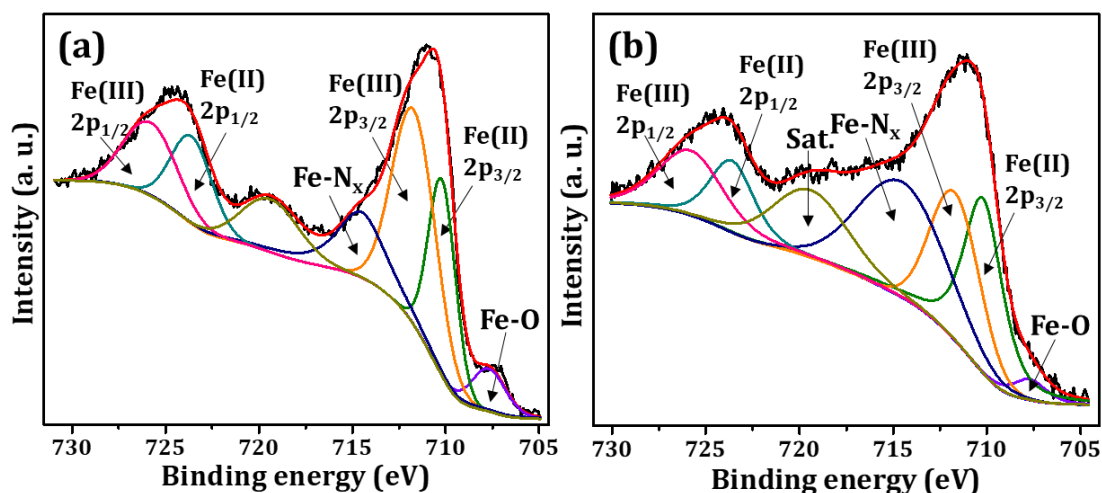


Figure 5.20 Deconvoluted Fe2p spectrum of (a) FeZ-NC and (b) FeCoZ-NC.

Compared to all the other catalysts, FeCoZ-NC contained M-N_x centres arising from Fe-N_x and Co-N_x. Z-N_x arose from the trace amount of Zn also contributed towards the active reaction centers. The presence of these M-N_x active centers was presumed to be beneficial for enhanced BOR performance of FeCoZ-NC catalyst.

The high-resolution N 1s spectra of Z-NC, Co-NC, CoZ-NC, FeZ-NC, and FeCoZ-NC was deconvoluted to four different peaks corresponding to pyridinic, pyrrolic, graphitic, and pyridinic N-oxide with binding energies of 398.8, 400.8, 402.6 and 403.9 eV respectively (**Figure 5.21 & Figure 5.23**). The pyridinic and graphitic nitrogen are believed to be the active N-sites capable of oxidation of borohydride.³⁰

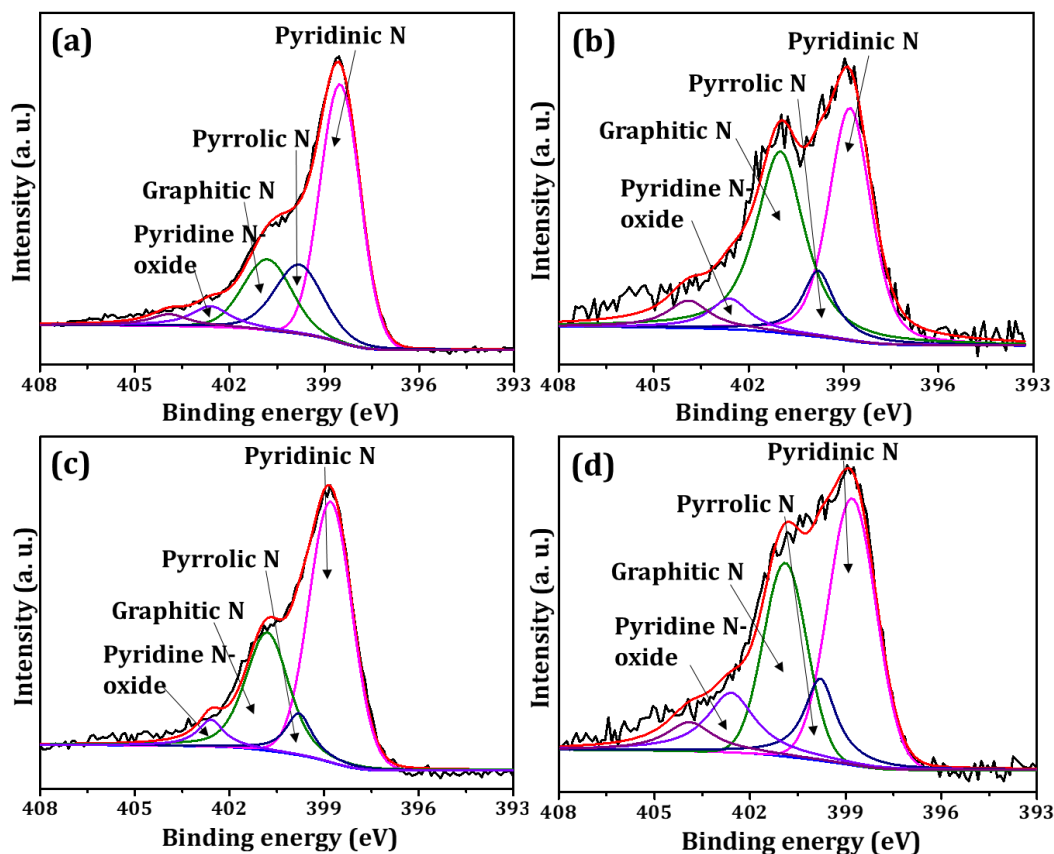


Figure 5.21 Deconvoluted N 1s XPS spectrum of (a) Z-NC, (b) Co-NC, (c) CoZ-NC, and (d) FeZ-NC.

The deconvoluted C 1s spectra of Z-NC, Co-NC, CoZ-NC, FeZ-NC, and FeCoZ-NC (**Figure 5.22 & Figure 5.23**) showed a major peak at 284.8 eV corresponding to the binding energy of sp² carbon. The three other peaks at binding energies of 285.5, 286.6, 288.4 eV respectively correspond to C-N, C-O, and C=O.

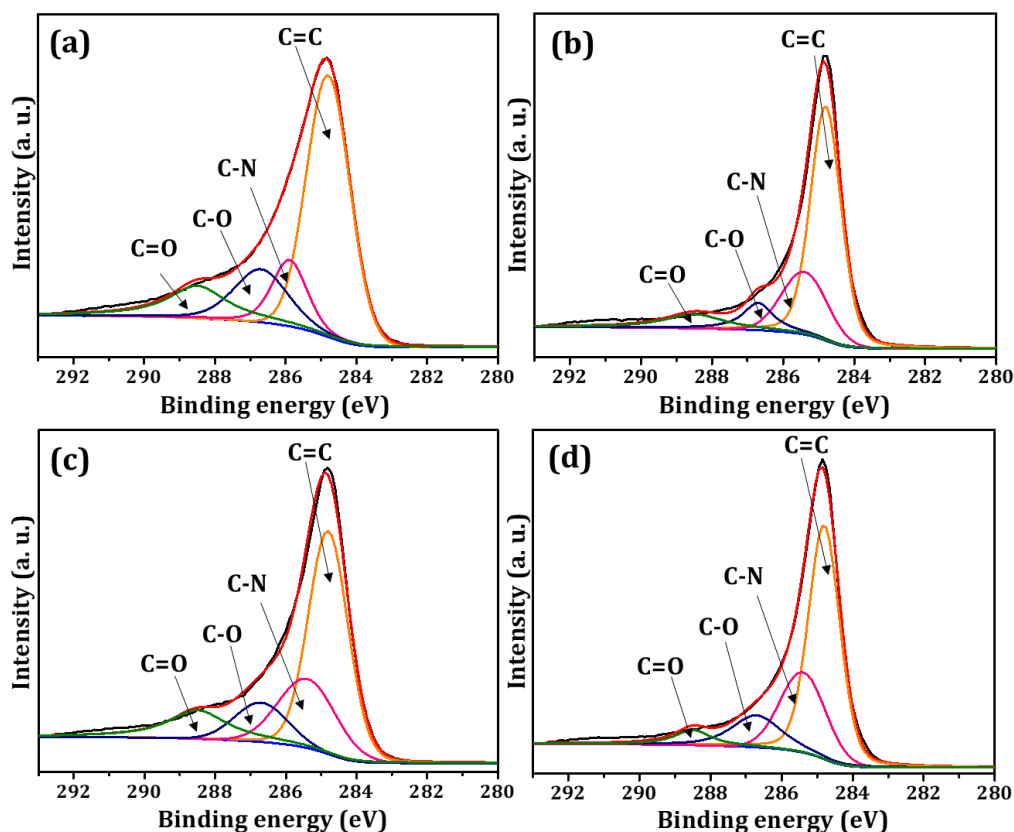


Figure 5.22 Deconvoluted C 1s XPS spectrum of (a) Z-NC, (b) Co-NC, (c) CoZ-NC, and (d) FeZ-NC.

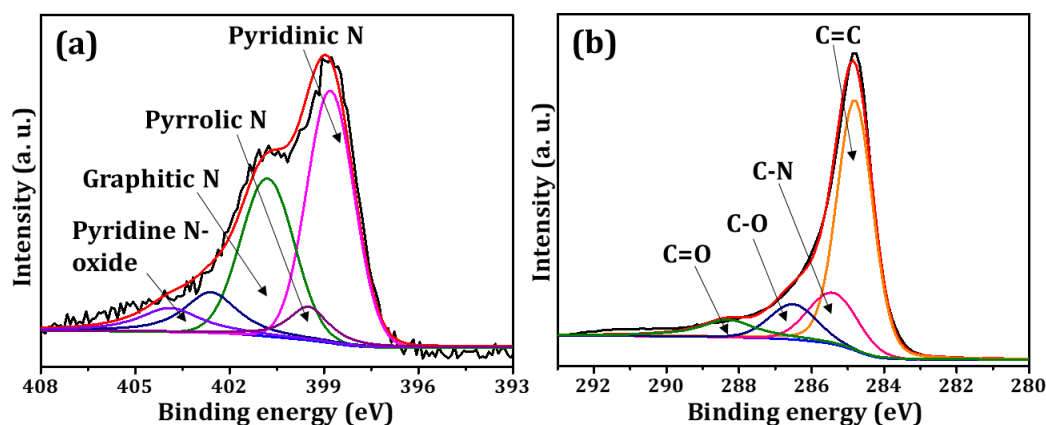


Figure 5.23 Deconvoluted (a) N 1s and (b) C 1s XPS spectrum of FeCoZ-NC.

5.3.5 Electrochemical Analysis

The electrocatalytic performance of the catalyst towards the sodium borohydride oxidation reaction was analyzed using a three-electrode system in an alkaline solution. The cyclic voltammetry curves (CVs) of FeCoZ-NC catalyst in the absence and presence of NaBH_4 are shown in **Figure 5.24**. The CV curve in the absence of NaBH_4 was rather different from that in the presence of NaBH_4 . In 1M KOH solution, without

NaBH₄, CV was devoid of any characteristics peak, whereas, in the presence of NaBH₄, there was an increase in current density, and a peak at 0.61 V was observed with a current density of 56.5 mA cm⁻². This enhancement in the current density represented that the FeCoZ-NC electrode had catalytic activity towards the electrochemical BOR.

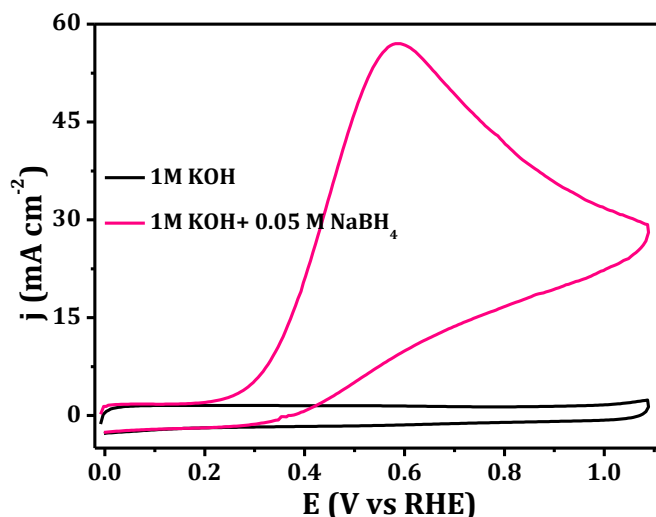


Figure 5.24 Comparison of CVs of FeCoZ-NC in the absence and presence of NaBH₄ and with no electrode rotation.

The comparison of the electrocatalytic activities of all the prepared catalysts was done by running CV in 1 M KOH+ 0.05 M NaBH₄ solution at a scan rate of 50 mV s⁻¹ (**Figure 5.25**). There was no peak corresponding to the oxidation of NaBH₄ in Z-NC and FeZ-NC indicating that these two catalysts were electrocatalytically inactive towards oxidation of BH₄⁻. The BOR inactivity in Z-NC was due to the absence of metallic species. Even though FeZ-NC contained Fe-N_x centers, it was also found to be BOR inactive suggesting that Fe-N_x was not contributing towards BOR catalysis. All the other catalysts containing Co-N_x active sites (Co-NC, CoZ-NC, and FeCoZ-NC) displayed BOR activity. The onset potential was found to be similar for Co-NC, CoZ-NC, and FeCoZ-NC, but the oxidation current density was the highest for FeCoZ-NC (56.5 mA cm⁻²). The higher peak current density of the CV curve implies higher electrocatalytic activity indicating that FeCoZ-NC has the highest BOR activity among the prepared catalysts. Co-N_x has thus substantial role in the enhancement of BOR activity while Fe-N_x active sites could not catalyze the BOR activity. The BOR performance of FeCoZ-NC containing both cobalt and iron surpassed Co-NC and CoZ-NC suggesting that the amount of Co-N_x active center was not the only factor determining the BOR performance. Factors like in situ porosity creation arising due

to Zn evaporation, N-doped carbon nanotube formation (evidenced from TEM), and the synergistic effect of Co and Fe dopants played a significant role.

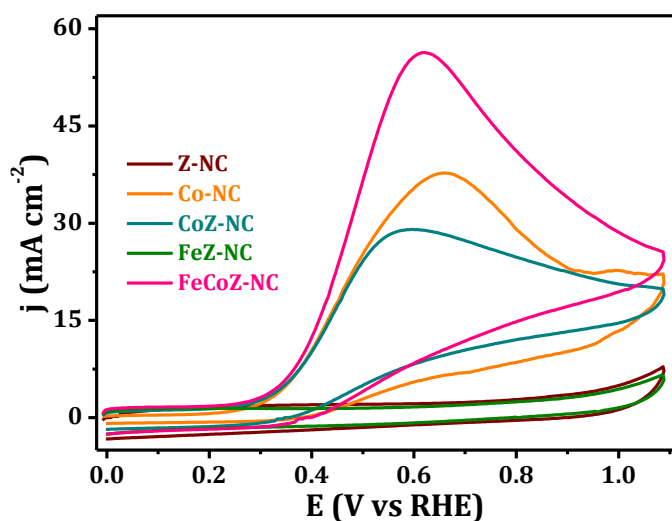


Figure 5.25 Comparison of CVs of Z-NC, Co-NC, CoZ-NC, FeZ-NC, and FeCoZ-NC in 1 M KOH+0.05 M NaBH₄ with no electrode rotation.

The catalytic performance of the FeCoZ-NC electrode was further explored by varying the concentration of NaBH₄. **Figure 5.26a** displayed the CVs of FeCoZ-NC under different concentrations of NaBH₄ at a fixed KOH concentration of 1 M. Obvious anodic peak was observed between 0.4 V to 0.8 V for all the CV curves and were attributed to the NaBH₄ electrooxidation. As the potential was scanned in the positive direction, the anodic current response of all the CVs got enhanced. The oxidation current density increased from 12 mA cm⁻² (0.01 M) to 57 mA cm⁻² (0.05 M) with increase in concentration of NaBH₄. The oxidation peak shifted towards the positive direction and the current increased linearly with NaBH₄ concentration.

The kinetics of electrooxidation of NaBH₄ can be evaluated by the following equation.¹⁴

$$j_p = zC_{NaBH_4}^\beta \quad (5.8)$$

Where j_p is the peak current density, z is a constant, C refers to the NaBH₄ concentration and β is the reaction order.

The plot of peak current density against the concentration of NaBH₄ (**Figure 5.26b**) gives a straight line implying that electrooxidation of NaBH₄ on FeCoZ-NC catalyst is

an irreversible process.³⁹ The BOR reaction order at FeCoZ-NC was calculated from the slope of $\ln j_p$ vs $\ln C_{\text{NaBH}_4}$ plot (**Figure 5.26c**) and the obtained value of 0.97, indicated a first-order reaction.^{40,41}

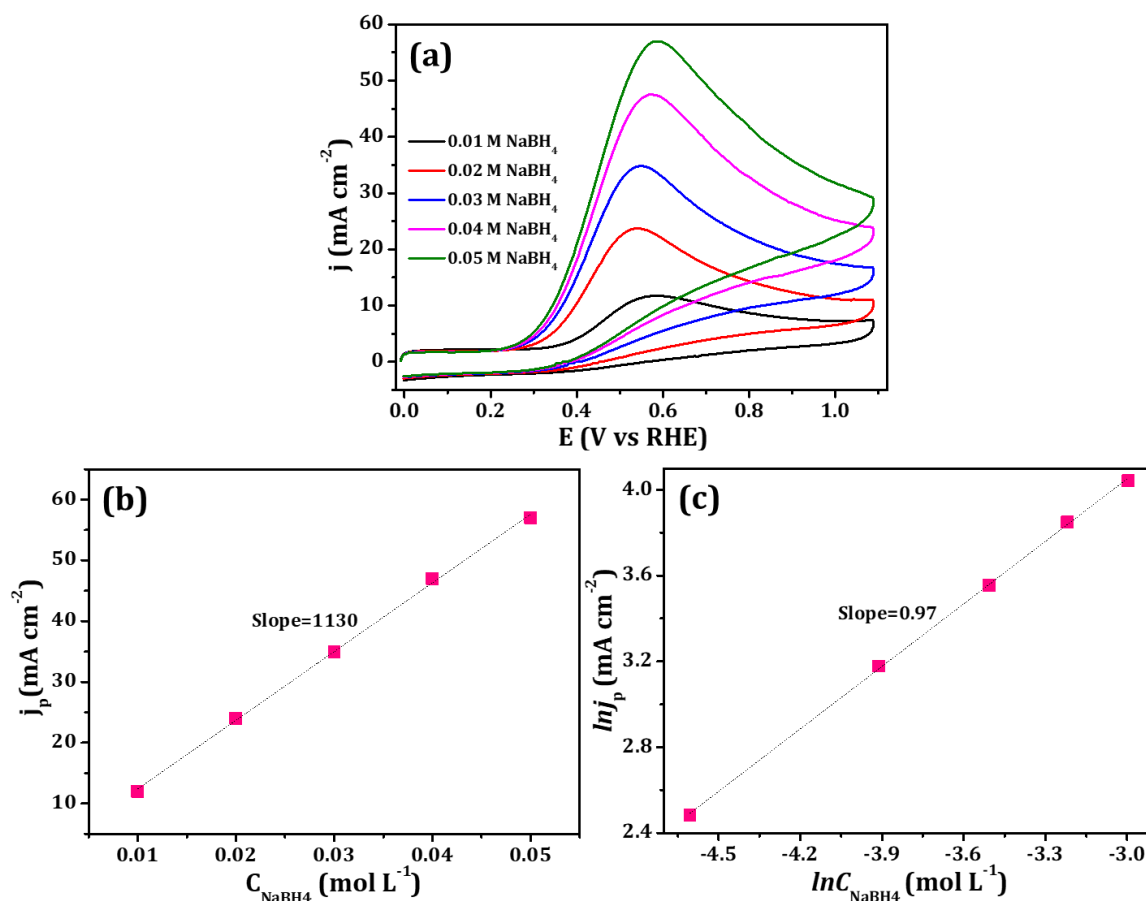


Figure 5.26 (a) CVs of FeCoZ-NC sample at different concentrations of NaBH₄ in 1 M KOH and (b) corresponding j_p vs C_{NaBH_4} plot and, (c) $\ln j_p$ vs $\ln C_{\text{NaBH}_4}$ plot.

The LSV of FeCoZ-NC was carried out at different scan rates in 1M KOH+0.05 M NaBH₄ and the result is shown in **Figure 5.27a**. With the increase of scan rate, there was an increase in current density which was due to the facilitated reactant diffusion and higher charge transfer at faster scan rates.⁴² Moreover, the peak potential moved to a more positive value suggesting that the electrooxidation of NaBH₄ is an irreversible process. The dependence of increased current density on the scan rate was determined by plotting peak potential (j_p) against the square root of scan rate (**Figure 5.27b**), which follows the Randles–Sevcik equation varying linearly with the square root of applied scan rate. This indicated the dominance of diffusion towards electrochemical response.

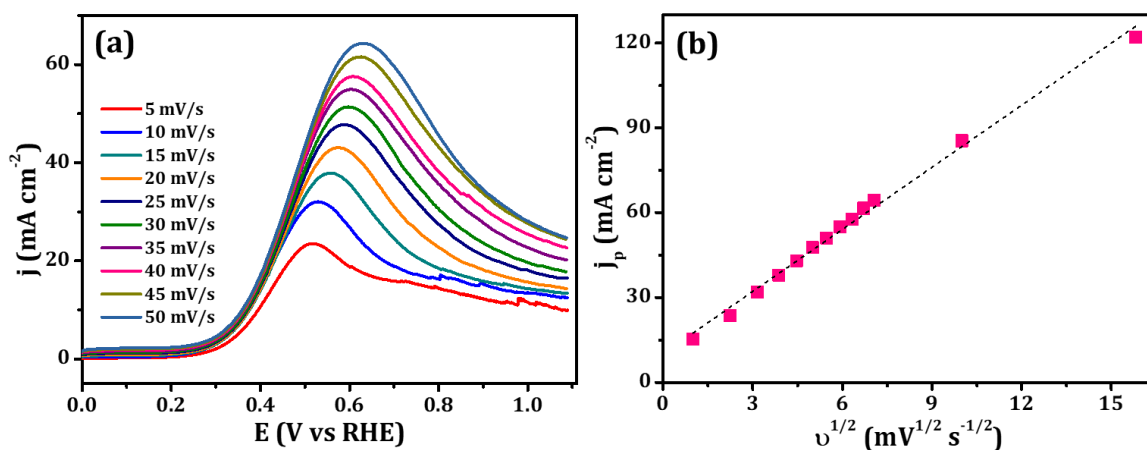


Figure 5.27 (a) LSVs of FeCoZ-NC recorded at different scan rates in 1 M KOH+0.05 M NaBH₄ and, (b) dependence of j_p on $v^{1/2}$.

LSV of Co-NC, CoZ-NC, and FeCoZ-NC at different electrode rotation speeds were carried out in 1M KOH+0.05 M NaBH₄ at a scan rate of 10 mV s⁻¹ (**Figure 5.28a, b & c**).

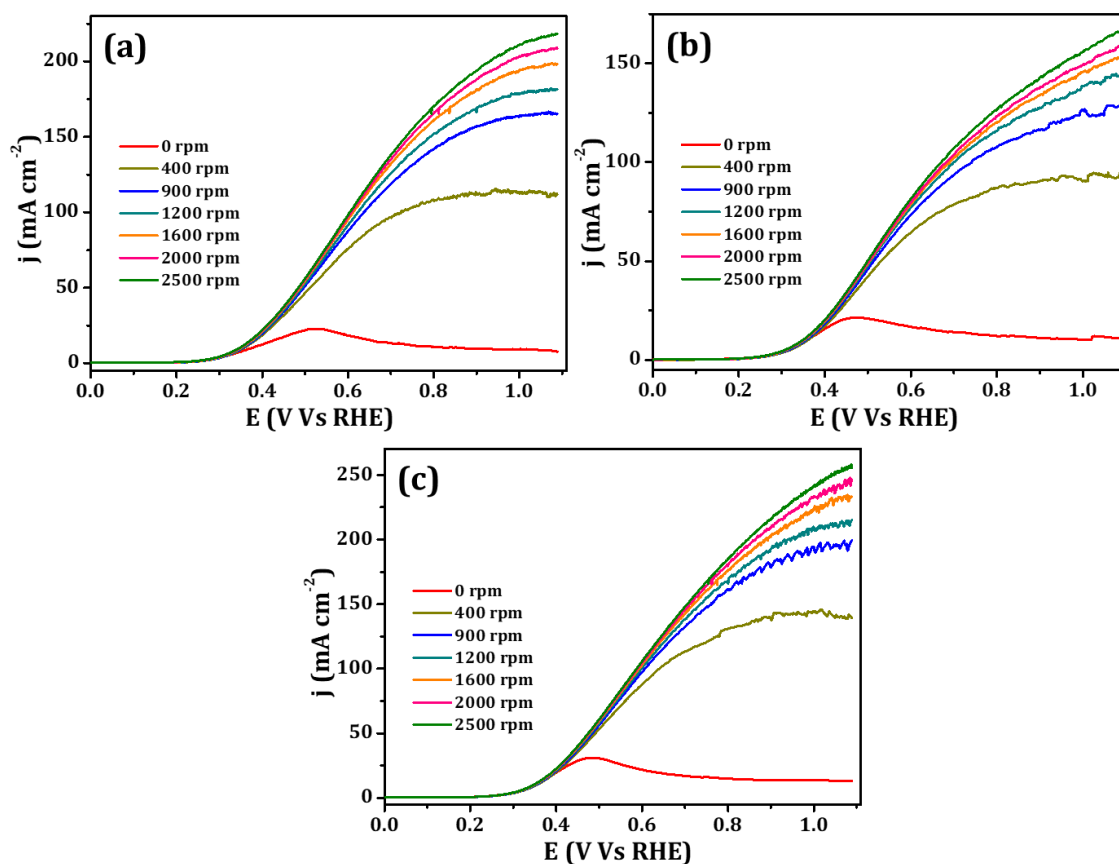


Figure 5.28 LSVs of (a) Co-NC, (b) CoZ-NC, (c) FeCoZ-NC recorded at different electrode rotation in 1 M KOH+0.05 M NaBH₄ at a scan rate of 10 mV s⁻¹.

The correlation between current values and rotation rates was given by Koutecky-Levich (K-L) equation.

$$\frac{1}{j} = \frac{1}{j_k} + \frac{1}{j_L} = \frac{1}{j_k} + \frac{1}{0.62nFD^{2/3}\nu^{-1/6}\omega^{1/2}} \quad (5.9)$$

$$\frac{1}{j} = \frac{1}{j_k} + \frac{1}{B\omega^{1/2}} \quad (5.10)$$

where j is the disk current density, j_k the kinetic controlled current density, j_L is the diffusion- limiting current density, F is the Faraday constant, D is the diffusion coefficient of the electrochemically active species, C is the concentration of BH_4^- , ν is the kinematic viscosity of the electrolyte solution, ω is the rotation rate of the electrode, and n is the number of exchanged electrons.

The K-L equation was used to calculate the number of electrons transferred during the BOR. K-L plots were obtained by plotting j^{-1} against $\omega^{-1/2}$. A linear relationship between j^{-1} and $\omega^{-1/2}$ was observed (**Figure 5.29**) and the number of electron transfers was calculated from the slope. The calculated n values in the BH_4^- electrooxidation reaction on Co-NC, CoZ-NC, and FeCoZ-NC electrodes were 5.3, 4.8, and 7.9 respectively. The highest number of exchanged electrons for FeCoZ-NC suggested that the direct electrooxidation of NaBH_4 was more likely to occur on this electrode rather than the hydrolysis of NaBH_4 .

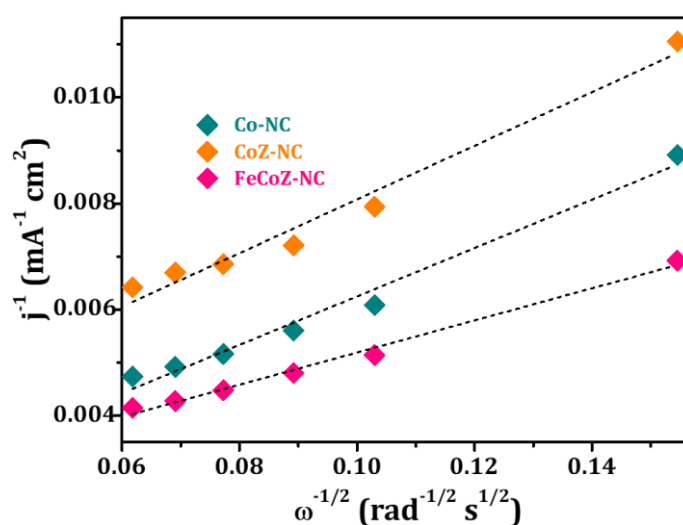


Figure 5.29 K-L plots comparison of Co-NC, CoZ-NC and FeCoZ-NC at 1.0 V.

Rotating ring disk electrode (RRDE) analysis was also carried out to find the number of electrons transferred per NaBH_4 molecule. RRDE measurements were done using a gold-ring rotating ring-disk electrode with a glassy carbon disc with a low catalyst loading of 0.04 mg cm^{-2} . A gold ring electrode was chosen for the experiment since gold is not electrocatalytically active towards BOR until a potential above $\sim 0.027 \text{ V}$. Therefore, RRDE measurements were carried out by setting the ring potential as 0.025 V . At this potential, the borohydride hydrolysis will be negligible at the ring electrode. Thus, the current obtained at the ring electrode will be due to the oxidation of hydrogen (HOR) produced by the disc electrode.

The number of electrons transferred per NaBH_4 molecule (n) was calculated from the RDE data based on the equation,

$$n = \frac{8I_d}{I_d + \frac{I_r}{N}} \quad (5.11)$$

Where, I_d is the disc current and I_r is the ring current. N is the current collection efficiency of the Au ring.⁴³

The number of electron transfer (n) was calculated by running chronoamperometry in which the disc potential was kept as 1 V . The CA analysis of FeCoZ-NC was carried out in 1 M KOH , with 0.05 M NaBH_4 , and the result is shown in **Figure 5.30a**. An n value of 7.85 obtained for FeCoZ-NC, was comparable to that obtained from the KL-plot. This result indicated near complete oxidation of NaBH_4 .

The electro-catalytic stability of FeCoZ-NC towards BOR was investigated by performing chronoamperometric analysis. The chronoamperometry was carried out at different potentials in $1 \text{ M KOH} + 0.05 \text{ M NaBH}_4$ solution. The test time at each potential was 1900 s . It can be seen from **Figure 5.30b** that, when the potential increases, the current density also increases, as the reaction driving force is large at a high potential.⁴⁴ Furthermore, the current density was significantly reduced at a high potential of 1 V and 0.8 V . This is owing to the rapid consumption of fuel in the solution at high potential, and the BH_4^- ions concentration on the surface of the FeCoZ-NC electrode is not enough to achieve steady-state electrooxidation.^{6,45} The smooth anodic current density platform in the CA curve indicated that FeCoZ-NC possessed good stability at these potentials.

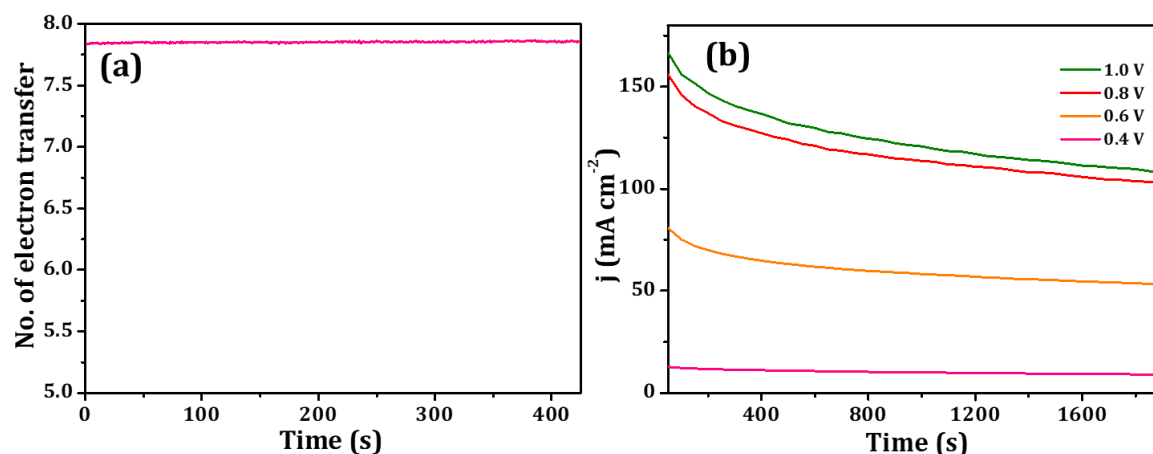


Figure 5.30 Number of electron transfers obtained at a disc potential of 1.0 V during RRDE measurement and (b) CA curves of FeCoZ-NC in 1 M KOH+0.05 M NaBH₄ tested at different fixed potentials.

The increase in borohydride oxidation current density and the lower onset potential in the FeCoZ-NC sample were mainly attributed to the presence of Co-N_x active sites. The *in situ* nitrogen doping on the carbon lattice, mainly pyridinic and graphitic N, created more active sites in addition to Co-N_x sites. The increased surface area and porosity arising from the evaporation of Zn facilitated the adsorption of more BH₄⁻ molecules to the catalyst surface. Metallic Co present in the catalyst also helped the oxidation of the adsorbed NaBH₄. Moreover, the enhanced hydrophilicity of the carbon lattice due to N-doping helped the accessibility of BH₄⁻ at the catalyst surface. The interconnected nanotubular structure formed by the catalytic activity of Fe enhanced the electrical conductivity and reactant diffusion. All the above factors made FeCoZ-NC a promising electrocatalyst for borohydride electrooxidation.

5.4 Conclusions

Fe, Co incorporated carbon nanotube catalyst (FeCoZ-NC) was developed from a single Fe, Co, Zn-ZIF precursor by a simple, fast, and aqueous room temperature synthesis approach. The carbon nanotube morphology achieved during carbonization by the catalytic action of doped Fe in the precursor enabled uniform distribution of metal/metal oxide nanoparticles as revealed from HRTEM. Moreover, the EDS analysis indicated the uniform distribution of nitrogen, and an almost equal amount of Fe and Co were also identified. It was found that both Fe and Co coexisted at the same position in the EDS image representing alloy type features of the metal centers

in the catalyst. XRD analysis showed the presence of metallic and oxide phases. The catalyst exhibited a high specific surface area of $321 \text{ m}^2 \text{ g}^{-1}$ with microporous features created by the evaporation of Zn during the carbonization of the trimetallic precursor. Catalytically active pyridinic and graphitic N and Co-N_x sites were identified from XPS. The borohydride oxidation current density reached 56.5 mA cm^{-2} at 0.61 V in 0.05 M NaBH₄+1 M KOH solution with good stability. The enhanced electrocatalytic performance towards NaBH₄ electrooxidation with better stability suggested that FeCoZ-NC is a promising catalyst for BOR.

References

1. Smith, W. The Role of Fuel Cells in Energy Storage. *J. Power Sources* **2000**, 86 (1), 74.
2. Tamaki, T.; Yamada, Y.; Kuroki, H.; Yamaguchi, T. Communication-Acid-Treated Nickel-Rich Platinum-Nickel Alloys for Oxygen Reduction and Methanol Oxidation Reactions in Alkaline Media. *J. Electrochem. Soc.* **2017**, 164 (7) F858.
3. Firouzjaie, H. A.; Mustain, W. E. Catalytic Advantages, Challenges, and Priorities in Alkaline Membrane Fuel Cells. *ACS Catal.* **2020**, 10 (1), 225.
4. Verma, A.; Basu, S. Direct Use of Alcohols and Sodium Borohydride as Fuel in an Alkaline Fuel Cell. *J. Power Sources* **2005**, 145 (2), 282.
5. Li, Z. P.; Liu, B. H.; Arai, K.; Asaba, K.; Suda, S. Evaluation of Alkaline Borohydride Solutions as the Fuel for Fuel Cell. *J. Power Sources* **2004**, 126 (1), 28.
6. Ma, X.; Ye, K.; Wang, G.; Duan, M.; Cheng, K.; Wang, G.; Cao, D. Facile Fabrication of Gold Coated Nickel Nanoarrays and its Excellent Catalytic Performance Towards Sodium Borohydride Electro-Oxidation. *Appl. Surf. Sci.* **2017**, 414, 353.
7. Lima, F. H. B.; Pasqualetti, A. M.; Molina Concha, M. B.; Chatenet, M.; Ticianelli, E. A. Borohydride Electrooxidation on Au and Pt Electrodes. *Electrochim. Acta* **2012**, 84, 202.
8. Graś, M.; Wojciechowski, J.; Lota, K.; Buchwald, T.; Ryl, J.; Lota, G. Correlation Between Partial Inhibition of Hydrogen Evolution Using Thiourea and Catalytic Activity of AB₅-Type Hydrogen Storage Alloy Towards Borohydride Electrooxidation. *J. Alloys Compd.* **2020**, 829, 154553.

9. An, L.; Jung, C. Y. Transport Phenomena in Direct Borohydride Fuel Cells. *Appl. Energy* **2017**, 205, 1270.
10. Olu, P. Y.; Bonnefont, A.; Braesch, G.; Martin, V.; Savinova, E. R.; Chatenet, M. Influence of the Concentration of Borohydride Towards Hydrogen Production and Escape for Borohydride Oxidation Reaction on Pt and Au Electrodes - Experimental and Modelling Insights. *J. Power Sources* **2018**, 375, 300.
11. Braesch, G.; Bonnefont, A.; Martin, V.; Savinova, E. R.; Chatenet, M. Borohydride Oxidation Reaction Mechanisms and Poisoning Effects on Au, Pt and Pd Bulk Electrodes: From Model (Low) To Direct Borohydride Fuel Cell Operating (High) Concentrations. *Electrochim. Acta* **2018**, 273, 483.
12. Pasqualetti, A. M.; Olu, P.-Y.; Chatenet, M.; Lima, F. H. B. Borohydride Electrooxidation on Carbon-Supported Noble Metal Nanoparticles: Insights into Hydrogen and Hydroxyborane Formation. *ACS Catal.* **2015**, 5 (5), 2778.
13. Zadick, A.; Petit, J. F.; Martin, V.; Dubau, L.; Demirci, U. B.; Geantet, C.; Chatenet, M. Ubiquitous Borane Fuel Electrooxidation on Pd/C and Pt/C Electrocatalysts: Toward Promising Direct Hydrazine-Borane Fuel Cells. *ACS Catal.* **2018**, 8 (4), 3150.
14. Li, B.; Song, C.; Huang, X.; Ye, K.; Cheng, K.; Zhu, K.; Yan, J.; Cao, D.; Wang, G. A Novel Anode for Direct Borohydride-Hydrogen Peroxide Fuel Cell: Au Nanoparticles Decorated 3D Self-Supported Reduced Graphene Oxide Foam. *ACS Sustain. Chem. Eng.* **2019**, 7 (13), 11129.
15. Rostamikia, G.; Janik, M. J. Direct Borohydride Oxidation: Mechanism Determination and Design of Alloy Catalysts Guided by Density Functional Theory. *Energy Environ. Sci.* **2010**, 3 (9), 1262.
16. Ye, K.; Ma, X.; Huang, X.; Zhang, D.; Cheng, K.; Wang, G.; Cao, D. The Optimal Design of Co Catalyst Morphology on a Three-Dimensional Carbon Sponge with Low Cost, Inducing Better Sodium Borohydride Electrooxidation Activity. *RSC Adv.* **2016**, 6 (47), 41608.
17. Song, C.; Wang, G.; Li, B.; Miao, C.; Ma, K.; Zhu, K.; Cheng, K.; Ye, K.; Yan, J.; Cao, D.; Yin, J. A Novel Electrode of Ternary CuNiPd Nanoneedles Decorated Ni Foam and its Catalytic Activity Toward NaBH₄ Electrooxidation. *Electrochim. Acta* **2019**, 299, 395.
18. Li, S.; Liu, Y.; Liu, Y.; Chen, Y. Study of CoO as an Anode Catalyst for a Membraneless Direct Borohydride Fuel Cell. *J. Power Sources* **2010**, 195 (21), 7202.

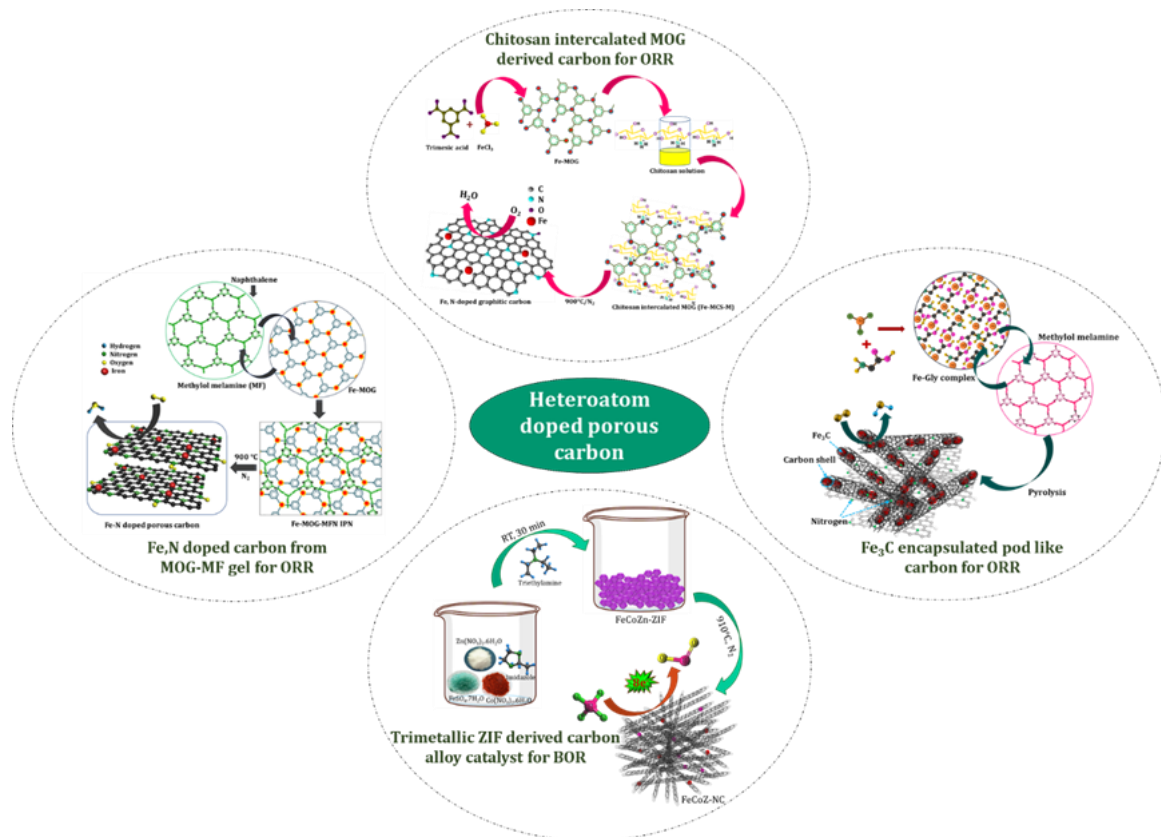
19. Zhang, J.; Zhang, D.; Cui, C.; Wang, H.; Jiao, W.; Gao, J.; Liu, Y. A Three-Dimensional Porous Co-P Alloy Supported on a Copper Foam as a New Catalyst for Sodium Borohydride Electrooxidation. *Dalton Trans.* **2019**, 48 (35), 13248.
20. Zhang, D.; Ye, K.; Cheng, K.; Cao, D.; Yin, J.; Xu, Y.; Wang, G. High Electrocatalytic Activity of Cobalt–Multiwalled Carbon Nanotubes–Cosmetic Cotton Nanostructures for Sodium Borohydride Electrooxidation. *Int. J. Hydrog. Energy* **2014**, 39 (18), 9651.
21. Martins, M.; Šljukić, B.; Metin, Ö.; Sevim, M.; Sequeira, C. A. C.; Şener, T.; Santos, D. M. F. Bimetallic PdM (M = Fe, Ag, Au) Alloy Nanoparticles Assembled on Reduced Graphene Oxide as Catalysts for Direct Borohydride Fuel Cells. *J. Alloys Compd.* **2017**, 718, 204.
22. Hansu, T. A.; Caglar, A.; Sahin, O.; Kivrak, H. Hydrolysis and Electrooxidation of Sodium Borohydride on Novel CNT Supported CoBi Fuel Cell Catalyst. *Mater. Chem. Phys.* **2020**, 239, 122031.
23. Guo, M.; Cheng, Y.; Yu, Y.; Hu, J. Ni-Co Nanoparticles Immobilized on a 3D Ni Foam Template as a Highly Efficient Catalyst for Borohydride Electrooxidation in Alkaline Medium. *Appl. Surf. Sci.* **2017**, 416, 439.
24. Yin, X.; Wang, Q.; Duan, D.; Liu, S.; Wang, Y. Amorphous NiB Alloy Decorated by Cu as the Anode Catalyst for a Direct Borohydride Fuel Cell. *Int. J. Hydrog. Energy* **2019**, 44 (21), 10971.
25. Tiwari, A.; Singh, V.; Nagaiah, T. C. Non-Noble Cobalt Tungstate Catalyst for Effective Electrocatalytic Oxidation of Borohydride. *ACS Appl. Mater. Interfaces* **2019**, 11 (24), 21465.
26. Antolini, E. Carbon Supports for Low-Temperature Fuel Cell Catalysts. *Appl. Catal. B* **2009**, 88 (1), 1.
27. Wang, W.; Xu, X.; Zhou, W.; Shao, Z. Recent Progress in Metal-Organic Frameworks for Applications in Electrocatalytic and Photocatalytic Water Splitting. *Adv. Sci.* **2017**, 4 (4), 1600371.
28. Zhu, Q. L.; Xia, W.; Akita, T.; Zou, R.; Xu, Q. Metal-Organic Framework-Derived Honeycomb-Like Open Porous Nanostructures as Precious-Metal-Free Catalysts for Highly Efficient Oxygen Electroreduction. *Adv. Mater.* **2016**, 28 (30), 6391.
29. Liu, J.; Wang, H.; Wu, C.; Zhao, Q.; Wang, X.; Yi, L. Preparation and Characterization of Nanoporous Carbon-Supported Platinum as Anode Electrocatalyst for Direct Borohydride Fuel Cell. *Int. J. Hydrog. Energy* **2014**, 39 (12), 6729.

30. Tiwari, A.; Nagaiah, T. C. Mesoporous Nitrogen-Rich Carbon as Metal-free Anode Catalyst for Borohydride Fuel Cells. *Energy Technol.* **2016**, 4 (4), 479.
31. Zhang, P.; Sun, F.; Xiang, Z.; Shen, Z.; Yun, J.; Cao, D. ZIF-Derived *in situ* Nitrogen-Doped Porous Carbons as Efficient Metal-Free Electrocatalysts for Oxygen Reduction Reaction. *Energy Environ. Sci.* **2014**, 7 (1), 442.
32. Kim, D.; Kim, D. W.; Hong, W. G.; Coskun, A. Graphene/ZIF-8 Composites with Tunable Hierarchical Porosity and Electrical Conductivity. *J. Mater. Chem. A* **2016**, 4 (20), 7710.
33. Thomas, M.; Illathvalappil, R.; Kurungot, S.; Nair, B. N.; Mohamed, A. A. P.; Anilkumar, G. M.; Yamaguchi, T.; Hareesh, U. S. Graphene Oxide Sheathed ZIF-8 Microcrystals: Engineered Precursors of Nitrogen-Doped Porous Carbon for Efficient Oxygen Reduction Reaction (ORR) Electrocatalysis. *ACS Appl. Mater. Interfaces* **2016**, 8 (43), 29373.
34. Yi, L.; Peng, X.; Ma, X.; Gao, Y.; Wang, X.; Lu, Y. Study of ZIF-Derived Iron and Nitrogen co-Doped Porous Carbon Supported Au Nanoparticles as Electrocatalyst for Borohydride Oxidation Reaction. *Ionics* **2022**, 28 (2), 849.
35. Yi, L.; Peng, X.; Ma, X.; Gao, Y.; Wang, X.; Lu, Y. Investigation of ZIF-Derived Co, N co-Doped Porous Carbon-Supported Au Nanoparticles as an Effective Catalyst for Borohydride Electrooxidation. *New J. Chem.* **2021**, 45 (45), 21206.
36. Unni, S. M.; Anilkumar, G. M.; Matsumoto, M.; Tamaki, T.; Imai, H.; Yamaguchi, T. Direct Synthesis of a Carbon Nanotube Interpenetrated Doped Porous Carbon Alloy as a Durable Pt-Free Electrocatalyst for the Oxygen Reduction Reaction in an Alkaline Medium. *Sustain. Energy Fuels* **2017**, 1 (7), 1524.
37. Shijina, K.; Illathvalappil, R.; Sumitha, N. S.; Sailaja, G. S.; Kurungot, S.; Nair, B. N.; Peer Mohamed, A.; Anilkumar, G. M.; Yamaguchi, T.; Hareesh, U. S. Melamine Formaldehyde–Metal Organic Gel Interpenetrating Polymer Network Derived Intrinsic Fe-N-Doped Porous Graphitic Carbon Electrocatalysts for Oxygen Reduction Reaction. *New J. Chem.* **2018**, 42 (23), 18690.
38. Zhang, D.; Wang, G.; Cheng, K.; Huang, J.; Yan, P.; Cao, D. Enhancement of Electrocatalytic Performance of Hydrogen Storage Alloys by Multi-Walled Carbon Nanotubes for Sodium Borohydride Oxidation. *J. Power Sources* **2014**, 245, 482.
39. Šljukić, B.; Milikić, J.; Santos, D. M.; Sequeira, C. A.; Macciò, D.; Saccone, A. Electrocatalytic Performance of Pt-Dy Alloys for Direct Borohydride Fuel Cells. *J. Power Sources* **2014**, 272, 335.

40. Oliveira, R. C.; Milikić, J.; Daş, E.; Yurtcan, A. B.; Santos, D. M.; Šljukić, B. Platinum/Polypyrrole-Carbon Electrocatalysts for Direct Borohydride-Peroxide Fuel Cells. *Appl. Catal. B* **2018**, 238, 454.
41. Santos, D.; Sequeira, C. Cyclic Voltammetry Investigation of Borohydride Oxidation at a Gold Electrode. *Electrochim. acta* **2010**, 55 (22), 6775.
42. Martins, M.; Metin, Ö.; Sevim, M.; Šljukić, B.; Sequeira, C. A.; Sener, T.; Santos, D. M. Monodisperse Pd Nanoparticles Assembled on Reduced Graphene Oxide-Fe₃O₄ Nanocomposites as Electrocatalysts for Borohydride Fuel Cells. *Int. J. Hydrog. Energy* **2018**, 43 (23), 10686.
43. Wu, C.; Zhu, J.; Wang, H.; Wang, G.; Chen, T.; Tan, Y. Porous Ni_{1-x}Cu_xO Nanowire Arrays as Noble-Metal-Free High-Performance Catalysts for Ammonia-Borane Electrooxidation. *ACS Catal.* **2020**, 10 (1), 721.
44. Zhang, D.; Wang, G.; Yuan, Y.; Li, Y.; Jiang, S.; Wang, Y.; Ye, K.; Cao, D.; Yan, P.; Cheng, K. Three-Dimensional Functionalized Graphene Networks Modified Ni Foam Based Gold Electrode for Sodium Borohydride Electrooxidation. *Int. J. Hydrog. Energy* **2016**, 41 (27), 11593.
45. Song, C.; Zhang, D.; Wang, B.; Cai, Z.; Yan, P.; Sun, Y.; Ye, K.; Cao, D.; Cheng, K.; Wang, G. Uniformly Grown PtCo-Modified Co₃O₄ Nanosheets as a Highly Efficient Catalyst for Sodium Borohydride Electrooxidation. *Nano Res.* **2016**, 9 (11), 3322.

Chapter 6

Summary and Scope of Future Work



Development of cost-effective catalysts for the fuel cell is of great importance because of the sluggish kinetics of oxygen reduction reaction (ORR) at the cathode and the extensive use of platinum-based catalyst. Heteroatom doped carbon with good electrical conductivity and surface area is considered to be a better alternative for Pt based catalysts. However, efficient modulation of the active sites by the simultaneous incorporation of porosity and heteroatoms, without affecting the electrical conductivity is still a challenging task. Among the diverse carbon precursors employed, MOGs are preferred as an excellent precursor for the preparation of porous carbons with heteroporous architecture.

MOGs are viscoelastic solid-like materials formed by metal-organic coordination force extending to 3D interconnected architectures. MOGs are potential precursor for high surface area porous carbon due to its flexibility in design and tunable pore structures. However, due to the lack of N in its structure, very little attention has been devoted to these materials. To address this issue, an inter penetrating network (IPN) structure was synthesized from a nitrogen abundant thermosetting polymer, melamine formaldehyde (MF) and the iron containing MOG. The introduction of MF into MOG precursor resulted in a polymer network of improved mechanical properties and yielded a stable end product upon pyrolysis. The strong covalently bonded organic polymer MF thus served as a less expensive nitrogen enriched precursor of carbon. Further, the incorporation of naphthalene into this IPN network altered the morphology and pore characteristics of the derived carbon thereby enhancing the electrocatalytic activity of the resultant Fe, N-doped heteroporous carbon. High BET surface area of $950 \text{ m}^2 \text{ g}^{-1}$ with a better degree of distribution of graphitic N and a good onset potential value of 0.91 V vs RHE in 0.1 M KOH solution was accomplished for the system.

In the quest for further improvements in doped carbon catalysts for ORR, an earth abundant natural polymer chitosan was chosen as the nitrogen source and substitute for melamine formaldehyde. Chitosan is a biopolymer with high nitrogen content (~7 wt.%) due to the presence of amine and acetamide containing functional groups in its structure. These functional groups are responsible for the nontoxic, biocompatible, and biodegradable properties of chitosan making it a green precursor for N-doped carbon materials. The intercalation of chitosan in the three dimensional network of

MOG provided stronger electrostatic interaction of cationic N sites of chitosan with Fe(III). The stronger gel network prevented the disintegration at the Fe-N sites, resulting in a pyrolysis product with higher amount of electrocatalytically active graphitic N. The morphological analysis revealed Fe distributed mesoporous graphitic carbon sheets, with a specific surface area value of $565 \text{ m}^2 \text{ g}^{-1}$. The higher percentage of graphitic N, apparent from the XPS data contributed to better catalytic performance. The electrocatalytic activity was comparable with that of the commercially available Pt/C via an efficient four-electron-dominant ORR pathway with a positive onset potential value of 0.925 V vs RHE . High durability after 5000 cycles further confirmed the feasibility of the developed electrocatalyst to be used for ORR.

Recent reports suggest that the activity of the Fe-N_x coordination active sites can be boosted by the coexistence of Fe/Fe₃C nanoparticles, in which the charge density of the Fe atom in the Fe-N_x configuration can be changed by metallic iron nanoparticles. Thus, iron carbide (Fe₃C) encapsulated hierarchical pod-like porous graphitic carbon structures were prepared by a simple pyrolysis of Fe-glycine complex integrated melamine formaldehyde resin precursor. The unique structure and stronger network of the resulting thermosetting resin facilitated the formation of porous carbon nanosheets while Fe catalyzed the formation of carbon nanotubes. The catalyst possessing high degree of graphitization with enhanced surface area ($205 \text{ m}^2 \text{ g}^{-1}$) exhibited high ORR activity with an onset potential of 0.95 V and a half-wave potential ($E_{1/2}$) of 0.80 V vs RHE in alkaline media through the four-electron reduction pathway.

Transition metal, N-doped porous carbon structures are also potential electrode materials for borohydride oxidation reactions in fuel cells. Carbon nanotube supported bimetallic electrocatalyst with high porosity was thus developed from a single trimetallic zeolitic imidazolate framework precursor (FeCoZn-ZIF) through a fast-aqueous room temperature synthesis strategy. Carbonization under an inert atmosphere yielded carbon alloy catalyst with enhanced porosity created by the Zn evaporation. The nanotubular structure of carbon assisted the faster electron transport. The oxidation current density reached 56.5 mA cm^{-2} at 0.61 V in $0.05 \text{ M NaBH}_4 + 1 \text{ M KOH}$ solution with good stability.

Suggestions for Future Work

- Establishing the pore structure correlation with the synthetic pathways of carbon structures.
- Investigations on the effect of multiple metals in the carbon matrix for oxygen reduction reaction activity.
- Online detection of formation of H₂ gas during the borohydride electrooxidation.
- Developing single atom /atomically dispersed metal catalysts based on high surface area porous carbon for electro catalytic applications.

ABSTRACT

Name of the Student: **Shijina K.**

Registration No.: **10CC18A39014**

Faculty of Study: **Chemical Sciences**

Year of Submission: **2022**

AcSIR academic centre/CSIR Lab: **CSIR-National Institute for Interdisciplinary Science and Technology (CSIR-NIIST)**

Name of the Supervisor: **Dr. U. S. Hareesh**

Title of the thesis: **Heteroatom doped porous carbon structures as electrocatalysts for fuel cells**

Fuel cells are well accepted as a green energy source because of its high efficiency, and sustainability. The basic chemical changes occurring in a fuel cell can be attributed to the reactions of oxygen reduction (ORR) at the cathode and hydrogen oxidation reaction (HOR) at the anode. The sluggish kinetics of oxygen reduction reaction and the extensive use of Pt-based catalyst are major barriers for the commercialization of fuel cells. Heteroatom doped porous carbon electrocatalysts gained much attention for the development of cost effective fuel cells. However, efficient modulation of the active sites by the incorporation of porosity and heteroatoms, without affecting the electrical conductivity is still a challenging task.

Chapter 1 provides an introduction to fuel cells, oxygen reduction reaction and a review of literature regarding the development of hetero atom doped porous carbon electrocatalysts. Chapter 2 focuses on the development of Fe, N-doped porous graphitic carbon electrocatalyst by the pyrolysis of an interpenetrating polymer network (IPN) comprising of melamine formaldehyde and metal organic gel. Incorporation of naphthalene into the IPN network altered the morphology and pore characteristics of the derived carbon and thereby enhanced the electrocatalytic activity of the resultant Fe, N-doped carbon. Chapter 3 reports a green precursor chitosan, as a nitrogen source for the intercalation with metal organic gel for the synthesis of N-doped Fe distributed mesoporous graphitic carbon. The higher percentage of graphitic N contributed to better catalytic performance. In chapter 4, iron carbide encapsulated pod-like graphitic carbon structures were prepared by simple pyrolysis involving Fe-glycine complex integrated melamine-formaldehyde resin precursor. The catalyst with high degree of graphitization and enhanced specific surface area exhibited the highest ORR activity. In chapter 5, carbon nanotube supported bimetallic electrocatalyst with high porosity was developed from a single trimetallic zeolitic imidazolate framework precursor for borohydride electrooxidation. The enhanced electrocatalytic performance induced by the morphological and textural features of the porous carbon catalysts enabled NaBH_4 electrooxidation via an eight-electron transfer indicating its potential as a promising catalyst for BOR.

Details of Publications Emanating from the Thesis

1. **Kottarathil Shijina**, Sreekanth Narayanaru, Sreekuttan M. Unni, Takanori Tamaki, Hidenori Kuroki, Unnikrishnan Nair Saraswathy Hareesh, Gopinathan M. Anilkumar, and Takeo Yamaguchi, Selective borohydride oxidation reaction of zeolitic imidazole framework derived bimetallic carbon alloy electrocatalysts for alkaline fuel cell applications, *ACS Applied Energy Materials*, **2022**
2. **Kottarathil Shijina**, Rajith Illathvalappil, S. Nisa, G. S. Sailaja, A. Peer Mohamed, Balagopal N. Nair, Gopinathan M. Anilkumar, Sreekumar Kurungot, Takeo Yamaguchi and U. S. Hareesh, Fe³⁺ stabilized 3D cross-linked glycine-melamine formaldehyde networks as precursor for highly efficient oxygen reduction catalyst in alkaline media, *Materials Letters*, **2020**, 264, 127365
3. **Kottarathil Shijina**, Rajith Illathvalappil, N. S. Sumitha, G. S. Sailaja, Sreekumar Kurungot, Balagopal N. Nair, A. Peer Mohamed, Gopinathan M. Anilkumar, Takeo Yamaguchi and U. S. Hareesh, Melamine formaldehyde-metal organic gel interpenetrating polymer network derived intrinsic Fe-N-doped porous graphitic carbon electrocatalysts for oxygen reduction reaction, *New Journal of Chemistry*, **2018**, 42, 18690.
4. **Kottarathil Shijina**, Rajith Illathvalappil, Sreekumar Kurungot, Balagopal N. Nair, A. Peer Mohamed, Takeo Yamaguchi, Gopinathan M. Anilkumar, U. S. Hareesh and G. S. Sailaja, Chitosan Intercalated Metal Organic Gel as a Green Precursor of Fe Entrenched and Fe Distributed N-Doped Mesoporous Graphitic Carbon for Oxygen Reduction Reaction, *ChemistrySelect*, **2017** (28), 8762–8770.

Details of Publications not related to Thesis

1. Midhun, M.; Pragatheeswaran, A.; Sankar, S.; **Shijina, K.**; Firozkhan, M.; Mohamed, A. A. P.; Ananthapadmanabhan, P.V.; Warriar, K.G.K.; Hareesh, U. S., Synthesis, spray granulation and plasma spray coating of lanthanum phosphate nanorods for thermal insulation coatings, *Ceramics International*, **2017**, 43 (6), 4858–4865.
2. **Shijina, K.**; Sankar, S.; Midhun, M.; Firozkhan, M.; Nair, B. N.; Warriar, K. G. K.; Hareesh, U. S., Very low thermal conductivity in lanthanum phosphate-zirconia ceramic nanocomposites processed using a precipitation-peptization synthetic approach, *New Journal of Chemistry*, **2016**, 40, (6), 5333-5337.

List of Conference Presentations

1. “Zeolitic Imidazole Framework Derived Bimetallic Carbon Alloy Catalyst for the Electrocatalytic Borohydride Oxidation Reaction” (poster presentation) in 28th **FCDIC Fuel Cell Symposium 2021** held at Tokyo, Japan.

2. "Fe, N-Doped Porous Carbon Electrocatalyst for Oxygen Reduction Reaction in Fuel Cell" (oral presentation) in National Seminar on Advanced Functional Materials for Analytical, Energy, Environmental and Biomedical Applications (**NSAFM-2019**) held at Trivandrum.
3. "Fe, N-Doped Porous Carbon Derived from Metal Organic Gel-Melamine Formaldehyde Interpenetrating Network as Highly efficient Durable Electrocatalyst for Fuel Cells" (poster presentation) in International Conference on Recent Trends in Materials Science and Technology (**ICMST-2018**) held at Trivandrum.
4. "Metal Organic Gel-Melamine Formaldehyde Interpenetrating Network Derived Fe, N Doped Porous Carbon as Electrocatalyst for Oxygen Reduction Reaction" (poster presentation) in Polymer Conference for Young Researchers (**PCYR-2018**) held at Trivandrum.
5. "Fe-N Doped Carbon as Electrocatalysts for Oxygen Reduction Reaction in Fuel cell" (oral presentation) in Research Scholar Symposium on Materials Science and Engineering (**2018**) held at Trivandrum.
6. "Chitosan Intercalated Metal Organic Gel as a Green Precursor of Fe-N Doped Mesoporous Graphitic Carbon for Oxygen Reduction Reaction" (poster presentation) in International Conference on Expanding Horizons of Technological Applications of Ceramics and Glasses (**EH-TACAG-2017**) held at Pune (Best poster presentation).



Corrigendum

Corrigendum to “Fe³⁺ stabilized 3D cross-linked glycine-melamine formaldehyde networks as precursor for highly efficient oxygen reduction catalyst in alkaline media” [Mater. Lett. 264 (2020) 127365]

Shijina Kottarathil ^{a,b,c}, Rajith Illathvalappil ^{b,d}, S. Nisa ^e, G.S. Sailaja ^{e,*}, A. Peer Mohamed ^a, Balagopal N. Nair ^f, M. Anilkumar Gopinathan ^f, Sreekumar Kurungot ^{b,d}, Takeo Yamaguchi ^c, U.S. Hareesh ^{a,b,*}

^a Materials Science and Technology Division (MSTD), CSIR-NIIST, Thiruvananthapuram, India

^b Academy of Scientific and Innovative Research (AcSIR), Ghaziabad-201002, India

^c Laboratory for Chemistry and Life Science, Tokyo Institute of Technology, Yokohama, Japan

^d Physical and Materials Chemistry Division, CSIR-National Chemical Laboratory, India

^e Department of Polymer Science and Rubber Technology, Cochin University of Science and Technology, India

^f R&D Centre, Noritake Company LTD, Japan

The authors regret for the inconvenience caused. In the originally published article, second affiliation was incorrect. Please find the correct affiliation below.

^bAcademy of Scientific and Innovative Research (AcSIR), Ghaziabad 201002, India.

The authors would like to apologise for any inconvenience caused.

DOI of original article: <https://doi.org/10.1016/j.matlet.2020.127365>.

* Corresponding authors at: Materials Science and Technology Division (MSTD), CSIR-NIIST, Thiruvananthapuram, India (U.S. Hareesh).

E-mail addresses: sailajags@cusat.ac.in (G.S. Sailaja), hareesh@niist.res.in (U.S. Hareesh).

<https://doi.org/10.1016/j.matlet.2022.132192>





Fe³⁺ stabilized 3D cross-linked glycine-melamine formaldehyde networks as precursor for highly efficient oxygen reduction catalyst in alkaline media



Shijina Kottarathil^{a,b,c}, Rajith Illathvalappil^{b,d}, Nisa S.^e, Sailaja G.S.^{e,*}, Peer Mohamed A.^a, Balagopal N. Nair^f, Anilkumar Gopinathan M.^f, Sreekumar Kurungot^{b,d}, Takeo Yamaguchi^c, Hareesh U.S.^{a,b,*}

^a Materials Science and Technology Division (MSTD), CSIR-NIIST, Thiruvananthapuram, India

^b Academy of Scientific and Innovative Research AcSIR, India

^c Laboratory for Chemistry and Life Science, Tokyo Institute of Technology, Yokohama, Japan

^d Physical and Materials Chemistry Division, CSIR-National Chemical Laboratory, India

^e Department of Polymer Science and Rubber Technology, Cochin University of Science and Technology, India

^f R&D Centre, Noritake Company LTD, Japan

ARTICLE INFO

Article history:

Received 2 December 2019

Received in revised form 3 January 2020

Accepted 13 January 2020

Available online 17 January 2020

Keywords:

Graphitic carbon alloy

Iron carbide

Fuel cell

ORR

ABSTRACT

Development of inexpensive oxygen reduction electrocatalyst with high activity and durability is very important. Herein, iron carbide encapsulated pod-like graphitic carbon structures were prepared by simple pyrolysis involving Fe-glycine complex integrated melamine-formaldehyde resin precursor. The best catalyst among those studied, Fe-Gly 2 MF-C, possessing high degree of graphitization ($I_D/I_G = 0.99$) and enhanced specific surface area ($205 \text{ m}^2/\text{g}$) exhibited the highest ORR activity with a half-wave potential of 0.80 V in alkaline medium through the four-electron reduction pathway.

© 2020 Elsevier B.V. All rights reserved.

1. Introduction

Carbon supported Pt-based catalysts have been widely used as efficient materials for the oxygen reduction reaction (ORR) [1,2]. Unfortunately, the limited availability, exorbitant price, low selectivity, and poor stability under the operating conditions are impediments to their widespread utilization [3,4]. Thus, rational design and synthesis of non-precious catalysts with comparable performance to that of Pt are of great significance. This has led to the emergence of inexpensive heteroatom doping. Recently, N-doped porous carbon materials as ORR catalysts have gained attraction by virtue of their high electrical conductivity, surface area and

porosity [5]. Besides N-doping, transition metal (Fe, Co, Ni, Cu, Mn, etc.) doping is also pursued for further improvements in the electrocatalytic activity [6,7]. Graphitic carbon shells activated by transition metals as encapsulated metal/metal carbide nanoparticles have emerged to be efficient ORR catalysts [8,9].

In this study, we report the synthesis of Fe₃C encapsulated tubular and sheet-like graphitic carbon by the carbonization of a hybrid thermosetting network structure formed by an optimized compositional mixing of Fe-glycine complex and melamine-formaldehyde (MF).

2. Experimental

Methylol melamine synthesized according to our previous report [10], was carefully introduced into the Fe-Glycine complex obtained by mixing required amount of glycine and FeCl₃ aqueous solutions, and allowed to complete polymerization at room temperature. The collected products were then pyrolyzed and characterized. (see SI for details)

* Corresponding author at: CSIR-NIIST, Materials Science and Technology Division, Industrial estate P. O., Thiruvananthapuram, Kerala-695019, India (Hareesh U.S.); Cochin University of Science and Technology, Department of Polymer Science and Rubber Technology, Kochi, Kerala-682022, India (Sailaja G.S.).

E-mail addresses: sailajags@cusat.ac.in (S. G.S.), gankumar@n.noritake.co.jp (A. Gopinathan M.), yamag@res.titech.ac.jp (T. Yamaguchi), hareesh@niist.res.in (Hareesh U.S.).

3. Results and discussion

During synthesis, Fe forms a strong coordinated complex with glycine which subsequently reacts with methylol melamine to form a cross-linked 3D structure (This complex formation occurs when Fe^{3+} is bonded to glycine through chelation between hydrophilic $-\text{COOH}$ and $-\text{NH}_2$ groups). The 3D cross-linked structure effectively reduces the agglomeration of iron particles by virtue of its strong interaction with the complex. Thus, Fe^{3+} gets stabilized within the network and results in the formation of N-doped porous graphitic carbon structure having uniform iron carbide distribution. Fe species transform the nearby graphitic carbon sheets into tubes during pyrolysis, thereby entrapping Fe_3C into the pod-like carbon structure (Fig. 1a).

XRD patterns (Fig. 1b) of the three samples showed peaks corresponding to graphitic carbon. (JCPDS: 75-1621) [11]. Fe-Gly 1 MF-C exhibited a less intense peak of Fe_3C at $49.1^\circ 2\theta$. With the increased amount of Fe, a greater number of Fe_3C peaks appeared at the 2θ values of 43.6° and 51° corresponding to (1 0 2) and

(1 2 2) planes, respectively (JCPDS:77-0255) [12] for Fe-Gly 2 MF-C and Fe-Gly 3 MF-C. In the Raman spectra (Fig. 1c), I_D/I_G ratio increased in the order Fe-Gly 1 MF-C (0.94) > Fe-Gly 2 MF-C (0.99) > Fe-Gly 3 MF-C (1.03), while increased Fe content caused a decrease in the degree of graphitization, since the graphitic structure of the resultant carbon gets deformed by the inclusion of Fe particles in the carbon lattice. Thus, the Fe-Gly 3 MF-C sample having the highest Fe content appeared to be more disordered in the Raman spectra. The Fe-Gly 1 MF-C sample with an enhanced graphitization degree may have increased electrical conductivity. Despite that, the decreased Fe content causes a reduction in the electrocatalytic active sites leading to reduced ORR activity. Thus, Fe-Gly 2 MF-C with moderate Fe content and good graphitization is presumed to show better ORR activity.

Electron micrographs of samples showed both sheet and tubular morphologies (Fig. 2a-c, Fig. S1). The HRTEM image (Fig. 2d) (SAED pattern in inset) was consistent with the (0 0 2) plane of the graphitic carbon with a d-spacing of 0.34 nm [13]. Unlike the other two samples, a slight difference in the morphology for

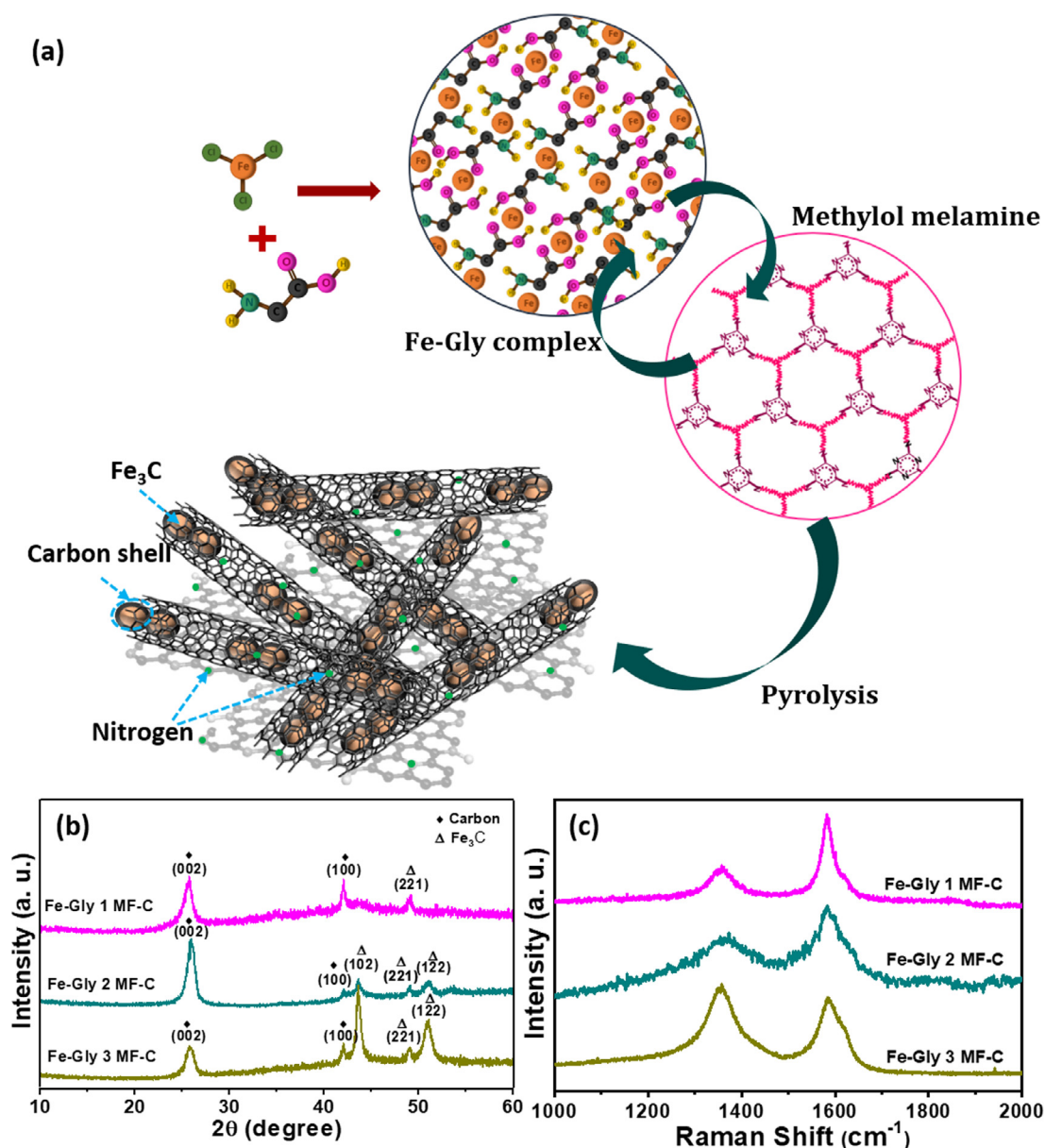


Fig. 1. (a) Schematic of the formation of Fe-Gly MF-C (b) XRD and (c) Raman spectra comparison.

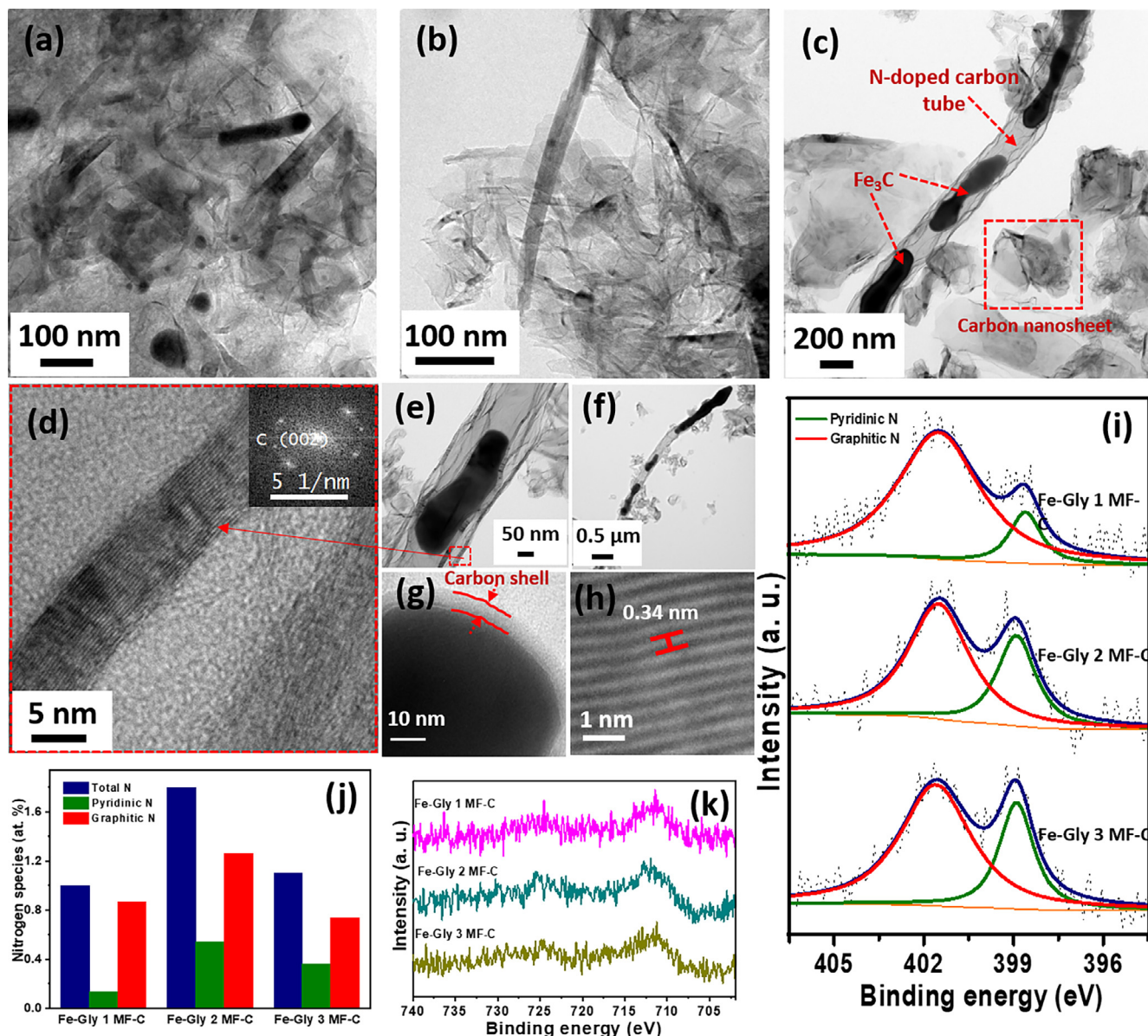


Fig. 2. TEM images of (a) Fe-Gly 1 MF-C (b) Fe-Gly 3 MF-C (c-h) Fe-Gly 2 MF-C (i) XPS deconvoluted N 1s spectra (j) atomic percentage of the different types of N species and (k) high-resolution Fe 2p XPS spectra.

Fe-Gly 2 MF-C was observed, where tubular hollow graphitic carbon enclosed with Fe_3C was seen. Even though the amount of Fe^{3+} used for the preparation of Fe-Gly 2 MF-C was less compared to Fe-Gly 3 MF-C, the TEM displayed more amount of Fe species (Fig. 2c). The increased Fe addition during Fe-Gly 3 MF-C synthesis may have caused agglomeration of Fe species upon pyrolysis and hence got washed off easily on acid treatment resulting in lesser Fe content in the catalyst microstructure. The formation of unique pod-like morphology in Fe-Gly 2 MF-C is ascribed to the creation of a strong 3D network structure with stabilized Fe^{3+} ions. This is possible by optimizing the metal/glycine ratio. The stabilization of Fe^{3+} ions reduced its agglomeration during pyrolysis and these stabilized Fe species catalyzes the tube formation of the nearby carbon resulting in pod-like carbon with embedded Fe_3C . With the Fe_3C particles being encapsulated inside the carbon structure, it is protected from acid attack. Occasionally, the Fe_3C particles are seemed to be protruding out of the tube (Fig. 2f), which will function as additional ORR active sites. The carbon tube, (Fig. 2c) depicts ~250 nm diameter and a wall thickness of ~8 nm (Fig. 2d) while

the entrapped Fe_3C particles possess an elongated morphology with a length of ~450 nm and a width of ~110 nm (Fig. 2e). HRTEM image of the Fe_3C (Fig. 2g) shows a graphitic carbon shell with a thickness of ~8 nm and d-spacing of 0.34 nm (Fig. 2h), thereby confirming the graphitic carbon structure surrounding the Fe_3C particle.

All the samples showed identical BET surface area (~205 m^2/g) and the pore size distribution curve obtained from NLDFT analysis indicated heteroporosity. The cumulative pore volume measured from BJH was found to be 0.54 $\text{cm}^3 \text{g}^{-1}$ for Fe-Gly 2 MF-C (Fig. S2).

The atomic percentages of elements present in the various samples obtained from XPS are summarized in Table S1. The deconvoluted N 1s spectra (Fig. 2i) shows pyridinic N (398.6 eV) and graphitic N (401.5 eV) species. Since the binding energy of the Fe-N bond is reported to be close to that of pyridinic N [14], the peak at ~398.6 eV is assigned to both pyridinic N and Fe-N. The fraction of the graphitic N was found higher in all the samples (Fig. 2j) and this may be due to the strong network structure of the precursors resulting in stronger Fe-N interaction. The strong

network ultimately led to the formation of entrapped N in the carbon matrix (graphitic N) upon pyrolysis rather than edge N species (pyridinic and pyrrolic N). In the high-resolution Fe 2p spectra (Fig. 2k), for all the samples, two main peaks appeared at 711.6 and 725 eV representing the binding energies of Fe 2p_{3/2} and Fe 2p_{1/2} of Fe³⁺ ion, respectively [15]. Further deconvolution of the peaks was found difficult as the percentage of Fe was very low.

The CV profiles for Fe-Gly 2 MF-C in N₂ and O₂ saturated 0.1 M KOH is given in Fig. 3a. Upon oxygen saturation, there is a rapid increase in current density in the cathodic direction owing to the reduction of oxygen. The ORR onset potential of Fe-Gly 1 MF-C and Fe-Gly 3 MF-C obtained from LSV curves were found to be 0.92 V whereas, for Fe-Gly 2 MF-C was 0.95 V which is only 50 mV lower than Pt/C (Fig. 3b). Also, there is only 30 mV difference in the E_{1/2} value of Fe-Gly 2 MF-C compared to Pt/C. In addition to the enhanced onset and E_{1/2}, Fe-Gly 2 MF-C also possessed a high limiting current density of -4.5 mA/cm².

The Koutecky-Levich (K-L) plots of all the samples have appeared to be linear indicating first order ORR kinetics (Fig. 3c).

The number of electrons transferred (n) and % H₂O₂ calculated from RRDE for Fe-Gly 2 MF-C was 3.8 and 10% respectively (Fig. 3d) with a Tafel slope of 73 mV/dec which is closer to that of Pt/C indicating faster ORR kinetics (Fig. 3e). Fe-Gly 2 MF-C exhibited excellent durability with a negligible shift in E_{1/2} (10 mV) after 5000 cycles of ADT (Fig. 3f), whereas Pt/C exhibited poor durability with a 30 mV shift in E_{1/2} (Fig. S3). The electrochemical properties of samples are listed in Table S2.

4. Conclusions

The optimized Fe-N co-doped catalyst (Fe-Gly 2 MF-C), exhibited excellent electrocatalytic behavior with an onset potential of 0.95 V with excellent stability during alkaline ORR. By virtue of the micro/mesoporous architecture, pod-like morphology and the incorporation of Fe/Fe₃C in carbon nanostructure, the catalytic activity gets enhanced. The present study thus provides an easy synthetic method for the development of Fe, N co-doped heteroporous carbon with outstanding electrocatalytic properties.

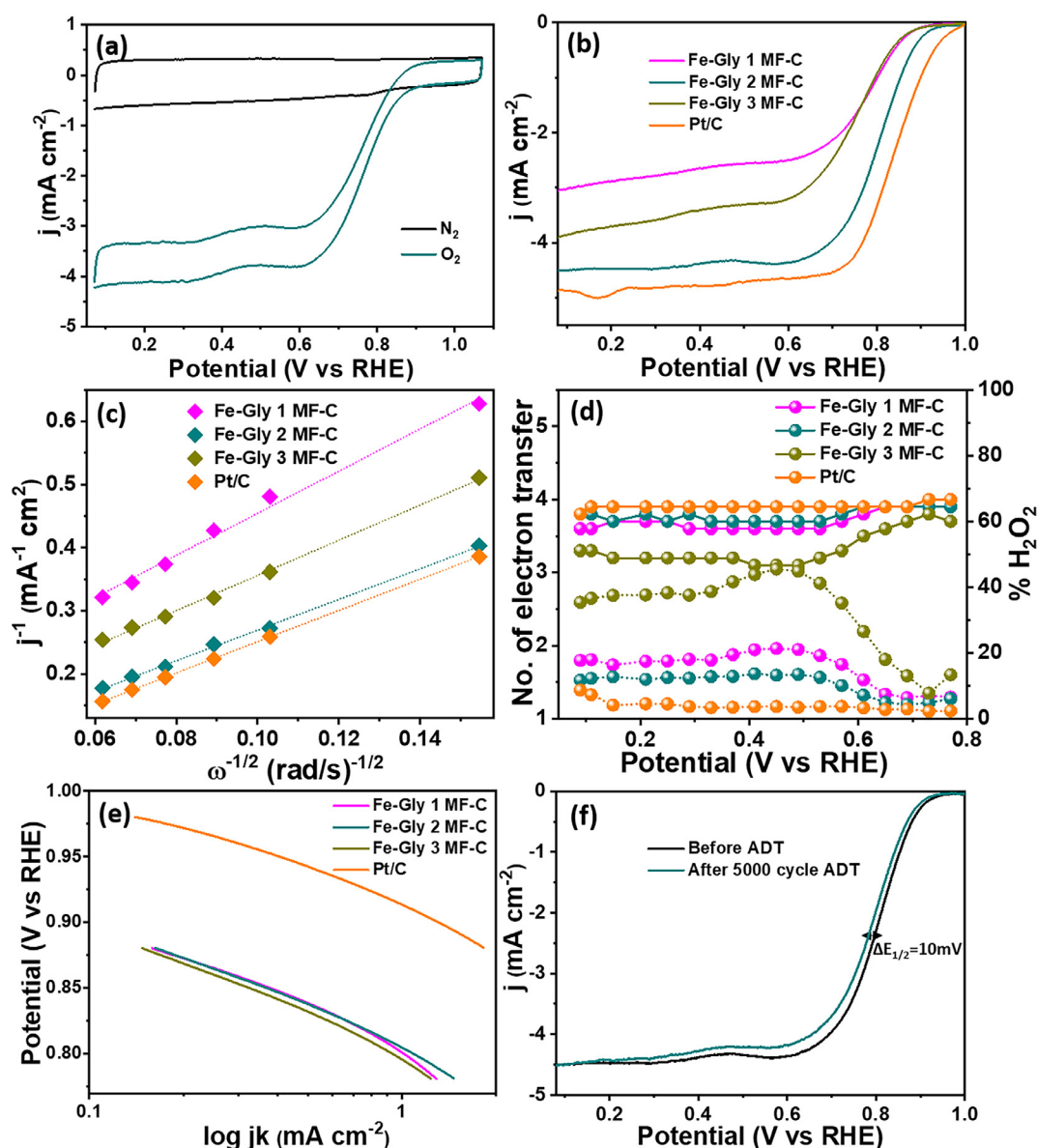


Fig. 3. (a) CVs of Fe-Gly 2 MF-C in N₂ and O₂ saturated 0.1 M KOH (b) LSV curves (c) K-L plots (d) number of electrons transferred & hydrogen peroxide yield obtained from the RRDE experiment (e) Tafel plots and (f) LSVs recorded before and after the 5000 cycle ADT of Fe-Gly 2 MF-C.

CRedit authorship contribution statement

K. Shijina: Methodology, Validation, Investigation, Writing - original draft. **Rajith Illathvalappil:** Investigation. **S. Nisa:** Investigation. **G.S. Sailaja:** Writing - review & editing, Conceptualization. **A. Peer Mohamed:** . **Balagopal N. Nair:** Writing - review & editing. **Gopinathan M. Anilkumar:** Writing - review & editing. **Sreekumar Kurungot:** Writing - review & editing. **Takeo Yamaguchi:** Writing - review & editing. **U.S. Hareesh:** Writing - review & editing, Supervision.

Declaration of Competing Interest

The authors declare that they have no known competing financial interests or personal relationships that could have appeared to influence the work reported in this paper.

Acknowledgments

Dr. K. K. Maiti, Mr. Kiran Mohan, and Mrs. Soumya are acknowledged for the Raman spectroscopy and electron microscopy analyses. Shijina K also acknowledges CSIR, Government of India for SRF.

Appendix A. Supplementary data

Supplementary data to this article can be found online at <https://doi.org/10.1016/j.matlet.2020.127365>.

References

- [1] B.C.H. Steele, A. Heinzl, *Nature* 414 (6861) (2001) 345–352.
- [2] M. Thomas, R. Illathvalappil, S. Kurungot, B.N. Nair, A.P. Mohamed, G.M. Anilkumar, T. Yamaguchi, U.S. Hareesh, *ChemistrySelect* 3 (30) (2018) 8688–8697.
- [3] K. Shijina, R. Illathvalappil, S. Kurungot, B.N. Nair, A.P. Mohamed, T. Yamaguchi, G.M. Anilkumar, U.S. Hareesh, G.S. Sailaja, *ChemistrySelect* 2 (28) (2017) 8762–8770.
- [4] Y. Munaiah, S. Boopathi, S. Senthil Kumar, P. Ragupathy, *Mater. Lett.* 239 (2019) 184–191.
- [5] M. Mukherjee, M. Samanta, S. Sarkar, G.P. Das, K.K. Chattopadhyay, *Mater. Lett.* 248 (2019) 8–11.
- [6] S.K. Singh, V. Kashyap, N. Manna, S.N. Bhange, R. Soni, R. Boukherroub, S. Szunerits, S. Kurungot, *ACS Catal.* 7 (10) (2017) 6700–6710.
- [7] T. Li, H. Deng, J. Liu, C. Jin, Y. Song, F. Wang, *Carbon* 143 (2019) 859–868.
- [8] Y. Qian, I.A. Khan, D. Zhao, *Small* 13 (37) (2017) 1701143.
- [9] W. Feng, M. Liu, J. Liu, Y. Song, F. Wang, *Catal. Sci. Technol.* 8 (19) (2018) 4900–4906.
- [10] K. Shijina, R. Illathvalappil, N.S. Sumitha, G.S. Sailaja, S. Kurungot, B.N. Nair, A. Peer Mohamed, G.M. Anilkumar, T. Yamaguchi, U.S. Hareesh, *New J. Chem.* 42 (23) (2018) 18690–18701.
- [11] R. Zhang, K. Huang, D. Wang, N. Hussain, A. Zhang, H. Wei, G. Ou, W. Zhao, C. Zhang, H. Wu, *Electrochim. Acta* 313 (2019) 255–260.
- [12] Y. Deng, G. Wang, K. Sun, B. Chi, X. Shi, Y. Dong, L. Zheng, J. Zeng, X. Li, S. Liao, *J. Power Sources* 417 (2019) 117–124.
- [13] Z. Miao, X. Wang, M.C. Tsai, Q. Jin, J. Liang, F. Ma, T. Wang, S. Zheng, B.J. Hwang, Y. Huang, S. Guo, Q. Li, *Adv. Energy Mater.* 8 (24) (2018) 1801226.
- [14] Q. Li, J. Zhao, M. Wu, C. Li, L. Han, R. Liu, *ChemistrySelect* 4 (2) (2019) 722–728.
- [15] Z. Yang, T. Zhao, X. Huang, X. Chu, T. Tang, Y. Ju, Q. Wang, Y. Hou, S. Gao, *Chem. Sci.* 8 (1) (2017) 473–481.